

Simulation of Fracture Processes using Global-Local Approach and Virtual Elements

Von der Fakultät für Maschinenbau
der Gottfried Wilhelm Leibniz Universität Hannover
zur Erlangung der *venia legendi* für das Fachgebiet Mechanik
angenommene Habilitationsschrift

von

Fadi Aldakheel

geboren am 01.01.1984 in Deirazzor - Syrien

Hauptberichter: Prof. Dr.-Ing. Peter Wriggers

Mitberichter: Prof. Dr. Laura De Lorenzis

Tag der Einreichung: 15.06.2020

Tag der mündlichen Prüfung: 15.03.2021

Institut für Kontinuumsmechanik der Gottfried Wilhelm Leibniz Universität Hannover

B21/2

Herausgeber:

Prof. Dr.-Ing. habil. Dr. h.c. mult. Dr.-Ing. E. h. Peter Wriggers

Organisation und Verwaltung:

Institut für Kontinuumsmechanik
Fakultät für Maschinenbau
Gottfried Wilhelm Leibniz Universität Hannover
An der Universität 1
D-30823 Garbsen
Web: www.ikm.uni-hannover.de

© Fadi Aldakheel
Institut für Kontinuumsmechanik
Fakultät für Maschinenbau
Gottfried Wilhelm Leibniz Universität Hannover
An der Universität 1
D-30823 Garbsen
Email: aldakheel@ikm.uni-hannover.de

Alle Rechte, insbesondere das der Übersetzung in fremde Sprachen, vorbehalten. Ohne Genehmigung des Autors ist es nicht gestattet, dieses Heft ganz oder teilweise auf fotomechanischem, elektronischem oder sonstigem Wege zu vervielfältigen.

ISBN 978-3-941302-41-9

Acknowledgements

This Habilitation is the outcome of three challenging and exciting years of my research work carried out between 2017 and 2020, during my employment as a leader of the **Material Modeling and Damage Mechanics Group** at the Institute of Continuum Mechanics at Leibniz Universitaet Hannover. I own my gratitude to all those who helped in making this thesis possible, as well as those who supported me in my life.

I would like to express my deep gratitude to my supervisor, Professor Peter Wriggers, for giving me the opportunity to do my Habilitation study under his guidance and for his support in academic and personal matters. I really appreciate his confidence in my work and the nomination for three of the most prestigious science awards: Richard-von-Mises Prize 2020, Heinz Maier-Leibnitz Prize 2021 and IACM John Argyris Award for Young Scientists 2022. My sincere thanks are extended to Professor Laura De Lorenzis (ETH Zürich), for her interest in my work, her comments and for her acceptance to become the co-examiner for my Habilitation thesis.

Next, I want to thank all my colleagues at the institute of Continuum Mechanics (IKM) for the pleasant working conditions, the excellent social atmosphere and their friendship.

With all my heart, I thank my family for their everlasting love, patience, encouragement and for supporting me to become the person that I am today. I would like to convey my heartfelt thanks to my beloved wife and our lovely children for all the support and understanding during the last years.

Hannover, March 2021

Fadi Aldakheel

Abstract

The underlying Habilitation aims to contribute to the research on fracture mechanics of solids across the scales. This active research field is driven by the investigation and development of new methods, processes and technologies applicable to engineering problems with complex material behavior of solids at fracture. It includes mathematically precise formulations of theoretical and computational models with emphasis on continuum physics as well as the development of variation methods and efficient numerical implementations tools. In particular, two directions will be considered in this contribution: (i) the construction of advanced multi-scale techniques and (ii) modern element technologies. On the multi-scale techniques, a robust and efficient Global-Local approach for numerically solving fracture-mechanics problems is developed in the first part of this contribution. This method has the potential to tackle practical field problems in which a large-structure might be considered and fracture propagation is a localized phenomenon. In this regard, failure is analyzed on a lower (Local) scale, while dealing with a purely linear problem on an upper (Global) scale. The modeling of crack formation at the Local scale is achieved in a convenient way by continuum phase-field formulations to fracture, which are based on the regularization of sharp crack discontinuities. For this purpose, a predictor-corrector scheme is designed in which the local domains are dynamically updated during the computation. To cope with different element discretizations at the interface between the two nested scales, a non-matching dual mortar method is formulated. Hence, more regularity is achieved on the interface. The development of advanced discretization schemes accounting for meshes with highly irregular shaped elements and arbitrary number of nodes is the main focus in the second part of this work. To this end, a relatively new method - the virtual element method (VEM) - will be presented here that leads to an exceptional efficient and stable formulation for solving a wide range of boundary value problems in science and engineering. The structure of VEM comprises a term in the weak formulation or the potential density functional in which the unknowns, being sought are replaced by their projection onto a polynomial space. This results in a rank-deficient structure, therefore it is necessary to add a stabilization term to the formulation. The performance of the virtual element method is comparable to using finite elements of higher order. It is even more robust than FEM in case of a severe distortion of the element.

Keywords: Computational Mechanics, Material Modeling, Virtual Element Method, Finite Element Method.

Zusammenfassung

Die vorliegende Habilitationsschrift enthält Beiträge zu Forschungsthemen im Bereich mehrskaliger Rissmechanik. Diese werden angetrieben durch die Entwicklung neuer Methoden, Prozesse und Technologien mit Anwendung in den Ingenieurwissenschaften zu komplexem Materialverhalten in Festkörpermechanik mit Rissbildung. Diese Habilitationsschrift legt Wert auf mathematisch präzise Beschreibungen von theoretischen sowie algorithmischen Modellen mit Fokus auf Kontinuumsmechanik. Ausserdem werden variationelle Methoden und deren effiziente numerische Behandlung diskutiert. Zwei Richtungen werden speziell betrachtet: (i) Konstruktion von fortgeschrittenen Multiskalenmethoden und (ii) moderne Element-Technologien. Hinsichtlich Multiskalentechniken wird ein robuster Glocal-Local-Ansatz für die numerische Lösung von Rissbildungsproblemen im ersten Teil der Habilitation entwickelt. Diese Methode hat das Potential auf realistische Probleme angewandt zu werden, wo grössere elastische Strukturen mit lokalisierten Rissen auftreten. Hier treten Schädigungsprozesse lokalisiert auf, während auf der globalen Skala lediglich ein linearisiertes Problem gerechnet werden muss. Die Rissmodellierung auf der lokalen Skala wird mit Hilfe eines Kontinuum-Phasenfeld-Ansatzes erreicht. Dieser basiert auf der Approximation von niederdimensionalen, scharf ausgeprägten, Materialunstetigkeiten. Hierzu wird mit einem sogenannten Predictor-Corrector-Verfahren gearbeitet, in welchem die lokalen Teilgebiete dynamisch aktualisiert werden. Die verschiedenen Element-Diskretisierungen der globalen und lokalen Teilgebiete wird am Interface mit Hilfe einer Dualen-Mortar-Methode erreicht. Somit wird eine höhere Regularität am Interface gewährleistet. Die Entwicklung von fortgeschrittenen Diskretisierungstechniken für Vernetzungen mit irregulären Elementen und beliebig vielen Knoten ist der Fokus im zweiten Teil dieser Schrift. Hierin wird eine relativ neue Methode - der virtuellen Finite-Elemente-Methode (VEM) - vorgestellt, welche hochgradig effizient und numerisch stabile Formulierungen erlaubt. Mit dieser können zahlreiche Randwertprobleme in Wissenschaft und Ingenieursanwendungen angegangen werden. Strukturell enthält die VEM einen zusätzlichen Term in der schwachen Formulierung oder ein Potential-Dichte-Funktional, in welcher die gesuchten Unbekannten durch eine Projektion auf den Raum der Polynome ersetzt werden. Diese Operation induziert eine Rang-Reduktion und daher muss ein Stabilisierungsterm zur Formulierung addiert werden. Die Leistungsfähigkeit der virtuellen Finite-Elemente-Methode verhält ist vergleichbar zu Finite-Elemente-Verfahren höherer Ordnung. Für stark verzerrte Elemente ist die VEM robuster als herkömmliche Finite-Elemente-Verfahren.

Stichworte: Berechnungsmechanik, Materialmodellierung, Virtuelle Elemente Methode, Finite Elemente Methode.

Contents

1. Introduction	1
1.1. Efficient Global-Local techniques for failure analysis	2
1.1.1. One-dimensional study	3
1.1.2. Adaptive concurrent multi-scale approach for anisotropic failure	7
1.1.3. Global-Local scheme for fracture in multi-field environments	7
1.1.4. Modeling of Local failure in multi-physics problems	8
1.2. Application of the Virtual Element Method (VEM) in Mechanics	8
1.2.1. Modeling of brittle fracture using an efficient virtual element scheme	11
1.2.2. Virtual element formulation for modeling of ductile fracture	12
1.2.3. VEM for 3D local thermo-elasto-plastic solids	12
1.2.4. Coupled thermomechanical response of gradient inelastic deformations	13
1.3. Outline of the work	13
I Efficient Global-Local Techniques for Failure Analysis	15
2. Global-Local approach for anisotropic failure in brittle solids	16
2.1. Introduction	16
2.2. Variational Anisotropic Phase-Field Brittle Fracture	19
2.2.1. The primary fields of anisotropic brittle solids	19
2.2.2. Variational formulation for the multi-field problem	19
2.2.3. Phase-field approximation of anisotropic crack topologies	21
2.2.4. Strain-energy decomposition	23
2.2.5. The Euler-Lagrange equations in a strong form	25
2.2.6. Crack driving force	26
2.2.7. Crack Driving State Function without Threshold	27
2.2.8. Crack Driving State Function with Threshold	28
2.2.9. Numerical Model Problem	30
2.3. Global-Local Formulation	30
2.3.1. Non-overlapping domain decomposition formulation	31
2.3.2. Global-Local formulation	34
2.3.3. Variational formulation for the Global-Local coupling system	37
2.3.4. Dirichlet-Neumann type boundary conditions	38
2.3.5. Robin-type boundary conditions	39
2.3.6. Derivation of Robin-Type Boundary conditions	41
2.3.7. Spatial discretization	44
2.3.8. Finite Element Analysis	44
2.4. Predictor-Corrector Adaptivity Applied to the Global-Local Formulation	46
2.4.1. Predictor step	46
2.4.2. Corrector step	48

2.4.3.	The final predictor-corrector scheme	48
2.4.4.	Homogenized phase-field solution on the global level	49
2.5.	Numerical Examples	51
2.5.1.	Goals of the computations	51
2.5.2.	Geometry, data and solution procedures	51
2.5.3.	Example 1: Isotropic single-edge-notched shear test	53
2.5.4.	Example 2: Analysis of transversely isotropic single-edge-notched tension test	56
2.5.5.	Example 3: Investigation of transversely isotropic heterogeneous L-shaped panel test	61
2.5.6.	Example 4: Investigation of transversely isotropic double-edge-notched tension	66
3.	Global-Local approach for hydraulic fracture in poroelastic media . . .	69
3.1.	Introduction	69
3.2.	Phase-field modeling of hydraulic fracture	70
3.2.1.	Governing equations	70
3.2.2.	Constitutive functions	74
3.2.3.	Variational formulations derived for the coupled multi-field problem	76
3.3.	Extension Towards Global-Local Formulations	76
3.3.1.	Governing formulations for the Global-Local coupling system	78
3.3.2.	Standard Dirichlet-Neumann boundary conditions	80
3.3.3.	Robin-type boundary conditions	80
3.4.	Numerical Examples	84
3.4.1.	Hydraulically induced crack driven by fluid volume injection	84
3.4.2.	Joining of two cracks driven by fluid volume injection	90
4.	A microscale model for failure in poro-elasto-plastic media	95
4.1.	Introduction	95
4.2.	Experimental investigation and geometrical set-up	97
4.3.	Governing equations for the multi-field problem	98
4.3.1.	Basic kinematics and constitutive formulation	98
4.3.2.	Energetic response function	102
4.3.3.	Plastic Dissipation	103
4.4.	Weak formulations for the coupled problem	104
4.5.	Representative numerical example	105
4.5.1.	Dried case (D)	106
4.5.2.	Wet case (W)	107
II	Advanced Virtual Element Method	109
5.	2D Virtual elements for phase-field modeling of brittle fracture	110
5.1.	Introduction	110

5.2.	Basic kinematics at small strains	112
5.2.1.	Displacement and crack phase-field	112
5.2.2.	Constitutive evolution of crack phase-field	114
5.3.	Variational based phase-field approach to brittle fracture	115
5.3.1.	Constitutive work density function	115
5.3.2.	Dissipation potential function	115
5.3.3.	Variational principle for the two-field evolution problem	116
5.3.4.	Time-discrete incremental variational formulation	117
5.3.5.	Crack driving state functions for different fracture criteria	118
5.4.	Formulation of the virtual element method	119
5.4.1.	Ansatz functions for VEM	119
5.4.2.	Construction of the virtual element	122
5.5.	Representative numerical examples	124
5.5.1.	Investigation of single-edge notched tension test	124
5.5.2.	Analysis of a three-point bending test	128
5.5.3.	Analysis of a crack in a Bi-Material plate	131
5.5.4.	Tensile test with two notches or holes	134
6.	2D Virtual elements for phase-field modeling of ductile fracture	135
6.1.	Introduction	135
6.2.	Governing equations for phase field ductile fracture	137
6.3.	Formulation of the virtual element method	141
6.3.1.	Ansatz functions for VEM	141
6.3.2.	Construction of the virtual element	143
6.4.	Representative numerical examples	147
6.4.1.	Single-edge notched shear test	147
6.4.2.	Axial stretch of a bar	149
7.	3D Virtual elements for finite thermo-plasticity problems	153
7.1.	Introduction	153
7.2.	Governing equations	154
7.2.1.	Basic kinematics at finite strains	154
7.2.2.	Energetic and dissipative response functions	156
7.2.3.	Global constitutive equations	158
7.3.	Virtual element discretization	159
7.4.	Representative numerical examples	163
7.4.1.	Necking of a bar	164
7.4.2.	Forming of a steel bolt	168
8.	Micromorphic approach for 3D gradient thermo-plastic solids	171
8.1.	Introduction	171
8.2.	Introduction of Primary Field Variables	173
8.2.1.	Deformation map and temperature field	173

8.2.2. Isotropic strain-gradient plasticity	174
8.2.3. Global primary fields and constitutive state variables	174
8.3. Constitutive Functions of the Coupled Problem	175
8.3.1. Energetic response function	175
8.3.2. Dissipative response function	176
8.3.3. Local-global constitutive equations	177
8.4. Representative Numerical Example	178
9. Conclusion and outlook	181
9.1. Global-Local approach for multi-physics problems at fracture	181
9.2. Virtual Elements for engineering applications	182
References	183

1. Introduction

The aim of this Habilitation is to summarize the effort spent by the **material modeling and damage mechanics group** led by the author of this *cumulative work* on modern element technologies in engineering failure analysis together with the development of Global-Local approach to allow for their incorporation into efficient numerical simulation tools. In doing so, the group could contribute to the goals of (i) the *collaborative research centre SFB 1153* [1], (ii) the *priority program SPP 2020* [2] and (iii) the *priority program SPP 1748* [3] at the Leibniz Universität Hannover (LUH). A key aspect of those projects is the development of new computational framework for modeling fracture processes across-scales. This is an intriguingly challenging task and plays an extremely important role in the safety assessment of various engineering and science applications. It combines continuum mechanics, applied mathematics and modeling techniques. Hence merges different fields and methodologies in a multidisciplinary sense to a scientific approach that helps to understand failure mechanisms. In this cumulative work we will illustrate our recent achievements in computational fracture mechanics that are related to modeling, discretization schemes along with multi-scale and multi-physics applications.

The modeling of crack formation can be achieved in a convenient way by continuum phase-field approaches to fracture, which are based on the regularization of sharp crack discontinuities. Phase-field modeling of fracture has been attracting considerable attention in recent years due to its capability of capturing complex crack patterns in various problems in solid mechanics. On the element technology, a new discretization scheme, the virtual element method (VEM), will be discussed in this contribution. VEM has proven to be a competitive discretization scheme for meshes with irregularly shaped elements that can even become non-convex. Furthermore, it allows exploration of features such as flexibility with regard to mesh generation and choice of element shapes, e.g. use very general polygonal and polyhedral meshes. For efficient and robust numerical solution procedures, we develop a multi-scale approach where the characteristic length of the local scale is of the same order as its global counter part. This is accomplished by introducing the so-called Global-Local approach. Hereby a multi-physics problem at fracture is solved on a lower (local) scale, while dealing with a purely linear elastic problem on an upper (global) scale. Besides its feasibility for having two ad-hoc finite element models for the global and local domain, enables computations/couplings with legacy codes for industrial applications in more efficient settings. Additionally, the reduction of unknowns (DOF) in this approach leads to a remarkable reduction of the computational time.

In particular, it will be shown in Part I of this Habilitation, entitled *efficient global-local techniques for failure analysis*, how such a multi-scale approach can be of advantage when large-structure problems are considered in which the fracture state only develops in smaller, localized, regions. Part II is entitled *Advanced Virtual element method* and will outline the recently developed virtual element method (VEM) as a new discretization scheme for solving failure-mechanics problems numerically. This is due to its flexible choice of nodes number in an element which can be changed easily during the simulation process. For comparison purposes, results of the standard finite element method (FEM) are also demonstrated. In this regard, the capability of VEM element with Voronoi mesh is comparable to using finite elements of higher order.

In the following Sections 1.1 and 1.2, a short introduction to the above mentioned

approaches to be modeled in this contribution is provided. This chapter closes with Section 1.3, which gives an overview of the content of this contribution.

1.1. Efficient Global-Local techniques for failure analysis

Analysis of crack initiation and propagation in brittle and ductile materials has been a topic of intensive research during the last years to predict failure mechanisms for various engineering applications. Machining, cutting and forming of materials are at the core of automobile, aerospace, medical fields, bridges or heavy industries. These applications can significantly benefit from a precisely predictive computational tool to model fracture behavior in the design phase of products. To this end, a Global-Local scheme is employed in this part as a computational framework for solving fracture mechanics problems. Global-Local technique has the potential to treat failure in large-scale problems, as shown in Figure 1.1.

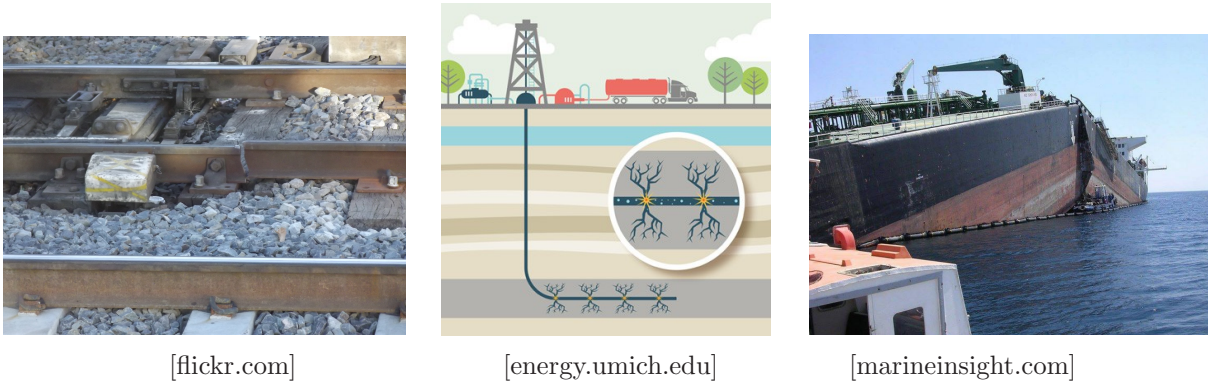


Figure 1.1: Engineering applications for failure in large-scale problems.

Departing point towards a *Global-Local approach* applied to fracture mechanics is the Domain Decomposition method [DDM] [146, 121, 167, 105, 144]. Hence, the Reference Model [RM] of a boundary value problem is split into an intact and fractured regions in DDM. Accordingly, by introduction of a fictitious domain, i.e. a coarse projection of the local domain into the global domain, we extend the resulting non-overlapping domain decomposition formulation toward a Global-Local formulation [GLM], as outlined in [17, 258, 143, 140, 138]. It is advantageous when nonlinear behavior develops in smaller and localized regions, sketched in Figure 1.2.

In the Global-Local approach, fracture is analyzed in a local domain, while dealing with linear problem on a global scale. Numerical tools for the prediction of fracture mechanism at the local (lower) scale are numerous, see [31, 202, 191]. Specifically, the continuum phase-field approach to fracture is employed. Due to its simplicity this methodology has gained a wide interest and started to be used in the engineering community since 2008. From there on many scientist have worked in this field and developed phase field approaches for finite elements, isogeometric analysis and lately also for the virtual element technology, see Part II of this work. The main driving force for these developments are the possibility to handle complex fracture phenomena within numerical methods in two and three dimensions. In recent years, several brittle [67, 188, 162, 259, 270, 6, 342, 285, 258, 160, 79, 295, 80, 119, 102, 17] and ductile [10, 22, 64, 19, 4, 110, 86, 108, 8, 190, 118, 186, 253] phase-field fracture formulations have been proposed in the literature. These studies range from the modeling of 2D/3D

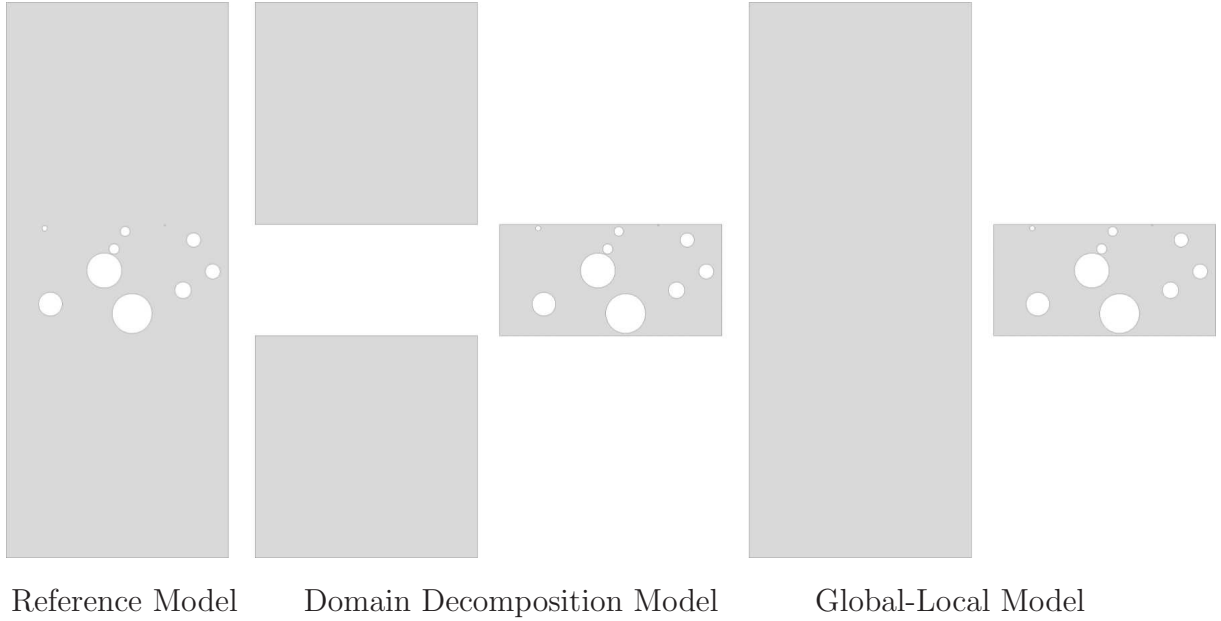


Figure 1.2: Illustration of Reference Model, Domain Decomposition Model, Global and Locals Models.

small and large strain deformations, variational formulations, multi-scale/physics problems, mathematical analysis, different decompositions and discretization techniques with many applications in science and engineering. All these examples and the citation therein demonstrate the potential of phase-field for crack propagation. In Part I of this work, the global-local approach is extended towards the phase-field modeling of fracture (i) in anisotropic brittle solids and (ii) in poro-elastic-plastic media.

Global-Local approach easily allows for different spatial discretizations for the global and local domains. Thus, a flexible choice of the discretization scheme can be employed on each domain independently; e.g. the Finite Element Method (FEM), Isogeometric Analysis (IGA) and the Virtual Element Method (VEM), as demonstrated in Figure 1.3. Hereby, the Global-domain is discretized using the standard finite element method and at the Local-scale we employed the virtual element method (zoo-animals).

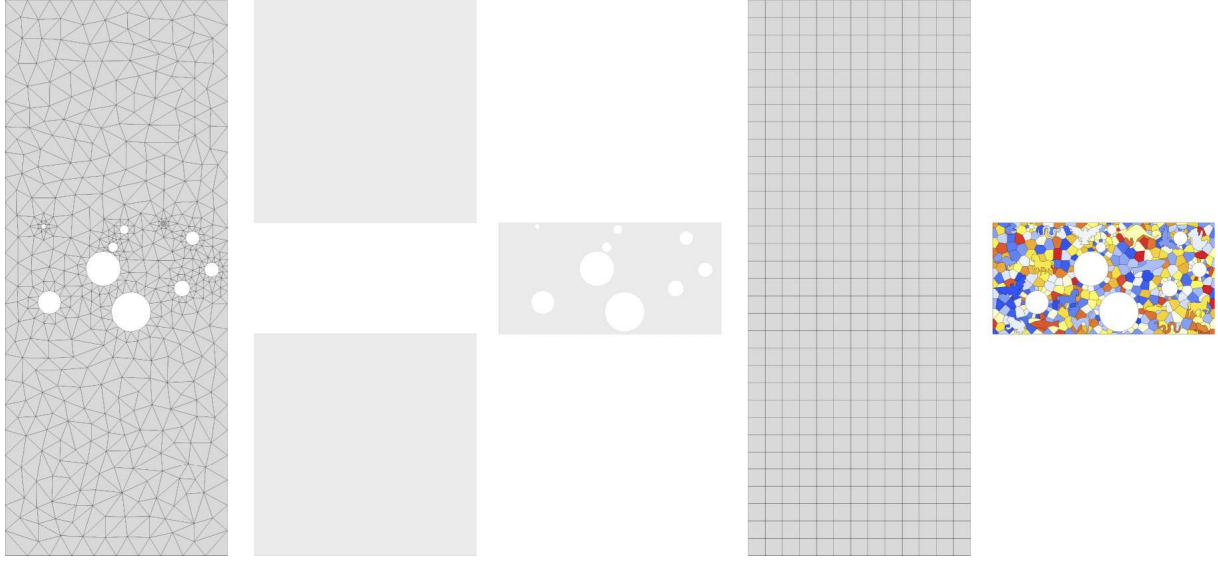
The research on phase-field approaches based on Global-Local framework is still vivid and point in many different directions. Three applications can be found in the next sections. Thereafter we put the focus on the Local-domain failure analysis using the recently developed virtual element method (VEM). This research direction on the Local scale represents a first link between Part I and Part II of this Habilitation.

1.1.1. One-dimensional study. A brief illustrative one-dimensional analysis for the Global-Local formulation is provided within this section. The discussion in this part is based on the recent work of ALDAKHEEL ET AL. [16].

The elastic energy functional $\mathcal{E}(u)$ for linear elasticity problem is described in terms of the displacement field $u \in H_0^1(\mathcal{B})$ and takes the following form

$$\mathcal{E}(u) = \int_{\mathcal{B}} \frac{1}{2} E(x) (u')^2 dx - \int_{\partial_N \mathcal{B}} \bar{\tau} \cdot u ds,$$

where $\bar{\tau} \in L_2(\mathcal{B})$ is an applied force quantity at the Neumann boundary conditions and E



Reference Model

Domain Decomposition Model

Global-Local Model

Figure 1.3: Illustration of different discretization schemes: Reference Model using FEM; Global-domain using FEM whereas Local-domain using VEM.

is a Young's modulus. Consider one dimensional boundary value problem (BVP), that is given in Figure 1.4 (first-row). We depict this as a *reference* BVP such that its discretized setting includes 3 elements and 4 nodal points with a length $8L$. The cross-section-area A is used as an identical unit area through the entire bar. Hence, the energy functional can be rewritten as

$$\mathcal{E}(u) = \int_0^{8L} \frac{1}{2} E(x) (u')^2 A dx - \int_{\partial_N \mathcal{B}} \bar{\tau} \cdot u ds.$$

A distribution of $E(x)$ is illustrated in Figure 1.4 as

- $E(x) = E_1$ for $0 \leq x \leq L$
- $E(x) = E_2$ for $L < x \leq 2L$
- $E(x) = E_3$ for $2L < x \leq 8L$

Minimization of the 1D linear elasticity leads to the Euler-Lagrange equation

$$\mathcal{E}_u(u; \delta u_G) := \int_0^{8L} E(x) u' \delta u' dx - \int_{\partial_N \mathcal{B}} \bar{\tau} \cdot \delta u ds = 0, \quad (\mathbf{R})$$

where \mathcal{E}_u is a directional derivative of the energy functional \mathcal{E} with respect to the displacement field u . Here, $\delta u \in H_0^1(0, 8L)$ is an arbitrary test function. We now aim to resolve **(R)** using the efficient Global-Local formulation. To this end, the corresponding Global BVP is given in Figure 1.4 (second-row). Its discretized setting includes 2 elements and 3 nodal points with a length $8L$. Here, a homogenized Young's modulus E_3 is considered for the entire *global* domain, thus $E_G = E_3$ at $0 \leq x \leq 8L$. Accordingly, a Local BVP is given in Figure 1.4 (fourth-row). Its discretized setting includes 2 elements and 3 nodal

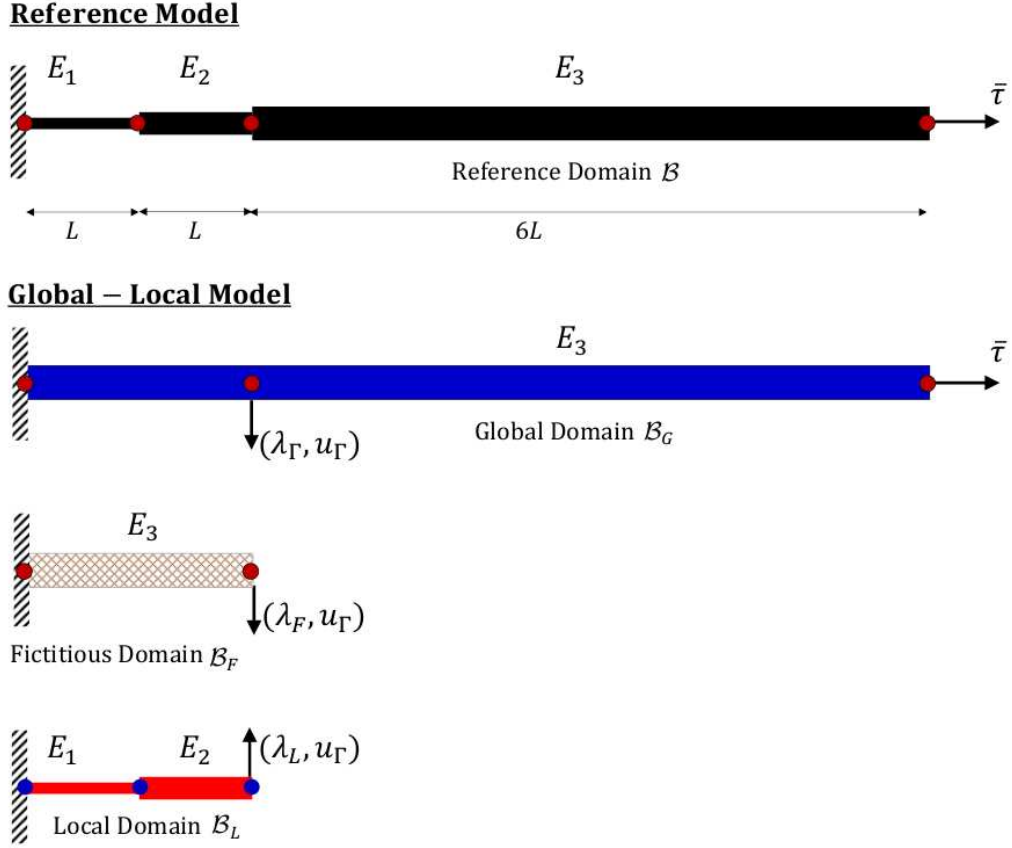


Figure 1.4: Geometry, loading setup and discretization for the one-dimensional bar. First row is a Reference domain, second row is a Global domain, third row is a Fictitious domain and the last row is a Local domain. Nodal points due to the discretization are depicted for each geometry.

points with a length of $2L$. Coarse representation of the Local domain within Global level is the so-called *Fictitious* domain, as plotted in Figure 1.4 (third-row). Without a theoretical explanation, a Global variational equation is defined to find $u_G \in H_0^1(0, 8L)$ through

$$\tilde{\mathcal{E}}_{u_G}(u_G; \delta u_G) := \underbrace{\int_0^{8L} E u_G' \delta u_G' dx}_{\text{standard terms}} - \underbrace{\int_{\Gamma_{N,G}} \bar{\tau} \cdot \delta u_G ds}_{\text{jump term}} - \int_{\Gamma_G} \lambda_\Gamma \cdot \delta u_G ds = 0, \quad (\text{G})$$

where λ_Γ is an interface residual that measure the discrepancy between Global and Local solutions at the interface (i.e. global nodal point 2). This in turn enters the global scale problem as a source term, enabling an update of the global solution. An interface residual quantity as a traction jump between Fictitious and Local domain takes the following form

$$\lambda_\Gamma(x) = \lambda_F(x) - \lambda_L(x) \quad \text{at} \quad x_G = 2L,$$

where $(\lambda_F, \lambda_L) \in L_2$ are a given fictitious and local traction quantities on the Global level through the previous solution field. To ensure the displacement continuity between the Global and Local domains, resulting global displacement field at the interface u_Γ is imposed on the local boundary value problem. Hence the local boundary value problem

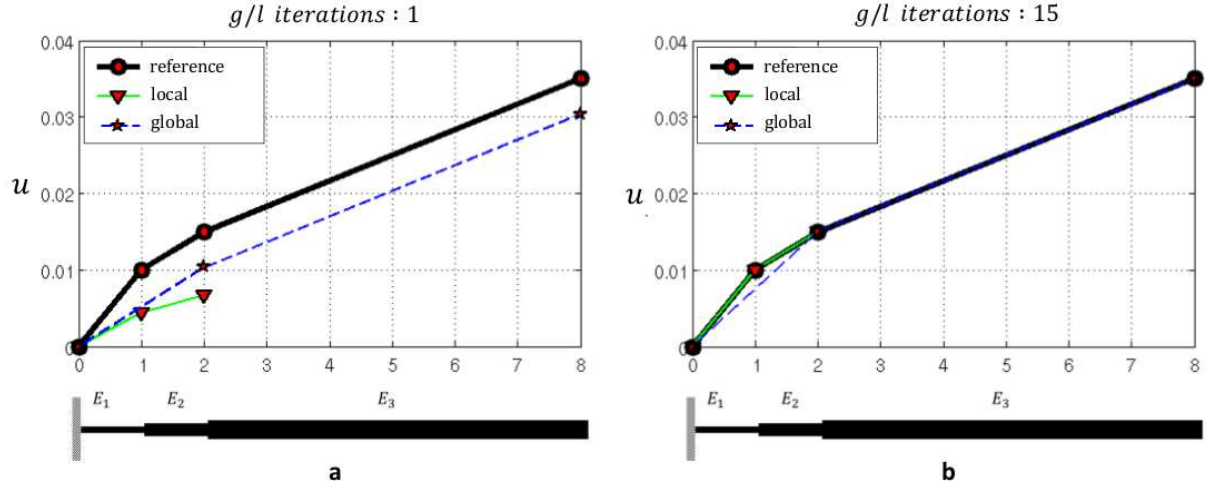


Figure 1.5: Displacement distribution along the bar: Reference, Global and Local solutions. (a) Global-Local solutions at the first iteration (b) Global-Local solutions at 15th iteration.

is constrained to find $(u_L, \lambda_L) \in (H_0^1(0, 2L), L_2)$ by

$$\begin{cases} \tilde{\mathcal{E}}_{u_L}(u_L, \lambda_L; \delta u_L) := \int_0^{2L} E(x) u_L' \delta u_L' dx - \int_{\Gamma_L} \lambda_L \cdot \delta u_L ds = 0, \\ \tilde{\mathcal{E}}_{\lambda_L}(u_L, \lambda_L; \delta \lambda_L) := u_\Gamma - u_L^3 = 0 \end{cases} \quad (\text{L})$$

Two boundary value problems namely (G) and (L) have to be solved in an iterative manner such that the convergence for the specific quantity is ensured. The convergence state is achieved when both displacement and traction continuity along the interface are held. To evaluate the Global-Local formulation, the boundary value problem given in Figure 1.4 is considered. We set $A = 1$, $L = 1$ and $(E_2, E_3) = (2E_1, 3E_1)$ with $E_1 = 10$. Resulting displacement distribution for the Reference, Global and Local boundary value

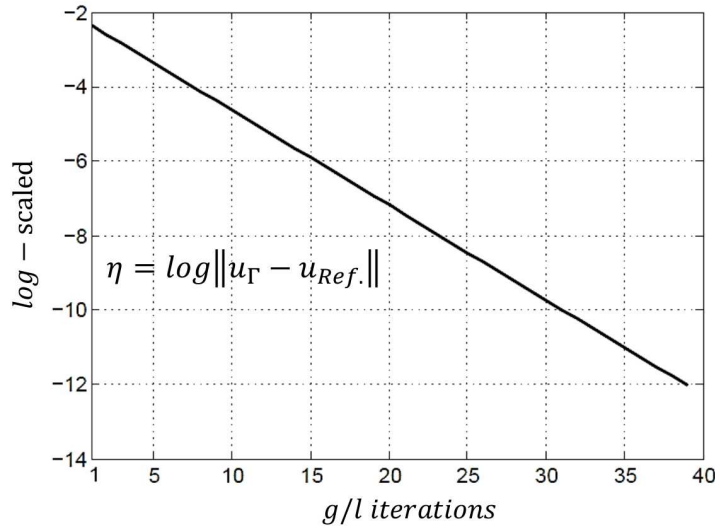


Figure 1.6: Convergence behavior of the Global-Local formulation for the one-dimensional boundary value problem.

problems is provided in Figure 1.5 for different iterations. It turns out that after 15 iterations Global-Local formulation indeed recovers the displacement obtained from the Reference solution.

Figure 1.6 shows the convergence behavior of the Global-Local iterative procedure for the one-dimensional boundary value problem given in Figure 1.4. Here, we set $TOL = 10^{-12}$ hence after 39 iterations we reached the required convergence. Further details on the theoretical formulation of the Global-Local framework are provided in the following sections at small and large deformation.

1.1.2. Adaptive concurrent multi-scale approach for anisotropic failure. A considerable number of materials exhibits *anisotropic behavior*. There span a wide spectrum of applications such as failure in rocks [111, 251], tearing experiments in thin sheets [297] and biomechanics [168, 39]. Numerical formulations for anisotropic phase-field modeling of brittle fracture are investigated, for instance, in [299, 254, 149, 203, 59]. Anisotropic materials exhibit heterogeneous behavior on the local domain through a fiber reinforced structure allowing for a homogeneous resolution on the global level. Therefore, heterogeneous materials often require distinct multi-scale treatments such that the full resolution on the local scale must be taken into account. In this section, we therefore propose a phase-field approach to brittle fracture in anisotropic solids based on the Global-Local scheme [17, 258, 143, 140, 138].

Robin-type boundary conditions [141, 211, 210] are introduced to relax the stiff local response at the global scale and enhancing its stabilization. The formulation is based on an optimized Schwarz method in a multiplicative manner (see for instance [211] or [210]). Another key goal in this research is the adaptive assignment of the local domain(s) during a computation. This is achieved with adaptivity as documented in the work of [162]. The adaptive procedure has two goals: (i) to adjust dynamically the local domain when fractures are propagating; (ii) to reduce the total computational cost because the local domains are tailored to the a priori unknown fracture path. This procedure is much cheaper than using a large local domain from the beginning. The key requirement for realizing this adaptive Global-Local scheme is a non-matching discretization method on the interface. To this end, a dual mortar method [321, 278] is implemented, thus providing sufficient regularity of the underlying meshes. Consequently, different meshes for the global and local domains can be employed that allow for a very flexible discretization and mesh generation.

1.1.3. Global-Local scheme for fracture in multi-field environments. Several pressurized [69, 242, 240, 313, 162, 163, 290, 257] and fluid-filled [239, 317, 196, 236, 234, 115, 160, 12, 200, 310, 198, 75, 199, 88, 161, 343, 318, 15] phase-field fracture formulations have been proposed recently in the literature. These studies range from modeling of pressurized and fluid-filled fractures, mathematical analysis, numerical modeling and simulations up to high-performance parallel computations. A related technique that has the potential to treat large-scale problems efficiently is a global-local technique proposed in [143, 138]. In this section, we extend the Global-Local approach towards fracture in porous media at finite strains. This technique has the potential to tackle practical field problems in which a large scale problem might be considered, in which fracture propagation is a localized phenomenon.

Our formulation can deal with non-matching grids at the interface, which is very inter-

esting for cases towards practical field problems as mentioned in [317] in which possibly various programming codes must be coupled. On the fine-scale level all (nonlinear) equations are solved. On the global level, only coarse representations of the pressure and crack phase-field are considered. Additionally, it required significantly less degrees of freedom than the Reference (single-scale) model, leads to a remarkable reduction of the computational time.

1.1.4. Modeling of Local failure in multi-physics problems. ¹

In the above investigations, failure is analyzed using the Global-Local (concurrent multi-scale) approach, in which the characteristic length of the Local scale is of the same order as its Global counterpart, i.e. $\mathfrak{L}_{local} \equiv \mathfrak{L}_{global}$, as classified in [206, 124, 140, 143]. In this section, the focus is put on the Local (lower) scale by developing a micro-mechanical model for failure in multi-physics problems. In compression with the Global-Local formulations, here the average size of this heterogeneous Local domain is much smaller than its Global specimen size, i.e. $\mathfrak{L}_{local} \ll \mathfrak{L}_{global}$, see [219, 124]. To this end, we proposed a water-induced micro-damage mechanisms of concrete using the *virtual element method* (VEM).

Within a multiscale point of view, concrete is considered as an over-complex system of solid skeletons (e.g. cement paste and stones), fluid bulk phases (e.g. water), pores with a high degree of heterogeneity. A great number of macro-meso-micro-nano-mechanically motivated approaches exist in the literature to model concrete failure behavior, see for example [319, 217, 282, 172, 78, 334, 291, 264, 153, 152, 180, 306, 208, 103, 346, 281, 137] and the citations therein. These approaches are based on dry geometries which are stored and tested in the air to analyze concrete damage processes. However, specimens that are submerged in water have a significantly lower failure resistance than dry specimens. This phenomenon was recognized in the past (e.g. in offshore vs. onshore wind turbines), but how the moisture content in the concrete microstructure influences its resistance against fracture is still unknown. This has motivated us to develop a micro-mechanical model to study the influence of water on deterioration and failure of high-strength concrete based on the experimental observations of [303]. The simulation of fracture processes in porous media at the micrometer length scale is achieved by utilizing the continuum phase-field method [67, 188, 162, 234, 115, 160, 12]. The outcome results stemmed out from the DFG-Priority Program SPP 2020 "Cyclic Damage Processes in High-Performance Concretes in the Experimental Virtual Lab".

1.2. Application of the Virtual Element Method (VEM) in Mechanics

With the ongoing development of modern element technologies, promising numerical simulation tools were created for failure analysis of solids. In this regard, discretization schemes like the Finite Difference Method [133, 194, 301], the Finite Element Method [43, 345, 323] and the Boundary Element Method [40, 262, 21, 272] are well established numerical tools for solving various science and engineering problems. Many of these methods cover the problem ranges that are described in Part I of this work. Additionally new

¹Sole authorship

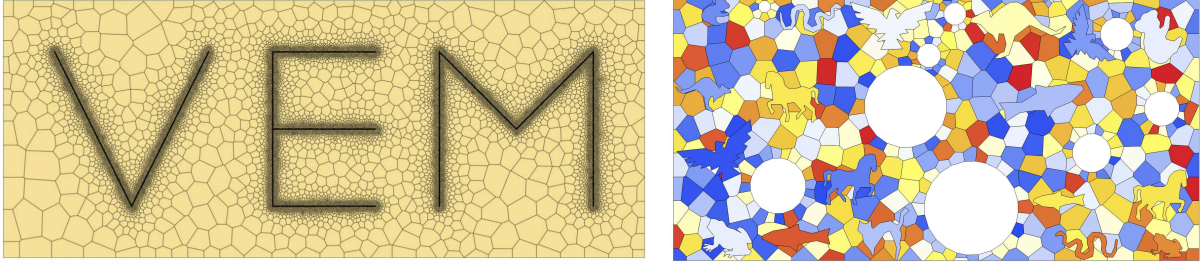


Figure 1.7: Virtual Elements for engineering applications. Arbitrary element shapes (irregular, convex, concave) with different node numbers.

approaches like Meshless methods for arbitrary deformations [255, 171, 53, 38], IsoGeometric Analysis [174, 92] and the eXtended Finite Element Method [51, 243, 44] for fracture mechanics problems are continuously evolved and can be efficiently used within a specific problem range. Hence, the art of modeling means here to pick the right numerical solution method that provides accurate results in the most time efficient way. Each of the methods described above has its own specifications and thus needs experts for a correct and efficient application.

In this contribution a relatively new discretization technique the Virtual Element Method (VEM) proposed in [46] will be presented that introduces some new features to the numerical solution of problems in solid mechanics. VEM can be seen as an extension of the classical Galerkin finite element method, being inspired from modern *mimetic finite difference schemes* and rooted in the pioneering work of [71]. VEM has proven to be a competitive discretization scheme for meshes with highly irregular shaped elements that can even be non convex, as sketched in Figure 1.7. Moreover, VEM allows the usage of an arbitrary polygonal (2D) and polyhedral (3D) element shapes with arbitrary number of nodes. Due to the construction of VEM, a stabilization procedures is required as described in [77] for linear Poisson problems. So far applications of virtual elements have been devoted to linear elastic deformations in [135, 36], contact problems in [328, 9], hyperelastic materials at finite deformations in [85, 329], second order ap-

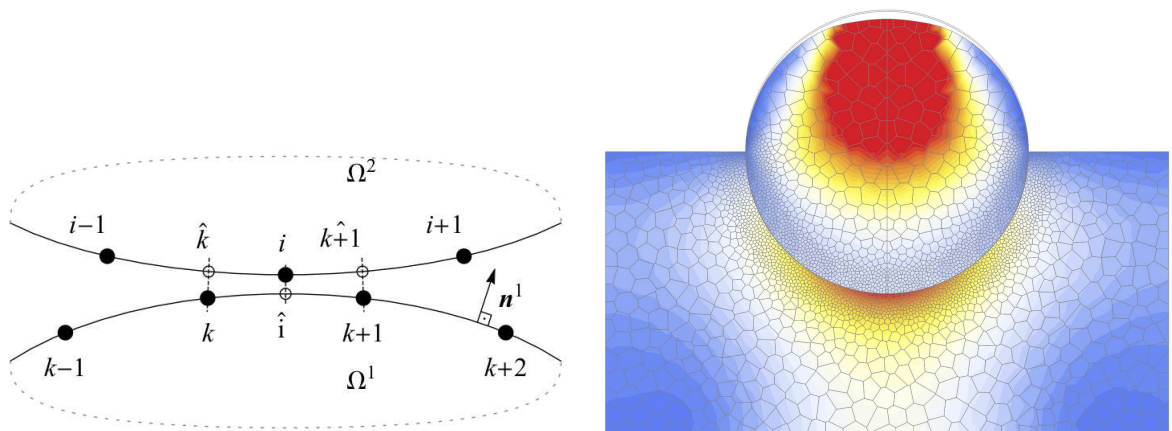


Figure 1.8: Virtual Elements for contact mechanics. Left: Contact discretization using node insertion in VEM. Right: Circular joint contact - Stress distribution σ_{VM} using locally refined VEM Voronoi element, see [9].

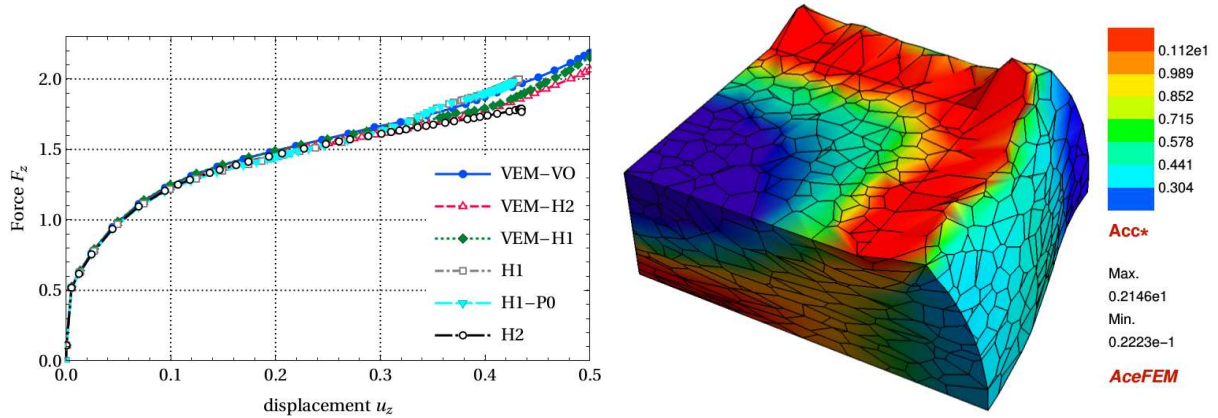


Figure 1.9: Virtual Elements for finite elastic-plastic deformations. Left: Load-deflection curves of punch problem for different element formulations. Right: Distribution of the equivalent plastic strain α at the final deformation state using VEM Voronoi mesh. VEM is more robust than FEM in case of a severe distortion of the element, as well documented in [169].

proximation (serendipity elements) in [49, 97], discrete fracture network simulations in [175, 54, 55, 256], anisotropic materials at finite strains in [330, 331], inelastic solids in [298], finite elasto-plastic deformations in [324, 169, 7], isotropic damage in [96], phase field modeling of fracture in [6, 8], finite strain elastodynamics in [90], finite crystal plasticity [45] and recently extended towards general element shapes in [333].

Key advantage of the virtual element method is that different numbers of nodes can be used to define an element. This characteristic fits extremely well into a general contact-mechanics formulation with non-matching meshes, since it allows to add additional nodes on the fly and thus to formulate a node-to-node contact approach, as shown in Figure 1.8. VEM is more robust than FEM in case of a severe distortion of the element, as depicted in Figure 1.9 for finite strain elasto-plastic deformations. Here, finite elements fail to converge at large deformation where material flows out under punch. Whereas, Virtual

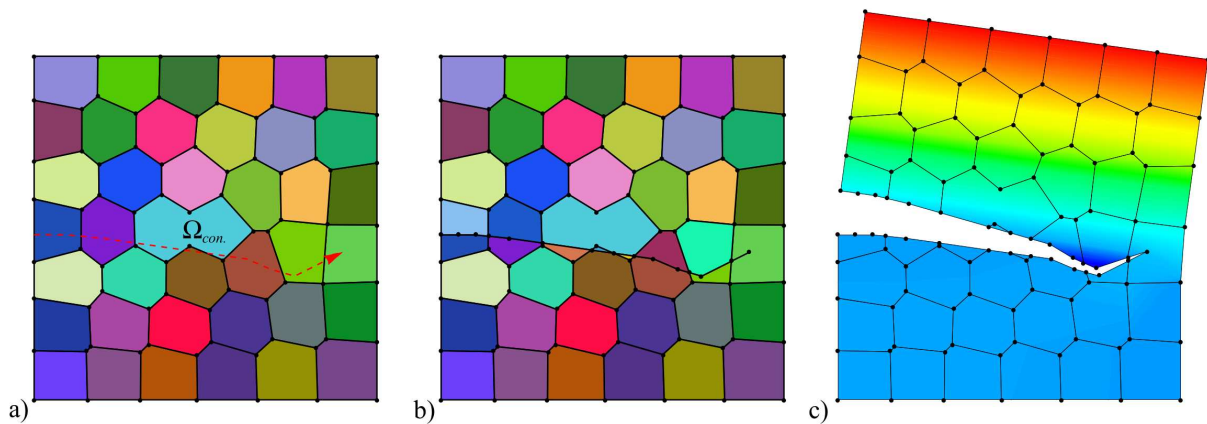


Figure 1.10: A virtual element method for crack propagation. A prescribed crack evolution during a tensile load condition. a)-b) A crack path on VEM mesh with a non-convex element Ω_{con} . c) Contour plot of the displacement field \bar{u}_y , where red and blue represent the maximum and minimum displacement, respectively as illustrated in [175].

elements did not need a refined load steps as was the case for FEM towards the failure, for more details the interested reader is referred to [169].

Another important aspect of VEM in fracture mechanics is that the crack path has the possibility to change its direction within a virtual element. Due to that, a kinked crack can be modeled using the efficient virtual element formulation without any restriction, as plotted in Figure 1.10 as an example of such crack trajectories.

The development of a virtual element typically includes a projection step and a stabilization step. In the projection step, the deformation φ_h which appears in the weak formulation or energy functional is replaced by its projection φ_Π onto a polynomial space. This results in a rank-deficient structure, so that it is necessary to add a stabilization term to the formulation, see [46] and [47] which depends in the linear case on a scalar value computed from the elasticity tensor. In [85] the scalar stabilization parameter was replaced by one that computed using the deformation depending fourth-order elasticity tensor. A new stabilization techniques for the virtual element method was lately developed in [329] who use a technique that was first described in [249], generalized in [60] and simplified in [187] in the context of hexahedral finite elements. The essence of the method is the addition to the positive semi-definite mean strain energy $\Psi(\varphi_\Pi)$ a positive-definite energy $\hat{\Psi}(\varphi_h)$ which is evaluated using full quadrature, and for consistency subtraction of a term involving $\hat{\Psi}(\varphi_\Pi)$ as a function of the mean strain. This stabilization was also applied in [324] where some correction were needed in case of plastic deformations.

The research on virtual element method (VEM) is still vivid and point in many different engineering directions. Three applications can be found in the next sections. Thereafter we put the focus on extended-gradient inelastic-theory to overcome the non-physical behavior observed in previous sections.

1.2.1. Modeling of brittle fracture using an efficient virtual element scheme.

This section represents an initial contribution to the use of the virtual element methodology for numerically solving *fracture-mechanics* problems. In contrast to the projection of the displacement field as the only global field being sought in most virtual element method applications [46, 36, 324], this work further extends VEM towards *multi-physics problems*. For this purpose, the fracture primary field is also projected onto a polynomial space. The modeling of crack formation can be achieved in a convenient way by continuum phase-field approaches to fracture, which are based on the regularization of sharp crack discontinuities [225, 24, 189, 259, 20, 245, 250].

The goal of this part is to present a consistent variational-based framework for the phase-field modeling of brittle fracture using an efficient virtual element method. It is based on a constitutive work density function and a dissipation function with threshold for fracture, which together define a minimization principle for the coupled problem. The work density function is decomposed into:

- (i) An energetic part defined to be exclusively elastic in nature which represents a degraded elastic free energy density. Besides the constitutive expression for the stresses, it also provides a locally energetic driving force for regularized fracture.
- (ii) The dissipative part governs fracture resistance with the inclusion of a fracture length scale parameter.

For brittle fracture, the material response corresponds to the sequence: $E(\text{elastic}) -$

F (fracture). On the computational side, a robust and efficient *monolithic scheme* is employed using the software tool ACEFEM program in the numerical implementation to compute the unknowns (displacement and crack phase-field), see [184]. Key observation is that the capability of VEM element with Voronoi mesh is comparable to using finite elements of higher order.

1.2.2. Virtual element formulation for modeling of ductile fracture. Most metals fail in a ductile fracture mode, preceded by significant plastic deformation, in contrast to *brittle* or *quasi-brittle* materials where fracture occurs without noticeable permanent deformation. Analysis of crack initiation and propagation in ductile materials has been a topic of intensive research during the last years to predict failure mechanisms for various engineering applications [252, 201, 195, 57].

The modeling of failure in ductile materials must account for complex phenomena such as nucleation, growth and coalescence of micro-voids, as well as the final rupture at the macro-scale. From a computational point of view, the tracking of sharp crack surfaces provides substantial difficulties and is often restricted to simple crack topologies. This difficulty can be overcome by recently developed phase-field approaches to fracture, which are based on the regularization of sharp crack discontinuities, see [113, 230, 22, 232, 64, 101, 86, 14, 108, 304, 338].

In the presented work, we examine the efficiency of VEM for predicting ductile failure mechanisms in solids due to crack initiation and propagation at finite strains. The coupling of plasticity to fracture mechanics is realized by a constitutive work density function that includes the stored elastic energy and the dissipated work due to plasticity and fracture. The latter represents a coupled resistance to plasticity and fracture, depending on the internal variables which enter plastic yield function and fracture threshold function. Key observation is that the capability of VEM element with Voronoi mesh is comparable to using finite elements of higher order. Furthermore, VEM is more robust than FEM in case of a severe distortion of the element, as highlighted in Figure 1.9.

1.2.3. VEM for 3D local thermo-elasto-plastic solids. Virtual elements were introduced in the last decade and applied to various problems in solid mechanics. The successful application of the method to 2D non-linear problems introduced above leads naturally to the question of its effectiveness and robustness in the *third* dimension. Hence, this section is concerned with the extensions of the virtual element method to problems of 3D finite strain thermo-plasticity. In previous sections of this Habilitation *thermal effects* were not included in the constitutive formulation, despite the fact that temperature distribution during heat accumulation has a *strong influence* on the mechanical properties as well documented in [32, 33, 288]. To this end, the model problem of von Mises type-plasticity using VEM [169] is extended to account for thermal effects in line with [327].

Low-order virtual element formulations for problems in three dimensions, with elements being arbitrary shaped polyhedra, are considered, as outlined in [7]. The constitutive formulation is based on a minimization of a specific pseudo-energy, with a novel construction of the stabilization energy for the coupled problem. For comparison purposes, results of the standard finite element method (FEM) are also demonstrated. It was shown that the capability of virtual elements is comparable to using finite elements of higher order. Additionally, a discretization based on VEM did not need any refined load steps and is more robust than FEM in case of severe distortions of the elements.

1.2.4. Coupled thermomechanical response of gradient inelastic deformations.²

In Section 1.2.2 and Section 1.2.3, the *local* theory of plasticity was considered in the constitutive modeling. Numerically, such a conventional formulation suffer from the so-called pathological mesh dependency behavior using virtual or finite element techniques. This leads to loss of ellipticity of the governing equations. Thus, an extended-gradient inelasticity is proposed within this section to get rid of the non-physical mesh dependency response [204, 274, 76, 309].

Inspired by the formulations introduced in Part I of this cumulative work, the coupled problem is split up into *Global* and *Local* constitutive equations in the micromorphic regularization setting as described in [131, 238]. The key point is the introduction of dual Global-Local field variables via a penalty method, where only the Global fields are restricted by boundary conditions. Hence, the problem of restricting the gradient variable to the plastic domain is relaxed, which makes the formulation very attractive for element implementation. To this end, we developed a constitutive model for coupled gradient thermo-plasticity under finite deformations in the logarithmic strain space [11]. In the mechanical part, the model problem of von Mises plasticity introduced before is extended towards gradient hardening/softening response. In the thermal part, we followed the investigations of Section 1.2.3 that demonstrate the effect of temperature on the mechanical fields resulting in a thermal expansion.

1.3. Outline of the work

This work is divided into two parts, briefly summarized below.

Part I is concerned with the efficient Global-Local techniques for solving fracture mechanics problems. Its first **Chapter 2** describes in detail the Global-Local approach supplemented with predictor-corrector adaptivity applied to anisotropic phase-field brittle fracture. It emphasizes on a Robin-type boundary conditions to relax the stiff local response at the global scale and enhancing its stabilization. To cope with different element discretizations at the interface between the two nested scales, a *non-matching* mortar method is formulated. Hence, more regularity is achieved on the interface. **Chapter 3** then focuses on the extension of the fracture phase-field formulations in porous media towards a global-local scheme. Here also a predictor-corrector strategy is adopted in which the local domain is dynamically adjusted to the current fracture pattern. In **Chapter 4** a micromechanical model for failure in multi-physics problems is developed. Here, the focus is laid on the Local (lower) scale, in which the average size of this heterogeneous Local domain is much smaller than its Global specimen size. This is achieved using the recently developed virtual element method (VEM).

Part II is concerned with a simple low order virtual element formulation and its extension to different nonlinear problems such as finite thermo-plasticity and phase-field approaches. In **Chapter 5** an efficient 2D virtual element method (VEM) for the phase-field modeling of isotropic brittle fracture is addressed. A rigorous variational-based framework is proposed for the fracture phase-field approach undergoing small strains. Here

²[Sole authorship](#)

a flexible choice of nodes number in an element that having arbitrary shape is feasible. This number can be changed easily during the simulation process. **Chapter 6** presents a 2D virtual element scheme for the phase-field modeling of isotropic ductile fracture. The formulation here is based on a minimization of a pseudo-potential density functional for the coupled problem undergoing large strains. **Chapter 7** is concerns with the extensions of the virtual element method to problems of 3D finite strain thermo-plasticity. Hereby, a conventional local theory of plasticity is considered in the constitutive modeling, leading numerically to mesh sensitive results. In **Chapter 8**, we overcome this difficulties by introducing an extended-gradient theory of thermo-plasticity that accounts for micro-structure based size effects.

Chapter 9 closes this Habilitation with some concluding remarks and possible future research directions in computational fracture mechanics.

— Part I —

Efficient Global-Local Techniques for Failure Analysis

2. Global-Local approach for anisotropic failure in brittle solids

This chapter addresses an efficient Global-Local approach supplemented with predictor-corrector adaptivity applied to anisotropic phase-field brittle fracture. The phase-field formulation is used to resolve the sharp crack surface topology on the anisotropic/non-uniform local state in the regularized concept. To resolve the crack phase-field by a given single preferred direction, second-order structural tensors are imposed to both the bulk and crack surface density functions. Accordingly, a split in tension and compression modes in anisotropic materials is considered. A Global-Local formulation is proposed, in which the full displacement/phase-field problem is solved on a *lower* (local) scale, while dealing with a purely linear elastic problem on an *upper* (global) scale. Robin-type boundary conditions are introduced to relax the stiff local response at the global scale and enhancing its stabilization. Another important aspect of this contribution is the development of an adaptive Global-Local approach, where a predictor-corrector scheme is designed in which the local domains are *dynamically updated* during the computation. To cope with different finite element discretizations at the interface between the two nested scales, a *non-matching* dual mortar method is formulated. Hence, more regularity is achieved on the interface. Several numerical results substantiate our developments. The recent publication of NOII & ALDAKHEEL ET AL [258] serve as the basis for the content of this chapter.

2.1. Introduction

Heterogeneous materials such as wood, composites and bones are composed of complicated constituents on different scales. Most of these anisotropic materials, even with similar constituents properties at the upper scale, can behave differently on the lower scale. Such heterogeneous responses of solid materials are related to non-uniform and anisotropic behavior on the lower scale.

The multi-scale family can be classified in two distinct classes denoted as *hierarchical* and *concurrent* multi-scale techniques. These are defined by differentiation of the global characteristic length scale \mathfrak{L}_{global} with its local domain counterpart \mathfrak{L}_{local} . In the hierarchical multi-scale method, the average size of the heterogeneous local domain is much smaller than its global specimen size, i.e. $\mathfrak{L}_{local} \ll \mathfrak{L}_{global}$, see [219, 124, 91]. This is often denoted as scale separation law, see computational homogenization approaches based on the Hill-Mandel principal; outlined for instance in [166, 219] among others. On the other hand, the concurrent multi-scale method implies $\mathfrak{L}_{local} \equiv \mathfrak{L}_{global}$, as classified in [206, 124]. Herein, the local periodicity (which is the underlying assumption of classical computational homogenization) is not applicable. Then, the full resolution of the non-linear response on the local scale must be taken into account, due to the strain localization effect, as outlined in [123]. These type of materials require a different multi-scale framework in which the non-linear response is consistently projected to the global scale; see for example [221, 215, 340, 157].

In the present contribution, we develop a multi-scale approach [173, 141, 207, 140, 143] when the characteristic length of the local scale is of the same order as its global counterpart. This is accomplished by introducing a Global-Local approach based on the idea of a *history-dependent algorithm* at the nodal level, see [221] and references cited therein. This algorithm refers to the procedure in which the boundary value problem of one scale is solved based on the given information from another scale (as a history

variable). Accordingly, the history-dependent algorithm contains both the *upscaling* and *downscaling* steps. In the upscaling step, the global response is achieved, whereas the lower scale information is retained, representing a *local-global-transition* procedure. However in the downscaling step, a *re-localization/re-meshing* of the coarse domain is performed at the local level, see [167, 84], thereafter solving a non-linear boundary value problem, based on the information passed from the global scale, representing *global-local-transition* procedure.

In this work, the Global-Local approach is employed as a computational framework for solving fracture mechanics problems as it was first formulated in [143]. Therein, the following assumptions were made [124, 158]: (i) The nonlinear phenomenological constitutive law (e.g. the failure mechanism) is embedded on the local scale and linear behavior is assumed on the global scale. (ii) The global level is free from geometrical imperfections and hence heterogeneities exist *only* on the local level. (iii) On the local level, we consider a divergence-free assumption for the stress state, such that it is free from any external imposed load. Accordingly, an interface energy functional based on the Localized Lagrange Multiplier method [260, 261] is desired for the coupling of different domains and scales.

Global-Local approaches easily allow for different spatial discretizations for the global and local domains. This enables computations and couplings with legacy codes for industrial applications in more efficient settings. In this regard, a flexible choice of the discretization scheme can be employed on each domain independently; e.g. the Finite Element Method (FEM) [323], Isogeometric Analysis (IGA) [174] and the Virtual Element Method (VEM) [332]. A typical application using a simplified Glocal-Local model was done in [317]. Therein, a (phase-field) fracture model (computed with deal.II [41] in C++) was employed as local problem using finite elements. The local setting was then coupled to a reservoir simulator (IPARS [312] based on Fortran) for computing the global problem. For this global problem, different discretization schemes, the mainly based on finite differences for subsurface fluid flow, were adopted.

In the following, we describe in more detail our main goals. First, we focus on the development of a new Global-Local formulation based on Robin-type boundary conditions [141, 211, 210]. These conditions relax the stiff local response transferred to the global scale and thus enhance the stabilization of the Global-Local approach. We briefly recall that Robin-type boundary conditions contain both Dirichlet and Neumann conditions. The formulation is based on an optimized Schwarz method in a multiplicative manner (see for instance [211] or [210]).

The second goal of this contribution is to use the Global-Local scheme for the analysis of anisotropic fracture processes. Specifically, the *continuum phase-field approach to brittle fracture* is employed [134, 67, 66, 154, 28, 225, 188]. Due to its capability of capturing complex crack patterns in various engineering applications, this methodology has attracted a considerable attention in recent years. Using such a variational approach, discontinuities in the displacement field are approximated across the lower-dimensional crack surface by an auxiliary phase-field function. The latter can be viewed as an indicator function, which introduces a diffusive transition zone between the broken and the unbroken material. The essential aspects of a phase-field fracture propagation formulation are techniques that must include resolution of the length-scale parameter with respect to spatial discretization, efficient and robust numerical solution procedures, and the enforce-

ment of the irreversibility of crack growth. Recent studies on phase-field modeling of isotropic brittle fracture have been devoted to the multiplicative decomposition of the deformation gradient into compressive-tensile parts in [164], coupled thermo-mechanical and multi-physics problems [231], dynamic cases in [62], a new fast hybrid formulation in [24], different choices of degradation functions in [280], and cohesive fracture in [307]. Further applications include hydraulic fracture [239, 159, 236], nonlinear solvers [313, 162], linear solvers [122, 163], crack penetration or deflection at an interface in [259] and the virtual element method in [6].

A considerable number of materials exhibits *anisotropic behavior*. There span a wide spectrum of applications such as failure in rocks [111, 251], tearing experiments in thin sheets [297] and biomechanics [168, 39]. Numerical formulations for anisotropic phase-field modeling of brittle fracture are investigated, for instance, in [299, 254, 149, 203, 59]. Anisotropic materials exhibit heterogeneous behavior on the local domain through a fiber reinforced structure allowing for a homogeneous resolution on the global level. Therefore, heterogeneous materials often require distinct multi-scale treatments such that the full resolution on the local scale must be taken into account. In this work, we therefore propose a phase-field approach to brittle fracture in anisotropic solids based on the previously described Global-Local scheme.

Our third main goal is the adaptive assignment of the local domain(s) during a computation. This is achieved with adaptivity. The adaptive procedure has two goals: (i) to adjust dynamically the local domain when fractures are propagating; (ii) to reduce the total computational cost because the local domains are tailored to the a priori unknown fracture path. This procedure is much cheaper than using a large local domain from the beginning. Our approach is inspired by [162] in which a dynamic update in form of a predictor-corrector scheme of crack-oriented mesh refinement was developed. We now apply this idea to the Global-Local approach. In the predictor step, mesh edges are identified below a given threshold value for the phase-field variable on the local level. On the global level, neighboring elements are subsequently found, then re-meshed. Afterwards, the old solution is interpolated. In the corrector step, we take the old solution and compute the problem again, but now on the newly determined local domain. Specifically, the predictor-corrector approach is now capable to deal with brutal fracture growth; i.e. when a complete failure happens in one load increment.

The key requirement for realizing this adaptive Global-Local scheme is a non-matching discretization method on the interface. To this end, a dual mortar method [321, 278] is implemented, thus providing sufficient regularity of the underlying meshes. Consequently, different meshes for the global and local domains can be employed that allow for a very flexible discretization and mesh generation.

In a final step, in addition to the local crack phase-field, we determine the coarse representation of the crack phase-field at the global level. This is a *post-processing* step and is computed based on either (a) solving the crack phase-field on the global level, denoted as *global crack phase-field* solution. Or, (b) by means of a *homogeneous crack phase-field* solution, which is an extension of the isotropic formulation given in [231, 230] to our proposed anisotropic phase-field setting.

The chapter is structured as follows: In Section 2.2, we outline the variational anisotropic phase-field formulation of brittle fracture. Section 2.3 presents the Global-Local approach to capture the local heterogeneities and constitutive non-linearities at the global level.

This is augmented by introducing a Robin-type boundary conditions. Then in Section 2.4, a robust and efficient predictor-corrector Global-Local adaptive approach is developed. Finally, Section 2.5 contains numerical results that demonstrate the modeling capabilities of the proposed approach. Qualitative and quantitative comparisons with a single scale phase-field solution are provided, as well.

2.2. Variational Anisotropic Phase-Field Brittle Fracture

2.2.1. The primary fields of anisotropic brittle solids. In the following, let $\mathcal{B} \subset \mathcal{R}^\delta$, $\delta = 2$ be a smooth open and bounded set with $\partial\mathcal{B}$ denoted as its boundary. We assume a Dirichlet boundaries conditions $\partial_D\mathcal{B}$ and Neumann condition on $\partial_N\mathcal{B} := \Gamma_N \cup \mathcal{C}$, where Γ_N denotes the outer domain boundary and the lower dimensional fracture $\mathcal{C} \in \mathcal{R}^{\delta-1}$ is the crack boundary, as illustrated in Fig. 3.1. Let $I := (0, t)$ denote the loading/time interval with $t > 0$ being the end time value. Using a phase-field approach, the fracture surface \mathcal{C} is approximated in $\mathcal{B}_L \subset \mathcal{B} \in \mathbb{R}^\delta$ so-called *local domain*. The intact region with no fracture is denoted as *complementary domain* $\mathcal{B}_C := \mathcal{B} \setminus \mathcal{B}_L \subset \mathcal{B} \in \mathbb{R}^\delta$, such that $\bar{\mathcal{B}}_C \cup \bar{\mathcal{B}}_L =: \mathcal{B}$ and $\bar{\mathcal{B}}_C \cap \bar{\mathcal{B}}_L = \emptyset$. We note that \mathcal{B}_L , i.e. the domain in which the smeared crack phase-field is approximated, and its boundary $\partial\mathcal{B}_L$ depend on the choice of the phase-field regularization parameter $l > 0$. This fracture length scale parameter l is related to the discretization of a domain. This means in particular that $h = o(l)$ (see e.g., [65] for the related problem of image segmentation) where h denotes the usual spatial discretization parameter. A simplified numerical analysis on $h = o(l)$ is provided in [213]. A detailed computational analysis was performed in [314, 163]. Moreover, the loading interval $\mathcal{T} := (t_0, T)$ is discretized using the discrete time (loading) points

$$0 = t_0 < t_1 < \dots < t_n < \dots < t_N = T,$$

with the end time value $T > 0$. The parameter $t \in \mathcal{T}$ denotes for rate-dependent problems the time, for rate-independent problems an incremental loading parameter.

A phase-field approach to fracture leads to a multi-field problem that depends on the *deformation field* and the *crack phase-field*

$$\mathbf{u} : \begin{cases} \mathcal{B} \times \mathcal{T} \rightarrow \mathcal{R}^\delta \\ (\mathbf{x}, t) \mapsto \mathbf{u}(\mathbf{x}, t) \end{cases} \quad \text{and} \quad d : \begin{cases} \mathcal{B} \times \mathcal{T} \rightarrow [0, 1] \\ (\mathbf{x}, t) \mapsto d(\mathbf{x}, t), \end{cases} \quad (2.1)$$

of a material point $\mathbf{x} \in \mathcal{B}$ at time $t \in \mathcal{T}$.

Specifically, we deal with a diffusive formulation that interpolates between the intact (unbroken) region with $d = 1$ and the fully fractured state of the material with $d = 0$ at $\mathbf{x} \in \mathcal{B}$. The Neumann boundary condition $\nabla d \cdot \mathbf{n} = 0$ is imposed on $\partial\mathcal{B}$ with \mathbf{n} being the outward normal to the surface. The strain is assumed to be small, i.e. the norm of the displacement gradient $\|\nabla\mathbf{u}\| < \epsilon$ is bounded by a small number ϵ .

2.2.2. Variational formulation for the multi-field problem. In this section, we recapitulate a variational approach to brittle fracture in elastic solids at small strains. The energy stored in a bulk strain density for isotropic materials is characterized by the three invariants,

$$I_1(\boldsymbol{\epsilon}) = \text{tr}(\boldsymbol{\epsilon}) \quad , \quad I_2(\boldsymbol{\epsilon}) = \text{tr}(\boldsymbol{\epsilon}^2) \quad , \quad I_3(\boldsymbol{\epsilon}) = \text{tr}(\boldsymbol{\epsilon}^3). \quad (2.2)$$

Additionally, it is assumed that the solid material is reinforced by only one family of fibers which is denoted as transversely isotropic material. A single preferred direction at point

with $\lambda > 0$ and $\mu > 0$ being the elastic Lamé constants. The anisotropic free-energy function is defined as

$$\tilde{\Psi}^{aniso}(I_4(\boldsymbol{\varepsilon}; \mathbf{M}), I_5(\boldsymbol{\varepsilon}; \mathbf{M})) := \frac{1}{2}\chi I_4^2 + 2\Xi I_5, \quad (2.8)$$

with the anisotropic material parameters χ and Ξ . A stress-free condition, i.e. $\boldsymbol{\varepsilon} = \mathbf{0}$, is required $\tilde{\Psi}^{iso}(I_1(\mathbf{0}), I_2(\mathbf{0})) = 0$. Moreover, $\tilde{\Psi}^{aniso}(I_4(\mathbf{0}; \mathbf{M}), I_5(\mathbf{0}; \mathbf{M})) = 0$ must hold true.

Using these definitions, to establish variational based anisotropic phase-field approach to brittle fractures, we define the bulk free energy functional which represents the stored energy in bulk as

$$\mathcal{E}_{bulk}(\mathbf{u}; \mathbf{M}) = \int_{\mathcal{B}_C} \Psi(\boldsymbol{\varepsilon}; \mathbf{M}) dx - \int_{\partial_N \mathcal{B}_C} \bar{\boldsymbol{\tau}} \cdot \mathbf{u} ds \quad (2.9)$$

Herein, $\bar{\boldsymbol{\tau}}$ denotes the traction forces on the complementary boundaries $\partial_N \mathcal{B}_C := \Gamma_N \cup \mathcal{C}$.

The total energetic functional is based on both the stored bulk energy as well as the fracture dissipation, defined in the work of [134],

$$\mathcal{E}(\mathbf{u}, \mathcal{C}; \mathbf{M}) = \mathcal{E}_{bulk}(\mathbf{u}; \mathbf{M}) + G_c \mathcal{H}^{\delta-1}(\mathcal{C}), \quad (2.10)$$

where G_c is the Griffith's critical elastic energy release rate and $\mathcal{H}^{\delta-1}$ is a $\delta-1$ dimensional Hausdorff measure. For the numerical treatment we regularize Eq. 2.10 following [67]. Specifically, the crack energy is approximated through a sequence of elliptic problems, so-called Ambrosio-Tortorelli functionals, see [26, 27]. Therein, $\mathcal{H}^{\delta-1}$ is regularized by the crack phase-field d . Finally, we account for the crack irreversibility constraint meaning the crack can only grow:

$$\dot{d} \leq 0. \quad (2.11)$$

In the incremental version, this condition reads:

$$d \leq d^{old},$$

where $d := d(t_n)$ and $d^{old} := d(t_{n-1})$. For stating the variational formulations, we now introduce:

$$\begin{aligned} \mathbf{V} &:= \{\mathbf{H}^1(\mathcal{B})^\delta : \mathbf{u} = \bar{\mathbf{u}} \text{ on } \partial_D \mathcal{B}\}, & W &:= \mathbf{H}^1(\mathcal{B}), \\ W_{in} &:= \{d \in \mathbf{H}^1(\mathcal{B})^{\delta-1} \mid 0 \leq d \leq d^{old}\}. \end{aligned} \quad (2.12)$$

As typical in problems with inequality constraints (see e.g., [179, 181]), W_{in} is a nonempty, closed, convex, subset of the linear function space W . Due to the inequality constraint in Eq. 2.11, W_{in} is no longer a linear space.

2.2.3. Phase-field approximation of anisotropic crack topologies. The variational approach of [68] is widely used for fracture failure phenomena in isotropic elastic solids. As a point of departure, in line with [224, 108], let a regularized macro crack topology of a sharp crack be represented by the exponential function $1 - \exp^{-|x|/l}$ satisfying

$d(0) = 0$. We define a regularized *isotropic crack surface energy functional* of the solid by,

$$G_c \mathcal{H}_{iso}^{\delta-1}(\mathcal{C}) := G_c \int_{\mathcal{B}} \gamma_l^{iso}(d, \nabla d) \, d\mathbf{x} \quad \text{with} \quad \gamma_l^{iso}(d, \nabla d) := \frac{1}{2l}(1-d)^2 + \frac{l}{2} \nabla d \cdot \nabla d, \quad (2.13)$$

in terms of the isotropic crack surface density function per unit volume of the solid γ_l^{iso} .

The above representation of a crack surface density function is extended for the class of anisotropic responses; as for instance outlined in [254, 299, 248]. Similarly to the deformation field, we define a total crack surface density function. It is additively decomposed into an isotropic and anisotropic crack surface density function, respectively, as follows

$$\gamma_l(d, \mathbf{Q} \nabla d) := \gamma_l^{iso}(d, \nabla d) + \gamma_l^{aniso}(\nabla d) \quad \text{for all} \quad \mathbf{Q} \in \mathcal{G} \subset \mathcal{O}(3), \quad (2.14)$$

where \mathcal{G} is a given symmetry group of the anisotropic material, i.e. the set of rotation and reflection vectors, and $\gamma_l^{aniso}(d, \nabla d)$ represents an augmented crack surface density for the anisotropic response. Let this function possess the property of the transversely isotropic material which has the coordinate-free representation for both matrix and fibers materials. This leads to

$$\gamma_l(d, \nabla d; \mathbf{M}) = \gamma_l(d^2, \nabla d \cdot \nabla d, \nabla d \cdot \mathbf{M} \cdot \nabla d). \quad (2.15)$$

Using this definition, an anisotropic crack surface density response can be defined as

$$\gamma_l^{aniso}(\nabla d; \mathbf{M}) := \alpha \frac{l}{2} \nabla d \cdot \mathbf{M} \cdot \nabla d. \quad (2.16)$$

This type of fracture function has the highest geometric resistance in the fiber direction and has an isotropic response along its orthogonal direction. Hence, the geometric resistance state at a material point \mathbf{x} depends on crack phase-field and the given single preferred direction \mathbf{a} . This results in a *crack-direction-dependent* problem.

The anisotropic term α in Eq. 2.16 behaves as a penalty-like parameter and hence for $\alpha \rightarrow \infty$ one obtains $\nabla d \cdot \mathbf{a} = 0$, which means that the crack lies parallel to the preferred orientation. For $\alpha \rightarrow 0$ the isotropic response will be recovered.

Formulation 1.1: Energy functional for the anisotropic crack topology *Let \mathbf{M} , χ , Ξ and α be given with the initial conditions $\mathbf{u}_0 = \mathbf{u}(\mathbf{x}, 0)$ and $d_0 = d(\mathbf{x}, 0)$. For the loading increments $n = 1, 2, \dots, N$, find $\mathbf{u} := \mathbf{u}^n \in V$ and $d := d^n \in W_{in}$ such that the functional*

$$\begin{aligned} \mathcal{E}(\mathbf{u}, d; \mathbf{M}) &:= \mathcal{E}_{bulk}(\mathbf{u}, d_+; \mathbf{M}) + \mathcal{E}_{frac}(d; \mathbf{M}) + \mathcal{E}_{ext}(\mathbf{u}) \\ &= \int_{\mathcal{B}} w_{bulk}(\boldsymbol{\varepsilon}, d; \mathbf{M}) \, dx + \int_{\mathcal{B}} w_{frac}(d, \nabla d; \mathbf{M}) \, dx - \int_{\partial_N \mathcal{B}} \bar{\boldsymbol{\tau}} \cdot \mathbf{u} \, ds, \end{aligned}$$

is minimized. The elastic bulk density w_{bulk} along with the fracture contribution w_{frac} both define the so-called total pseudo-energy density function as

$$\begin{aligned} w(\boldsymbol{\varepsilon}, d, \nabla d; \mathbf{M}) &= w_{bulk}(\boldsymbol{\varepsilon}, d; \mathbf{M}) + w_{frac}(d, \nabla d; \mathbf{M}), \\ w_{bulk}(\boldsymbol{\varepsilon}, d; \mathbf{M}) &= g(d_+) \Psi(\boldsymbol{\varepsilon}; \mathbf{M}), \\ w_{frac}(d, \nabla d; \mathbf{M}) &= G_c \gamma_l(d, \nabla d; \mathbf{M}). \end{aligned}$$

Remark 1: In the case of elastic cracks, it can be shown that the phase field satisfies $0 \leq d \leq 1$. When additional physics are included for instance a fluid inside the fracture [241] or non-isothermal effects [257], the energy functional must be modified to cope with negative values of d . Hence in order to allow for future extensions, we work in the remainder of this work with d_+ rather than d . A detailed discussion is provided in [241].

Remark 2: The comparison of the bulk energy functional in Eq. 2.10 and Formulation 2.1 is two-fold. First, the integration is changed from \mathcal{B}_C to the entire domain \mathcal{B} due to the presence of the phase-field function d . Second, the presence of d in the bulk energy through the degradation function $g(d)$ defines the transition state from the unbroken to fracture state hence results in the degradation of the solid material as well as the crack propagation.

2.2.4. Strain-energy decomposition. Since the fracturing material behaves quite differently in *tension* and *compression*, a consistent split for the strain energy density function is employed, where we apply the decomposition *only* to the isotropic strain energy function, i.e. $\Psi^{iso}(I_1(\boldsymbol{\varepsilon}), I_2(\boldsymbol{\varepsilon}))$. Hence, instead of dealing directly with $\boldsymbol{\varepsilon}(\mathbf{u})$, we perform additive decomposition of the strain tensor as

$$\boldsymbol{\varepsilon} = \boldsymbol{\varepsilon}^+ + \boldsymbol{\varepsilon}^- \quad \text{with} \quad \boldsymbol{\varepsilon} := \sum_{i=1}^{\delta} \langle \varepsilon_i \rangle_{\pm} \mathbf{N}_i \otimes \mathbf{N}_i ,$$

with the tension $\boldsymbol{\varepsilon}^+$ and compression $\boldsymbol{\varepsilon}^-$ strains. Here, $\langle x \rangle_{\pm} := \frac{x \pm |x|}{2}$ is a ramp function of \mathcal{R}_{\pm} expressed by the Macauley bracket. $\{\varepsilon_i\}$ are the principal strains and $\{\mathbf{N}_i\}$ are the principal strain directions. The tension/compression fourth-order projection tensor is defined as

$$\mathbb{P}_{\boldsymbol{\varepsilon}}^{\pm} := \frac{\partial \boldsymbol{\varepsilon}^{\pm}}{\partial \boldsymbol{\varepsilon}} = \frac{\partial \left(\sum_{i=1}^{\delta} \langle \varepsilon_i \rangle_{\pm} \mathbf{N}_i \otimes \mathbf{N}_i \right)}{\partial \boldsymbol{\varepsilon}} . \quad (2.17)$$

It turns out that, $\mathbb{P}_{\boldsymbol{\varepsilon}}^{\pm}$ projects the total strain into its positive and negative parts accordingly, i.e $\boldsymbol{\varepsilon}^{\pm} = \mathbb{P}_{\boldsymbol{\varepsilon}}^{\pm} : \boldsymbol{\varepsilon}$. So, a decoupled representation of the strain-energy function into a so-called tension and compression contribution is given as follows,

$$\Psi^{iso}(I_1(\boldsymbol{\varepsilon}), I_2(\boldsymbol{\varepsilon})) := \underbrace{\tilde{\Psi}^{iso,+}(I_1^+(\boldsymbol{\varepsilon}), I_2^+(\boldsymbol{\varepsilon}))}_{\text{tension term}} + \underbrace{\tilde{\Psi}^{iso,-}(I_1^-(\boldsymbol{\varepsilon}), I_2^-(\boldsymbol{\varepsilon}))}_{\text{compression term}} . \quad (2.18)$$

Herein, the positive and negative principal invariants are

$$\mathbf{I}_1^{\pm}(\boldsymbol{\varepsilon}) := \langle \mathbf{I}_1(\boldsymbol{\varepsilon}) \rangle_{\pm}, \quad \mathbf{I}_2^{\pm}(\boldsymbol{\varepsilon}) := \mathbf{I}_2(\boldsymbol{\varepsilon}^{\pm}). \quad (2.19)$$

Remark 3: An alternative definition to $\mathbf{I}_1^{\pm}(\boldsymbol{\varepsilon}) := \langle \mathbf{I}_1(\boldsymbol{\varepsilon}) \rangle_{\pm}$, can be defined by using the same description introduced in $\mathbf{I}_2^{\pm}(\boldsymbol{\varepsilon})$ for the first principal invariant which results in $\mathbf{I}_1^{\pm}(\boldsymbol{\varepsilon}) := \mathbf{I}_1(\boldsymbol{\varepsilon}^{\pm})$. This provides a new description for the strain-energy function represented in Eq. 2.18. However, that is beyond the scope of present chapter and will be investigated in future work.

Physically, it is trivial to assume that the degradation induced by the phase field acts only on the tensile and shear counterpart of the elastic strain density function. Hence, it is that assumed there is no degradation in compression, which also prevents interpenetration

of the crack lips during crack closure, see [224]. It turns out that the bulk work density function for the fracturing material becomes,

$$w_{bulk}(\boldsymbol{\varepsilon}, d; \mathbf{M}) := g(d_+) \left[\tilde{\Psi}^{iso,+}(I_1^+, I_2^+) + \tilde{\Psi}^{aniso}(I_4, I_5) \right] + \tilde{\Psi}^{iso,-}(I_1^-, I_2^-). \quad (2.20)$$

Here a monotonically decreasing quadrature degradation function, i.e.

$$g(d_+) := (1 - \kappa)d_+^2 + \kappa, \quad (2.21)$$

describes the degradation of the solid with the evolving crack phase-field parameter d . The small residual stiffness κ is introduced to prevent numerical problems. The constitutive stress response corresponding to Eq. 2.20 reads

$$\begin{aligned} \sigma(\boldsymbol{\varepsilon}, d; \mathbf{M}) &:= \frac{\partial w_{bulk}(\boldsymbol{\varepsilon}, d; \mathbf{M})}{\partial \boldsymbol{\varepsilon}} = \sigma_\varepsilon^{iso} + \sigma_\varepsilon^{aniso}, \\ \sigma_\varepsilon^{iso} &= g(d_+) \frac{\partial \tilde{\Psi}^{iso,+}}{\partial \boldsymbol{\varepsilon}} + \frac{\partial \tilde{\Psi}^{iso,-}}{\partial \boldsymbol{\varepsilon}} = g(d_+) \tilde{\sigma}_\varepsilon^{iso,+} + \tilde{\sigma}_\varepsilon^{iso,-}, \\ \sigma_\varepsilon^{aniso} &= g(d_+) \frac{\partial \tilde{\Psi}^{aniso}}{\partial \boldsymbol{\varepsilon}} = g(d_+) \tilde{\sigma}_\varepsilon^{aniso}, \end{aligned} \quad (2.22)$$

with,

$$\tilde{\sigma}_\varepsilon^{iso,\pm} := \lambda \mathbf{I}_1^\pm(\boldsymbol{\varepsilon}) \mathbf{I} + 2\boldsymbol{\mu} \boldsymbol{\varepsilon}_\pm \quad \text{and} \quad \tilde{\sigma}_\varepsilon^{aniso} = \chi \mathbf{I}_4 \mathbf{M} + 2\boldsymbol{\Xi}(\boldsymbol{\varepsilon} \cdot \mathbf{M} + \mathbf{M} \cdot \boldsymbol{\varepsilon}) \quad (2.23)$$

Formulation 1.2: Energy functional for the anisotropic crack topology *Let \mathbf{M} , χ , $\boldsymbol{\Xi}$ and α be given with the initial conditions $u_0 = u(x, 0)$ and $d_0 = d(x, 0)$. For the loading increments $n = 1, 2, \dots, N$, find $u := u^n \in V$ and $d := d^n \in W_{in}$ such that the functional*

$$\begin{aligned} \mathcal{E}(u, d; \mathbf{M}) &= \underbrace{\int_{\mathcal{B}} [g(d_+) \tilde{\Psi}^{iso,+} + \tilde{\Psi}^{iso,-}] d\mathbf{x}}_{\text{matrix deformation term}} + \underbrace{\int_{\mathcal{B}} g(d_+) \tilde{\Psi}^{aniso} d\mathbf{x}}_{\text{fiber deformation term}} \\ &+ G_c \underbrace{\int_{\mathcal{B}} \gamma_l^{iso} d\mathbf{x}}_{\text{matrix fracture term}} + G_c \underbrace{\int_{\mathcal{B}} \gamma_l^{aniso} d\mathbf{x}}_{\text{fiber fracture term}} - \underbrace{\int_{\partial_N \mathcal{B}} \bar{\tau} \cdot u ds}_{\text{external load}}, \end{aligned}$$

is minimized.

The minimization problem for the given energy functional of the anisotropic crack topology in Formulation 2.2 takes the following compact form:

$$\boxed{\{\mathbf{u}, \mathbf{d}\} = \arg\{ \min_{\mathbf{u} \in V} \min_{d \in W_{in}} [\mathcal{E}(\mathbf{u}, \mathbf{d}; \mathbf{M})] \}. \quad (2.24)}$$

The stationary points of the energy functional in Formulation 2.2 are characterized by the first-order necessary conditions, namely the so-called Euler-Lagrange equations, which are obtained by differentiation with respect to u and d .

Formulation 1.3: Euler-Lagrange equations Let \mathbf{M} , χ , Ξ and α be given with the initial conditions $u_0 = u(x, 0)$ and $d_0 = d(x, 0)$. For the loading increments $n = 1, 2, \dots, N$, find $u := u^n \in V$ and $d := d^n \in W_{in}$:

$$\begin{aligned} \mathcal{E}_u(u, d; \delta u) &= \int_{\mathcal{B}} g(d_+) \tilde{\sigma}_\varepsilon^{iso,+}(u) : \varepsilon(\delta u) d\mathbf{x} + \int_{\mathcal{B}} \tilde{\sigma}_\varepsilon^{iso,-}(u) : \varepsilon(\delta u) d\mathbf{x} \\ &\quad + \int_{\mathcal{B}} g(d_+) \tilde{\sigma}_\varepsilon^{aniso}(u) : \varepsilon(\delta u) d\mathbf{x} - \int_{\partial_N \mathcal{B}} \bar{\tau} \cdot \delta u ds = 0 \quad \forall \delta u \in V, \\ \mathcal{E}_d(u, d; \delta d - d) &= (1 - \kappa) \int_{\mathcal{B}} d_+ [\tilde{\sigma}_\varepsilon^{iso,+}(u) + \tilde{\sigma}_\varepsilon^{aniso}(u)] : \varepsilon(u) \cdot (\delta d - d) d\mathbf{x} \quad (2.25) \\ &\quad + G_c \int_{\mathcal{B}} \left(\frac{1}{l} (d - 1) \cdot (\delta d - d) + l \nabla d \cdot \nabla (\delta d - d) \right) d\mathbf{x} \\ &\quad + G_c \int_{\mathcal{B}} \alpha l \nabla d \cdot \mathbf{M} \cdot \nabla (\delta d - d) d\mathbf{x} \geq 0 \quad \forall \delta d \in W \cap L^\infty. \end{aligned}$$

\mathcal{E}_u and \mathcal{E}_d are the directional derivatives of the energy functional with respect to u and d , respectively. Furthermore, $\delta u \in \{\mathbf{H}^1(\mathcal{B})^\delta : \delta u = 0 \text{ on } \partial_D \mathcal{B}\}$ is the deformation test function and $\delta d \in H^1(\mathcal{B})$ is the phase-field test function.

2.2.5. The Euler-Lagrange equations in a strong form. In order to complete our derivations, the strong form of Formulation 2.3 will be derived in this section. Using integration by parts, we obtain a quasi-stationary elliptic system for the displacements and the phase-field variable, where the latter one is subject to an inequality constraint in time and therefore needs to be complemented with a complementary condition:

Formulation 1.4: Strong form of the Euler-Lagrange equations Let \mathbf{M} , χ , Ξ and α be given with the initial conditions $\mathbf{u}_0 = \mathbf{u}(\mathbf{x}, 0)$ and $d_0 = d(\mathbf{x}, 0)$. For the loading increments $n = 1, 2, \dots, N$, we solve a displacement equation where we seek $\mathbf{u} := \mathbf{u}^n : \mathcal{B} \rightarrow \mathbb{R}^d$ such that

$$\begin{aligned} -\operatorname{div}(\boldsymbol{\sigma}) &= \mathbf{0} \quad \text{in } \mathcal{B}, \\ \mathbf{u} &= \bar{\mathbf{u}} \quad \text{on } \partial_D \mathcal{B}, \\ \boldsymbol{\sigma} \cdot \mathbf{n} &= \bar{\boldsymbol{\tau}} \quad \text{on } \partial_N \mathcal{B}, \end{aligned}$$

in terms of the stress tensor $\boldsymbol{\sigma}$ defined in Eq. 2.22 and the given displacement field $\bar{\mathbf{u}}$. The phase-field system consists of four parts: the PDE, the inequality constraint and a compatibility condition (in fracture mechanics called Rice condition [279]) along with the Neumann-type boundary conditions. Find $d := d^n : \mathcal{B} \rightarrow [0, 1]$ such that

$$\begin{aligned} -\left(2(1 - \kappa) d_+ [\tilde{\Psi}^{iso,+} + \tilde{\Psi}^{aniso}] - \frac{G_c}{l} (1 - d) - G_c l \Delta d - G_c \alpha l \operatorname{div}(\nabla d \cdot \mathbf{M}) \right) &\geq 0 \quad \text{in } \mathcal{B}, \\ \dot{d} &\leq 0 \quad \text{in } \mathcal{B}, \\ -\left(2(1 - \kappa) d_+ \tilde{\Psi}^{iso,+}(\varepsilon(\mathbf{u})) - \frac{G_c}{l} (1 - d) - G_c l \Delta d - G_c \alpha l \operatorname{div}(\nabla d \cdot \mathbf{M}) \right) \dot{d} &= 0 \quad \text{in } \mathcal{B}, \\ (\mathbf{I} + \alpha \mathbf{M}) \nabla d \cdot \mathbf{n} &= 0 \quad \text{on } \partial \mathcal{B}. \end{aligned}$$

The mentioned inequality minimization problem for the phase-field equation can be resolved through: (a) fixing the fracture with *Dirichlet conditions* [67], (b) *Penalty method*, see [240] (including a mathematical analysis), (c) *an Augmented Lagrangian penalization*

see [313], (d) *Primal-dual active set method*; see [162, 196], (e) *Maximum crack driving state function*, see [224, 231]. In the present work, we consider the maximum crack driving state function to prevent the crack healing by having a positive crack dissipation known as irreversibility criteria and given in details in next section.

2.2.6. Crack driving force. In this section, a formulation for the crack phase-field PDE equation in Formulation 2.4 is reformulated based on the crack driving force. A thermodynamical consistency for the preservation of the energy balance due to the fracture dissipation results to the Karush-Kuhn-Tucker form, see [230]. As a point of departure, the modular structure of the anisotropic phase-field fracture equation assumes the following form

$$\underbrace{\eta \dot{d}}_{\text{crack update}} = \underbrace{-g'(d_+) \tilde{D}}_{\text{crack driving force}} - \underbrace{l \delta_d \gamma_l}_{\text{resistance}} \leq 0, \quad (2.26)$$

as outlined in the works of MIEHE and coworkers [231, 230, 10, 14]. Here, \tilde{D} is a *crack driving state function* which depends on a *state* array of strain- or stress like quantities. To get rid of the above inequality evolution problem, we maximize the inequality equation given in (2.26) for the full process history $s \in [0, t_n]$,

$$-g'(d_+) \max_{s \in [0, t_n]} \tilde{D} = l \delta_d \gamma_l. \quad (2.27)$$

We introduce maximum positive crack driving force \mathcal{H} in $t \in [0, t_n]$ denoted as,

$$\mathcal{H}(\mathbf{x}, t) := \max_{s \in [0, t_n]} \tilde{D}(\text{state}(\mathbf{x}, \varepsilon(s))), \quad (2.28)$$

and hence (2.26) can be restated as,

$$\boxed{\underbrace{\eta \dot{d}}_{\text{crack update}} = \underbrace{-g'(d_+) \mathcal{H}}_{\text{max crack driving force}} - \underbrace{l \delta_d \gamma_l}_{\text{resistance}}.} \quad (2.29)$$

Depending on the type of the crack driving state function which can be either without or with threshold, \tilde{D} can take different description, see [4, 6, 8]. The crack phase-field evolution in (2.29) is defined in the domain \mathcal{B} that is augmented with an imposed Neumann homogeneous boundary condition as

$$(\mathbf{I} + \alpha \mathbf{M}) \nabla d \cdot \mathbf{n} = 0 \quad \text{on } \partial \mathcal{B}. \quad (2.30)$$

Note, that in Eq. 2.26 the rate-independent case is recovered for $\eta \rightarrow 0$, where the crack topology is then simply determined by an equilibrium between the crack driving force and the geometric crack resistance. These equations are interpreted as generalized Ginzburg-Landau-type evolution equations for the crack phase-field d . Equation 2.29 restated for the rate-independent limit $\eta \rightarrow 0$ to the so-called Karush-Kuhn-Tucker form:

$$\boxed{\dot{d} \leq 0; \quad -\delta_d w \geq 0, \quad \dot{d} [-\delta_d w] = 0.} \quad (2.31)$$

This condition provides a natural assumption due to the positive fracture dissipation known as crack irreversibility condition. The latter constraint is ensured by a specific constitutive

assumption that relates the functional derivative to a positive energetic driving force. The last condition in (2.31) is the balance law for the evolution of the crack phase-field which ensures the principal of maximum dissipation during the crack phase-field evolution (see e.g. [224]). It is known as compatibility condition.

Remark 4: *Karush-Kuhn-Tucker stated in (2.31) along with (2.30) are the modular structure of the Euler-Lagrange equations in a strong form which are given in Formulation 2.4.*

By defining the maximum positive crack driving force \mathcal{H} in terms of the crack driving state function \tilde{D} at hand, Formulation 2.3 can be stated as an equality minimization. Thus \mathcal{H} substitutes the corresponding $[\tilde{\Psi}^{iso,+} + \tilde{\Psi}^{aniso}]$ term in the original \mathcal{E}_d .

2.2.7. Crack Driving State Function without Threshold. A crack driving state function without threshold is frequently used in literature, see [225, 224]. By considering the phase-field formulation with specific degradation function given in Eq. 2.21, the accumulated dissipative fracture density for the case of without threshold extended to the anisotropic setting as,

$$w_{frac}(d, \nabla d; \mathbf{M}) := G_c \gamma_l(d, \nabla d; \mathbf{M}) = G_c \left(\frac{1}{2l} (1-d)^2 + \frac{l}{2} \nabla d \cdot \nabla d + \alpha \frac{l}{2} \nabla d \cdot \mathbf{M} \cdot \nabla d \right). \quad (2.32)$$

To derive the crack driving state function we recall the irreversibly inequality condition, i.e. $\dot{d} \leq 0$. It follows that the left hand side of (2.26) has to be always positive to avoid the crack healing process

$$-\delta_d w = (\kappa - 1) 2d_+ [\tilde{\Psi}^{iso,+} + \tilde{\Psi}^{aniso}] - G_c \delta_d \gamma_l(d, \nabla d; \mathbf{M}) \leq 0. \quad (2.33)$$

Maximization of this inequality in the full process history $s \in [0, t_n]$, yields

$$(\kappa - 1) 2d_+ \max_{s \in [0, t_n]} [\tilde{\Psi}^{iso,+} + \tilde{\Psi}^{aniso}] = G_c \delta_d \gamma_l(d, \nabla d; \mathbf{M}). \quad (2.34)$$

To follow the modular structure of the phase-field fracture equation defined in Eq. 2.26, we multiply (2.34) by $\frac{1}{G_c}$. With the definition of a positive crack driving force and shown by \mathcal{H} , hence (2.34) is restated as

$$(\kappa - 1) 2d_+ \mathcal{H} = l \delta_d \gamma_l \text{ if } \mathcal{H} := \max_{s \in [0, t_n]} \tilde{D} \text{ with } \tilde{D} := \frac{l [\tilde{\Psi}^{iso,+} + \tilde{\Psi}^{aniso}]}{G_c}. \quad (2.35)$$

It is evident that the crack driving state function given by (2.35) is directly effected by the regularization parameter l . Hence the crack driving state function has the property of length-scale dependency. The functional derivative of γ_l with respect to d is obtained as follows,

$$\int_{\mathcal{B}} \delta_d \gamma_l(d, \nabla d; \mathbf{M}) dx := \int_{\mathcal{B}} \left(\frac{\partial \gamma_l}{\partial d} + \frac{\partial \gamma_l}{\partial \nabla d} \right) dx = \int_{\mathcal{B}} \left(\frac{\partial \gamma_l}{\partial d} - \nabla \cdot \left[\frac{\partial \gamma_l}{\partial \nabla d} \right] \right) dx, \quad (2.36)$$

which leads to,

$$\int_{\mathcal{B}} \delta_d \gamma_l(d, \nabla d; \mathbf{M}) dx = \int_{\mathcal{B}} \frac{1}{l} [(d-1) - l^2 \Delta d - \alpha l^2 \operatorname{div}(\nabla d \cdot \mathbf{M})] dx. \quad (2.37)$$

Furthermore $\frac{\partial \gamma_l(d, \nabla d; \mathbf{M})}{\partial \nabla d} \cdot \mathbf{n} = (\mathbf{I} + \alpha \mathbf{M}) l \nabla d \cdot \mathbf{n} = 0$ refers to (2.30).

Formulation 1.5: Final Euler-Lagrange equations Let \mathbf{M} , χ , Ξ and α be given with the initial conditions $\mathbf{u}_0 = \mathbf{u}(x, 0)$ and $d_0 = d(x, 0)$. For the loading increments $n = 1, 2, \dots, N$, find $\mathbf{u} := \mathbf{u}^n \in V$ and $d := d^n \in W$:

$$\begin{aligned} \mathcal{E}_{\mathbf{u}}(\mathbf{u}, d_+; \delta \mathbf{u}) &= \int_{\mathcal{B}} g(d_+) \tilde{\boldsymbol{\sigma}}_{\varepsilon}^{iso,+}(\mathbf{u}) : \varepsilon(\delta \mathbf{u}) d\mathbf{x} + \int_{\mathcal{B}} \tilde{\boldsymbol{\sigma}}_{\varepsilon}^{iso,-}(\mathbf{u}) : \varepsilon(\delta \mathbf{u}) d\mathbf{x} \\ &\quad + \int_{\mathcal{B}} g(d_+) \tilde{\boldsymbol{\sigma}}_{\varepsilon}^{aniso}(\mathbf{u}) : \varepsilon(\delta \mathbf{u}) d\mathbf{x} - \int_{\partial_N \mathcal{B}} \bar{\boldsymbol{\tau}} \cdot \delta \mathbf{u} ds = 0 \quad \forall \delta \mathbf{u} \in V, \\ \mathcal{E}_d(\mathbf{u}, d; \delta d) &= (1 - \kappa) \int_{\mathcal{B}} 2d_+ \mathcal{H} \delta d d\mathbf{x} \\ &\quad + \int_{\mathcal{B}} \left((d - 1) \delta d + l^2 \nabla d \cdot \nabla \delta d \right) d\mathbf{x} \\ &\quad + \int_{\mathcal{B}} \alpha l^2 \nabla d \cdot \mathbf{M} \cdot \nabla \delta d d\mathbf{x} = 0 \quad \forall \delta d \in W. \end{aligned} \quad (2.38)$$

2.2.8. Crack Driving State Function with Threshold. Alternative to crack driving state function *without* threshold (introduced above) is an extension to damage-like criteria by considering the threshold state for crack initiation. This is mainly because of two reason, first, in the case of without threshold damage due to the effect of degradation function in the bulk material may occurs in the low stress level then linear elastic is not defined prior to the fracture initiation. Second, the crack driving state derived in Eq. 2.35 is directly related to the length scale, hence the stationary solution of the crack phase filed from Eq. 2.29 is dependent on the length-scale solution, strongly. Hence, by considering the phase-field modular structure with specific degradation function given in Eq. 2.21, the accumulated dissipative fracture density for the case of with threshold extended for the anisotropic setting given as,

$$w_{frac}(d, \nabla d; \mathbf{M}) = 2\psi_c \left[1 - d + \frac{l^2}{2} \nabla d \cdot \nabla d + \alpha \frac{l^2}{2} \nabla d \cdot \mathbf{M} \cdot \nabla d \right]. \quad (2.39)$$

Here, ψ_c denotes a *specific fracture energy density*. It is noted that, despite to the definition used in Eq. 2.32, the crack phase field d enters the formulation by a linear term, more details in [267], [220] and [231]. Hence, the extension to the anisotropic setting of the “total” pseudo-energy density reads,

$$w(\boldsymbol{\varepsilon}, d, \nabla d; \mathbf{M}) = (1 - \kappa) d_+^2 [\tilde{\Psi}^{iso,+} + \tilde{\Psi}^{aniso} - \psi_c] + \psi_c + 2\psi_c l \gamma_l(d, \nabla d; \mathbf{M}). \quad (2.40)$$

Then, for the rate-independent loading criterion, i.e. $\eta \rightarrow 0$, the directional derivative of total pseudo-energy density with respect to d reads

$$-\delta_d w = (\kappa - 1) 2d_+ [\tilde{\Psi}^{iso,+} + \tilde{\Psi}^{aniso} - \psi_c] - 2\psi_c \delta_d \gamma_l(d, \nabla d; \mathbf{M}) \leq 0 \quad (2.41)$$

In similar manner of the previous section, by maximizing the inequality equation in Eq. 2.41 with respect to the $\boldsymbol{\varepsilon}$ up to current time, i.e. $t \in [0, t_n]$, inequality formulation in Eq. 2.41 becomes equality and re-stated into the form,

$$(\kappa - 1) d_+ \mathcal{H} = l \delta_d \gamma_l \quad \text{if} \quad \mathcal{H} := \max_{s \in [0, t_n]} \tilde{D} \quad \text{with} \quad \tilde{D} := \left\langle \frac{\tilde{\Psi}^{iso,+} + \tilde{\Psi}^{aniso}}{\psi_c} - 1 \right\rangle_+ \quad (2.42)$$

It is noted, that this criterion is independent of the regularization parameter l , due to the introduction of ψ_c that is specific material properties for the fracturing solid material. To

specify crack driving state function in terms of the critical fracture stress σ_c as a basic material properties value rather than ψ_c , then the crack driving state function based on positive effective stress based criterion reads,

$$\widehat{\boldsymbol{\sigma}} := \widetilde{\boldsymbol{\sigma}}_{\boldsymbol{\varepsilon}}^{iso,+} + \widetilde{\boldsymbol{\sigma}}_{\boldsymbol{\varepsilon}}^{aniso} := \sum_{i=1}^{\delta} \langle \widehat{\boldsymbol{\sigma}}_{\boldsymbol{\varepsilon},i} \rangle_+ \mathbf{N}_i \otimes \mathbf{N}_i \quad \rightarrow \quad \widetilde{D} = \zeta \left\langle \sum_{i=1}^{\delta} \left(\langle \widehat{\boldsymbol{\sigma}}_{\boldsymbol{\varepsilon},i} \rangle_+ / \sigma_c \right)^2 - 1 \right\rangle_+ . \quad (2.43)$$

This threshold-type crack driving state function characterized an anisotropic failure surface in terms of the effective principal directions of the stress state. $\zeta > 0$ is used to control the growth of the crack phase-field in the post-equilibrium fracture state.

An alternative way to describe an anisotropic failure surface may be described in terms of the,

- Rankin model through a maximum principal tensile-stress stated as,

$$\widetilde{D} = \zeta \left\langle \max_{i=1}^{\delta} \left(\langle \widetilde{\boldsymbol{\sigma}}_{\boldsymbol{\varepsilon},i}^{iso} \rangle_+ / \sigma_c \right)^2 - 1 \right\rangle_+ .$$

- Mohr-Coulomb model through a frictional shear stress stated as,

$$\widetilde{D} = \zeta \left\langle \left(\sigma_m / \sigma_c \right)^2 - 1 \right\rangle_+ .$$

whereas $m := m(\theta) = \frac{1+\sin\theta}{1-\sin\theta}$ in which the θ refers to the angle of internal friction and $\sigma_m := m(\theta) \cdot \max_{i=1}^{\delta} \left(\langle \widetilde{\boldsymbol{\sigma}}_{\boldsymbol{\varepsilon},i}^{iso} \rangle_+ \right) - \min_{i=1}^{\delta} \left(\langle \widetilde{\boldsymbol{\sigma}}_{\boldsymbol{\varepsilon},i}^{iso} \rangle_+ \right)$.

- Linearized Mogi-Coulomb failure through a maximum distortion energy stated as,

$$\widetilde{D} = \zeta \left\langle \left[p(c, \theta) + \frac{q(\theta)}{2} \left(\max_{i=1}^{\delta} \left(\langle \widetilde{\boldsymbol{\sigma}}_{\boldsymbol{\varepsilon},i}^{iso} \rangle_+ \right) + \min_{i=1}^{\delta} \left(\langle \widetilde{\boldsymbol{\sigma}}_{\boldsymbol{\varepsilon},i}^{iso} \rangle_+ \right) \right) \right]^2 / \tau_{oct}^2 - 1 \right\rangle_+ ,$$

whereas τ_{oct} is the octahedral shear stress and c is apparent cohesion of the material.

- Tresca model through a maximum shear stress stated as,

$$\widetilde{D} = \zeta \left\langle \left[\max_{i=1}^{\delta} \left(\langle \widetilde{\boldsymbol{\sigma}}_{\boldsymbol{\varepsilon},i}^{iso} \rangle_+ \right) - \min_{i=1}^{\delta} \left(\langle \widetilde{\boldsymbol{\sigma}}_{\boldsymbol{\varepsilon},i}^{iso} \rangle_+ \right) \right]^2 / \tau_c^2 - 1 \right\rangle_+ ,$$

whereas τ_c is the critical state value for the shear stress.

- Beltrami model through a maximum principal strain stated as,

$$\widetilde{D} = \zeta \left\langle \max_{i=1}^{\delta} \left(\langle \widetilde{\boldsymbol{\varepsilon}}_{\boldsymbol{\varepsilon},i}^{iso} \rangle_+ / \varepsilon_c \right)^2 - 1 \right\rangle_+ .$$

Additionally, Von-Mises failure criterion or Drucker-Prager failure criteria specifically for the ductile fracture can be used.

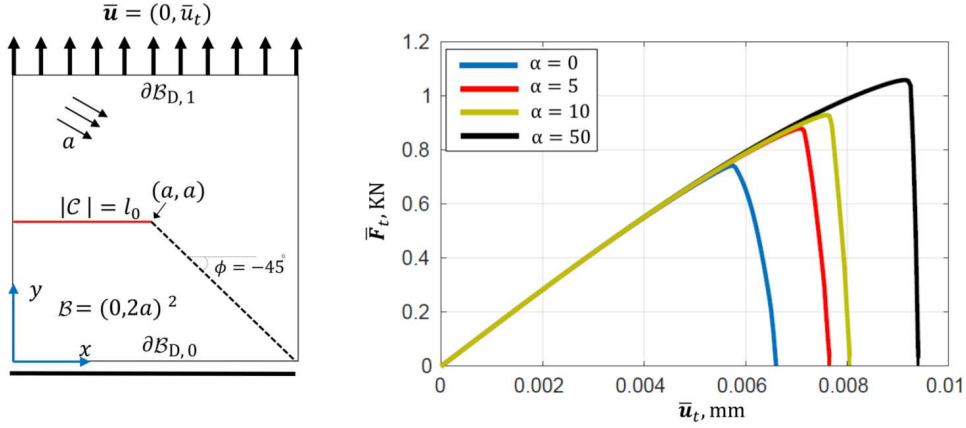


Figure 2.2: Single-edge-notched plate under tension test by the structural director \mathbf{a}_0 inclined under an angle $\phi = -45^\circ$ (a) Geometry and loading setup for the 2D test scenarios; (b) load-displacement curve for the varying fracture anisotropy parameter α and fixing χ deformation anisotropy parameter.

2.2.9. Numerical Model Problem. We now consider a boundary value problem applied to the square plate shown in Fig. 2.2a and let $a = 0.5$ hence $\mathcal{B} = [0, 1]^2 \text{ mm}^2$ that includes a predefined single notch from the left edge to the center of body as depicted in Fig. 2.2a. The geometry and loading setup for the following test is shown in Fig. 2.2a. The material parameters for the transversely isotropic chosen as $\lambda = 121.15 \text{ kN/mm}^2$, $\mu = 80.77 \text{ kN/mm}^2$, $\chi = 50 \text{ kN/mm}^2$ and $G_c = 2.7 \times 10^{-3} \text{ kN/mm}$. The preferred fibre direction given by the structural director \mathbf{a} that is inclined under $\theta = -45^\circ$ with respect to the x -axis of a fixed cartesian coordinate system.

To investigate the influence of the fracture anisotropic parameter namely α as the model parameter in the Formulation 2.5, the computations are performed for four different values of α , namely $\alpha = 0$, $\alpha = 5$, $\alpha = 10$ and $\alpha = 50$. We fixed and set $\chi = 50$, because of its very negligible effect on the fracture model. Load-displacement curve for the varying fracture anisotropy parameter α is shown in Fig. 2.2b. Additionally, the effect of α on the crack phase-field resolution is shown in Figure 2.3. It is evident, that the fracture path follows the fibre direction which is $\phi = -45^\circ$ if α is increased, see Fig. 2.3 for $\alpha = 50$. This results confirm that α behave as a penalty-like parameter in the crack surface density.

2.3. Global-Local Formulation

Departing point towards a *Global-Local approach* applied to the anisotropic phase-field formulation is the domain decomposition method [146]. We split the single-scale energy functional \mathcal{E} indicated in Formulation 2.2 to the intact and fractured region, i.e. \mathcal{B}_C and \mathcal{B}_L , respectively.

Accordingly, by introduction of the Fictitious domain \mathcal{B}_F , i.e. a coarse projection of the local domain into the global domain (later \mathcal{B}_G refers to the global domain, we extend the resulting non-overlapping domain decomposition formulation toward a Global-Local formulation applied to the anisotropic phase-field fracture. The Global-Local formulation applied to isotropic phase-field was first proposed by GERASIMOV ET AL. [143]. The main objective was to introduce an adoption of the phase-field formulation within legacy codes, specifically for industrial applications.

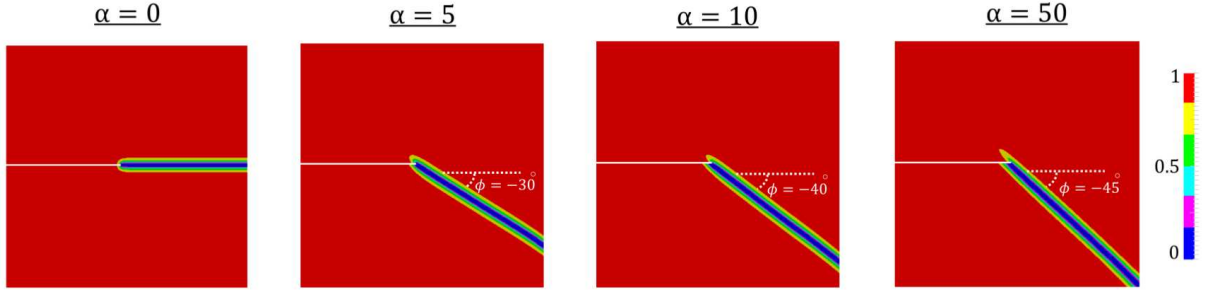


Figure 2.3: Fracture of transversely isotropic single-edge-notched plate under tension. Crack paths for different anisotropy parameters for a fixed deformation anisotropy parameter $\chi = 50$ and varying fracture anisotropy parameter $\alpha = 0$, $\alpha = 5$, $\alpha = 10$ and $\alpha = 50$. For α getting comparatively large, i.e. $\alpha = 50$, the crack follows the direction of the fibre direction due to the anisotropy parameter's role as a penalty-like factor.

An important definition for the subsequent treatment is the energy functional. We recall that the energy functional for the single-scale problem denoted as \mathcal{E} . We further define the energy functional for the domain decomposition by $\hat{\mathcal{E}}$ and the Global-Local formulations as $\tilde{\mathcal{E}}$.

2.3.1. Non-overlapping domain decomposition formulation. Recall, the complementary domain $\mathcal{B}_C := \mathcal{B} \setminus \mathcal{B}_L \subset \mathcal{B} \in \mathbb{R}^d$ corresponds to the intact region and let \mathcal{B}_L is an open domain, where the fracture surface is approximated in this region, see Fig. 2.4(a). It is assumed the fracture surface in \mathcal{B}_L represents a reasonably small 'fraction' of \mathcal{B} such that $|\mathcal{B}_L| \ll |\mathcal{B}_C|$. We further define an interface between an unfractured domain \mathcal{B}_C and fractured domain \mathcal{B}_L by $\Gamma \in \mathcal{R}^{\delta-1} \subset \mathcal{B}$ in the continuum setting to be the interface between \mathcal{B}_L and \mathcal{B}_C , such that $\mathcal{B} \equiv \mathcal{B}_L \cup \Gamma \cup \mathcal{B}_C$. We further assume that \mathcal{B}_L is free from any externally imposed load and hence we have prescribed loads *only* in \mathcal{B}_C . Such an assumption is standard for the multi-scale setting, see FISH [124].

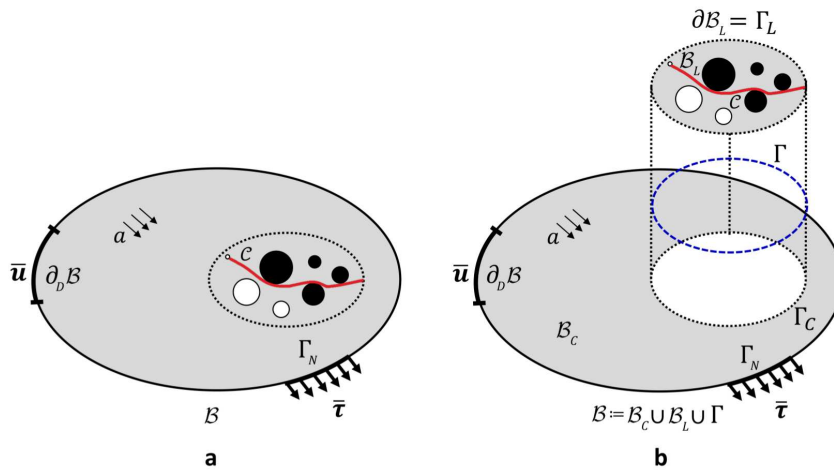


Figure 2.4: Domain decomposition scheme. (a) Geometry and loading setup of the single-scale boundary value problem. (b) Non-overlapping domain decomposition setting whereas \mathcal{B} is decomposed into the intact and fracture region denoted as complementary and local domains \mathcal{B}_L and \mathcal{B}_C , respectively.

Consider a domain decomposition with geometric sketch in Fig. 2.4(b) applied to the

single-scale domain plotted in Fig. 2.4(a). Two functions on \mathcal{B}_L and \mathcal{B}_C are considered, namely $\mathbf{u}_L \in \mathbf{V}_L$ and $\mathbf{u}_C \in \mathbf{V}_C$, where we introduce additional three sets:

$$\mathbf{V}_L := \mathbf{H}_0^1(\mathcal{B}_L)^\delta, \quad \mathbf{V}_C := \mathbf{V}(\mathcal{B}_C), \quad \text{and } W_L := W_{in}(\mathcal{B}_L),$$

referring to the spaces defined in Eq. 2.12.

A descriptive motivation of the domain decomposition approach applied to the variational anisotropic phase-field modeling is related to two restriction in the model: (i) the strong coupling scheme that is the strong displacement continuity condition that holds along with (ii) the predefined interface. To this end, one needs to assume that the discrete interfaces for both complementary and local domain do exactly coincide in the strong sense, yielding

$$\mathbf{u}_L \stackrel{!}{=} \mathbf{u}_C \quad \text{at } \mathbf{x} \in \Gamma = \Gamma_C = \Gamma_L. \quad (2.44)$$

This displacement continuity is often called *primal* approach in the literature, see e.g. MANDEL [212].

Let the *single-scale displacement field* $\mathbf{u} \in \mathbf{V}$ be the solution of the multi-field variational problem in (3.30). It is decomposed as

$$\mathbf{u}(\mathbf{x}, t) := \begin{cases} \mathbf{u}_L & \text{for } \mathbf{x} \in \mathcal{B}_L, \\ \mathbf{u}_C & \text{for } \mathbf{x} \in \mathcal{B}_C. \end{cases} \quad (2.45)$$

Since the fracture surface lives only in \mathcal{B}_L we introduce scalar-valued function $d_L : \mathcal{B}_L \rightarrow [0, 1] \in W_L$. The *single-scale phase-field* d is then decomposed in the following form

$$d(\mathbf{x}, t) := \begin{cases} d_L & \text{for } \mathbf{x} \in \mathcal{B}_L, \\ 1 & \text{for } \mathbf{x} \in \mathcal{B}_C. \end{cases} \quad (2.46)$$

By imposing (2.45) and (2.46) to the energy functional, indicated in Formulation 2.2, energy functionals corresponding to \mathcal{B}_C and \mathcal{B}_L reads

$$\widehat{\mathcal{E}}_C(\mathbf{u}_C; \mathbf{M}) := \int_{\mathcal{B}_C} w(\boldsymbol{\varepsilon}_C, 1, 1; \mathbf{M}) \, d\mathbf{x} - \int_{\partial_N \mathcal{B}_C} \bar{\boldsymbol{\tau}} \cdot \mathbf{u}_C \, ds, \quad (2.47)$$

and

$$\widehat{\mathcal{E}}_L(\mathbf{u}_L, d_L; \mathbf{M}) := \int_{\mathcal{B}_L} w(\boldsymbol{\varepsilon}_L, d_L, \nabla d_L; \mathbf{M}) \, d\mathbf{x}, \quad (2.48)$$

for the total energy density defined in Formulation 2.1. With the strong displacement continuity in (3.31) we obtain

$$\mathcal{E}(\mathbf{u}, d; \mathbf{M}) \equiv \widehat{\mathcal{E}}(\mathbf{u}_C, \mathbf{u}_L, d_L; \mathbf{M}) := \widehat{\mathcal{E}}_C(\mathbf{u}_C; \mathbf{M}) + \widehat{\mathcal{E}}_L(\mathbf{u}_L, d_L; \mathbf{M}), \quad (2.49)$$

where \mathcal{E} is the original single-scale functional in Formulation 2.2. As a result, the domain decomposition variational formulation is *equivalent* to the single-scale formulation Eq. 3.30

$$\{\mathbf{u}_C, \mathbf{u}_L, d_L\} = \arg\left\{ \min_{\mathbf{u}_C \in \mathbf{V}_C, \mathbf{u}_L \in \mathbf{V}_L} \min_{d_L \in W_L} [\widehat{\mathcal{E}}(\mathbf{u}_C, \mathbf{u}_L, d_L; \mathbf{M})] \right\}. \quad (2.50)$$

Note, the major advantage of using this minimization problem instead of the one in (3.30) is the reduction of the nonlinearity order of the complementary domain (which is free from the fracture state), and more specifically in small deformation setting that is a linear minimization problem.

Remark 5: The strong displacement continuity requirement given in Eq. 3.31 is too restrictive from the computational standpoint [120]. To resolve the phase field problem, one requires $h_L \ll h_G$. However, if we assume $\mathbf{u}_L \stackrel{!}{=} \mathbf{u}_C$ on Γ , this yields $\Gamma_L = \Gamma_C$ in a discretized setting hence $h_L = h_G$ on Γ which has the contradiction with $h_L \ll h_G$.

Following Remark 3.1, we relax Eq. 3.31 in a weak sense by introducing traction-like terms in the corresponding energy functionals (2.23) and (2.26). This results in

$$\widehat{\mathcal{E}}_C(\mathbf{u}_C, \lambda_C; M) := \int_{\mathcal{B}_C} w(\varepsilon_C, \mathbf{1}, \mathbf{1}; M) \, d\mathbf{x} - \int_{\Gamma_C} \lambda_C \cdot \mathbf{u}_C \, ds - \int_{\Gamma_{N,C}} \bar{\boldsymbol{\tau}} \cdot \mathbf{u}_C \, ds, \quad (2.51)$$

and

$$\widehat{\mathcal{E}}_L(\mathbf{u}_L, \mathbf{d}_L, \lambda_L; M) := \int_{\mathcal{B}_L} w(\varepsilon_L, \mathbf{d}_L, \nabla \mathbf{d}_L; M) \, d\mathbf{x} - \int_{\Gamma_L} \lambda_L \cdot \mathbf{u}_L \, ds, \quad (2.52)$$

with $\lambda_C, \lambda_L \in \mathbf{L}^2(\Gamma)$ being the unknown Lagrange multipliers, which represent traction forces on the interface. The saddle point problem including complementary and local domains assumes the form

$$\widehat{\mathcal{E}}(\mathbf{u}_C, \mathbf{u}_L, \mathbf{d}_L, \lambda_L, \lambda_C; M) := \widehat{\mathcal{E}}_C(\mathbf{u}_C, \lambda_C; M) + \widehat{\mathcal{E}}_L(\mathbf{u}_L, \mathbf{d}_L, \lambda_L; M),$$

which is under-determined, since no relation is yet specified between \mathbf{u}_L and \mathbf{u}_C , nor between λ_L and λ_C . The latter is achieved by introducing the functional

$$\widehat{\mathcal{E}}_\Gamma(\mathbf{u}_\Gamma, \lambda_C, \lambda_L) := \int_{\Gamma} \mathbf{u}_\Gamma \cdot (\lambda_L + \lambda_C) \, ds, \quad (2.53)$$

with $\mathbf{u}_\Gamma \in \mathbf{H}^1(\Gamma)$ representing the (unknown) Lagrange multiplier, which has the dimension of a displacement, called also displacement interface. Summing \mathcal{E}_C and \mathcal{E}_L with \mathcal{E}_Γ , we get

$$\begin{aligned} \widehat{\mathcal{E}}(\mathbf{u}_C, \mathbf{u}_L, \mathbf{d}_L, \mathbf{u}_\Gamma, \lambda_C, \lambda_L; M) &:= \int_{\mathcal{B}_C} w(\varepsilon_C, \mathbf{1}, \mathbf{1}; M) \, d\mathbf{x} + \int_{\mathcal{B}_L} w(\varepsilon_L, \mathbf{d}_L, \nabla \mathbf{d}_L; M) \, d\mathbf{x} \\ &+ \int_{\Gamma} \{ \lambda_C \cdot (\mathbf{u}_\Gamma - \mathbf{u}_C) + \lambda_L \cdot (\mathbf{u}_\Gamma - \mathbf{u}_L) \} \, ds - \int_{\Gamma_{N,C}} \bar{\boldsymbol{\tau}} \cdot \mathbf{u}_C \, ds. \end{aligned} \quad (2.54)$$

Here the introduction of the intermediate displacement \mathbf{u}_Γ satisfies the weak traction continuity between λ_L and λ_C along Γ . This is in addition to the weak displacement continuity between \mathbf{u}_L and \mathbf{u}_C across Γ . Hence, both displacement and traction continuity are imposed implicitly in the weak sense to the energy functional, see PARK & FELIPPA [260]. The coupling interface energy functional used in Eq. 2.54 (i.e. third term) is called *Localized Lagrange Multipliers*, see e.g. [261, 292].

The variational formulation of Eq. 2.54 is equivalent to the single-scale minimization problem in Eq. 3.30, such that $\mathcal{E} \approx \widehat{\mathcal{E}}$, yields

$$\mathbf{s} = \arg\left\{ \min_{\mathbf{u}_C \in \mathbf{V}_C, \mathbf{u}_L \in \mathbf{V}_L, \mathbf{u}_\Gamma \in \mathbf{H}^1(\Gamma), \mathbf{d}_L \in W_L} \max_{\lambda_C, \lambda_L \in \mathbf{L}^2(\Gamma)} [\widehat{\mathcal{E}}(\mathbf{u}_C, \mathbf{u}_L, \mathbf{d}_L, \mathbf{u}_\Gamma, \lambda_C, \lambda_L; M)] \right\}, \quad (2.55)$$

where $\mathbf{s} := (\mathbf{u}_C, \mathbf{u}_L, d_L, \mathbf{u}_\Gamma, \lambda_C, \lambda_L)$. Accordingly, the displacement field \mathbf{u} , is decomposed as

$$\mathbf{u} = \begin{cases} \mathbf{u}_L & \text{for } \mathbf{x} \in \mathcal{B}_L, \\ \mathbf{u}_C & \text{for } \mathbf{x} \in \mathcal{B}_C, \\ \mathbf{u}_\Gamma & \text{for } \mathbf{x} \in \Gamma, \end{cases} \quad (2.56)$$

which is based on the solution triple $(\mathbf{u}_C, \mathbf{u}_L, \mathbf{u}_\Gamma)$ as a minimizer of the (2.54). Note, the representation for d in terms of d_L defined by (2.46) remains same.

2.3.2. Global-Local formulation. In this section, the formulation is extended to a Global-Local approach in line with [143]. Specifically in this work, we extend the Global-Local formulation to the anisotropic crack phase-field which is augmented by Robin-type boundary conditions [121, 211, 210, 136]. The latter relaxes the stiff local response observed at the global level which is due to the local non-linearity projected to the global level and leads to further reductions of the computational time. Additionally, to have more regularity along the coupling interface, a non-matching finite element discretization is used on the interface.

Let us define open and bounded *fictitious domain* \mathcal{B}_F to recover the space of \mathcal{B} that is obtained by removing \mathcal{B}_L from its continuum domain, see Fig. 3.2. Indeed, the fictitious domain is prolongation of the \mathcal{B}_C towards \mathcal{B} . This gives the same constitutive modeling used in \mathcal{B}_C for \mathcal{B}_F . Thus, the energy functional of the complementary and fictitious domain is the same. We also use the identical discretization space for both \mathcal{B}_F and \mathcal{B}_C , which results $h_F := h_C$. We further define, an open and bounded *global domain* \mathcal{B}_G such that $\mathcal{B}_G = \mathcal{B}_F \cup \Gamma \cup \mathcal{B}_C$. It yields the same energy functional for \mathcal{B}_C , \mathcal{B}_F and \mathcal{B}_G . Hence, the material parameters are identical for \mathcal{B}_C , \mathcal{B}_F and \mathcal{B}_G . Additionally, this unification yields on identical discretization space for the global domains \mathcal{B}_F and \mathcal{B}_C , and results in $h_G \approx h_F \approx h_C$ referring to the element size.

Note that, the fictitious domain \mathcal{B}_F is assumed to be free from geometrical *imperfections* which may be present in \mathcal{B}_L , see Fig. 3.2(b). Thus, the global domain is assumed to be free from any given imperfection. Let us also define, global and local interfaces denoted as $\Gamma_G \subset \mathcal{B}_G$ and $\Gamma_L \subset \mathcal{B}_L$, such that in the continuum setting we have $\Gamma = \Gamma_G = \Gamma_L$. However in a discrete setting we might have $\Gamma \neq \Gamma_G \neq \Gamma_L$ due to the presence of different meshing schemes (i.e. different element size/type used in \mathcal{B}_G and \mathcal{B}_L such that $h \neq h_L \neq h_G$ on Γ).

It is assumed that there exists a continuous prolongation of \mathbf{u}_C into \mathcal{B}_F . Hence, we introduce a function $\mathbf{u}_G \in \mathbf{V}(\mathcal{B}_G)$ such that $\mathbf{u}_G|_{\mathcal{B}_C} \equiv \mathbf{u}_C$ and $\mathbf{u}_G = \mathbf{u}_C$ on Γ in the sense of a trace. Thus, the boundary conditions for \mathcal{B}_G is same as the \mathcal{B}_C , therefore it holds $\mathbf{u}_G = \bar{\mathbf{u}}$ on $\partial_D \mathcal{B}$ and $\boldsymbol{\tau} = \bar{\boldsymbol{\tau}}$ on $\Gamma_{N,G}$. By means of the fictitious domain, the first term in Eq. 2.54 is recast as follows

$$\begin{aligned} \int_{\mathcal{B}_C} w(\varepsilon(\mathbf{u}_C), 1, 1; \mathbf{M}) \, d\mathbf{x} &= \int_{\mathcal{B}_C} w(\varepsilon(\mathbf{u}_G), 1, 1; \mathbf{M}) \, d\mathbf{x} \\ &= \int_{\mathcal{B}_G} w(\varepsilon(\mathbf{u}_G), 1, 1; \mathbf{M}) \, d\mathbf{x} - \int_{\mathcal{B}_F} w(\varepsilon(\mathbf{u}_G), 1, 1; \mathbf{M}) \, d\mathbf{x}. \end{aligned} \quad (2.57)$$

Note, we substitute \mathbf{u}_G for \mathbf{u}_C in the second and fourth integrals in Eq. 2.57. That is trivial by means of the prolongation concept such that $\mathbf{u}_G|_{\mathcal{B}_F} \equiv \mathbf{u}_F$ and $\mathbf{u}_G = \mathbf{u}_F$ on Γ .

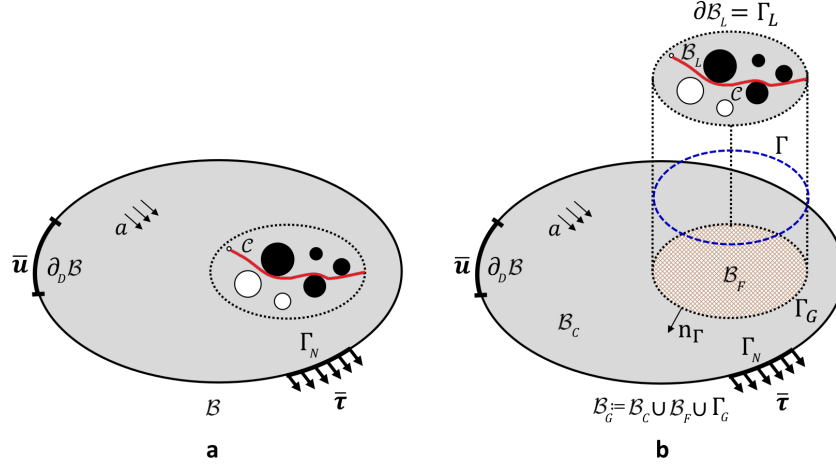


Figure 2.5: Illustration of the Global-Local formulation. (a) Geometry and loading setup of the single-scale boundary value problem. (b) Global-Local setting, by introduction of the fictitious domain \mathcal{B}_F through prolongation of \mathcal{B}_C to the entire domain whereas its unification is so-called global domain $\mathcal{B}_G := \mathcal{B}_C \cup \Gamma \cup \mathcal{B}_F$.

This provides the *Global-Local* approximation of the single-scale energy functional \mathcal{E} indicated in Formulation 2.2 by

$$\begin{aligned}
\tilde{\mathcal{E}} := & \underbrace{\int_{\mathcal{B}_G} w(\boldsymbol{\varepsilon}_G, 1, 1; \mathbf{M}) \, d\mathbf{x} - \int_{\mathcal{B}_F} w(\boldsymbol{\varepsilon}_F, 1, 1; \mathbf{M}) \, d\mathbf{x} - \int_{\Gamma_{N,G}} \bar{\boldsymbol{\tau}} \cdot \mathbf{u}_G \, ds}_{\text{global terms}} \\
& + \underbrace{\int_{\mathcal{B}_L} w(\boldsymbol{\varepsilon}_L, d_L, \nabla d_L; \mathbf{M}) \, d\mathbf{x}}_{\text{local term}} \\
& + \underbrace{\int_{\Gamma} \{\lambda_C \cdot (\mathbf{u}_\Gamma - \mathbf{u}_G) + \lambda_L \cdot (\mathbf{u}_\Gamma - \mathbf{u}_L)\} \, ds}_{\text{coupling terms}}.
\end{aligned} \tag{2.58}$$

where the approximation $\mathcal{E}(\mathbf{u}, \mathbf{d}; \mathbf{M}) \equiv \tilde{\mathcal{E}}(\mathbf{u}_G, \mathbf{u}_L, d_L, \mathbf{u}_\Gamma, \lambda_C, \lambda_L; \mathbf{M})$ holds.

Formulation 1.6: Global-Local energy functional for anisotropic crack topology

Let \mathbf{M} , χ , Ξ and α be given with initial conditions $\mathbf{u}_0 = \mathbf{u}(\mathbf{x}, 0)$ and $d_0 = d(\mathbf{x}, 0)$. For the loading increments $n = 1, 2, \dots, N$, find $\mathbf{u}_G := \mathbf{u}_G^n \in \mathbf{V}_G$, $\mathbf{u}_L := \mathbf{u}_L^n \in \mathbf{V}_L$, $\mathbf{u}_\Gamma := \mathbf{u}_\Gamma^n \in \mathbf{H}^1(\Gamma)$, $d_L := d_L^n \in W_L$, $\lambda_C := \lambda_C^n \in \mathbf{L}^2(\Gamma)$ and $\lambda_L := \lambda_L^n \in \mathbf{L}^2(\Gamma)$, such that

the functional

$$\begin{aligned}
\tilde{\mathcal{E}}(\mathbf{u}_G, \mathbf{u}_L, d_L, \mathbf{u}_\Gamma, \lambda_C, \lambda_L; \mathbf{M}) = & \\
& \underbrace{\int_{\mathcal{B}_G} \left(\frac{\lambda}{2} I_1^2 + \mu I_2 \right) d\mathbf{x}}_{\text{global matrix deformation term}} + \underbrace{\int_{\mathcal{B}_G} \left(\frac{1}{2} \chi I_4^2 + 2\Xi I_5 \right) d\mathbf{x}}_{\text{global fiber deformation term}} - \underbrace{\int_{\Gamma_{N,G}} \bar{\boldsymbol{\tau}} \cdot \mathbf{u}_G ds}_{\text{global external load}} \\
& - \underbrace{\int_{\mathcal{B}_F} \left(\frac{\lambda}{2} I_1^2 + \mu I_2 \right) d\mathbf{x}}_{\text{fictitious matrix deformation term}} - \underbrace{\int_{\mathcal{B}_F} \left(\frac{1}{2} \chi I_4^2 + 2\Xi I_5 \right) d\mathbf{x}}_{\text{fictitious fiber deformation term}} \\
& + \underbrace{\int_{\mathcal{B}_L} g(d_{L+}) \left(\frac{\lambda}{2} I_1^{+2} + \mu I_2^+ \right) d\mathbf{x}}_{\text{local matrix deformation term}} + \underbrace{\int_{\mathcal{B}_L} \left(\frac{\lambda}{2} I_1^{-2} + \mu I_2^- \right) d\mathbf{x}}_{\text{local matrix deformation term}} + \underbrace{\int_{\mathcal{B}_L} g(d_{L+}) \left(\frac{1}{2} \chi I_4^2 + 2\Xi I_5 \right) d\mathbf{x}}_{\text{local fiber deformation term}} \\
& + G_c \underbrace{\int_{\mathcal{B}_L} \left\{ \frac{1}{2l} (1 - d_L)^2 + \frac{l}{2} \nabla d_L \cdot \nabla d_L \right\} d\mathbf{x}}_{\text{local matrix fracture term}} + G_c \underbrace{\int_{\mathcal{B}_L} \left(\alpha \frac{l}{2} \nabla d_L \cdot \mathbf{M} \cdot \nabla d_L \right) d\mathbf{x}}_{\text{local fiber fracture term}} \\
& + \underbrace{\int_{\Gamma} \left\{ \lambda_C \cdot (\mathbf{u}_\Gamma - \mathbf{u}_G) + \lambda_L \cdot (\mathbf{u}_\Gamma - \mathbf{u}_L) \right\} ds}_{\text{interface coupling term}},
\end{aligned}$$

is minimized.

Note, we are not any more using $\partial_N \mathcal{B}$ for the applied surface load and hence $\Gamma_{N,G}$ is considered. This is because the global domain is free from any fracture state. The minimization problem for the Global-Local energy functional given in Formulation 2.6 that is applied to the anisotropic crack topology takes the following compact form,

$$\mathbf{s} = \arg \left\{ \min_{\mathbf{u}_G \in \mathbf{V}_G, \mathbf{u}_L \in \mathbf{V}_L, \mathbf{u}_\Gamma \in \mathbf{H}^1(\Gamma), d_L \in W_L} \max_{\lambda_C, \lambda_L \in \mathbf{L}^2(\Gamma)} \left[\tilde{\mathcal{E}}(\mathbf{u}_G, \mathbf{u}_L, d_L, \mathbf{u}_\Gamma, \lambda_C, \lambda_L; \mathbf{M}) \right] \right\} \quad (2.59)$$

where $\mathbf{s} := (\mathbf{u}_G, \mathbf{u}_L, d_L, \mathbf{u}_\Gamma, \lambda_C, \lambda_L)$.

The relation between the solution \mathbf{u} of the minimization problem in Eq. 3.30 and the solution triple $(\mathbf{u}_G, \mathbf{u}_L, \mathbf{u}_\Gamma)$ of Eq. 2.59 reads

$$\mathbf{u} = \begin{cases} \mathbf{u}_L, & \text{for } \mathbf{x} \in \mathcal{B}_L, \\ \mathbf{u}_G, & \text{for } \mathbf{x} \in \mathcal{B}_G, \\ \mathbf{u}_\Gamma, & \text{for } \mathbf{x} \in \Gamma. \end{cases}$$

Remark 6: When using standard single scale phase-field modeling, we are most of the time not dealing with a uniform mesh and hence the domain is divided into coarser and finer mesh elements. To resolve the crack phase-field, we need to have $l \geq h$ must hold at every point of the domain such that $l \geq h_c \geq h_f$ (c and f refers to the coarse and fine region in domain, respectively) satisfied. This typically leads to a finer mesh even for the area which is sufficiently far from the fracture zone, and therefore increases the computational time considerably. However, this is not the case for the Global-Local approach where the phase-field formulation is only embedded within the local domain and not the entire domain. Hence the computational time is reduced drastically.

2.3.3. Variational formulation for the Global-Local coupling system. Now we consider the weak formulation of Eq. 2.59. The directional derivatives of the functional $\tilde{\mathcal{E}}$ yield for the global weak form

$$\begin{aligned} \tilde{\mathcal{E}}_{\mathbf{u}_G}(\mathbf{s}; \delta \mathbf{u}_G) &:= \int_{\mathcal{B}_G} \boldsymbol{\sigma}(\mathbf{u}_G; \mathbf{M}) : \boldsymbol{\varepsilon}(\delta \mathbf{u}_G) \, d\mathbf{x} - \int_{\mathcal{B}_F} \boldsymbol{\sigma}(\mathbf{u}_G; \mathbf{M}) : \boldsymbol{\varepsilon}(\delta \mathbf{u}_G) \, d\mathbf{x} \\ &\quad - \int_{\Gamma_G} \lambda_C \cdot \delta \mathbf{u}_G \, ds - \int_{\Gamma_{N,G}} \bar{\boldsymbol{\tau}} \cdot \delta \mathbf{u}_G \, ds = 0, \end{aligned} \quad (\text{G})$$

where $\boldsymbol{\sigma}(\mathbf{u}_G) := \partial_{\boldsymbol{\varepsilon}} w(\boldsymbol{\varepsilon}(\mathbf{u}_G), \mathbf{1}, \mathbf{1}; \mathbf{M})$ and $\delta \mathbf{u}_G \in \{\mathbf{H}^1(\mathcal{B}_G) : \delta \mathbf{u}_G = \mathbf{0} \text{ on } \partial_D \mathcal{B}\}$ is the test function. The local weak formulations assumes the form

$$\left\{ \begin{aligned} \tilde{\mathcal{E}}_{\mathbf{u}_L}(\mathbf{s}; \delta \mathbf{u}_L) &:= \int_{\mathcal{B}_L} \boldsymbol{\sigma}(\mathbf{u}_L, d_L; \mathbf{M}) : \boldsymbol{\varepsilon}(\delta \mathbf{u}_L) \, d\mathbf{x} - \int_{\Gamma_L} \lambda_L \cdot \delta \mathbf{u}_L \, ds = 0, \\ \tilde{\mathcal{E}}_{d_L}(\mathbf{s}; \delta d_L) &:= (1 - \kappa) \int_{\mathcal{B}_L} 2d_L \mathcal{H}(\boldsymbol{\varepsilon}(\mathbf{u}_L); \mathbf{M}) \cdot \delta d_L \, d\mathbf{x} + \int_{\mathcal{B}_L} (d_L - 1) \cdot \delta d_L \, d\mathbf{x} \\ &\quad + \int_{\mathcal{B}_L} l^2 \nabla d_L \cdot \nabla(\delta d_L) \, d\mathbf{x} + \int_{\mathcal{B}_L} \alpha l^2 \nabla d_L \cdot \mathbf{M} \cdot \nabla(\delta d_L) \, d\mathbf{x} = 0, \end{aligned} \right. \quad (\text{L})$$

where $\boldsymbol{\sigma}(\mathbf{u}_L, d_L; \mathbf{M}) = \partial_{\boldsymbol{\varepsilon}} w(\boldsymbol{\varepsilon}_L, d_L, \nabla d_L; \mathbf{M}) = \boldsymbol{\sigma}_{\boldsymbol{\varepsilon}}^{iso}(\boldsymbol{\varepsilon}_L, d_L) + \boldsymbol{\sigma}_{\boldsymbol{\varepsilon}}^{aniso}(\boldsymbol{\varepsilon}_L, d_L, \mathbf{M})$ is defined in Eq. 2.22, $\delta \mathbf{u}_L \in \mathbf{H}^1(\mathcal{B}_L)$ is the local test function and $\delta d_L \in \mathbf{H}^1(\mathcal{B}_L)$ is the local phase-field test function.

The variational derivatives of $\tilde{\mathcal{E}}$ with respect to $(\mathbf{u}_\Gamma, \lambda_C, \lambda_L)$ provide kinematic equations due to weak coupling between global and local form

$$\tilde{\mathcal{E}}_{\mathbf{u}_\Gamma}(\mathbf{s}; \delta \mathbf{u}_\Gamma) := \int_{\Gamma} (\lambda_C + \lambda_L) \cdot \delta \mathbf{u}_\Gamma \, ds = 0, \quad (\text{C}_1)$$

$$\tilde{\mathcal{E}}_{\lambda_C}(\mathbf{s}; \delta \lambda_C) := \int_{\Gamma} (\mathbf{u}_\Gamma - \mathbf{u}_G) \cdot \delta \lambda_C \, ds = 0, \quad (\text{C}_2)$$

$$\tilde{\mathcal{E}}_{\lambda_L}(\mathbf{s}; \delta \lambda_L) := \int_{\Gamma} (\mathbf{u}_\Gamma - \mathbf{u}_L) \cdot \delta \lambda_L \, ds = 0. \quad (\text{C}_3)$$

Herein $\delta \mathbf{u}_\Gamma \in \mathbf{H}^1(\Gamma)$ and $\delta \lambda_C, \delta \lambda_L \in \mathbf{L}^2(\Gamma)$ are the corresponding test functions.

Let us now focus on the global variational in (G). The presence of the two domain integrals over \mathcal{B}_G and \mathcal{B}_F would imply in this case the need to simultaneously access the corresponding stiffness matrices. Avoiding this can be done as follows: We focus on the domain integral over \mathcal{B}_F in (G). The idea is to transform the domain integral in \mathcal{B}_F to the global interface Γ_G . The divergence theorem leads to

$$\int_{\mathcal{B}_F} \boldsymbol{\sigma}(\mathbf{u}_G) : \boldsymbol{\varepsilon}(\delta \mathbf{u}_G) \, d\mathbf{x} = - \int_{\mathcal{B}_F} \mathbf{div}(\boldsymbol{\sigma}(\mathbf{u}_G)) \cdot \delta \mathbf{u}_G \, d\mathbf{x} + \int_{\partial \mathcal{B}_F} \boldsymbol{\sigma}(\mathbf{u}_G) \cdot \mathbf{n}_{\partial \mathcal{B}_F} \cdot \delta \mathbf{u}_G \, ds, \quad (2.60)$$

where $\mathbf{n}_{\partial \mathcal{B}_F}$ is the unit outward normal vector to $\partial \mathcal{B}_F$.

The first term in the right-hand side of in Eq. 2.60 can be canceled by using the divergence-free assumption for the stress (no body forces in \mathcal{B}_F). Following a detailed argument in GERASIMOV ET AL. [143], the second term can be further simplified

$$\int_{\partial \mathcal{B}_F} \boldsymbol{\sigma}(\mathbf{u}_G) \cdot \mathbf{n}_{\partial \mathcal{B}_F} \cdot \delta \mathbf{u}_G \, ds = \int_{\Gamma_G} \boldsymbol{\sigma}(\mathbf{u}_G) \cdot \mathbf{n}_\Gamma \cdot \delta \mathbf{u}_G \, ds + \int_{\partial \mathcal{B}_F \cap \Gamma_{N,G}} \bar{\boldsymbol{\tau}} \cdot \delta \mathbf{u}_G \, ds.$$

Here, $\mathbf{n}_\Gamma := \mathbf{n}_{\partial\mathcal{B}_F}$ denotes the normal vector on Γ_G , outward of \mathcal{B}_F , as illustrated in Fig. 3.2. Furthermore, it is possible to choose \mathcal{B}_L and its coarse representation into the global level as \mathcal{B}_F such that $\partial\mathcal{B}_F \cap \Gamma_{N,G} = \emptyset$. This is in line with the assumption that the local domain \mathcal{B}_L and additionally \mathcal{B}_F is free from any applied external load. Thus, the last surface integral cancels and (2.60) can be restated as,

$$\int_{\mathcal{B}_F} \boldsymbol{\sigma}(\mathbf{u}_G) : \boldsymbol{\varepsilon}(\boldsymbol{\delta}\mathbf{u}_G) \, d\mathbf{x} = \int_{\Gamma_G} \boldsymbol{\sigma}(\mathbf{u}_G) \cdot \mathbf{n}_\Gamma \cdot \boldsymbol{\delta}\mathbf{u}_G \, d\mathbf{s}, \quad (2.61)$$

such that there exists a fictitious Lagrange multiplier $\lambda_F \in \mathbf{L}^2(\Gamma)$ with

$$\int_{\Gamma_G} \boldsymbol{\sigma}(\mathbf{u}_G) \cdot \mathbf{n}_\Gamma \cdot \boldsymbol{\delta}\mathbf{u}_G \, d\mathbf{s} =: \int_{\Gamma_G} \lambda_F \cdot \boldsymbol{\delta}\mathbf{u}_G \, d\mathbf{s}. \quad (2.62)$$

Here, λ_F is a traction-like quantity on Γ_G . Due to (2.61)–(2.62), the *partitioned* representation of equation (G) takes the following form

$$\int_{\mathcal{B}_G} \boldsymbol{\sigma}(\mathbf{u}_G) : \boldsymbol{\varepsilon}(\boldsymbol{\delta}\mathbf{u}_G) \, d\mathbf{x} - \int_{\Gamma_G} \lambda_F \cdot \boldsymbol{\delta}\mathbf{u}_G \, d\mathbf{s} - \int_{\Gamma_G} \lambda_C \cdot \boldsymbol{\delta}\mathbf{u}_G \, d\mathbf{s} - \int_{\Gamma_{N,G}} \bar{\boldsymbol{\tau}} \cdot \boldsymbol{\delta}\mathbf{u}_G \, d\mathbf{s} = \mathbf{0}, \quad (G_1)$$

with λ_F satisfying

$$\int_{\Gamma_G} \lambda_F \cdot \boldsymbol{\delta}\mathbf{u}_G \, d\mathbf{s} = \int_{\mathcal{B}_F} \boldsymbol{\sigma}(\mathbf{u}_G) : \boldsymbol{\varepsilon}(\boldsymbol{\delta}\mathbf{u}_G) \, d\mathbf{x}. \quad (G_2)$$

Equations (G₁), (G₂) refer to the global system of equations. The system of equations (L) is called a local variational equation and additionally (C₁), (C₂), (C₃) refer to the coupling terms. The entire system is the basis for the *Global-Local approach*.

2.3.4. Dirichlet-Neumann type boundary conditions. To accommodate a Global-Local computational scheme, instead of finding the stationary solution of the (G₁), (G₂), (L) along with (C₁), (C₂), (C₃) in the monolithic sense, an alternate minimization is used. This is in line with [143], which leads to the Global-Local formulation through the concept of non-intrusiveness. Here the global and local level are solved in a multiplicative manner according to the idea of Schwarz' alternating method [244].

Let $k \geq 0$ be the Global-Local iteration index at a fixed loading step n . The iterative solution procedure for Global-Local computational scheme is as follows:

- Dirichlet local problem: solution of local problem (L) coupled with (C₃),
- Pre-processing global level: recovery phase using (C₁) and (G₂),
- Neumann global problem: solution of global problem (G₁),
- Post-processing global level: recovery phase using (C₂).

The detailed scheme for applying the Dirichlet-Neumann type boundary conditions to the isotropic phase-field fracture modeling is described in [143].

Despite of its strong non-intrusiveness implementation point of view [140], there are two shortcomings embedded in the system which have to be resolved. (a) Due to the

extreme difference in stiffness between the local domain and its projection to the global level, i.e. fictitious domain, the relaxation/acceleration techniques has to be used, see [143]. (b) Additionally, it turns out that if the solution vector $(\mathbf{u}_G^k, \mathbf{u}_L^k, d_L^k, \mathbf{u}_\Gamma^k, \lambda_C^k, \lambda_L^k)$ is plugged into equations (G_1) , (G_2) , (L) , (C_1) , (C_2) , (C_3) , the imbalanced quantities follow

$$\int_{\Gamma} (\mathbf{u}_\Gamma^k - \mathbf{u}_L^k) \cdot \delta \lambda_L \, ds \neq 0 \quad \text{and} \quad \int_{\Gamma} \lambda_F^k \cdot \delta \mathbf{u}_G \, ds \neq \int_{\mathcal{B}_F} \boldsymbol{\sigma}(\mathbf{u}_G^k) : \boldsymbol{\varepsilon}(\delta \mathbf{u}_G) \, dx, \quad (2.63)$$

resulting in the *iterative* Global-Local computation scheme. Figure 2.6a depicts one iteration of the Global-Local approach by means of the Dirichlet-Neumann type boundary conditions. The aforementioned difficulties motivate us to provide an alternative coupling conditions that overcome these challenges, which are explained in the following section.

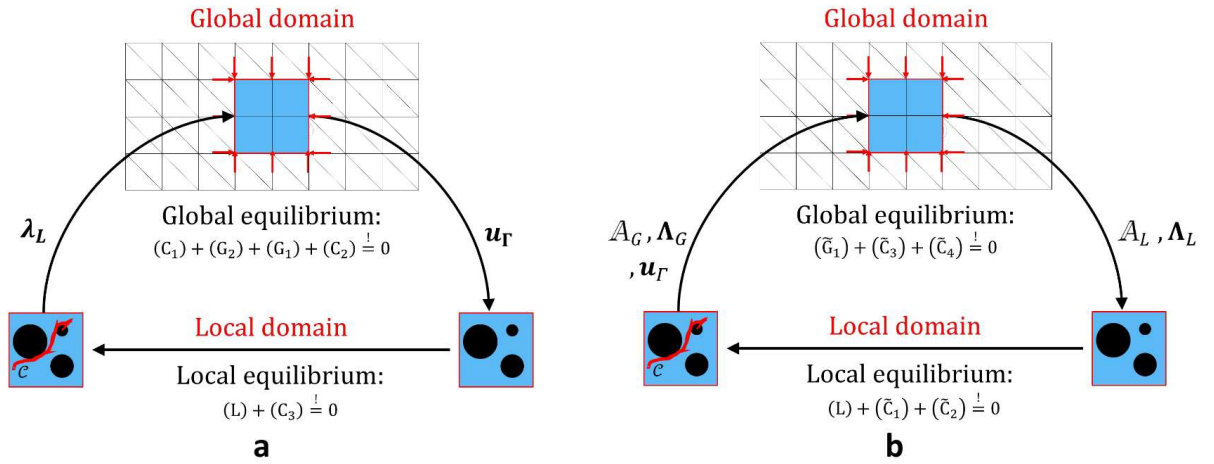


Figure 2.6: Global-Local iterative scheme with (a) Dirichlet-Neumann type boundary conditions; (b) Robin-type boundary conditions.

2.3.5. Robin-type boundary conditions. In this section, the Global-Local formulation is enhanced using Robin-type boundary conditions to relax the stiff local response that is observed at the global level (due to the local non-linearity). Furthermore the computational time is reduced. This improves the resolution of the imbalanced quantities in (3.36) and it accelerates the Global-Local computational iterations.

Recall, the coupling equations denoted in (C_1) , (C_2) and (C_3) arise from the stationary of the interface energy functional. That provides the boundary conditions which have to be imposed on the global and local levels. At that level the Robin-type boundary conditions are formulated.

- **Robin-type boundary conditions at the local level**

At the local level the new coupling term is introduced as a combination of (C_1) and (C_2)

$$\tilde{\mathcal{E}}_{\mathbf{u}_\Gamma}(s; \delta \mathbf{u}_\Gamma) + A_L \tilde{\mathcal{E}}_{\lambda_C}(s; \delta \lambda_C) = \int_{\Gamma} (\lambda_C + \lambda_L) \cdot \delta \mathbf{u}_\Gamma \, ds + A_L \int_{\Gamma} (\mathbf{u}_\Gamma - \mathbf{u}_G) \cdot \delta \lambda_C \, ds = 0. \quad (2.64)$$

This leads for iteration k to

$$\int_{\Gamma} (\lambda_C^{k-1} + \lambda_L^k) \cdot \delta \mathbf{u}_\Gamma \, ds + A_L \int_{\Gamma} (\mathbf{u}_\Gamma^{k, \frac{1}{2}} - \mathbf{u}_G^{k-1}) \cdot \delta \lambda_C \, ds = 0. \quad (2.65)$$

Herein, A_L is a local augmented stiffness matrix applied on the interface which serves as regularization of the local Jacobian matrix. By means of (2.65) at iteration k , the local system of equations results in the following boundary conditions

$$\int_{\Gamma} \lambda_L^k \cdot \delta \mathbf{u}_{\Gamma} \, ds + A_L \int_{\Gamma} \mathbf{u}_{\Gamma}^{k, \frac{1}{2}} \cdot \delta \lambda_C \, ds = \Lambda_L^{k-1}, \quad (\tilde{C}_1)$$

$$\int_{\Gamma} (\mathbf{u}_{\Gamma}^{k, \frac{1}{2}} - \mathbf{u}_L^k) \cdot \delta \lambda_L \, ds = 0, \quad (\tilde{C}_2)$$

with

$$\Lambda_L^{k-1} := \Lambda_L(\lambda_C^{k-1}, \mathbf{u}_G^{k-1}; A_L) = A_L \int_{\Gamma} \mathbf{u}_G^{k-1} \cdot \delta \lambda_C \, ds - \int_{\Gamma} \lambda_C^{k-1} \cdot \delta \mathbf{u}_{\Gamma} \, ds. \quad (2.66)$$

Along with (L), the local system of equations has to be solved for $(\mathbf{u}_L^k, \lambda_L^k, \mathbf{u}_{\Gamma}^{k, \frac{1}{2}})$ for given local Robin-type parameters (Λ_L^{k-1}, A_L) .

- *Robin-type boundary conditions at the global level*

Accordingly, at the global level, the new coupling term is stated as a combination of (C₁) and (C₃)

$$\tilde{\mathcal{E}}_{\mathbf{u}_{\Gamma}}(\mathbf{s}; \delta \mathbf{u}_{\Gamma}) + A_G \tilde{\mathcal{E}}_{\lambda_L}(\mathbf{s}; \delta \lambda_L) = \int_{\Gamma} (\lambda_C + \lambda_L) \cdot \delta \mathbf{u}_{\Gamma} \, ds + A_G \int_{\Gamma} (\mathbf{u}_{\Gamma} - \mathbf{u}_L) \cdot \delta \lambda_L \, ds = 0. \quad (2.67)$$

This leads for iteration k to

$$\int_{\Gamma} (\lambda_C^k + \lambda_L^k) \cdot \delta \mathbf{u}_{\Gamma} \, ds + A_G \int_{\Gamma} (\mathbf{u}_{\Gamma}^k - \mathbf{u}_L^k) \cdot \delta \lambda_L \, ds = 0,$$

where, A_G is a global augmented stiffness matrix applied on the interface.

Through (2.67) at the iteration k , the Robin-type boundary condition at the global level follows

$$\int_{\Gamma} \lambda_C^k \cdot \delta \mathbf{u}_{\Gamma} \, ds + A_G \int_{\Gamma} \mathbf{u}_{\Gamma}^k \cdot \delta \lambda_L \, ds = \Lambda_G^k, \quad (\tilde{C}_3)$$

$$\int_{\Gamma} (\mathbf{u}_{\Gamma}^{k, \frac{1}{2}} - \mathbf{u}_G^k) \cdot \delta \lambda_C \, ds = 0, \quad (\tilde{C}_4)$$

with

$$\Lambda_G^k := \Lambda_L(\lambda_G^k, \mathbf{u}_L^k; A_G) = A_G \int_{\Gamma} \mathbf{u}_L^k \cdot \delta \lambda_L \, ds - \int_{\Gamma} \lambda_L^k \cdot \delta \mathbf{u}_{\Gamma} \, ds. \quad (2.68)$$

Together with (G₁) and (G₂), the global system of equations has to be solved for $(\mathbf{u}_G^k, \lambda_C^k, \mathbf{u}_{\Gamma}^k)$ for a given $(\Lambda_G^k, A_G, \mathbf{u}_{\Gamma}^{k, \frac{1}{2}})$. Here, A_G and Λ_G^k stand for global Robin-type parameters.

Based on the new boundary conditions provided in (\tilde{C}_1), (\tilde{C}_2), (\tilde{C}_3) and (\tilde{C}_4) the imbalanced quantities in the Global-Local iterations read

$$\int_{\Gamma} (\mathbf{u}_{\Gamma}^k - \mathbf{u}_{\Gamma}^{k, \frac{1}{2}}) \cdot \delta \lambda_L \, ds \neq 0 \quad \text{and} \quad \int_{\Gamma} \lambda_F^k \cdot \delta \mathbf{u}_G \, ds \neq \int_{\mathcal{B}_F} \boldsymbol{\sigma}(\mathbf{u}_G^k) : \boldsymbol{\varepsilon}(\delta \mathbf{u}_G) \, dx, \quad (2.69)$$

For the specific Robin-type boundary conditions, we can resolve Eq. 2.69₁ such that this term does not produce any error in the iterative procedure. To do so, following Section 2.3.6, the global and local augmented stiffness matrices within the Robin-type boundary conditions are given by

$$\boxed{A_G = \mathbf{L}_L^T \mathbf{T}_L^{-T} \mathcal{S}_L \quad \text{and} \quad A_L := \mathcal{S}_C.} \quad (2.70)$$

A_G and A_L can be seen as augmented stiffness matrices regularize the Jacobian stiffness matrix at the global and local levels, respectively.

In the Robin-type boundary condition given in (\tilde{C}_1) and (\tilde{C}_3) , we can extract different criteria, e.g.

- $A_L \rightarrow \infty$: Dirichlet boundary conditions and $A_G \rightarrow 0$: Neumann boundary conditions;
- $A_L \rightarrow 0$: Neumann boundary conditions and $A_G \rightarrow \infty$: Dirichlet boundary conditions;
- $A_L = \mathcal{S}_C$: Robin-type boundary conditions and $A_G \rightarrow \infty$: Dirichlet boundary conditions;

Hence, depending on the Robin-type parameters, a family of boundary conditions can be formulated.

Additionally to achieve a balance state of Eq. 2.69₂, the following partitioned representation of equation (G)

$$\int_{\mathcal{B}_G} \boldsymbol{\sigma}(\mathbf{u}_G) : \boldsymbol{\varepsilon}(\delta \mathbf{u}_G) \, dx - \int_{\Gamma} \boldsymbol{\lambda}_F \cdot \delta \mathbf{u}_G \, ds - \int_{\Gamma} \boldsymbol{\lambda}_C \cdot \delta \mathbf{u}_G \, ds - \int_{\Gamma_{N,G}} \bar{\boldsymbol{\tau}} \cdot \delta \mathbf{u}_G \, ds = 0, \quad (\tilde{G}_1)$$

is equipped with a linearized $\Delta \boldsymbol{\lambda}_F$ satisfying

$$\int_{\Gamma} \Delta \boldsymbol{\lambda}_F \cdot \delta \mathbf{u}_G \, ds = \int_{\Gamma} \mathcal{S}_F \Delta \mathbf{u}_G \cdot \delta \mathbf{u}_G \, dx. \quad (\tilde{G}_2)$$

Note that now the second imbalance quantity shown in (2.69) does not anymore produce an error. We are not solving for $\boldsymbol{\lambda}_F$ and in the linearized equation of (\tilde{G}_1) this term is replaced by (\tilde{G}_2) . The linearized equation of (\tilde{G}_1) is solved within a single iteration, because we are dealing with a linear elastic constitutive equations.

The detailed Global-Local formulation using Robin-type boundary conditions is depicted in Algorithm 3.3. Accordingly, Fig. 2.6b depicts one iteration of the Global-Local coupling scheme by means of the Robin-type boundary conditions. The Global-Local setting provides a generic two-scale finite element algorithms that enables capturing local non-linearities.

2.3.6. Derivation of Robin-Type Boundary conditions. In this section, we investigate the relationship between $\Delta \hat{\mathbf{u}}$ and $\Delta \hat{\boldsymbol{\lambda}}$ (in the incremental sense) for the complementary, fictitious and local domain at the converged solution state. Doing that,

Robin-type boundary conditions can be derived such that all coupling terms given in (C₁), (C₂) and (C₃) satisfied, simultaneously, at a Global-Local iteration k .

Recall the complementary term used in Eq. 2.54 and let \mathbf{u}_C and λ_C be the stationary of the following functional,

$$\mathcal{L}(\mathbf{u}_C, \lambda_C; M) := \int_{\mathcal{B}_C} \mathbf{w}(\varepsilon_C, \mathbf{1}, \mathbf{1}; M) \, d\mathbf{x} + \int_{\Gamma} \lambda_C \cdot (\mathbf{u}_\Gamma - \mathbf{u}_C) \, d\mathbf{s} - \int_{\Gamma_{N,C}} \bar{\boldsymbol{\tau}} \cdot \mathbf{u}_C \, d\mathbf{s}. \quad (2.71)$$

Here, $\Gamma \in \mathcal{R}^{\delta-1} \subset \mathcal{B}_C$ is denoted as an interface and $\mathbf{u}_\Gamma := \text{tr } \mathbf{u}_C \in \mathbf{H}^{1/2}(\Gamma)$ can be given implicitly, i.e. $(\tilde{C}_1)+(\tilde{C}_2)$ or explicitly, i.e. (\tilde{C}_4) . Recall Eq. 2.71 lives in \mathcal{B}_C (the following description holds true for \mathcal{B}_F except $\bar{\boldsymbol{\tau}} = \mathbf{0}$). The stationary points of the energy functional for the \mathcal{L} is characterized by the first-order necessary conditions through $\mathcal{L}_1 = \mathcal{L}_u(\mathbf{u}_C, \lambda_C; \mathbf{w}) = \mathbf{0}$ and $\mathcal{L}_2 = \mathcal{L}_{\lambda}(\mathbf{u}_C, \lambda_C; \kappa) = \mathbf{0}$. We split \mathcal{L}_1 into inner nodes and interface nodes denoted as, $\{a, b\}$, respectively, by

$$\begin{aligned} \mathcal{L}_1^a(\mathbf{u}) &= \mathbf{f}^a - \bar{\mathbf{F}} \stackrel{!}{=} \mathbf{0} & \mathbf{x} \in \mathcal{B} \setminus \Gamma, \\ \mathcal{L}_1^b(\mathbf{u}) &= \mathbf{f}^b - \mathbf{L}_G^T \hat{\lambda}_C \stackrel{!}{=} \mathbf{0} & \mathbf{x} \in \Gamma, \\ \mathcal{L}_2 &= \mathbf{L}_G \hat{\mathbf{u}}_\Gamma - \mathbf{J}_G \hat{\mathbf{u}}_C \stackrel{!}{=} \mathbf{0} & \mathbf{x} \in \Gamma. \end{aligned} \quad (2.72)$$

Here, $\mathbf{f} = \int_{\mathcal{B}} (\mathbf{B}_u^G)^T \boldsymbol{\sigma}(\mathbf{u}_C) \, d\mathbf{x}$ is an internal nodal force vector and $\bar{\mathbf{F}} = \int_{\Gamma_N} (\mathbf{N}_u^G)^T \bar{\boldsymbol{\tau}} \, d\mathbf{s}$ stands for the external force vector. It is trivial that the Lagrange multiplier acts as an external force on the interface. A Newton-type solution for the residual based system of equations for $(\mathbf{u}_C, \lambda_C)$ is provided by the linearization

$$\begin{aligned} (\mathbf{f}^a - \bar{\mathbf{F}}) + \mathbf{K}_{aa} \Delta \hat{\mathbf{u}}_{C,a} + \mathbf{K}_{ab} \Delta \hat{\mathbf{u}}_{C,b} &= \mathbf{0}, \\ (\mathbf{f}^b - \mathbf{L}_G^T \hat{\lambda}_C) + \mathbf{K}_{ba} \Delta \hat{\mathbf{u}}_{C,a} + \mathbf{K}_{bb} \Delta \hat{\mathbf{u}}_{C,b} - \mathbf{L}_G^T \Delta \hat{\lambda}_C &= \mathbf{0}, \\ (\mathbf{L}_G \hat{\mathbf{u}}_\Gamma - \mathbf{L}_G \Delta \hat{\mathbf{u}}_b) + \mathbf{L}_G \Delta \hat{\mathbf{u}}_\Gamma - \mathbf{L}_G \Delta \hat{\mathbf{u}}_{C,b} &= \mathbf{0}. \end{aligned} \quad (2.73)$$

where $\mathbf{K} := \partial \mathbf{f} / \partial \hat{\mathbf{u}}_C$ is the standard tangent stiffness matrix. Here, we have the following iterative update

$$\hat{\mathbf{u}}_{C,a} \leftarrow \hat{\mathbf{u}}_{C,a} + \Delta \hat{\mathbf{u}}_{C,a}, \quad \hat{\mathbf{u}}_{C,b} \leftarrow \hat{\mathbf{u}}_{C,b} + \Delta \hat{\mathbf{u}}_{C,b}, \quad \text{and} \quad \hat{\lambda}_C \leftarrow \hat{\lambda}_C + \Delta \hat{\lambda}_C. \quad (2.74)$$

Let us assume that the equilibrium state is achieved such that $\mathcal{L}_1^a = \mathbf{0}$, $\mathcal{L}_1^b = \mathbf{0}$ and $\mathcal{L}_2 = \mathbf{0}$. Thus, Eq. 2.73 takes the form

$$\mathcal{S}_C \Delta \hat{\mathbf{u}}_{C,b} = \mathcal{S}_C \Delta \hat{\mathbf{u}}_\Gamma =: \mathbf{L}_G^T \Delta \hat{\lambda}_C \quad \text{with} \quad \mathcal{S}_C := \mathcal{S}(\mathbf{K}_C) = \mathbf{K}_{bb} - \mathbf{K}_{ba} \mathbf{K}_{aa}^{-1} \mathbf{K}_{ab}, \quad (2.75)$$

where \mathcal{S} refers to the *Steklov-Poincaré mapping* [177]. By means of Eq. 2.75, displacement $\hat{\mathbf{u}}_C$ is extracted from the interface Γ and through the Poincaré-Steklov mapping \mathcal{S} returns the outward normal stress derivative with respect to the trace of the displacement. That is called Dirichlet-to-Neumann mapping [105, 147].

In a similar way, we have the following identity

$$\mathcal{S}_L \Delta \hat{\mathbf{u}}_{L,b} = \mathbf{T}_L^T \Delta \hat{\lambda}_L \quad \text{and} \quad \mathcal{S}_F \Delta \hat{\mathbf{u}}_{F,b} = \mathbf{L}_G^T \Delta \hat{\lambda}_F. \quad (2.76)$$

Here, $\mathbf{T}_L := \mathbf{J}_L|_{\Gamma_L}$ is the restriction of \mathbf{J}_L from \mathcal{B}_L to Γ_L . Furthermore, we define $\mathcal{S}_L := \mathcal{S}(\mathbf{K}_L)$ and $\mathcal{S}_F := \mathcal{S}(\mathbf{K}_F)$ in Eq. 2.76.

Proposition *Let the global solutions be at the converged state and let the following identity holds true:*

$$\mathbf{u}_\Gamma^{k, \frac{1}{2}} = \mathbf{u}_\Gamma^k \in \Gamma, \quad (2.77)$$

then the Global-Local formulation is converged. In addition, (2.77) holds true if and only if

$$\Delta \lambda_L = \lambda_L^k - \lambda_L^{k-1} = 0. \quad (2.78)$$

Proof. The proof constitutes of two parts. Note, the Global-Local procedure is in the convergence state if, all the coupling terms (C₁), (C₂) and (C₃) holds true at iteration k .

(a) Let condition $\mathbf{u}_\Gamma^{k, \frac{1}{2}} = \mathbf{u}_\Gamma^k$ hold, then it is evident (C₂) and (C₃) are satisfied in iteration k . Accordingly, replacing Eq. 2.68 in ($\tilde{\text{C}}_3$) yields

$$\int_\Gamma (\lambda_C^k + \lambda_L^k) \cdot \delta \mathbf{u}_\Gamma \, ds + A_G \int_\Gamma (\mathbf{u}_\Gamma^k - \mathbf{u}_L^k) \cdot \delta \lambda_L \, ds = 0, \quad (2.79)$$

where the second term due to ($\tilde{\text{C}}_2$) and the identity of $\mathbf{u}_\Gamma^{k, \frac{1}{2}} = \mathbf{u}_\Gamma^k$ becomes zero. Hence this results in the continuity of tractions at iteration k , i.e. (C₁) is satisfied.

(b) Let $\Delta \lambda_L = \lambda_L^k - \lambda_L^{k-1} = 0$ hold, then (2.66) can be restated as

$$\lambda_L^{k-1} = \lambda_L^k = A_L \int_\Gamma \mathbf{u}_G^k \cdot \delta \lambda_C \, ds - \int_\Gamma \lambda_C^k \cdot \mathbf{v}_\Gamma \, ds, \quad (2.80)$$

and therefore ($\tilde{\text{C}}_1$) is restated as,

$$\int_\Gamma (\lambda_C^k + \lambda_L^k) \cdot \delta \mathbf{u}_\Gamma \, ds + A_L \int_\Gamma (\mathbf{u}_\Gamma^{k, \frac{1}{2}} - \mathbf{u}_G^k) \cdot \delta \lambda_C \, ds = \int_\Gamma (\lambda_C^k + \lambda_L^k) \cdot \delta \mathbf{u}_\Gamma \, ds = 0, \quad (2.81)$$

where ($\tilde{\text{C}}_4$) is used. Subtracting Eq. 2.81 from ($\tilde{\text{C}}_3$) yields

$$A_G \int_\Gamma (\mathbf{u}_\Gamma^k - \mathbf{u}_L^k) \cdot \delta \lambda_L \, ds = A_G \int_\Gamma (\mathbf{u}_\Gamma^k - \mathbf{u}_\Gamma^{k, \frac{1}{2}}) \cdot \delta \lambda_L \, ds = 0, \quad (2.82)$$

which results in $\mathbf{u}_\Gamma^k = \mathbf{u}_\Gamma^{k, \frac{1}{2}}$. Herein, Eq. $\tilde{\text{C}}_2$ is used. Reciprocally, if $\mathbf{u}_\Gamma^{k, \frac{1}{2}} = \mathbf{u}_\Gamma^k \in \Gamma$ satisfied then $\Delta \lambda_L = 0$ holds.

Remark B.1. Let the Global-Local approach be in the converged state such that $\mathbf{u}_\Gamma^{k, \frac{1}{2}} = \mathbf{u}_\Gamma^k \in \Gamma$. We underline if $\mathcal{B} = \mathcal{B}_C \cup \Gamma \cup \mathcal{B}_L$ holds, then the Global-Local mesh compared with a single scale mesh is one to one, and the resulting Global-Local solutions are identical with the single scale solutions. This is because the two finite element meshes which correspond to the complementary and local domains are ‘exactly’ identical to the single scale mesh. We now determine specific Robin-type boundary conditions such that $\Delta\lambda_L = 0$ holds

which results in $\mathbf{u}_\Gamma^k = \mathbf{u}_\Gamma^{k, \frac{1}{2}}$ by means of Proposition 1 and that yields the Global-Local iterative process to be in the converged state.

Recall (2.66) and find A_L such that $\Delta\lambda_L = \lambda_L^k - \lambda_L^{k-1} = 0$. Hence we have,

$$\Delta\lambda_L = A_L \int_\Gamma \Delta\mathbf{u}_G \cdot \delta\lambda_C \, ds - \int_\Gamma \Delta\lambda_C \cdot \delta\mathbf{u}_\Gamma \, ds = \mathbf{0}, \quad (2.83)$$

resulting to

$$A_L \int_\Gamma \Delta\mathbf{u}_G \cdot \delta\lambda_C \, ds = \int_\Gamma \Delta\lambda_C \cdot \delta\mathbf{u}_\Gamma \, ds \rightarrow A_L \mathbf{J}_G \Delta\hat{\mathbf{u}}_G = \mathbf{L}_G^T \Delta\hat{\lambda}_C, \quad (2.84)$$

By means of (2.75) and considering (2.90)₁, this equality holds if $A_L := \mathcal{S}_C$ which is the Dirichlet-to-Neumann operator assigned to $\Gamma_G \in \mathcal{B}_C$.

In a similar manner, let us find A_G such that $\Delta\lambda_G = \lambda_G^k - \lambda_G^{k-1} = 0$. This yields

$$A_G \int_\Gamma \Delta\mathbf{u}_L \cdot \delta\lambda_L \, ds = \int_\Gamma \Delta\lambda_L \cdot \delta\mathbf{u}_\Gamma \, ds \rightarrow A_G \mathbf{J}_L \Delta\hat{\mathbf{u}}_L = \mathbf{L}_L^T \Delta\hat{\lambda}_L. \quad (2.85)$$

By means of (2.76)₁ and (2.90)₂, we have $A_G = \mathbf{L}_L^T \mathbf{T}_L^{-T} \mathcal{S}_L$. Based on Proposition 1 the converged state of the Global-Local iteration is independent of the choice of A_G hence one can simply replace \mathcal{S}_L by the identity tensor. Hence, there is no need to access \mathcal{S}_L at the global level.

2.3.7. Spatial discretization. The computational domain is subdivided into bilinear quadrilateral elements denoted as Q_1 . Both subproblems are discretized with a Galerkin finite element method using H^1 -conforming bilinear (2D) elements, i.e., the ansatz and test space uses Q_1^c -finite elements, e.g., for details, we refer readers to the [89]. Consequently, the discrete spaces have the property $V_h \subset V$ and $W_h \subset W$. Here, h refers to the finite element size. Accordingly, a finite element discretization is illustrated in Section 2.3.8 for the primal fields refers to the $(\mathbf{u}_G, \mathbf{u}_L, d_L, \mathbf{u}_\Gamma, \lambda_C, \lambda_L)$ and its constitutive state variables represented by $(\boldsymbol{\varepsilon}_G, \boldsymbol{\varepsilon}_L, d_L, \nabla d_L)$.

2.3.8. Finite Element Analysis. Let \mathcal{P} be a finite element partition of \mathcal{B} into quadrilaterals, and N_i denotes the nodal shape function associated with the node i . The scalar-valued quantity $\hat{\bullet}_i$ represents the nodal value. For the global-local formulation, we assume the existence of the partitions \mathcal{P}_G and \mathcal{P}_L . The solution discretization are given by

$$\mathbf{u}_G = \mathbf{N}_u^G \hat{\mathbf{u}}_G, \quad \mathbf{u}_L = \mathbf{N}_u^L \hat{\mathbf{u}}_L, \quad d_L = \mathbf{N}_d^L \hat{m} d_L, \quad (2.86)$$

and its derivative

$$\boldsymbol{\varepsilon}(\mathbf{u}_G) = \mathbf{B}_u^G \hat{\mathbf{u}}_G, \quad \boldsymbol{\varepsilon}(\mathbf{u}_L) = \mathbf{B}_u^L \hat{\mathbf{u}}_L, \quad \nabla d_L = \mathbf{B}_d^L \hat{d}_L. \quad (2.87)$$

Algorithm 2.1: Global-Local iterative scheme combined with Robin boundary conditions.

Input: loading data $(\bar{\mathbf{u}}_n, \bar{\boldsymbol{\tau}}_n)$ on $\partial_D \mathcal{B}$ and Γ_N , respectively;

solution $(\mathbf{u}_{G,n-1}, \mathbf{u}_{L,n-1}, d_{L,n-1}, \mathbf{u}_{\Gamma,n-1}, \lambda_{C,n-1}, \lambda_{L,n-1})$ and $\mathcal{H}_{L,n-1}$ from step $n-1$.

Global-Local iteration $k \geq 1$:

Local boundary value problem:

- given $A_L, \Lambda_L^{k-1}, \mathcal{H}_{L,n-1}$; solve

phase-field part:

$$\begin{aligned} (1 - \kappa) \int_{\mathcal{B}_L} d_L + \mathcal{H}(\varepsilon(\mathbf{u}_L)) \cdot \delta d_L dx + G_c \int_{\mathcal{B}_L} \frac{1}{l} (d_L - 1) \cdot \delta d_L dx \\ + G_c \int_{\mathcal{B}_L} l \nabla d_L \cdot \nabla (\delta d_L) dx + G_c \int_{\mathcal{B}_L} \alpha l \nabla d_L \cdot \mathbf{M} \cdot \nabla (\delta d_L) dx = 0, \end{aligned}$$

mechanical part:

$$\begin{cases} \int_{\Omega_L} \boldsymbol{\sigma}(\mathbf{u}_L, d_L) : \varepsilon(\delta \mathbf{u}_L) dx - \int_{\Gamma} \boldsymbol{\lambda}_L \cdot \delta \mathbf{u}_L ds = 0, \\ \int_{\Gamma} \boldsymbol{\lambda}_L \cdot \delta \mathbf{u}_{\Gamma} ds + A_L \int_{\Gamma} \mathbf{u}_{\Gamma} \cdot \delta \boldsymbol{\lambda}_C ds = \Lambda_L^{k-1}, \\ \int_{\Gamma} (\mathbf{u}_{\Gamma} - \mathbf{u}_L) \cdot \delta \boldsymbol{\lambda}_L ds = 0, \end{cases}$$

set $(\mathbf{u}_L, d_L, \mathbf{u}_{\Gamma}, \boldsymbol{\lambda}_L) =: (\mathbf{u}_L^k, d_L^k, \mathbf{u}_{\Gamma}^{k, \frac{1}{2}}, \boldsymbol{\lambda}_L^k)$,

- given $(\mathbf{u}_L^k, \boldsymbol{\lambda}_L^k; A_G)$, set

$$\Lambda_G^k = A_G \int_{\Gamma} \mathbf{u}_L^k \cdot \delta \boldsymbol{\lambda}_C ds - \int_{\Gamma} \boldsymbol{\lambda}_L^k \cdot \delta \mathbf{u}_{\Gamma} ds.$$

Global boundary value problem:

- given $A_G, \Lambda_G^k, \mathbf{u}_{\Gamma}^{k, \frac{1}{2}}$, solve

$$\begin{cases} \int_{\Omega_G} \boldsymbol{\sigma}(\mathbf{u}_G) : \varepsilon(\delta \mathbf{u}_G) dx - \int_{\Gamma} \boldsymbol{\lambda}_F \cdot \delta \mathbf{u}_G ds - \int_{\Gamma} \boldsymbol{\lambda}_C \cdot \delta \mathbf{u}_G ds \\ \quad - \int_{\Gamma_N} \bar{\boldsymbol{\tau}} \cdot \delta \mathbf{u}_G ds = 0, \\ \int_{\Gamma} \boldsymbol{\lambda}_C \cdot \delta \mathbf{u}_{\Gamma} ds + A_G \int_{\Gamma} \mathbf{u}_{\Gamma} \cdot \delta \boldsymbol{\lambda}_C ds = \Lambda_G^k, \\ \int_{\Gamma} (\mathbf{u}_{\Gamma}^{k, \frac{1}{2}} - \mathbf{u}_G) \cdot \delta \boldsymbol{\lambda}_C ds = 0, \end{cases}$$

set $(\mathbf{u}_G, \mathbf{u}_{\Gamma}, \boldsymbol{\lambda}_C) =: (\mathbf{u}_G^k, \mathbf{u}_{\Gamma}^k, \boldsymbol{\lambda}_C^k)$,

- given $(\mathbf{u}_G^k, \boldsymbol{\lambda}_C^k; A_L)$, set

$$\Lambda_L^k = A_L \int_{\Gamma} \mathbf{u}_G^k \cdot \delta \boldsymbol{\lambda}_C ds - \int_{\Gamma} \boldsymbol{\lambda}_C^k \cdot \delta \mathbf{u}_{\Gamma} ds.$$

- if fulfilled, set

$$(\mathbf{u}_G^k, \mathbf{u}_L^k, d_L^k, \mathbf{u}_{\Gamma}^k, \boldsymbol{\lambda}_C^k, \boldsymbol{\lambda}_L^k) =: (\mathbf{u}_{G,n}, \mathbf{u}_{L,n}, d_{L,n}, \mathbf{u}_{\Gamma,n}, \boldsymbol{\lambda}_{C,n}, \boldsymbol{\lambda}_{L,n}) \text{ and stop;}$$

else $k+1 \rightarrow k$.

Output: solution $(\mathbf{u}_{G,n}, \mathbf{u}_{L,n}, d_{L,n}, \mathbf{u}_{\Gamma,n}, \boldsymbol{\lambda}_{C,n}, \boldsymbol{\lambda}_{L,n})$ and $\mathcal{H}_{L,n}$.

To construct the discretization of the Lagrange multipliers λ_C , λ_L , \mathbf{u}_{Γ} and the supplementary quantity λ_F on Γ , we write

$$\boldsymbol{\lambda}_C = N_{\lambda}^G \hat{\boldsymbol{\lambda}}_C, \quad \boldsymbol{\lambda}_L = N_{\lambda}^L \hat{\boldsymbol{\lambda}}_L, \quad \mathbf{u}_{\Gamma} = N_u^{\Gamma} \hat{\mathbf{u}}_{\Gamma}, \quad \boldsymbol{\lambda}_F = N_{\lambda}^G \hat{\boldsymbol{\lambda}}_F. \quad (2.88)$$

We assume that $\mathbf{N}_\lambda^G = \mathbf{N}_u^G = \mathbf{N}_u^\Gamma$ and $\mathbf{N}_\lambda^L := \mathbf{N}_u^L$. This discretization for the Lagrange multipliers satisfies the *inf-sup* condition, see e.g. [321, 322].

Thus, coupling terms are discretized by

$$\begin{aligned} \mathbf{J}_G &= \int_{\mathcal{B}_G} (\mathbf{N}_\lambda^G)^T \mathbf{N}_u^G \, d\mathbf{x}, & \mathbf{J}_L &= \int_{\mathcal{B}_L} (\mathbf{N}_\lambda^L)^T \mathbf{N}_u^L \, d\mathbf{x}, \\ \mathbf{L}_G &= \int_{\Gamma_G} (\mathbf{N}_\lambda^G)^T \mathbf{N}_u^\Gamma \, ds, & \mathbf{L}_L &= \int_{\Gamma_L} (\mathbf{N}_\lambda^L)^T \mathbf{N}_u^\Gamma \, ds. \end{aligned} \quad (2.89)$$

Following our discretization, $\mathbf{J}_G : \mathcal{B}_G \rightarrow \Gamma_G$ and $\mathbf{J}_L : \mathcal{B}_L \rightarrow \Gamma_L$ become signed Boolean mappings [52] which are used to project the entire domain to interface contributions, such that

$$\hat{\mathbf{u}}_{G,b} := \mathbf{J}_G \hat{\mathbf{u}}_G \quad \text{and} \quad \hat{\mathbf{u}}_{L,b} := \mathbf{J}_L \hat{\mathbf{u}}_L. \quad (2.90)$$

Here, b are denoted as interface nodes. In order to handle a non-matching finite element discretization on the interface, more specifically to compute \mathbf{L}_L and \mathbf{L}_G , a dual mortar method [321] is implemented. This provides sufficient regularity of the underlying FE meshes.

2.4. Predictor-Corrector Adaptivity Applied to the Global-Local Formulation

We assume the Global-Local formulation is at the converged state, which is denoted as $(\mathbf{m}_{u_{G,n}}, \mathbf{u}_{L,n}, d_{L,n}, \mathbf{u}_{\Gamma,n}, \lambda_{C,n}, \lambda_{L,n})$. The Global-Local approach is augmented by a *dynamic allocation* of a local state using an adaptive scheme which has to be performed at time step t_n . By the adaptivity procedure, we mean: (a) to determine which global elements need to be refined and identified by $\mathcal{B}_G^{adapt} \subset \mathcal{B}_G$; (b) to create the new fictitious domain $\mathcal{B}_F^{new} := \mathcal{B}_F^{old} \cup \mathcal{B}_F^{adapt}$ with $\mathcal{B}_F^{adapt} := \mathcal{B}_G^{adapt}$ and as a result a new local domain is defined as $\mathcal{B}_L^{new} := \mathcal{B}_L^{old} \cup \mathcal{B}_L^{adapt}$, see Fig. 3.3; (c) to determine a new local interface denoted as Γ_L ; (d) to interpolate the old global solution in \mathcal{B}_L^{adapt} . All these steps refer to predictor steps. The corrector step is explained thereafter. We briefly notice that the principal idea of this adaptive scheme is inspired from [162] in which a predictor-corrector scheme for mesh refinement in the crack zone was proposed.

2.4.1. Predictor step. In this section, we start explaining the predictor step.

- **Determining global elements which have to be refined**

Recall that the interfaces at the global, fictitious and local domains are denoted by $\Gamma_G \subset \mathcal{B}_G$, $\Gamma_F \subset \mathcal{B}_F$ and $\Gamma_L \subset \mathcal{B}_L$. We denote $e_G \in \mathcal{B}_G$, $e_F \in \mathcal{B}_F$ and $e_L \in \mathcal{B}_L$ as the elements in the global, fictitious and local domain. Let $E_{G,i}^1, E_{G,i}^2, E_{G,i}^3$ and $E_{G,i}^4$ refer to the left, top, right and bottom global edges for the i^{th} element $e_{G,i}$, respectively (because, it is quadrilateral hence it has four edges). Accordingly, $E_{F,i}^q \in e_{F,i}$ and $E_{L,i}^q \in e_{L,i}$ with $q = (1, 2, 3, 4)$ refer to the fictitious and local edges, see Fig. 3.3.

We now develop a procedure, to determine the global elements $e_{G,i}$ which have at least one edge $E_{G,i}^q$ such that their fine resolution at the local level, i.e. $E_{L,i}^q$, reaches to the crack phase-field threshold value. Thus $e_{G,i}$ has to be refined. The predictor step for the adaptive scheme of the Global-Local formulation is explained in Algorithm 2.2.

Algorithm 2.2: *Predictor step for the adaptive procedure.*

Let $0 < \text{TOL}_d < 1$ be given. For the $d_L := d_{L,n} \in \mathcal{B}_L$, find corresponding $e_G \in \mathcal{B}_G$ which must be refined using the following steps:

1. Find $\mathbf{x}_L \in \Gamma_L$ such that $d_L(\mathbf{x}_L) < \text{TOL}_d$ on Γ_L :

Checking criterion: If "Yes" proceed to step 2. If "No" stop,

2. find $E_{L,i}^q \in \Gamma_L$ such that $\mathbf{x}_L \in E_{L,i}^q$,
3. find $E_{G,i}^q = \mathcal{P}^{-1}E_{L,i}^q$ (corresponding edge in \mathcal{B}_G),
4. find $e_G \in \mathcal{B}_G$ and $e_G \notin \mathcal{B}_F$ such that $E_{G,i}^q \in e_G$.

Here, $\mathcal{P} : \Gamma_G \rightarrow \Gamma_L$ is denoted as a projection/geometrical operator which maps the global to the local interface by $E_{L,i}^q := \mathcal{P}E_{G,i}^q$.

- **Creating new fictitious and local domains:** $(\mathcal{B}_F^{\text{new}}, \mathcal{B}_L^{\text{new}})$

We are now able to determine a new fictitious and local domains. Knowing e_G from the previous step, the new fictitious domain is $\mathcal{B}_F^{\text{new}} := \mathcal{B}_F^{\text{old}} \cup \mathcal{B}_F^{\text{adapt}}$ such that $\mathcal{B}_F^{\text{adapt}} := e_G$. As a result, a new local domain is $\mathcal{B}_L^{\text{new}} := \mathcal{B}_L^{\text{old}} \cup \mathcal{B}_L^{\text{adapt}}$ such that $\mathcal{B}_L^{\text{adapt}}$ is a fine discretization (including heterogeneity as well) of $\mathcal{B}_F^{\text{adapt}}$, see Fig. 3.3.

- **Determining the coupling interface:** $(\Gamma_G, \Gamma_F, \Gamma_L)$

So far, we have identified *new* fictitious and local domains. Next, we determine $\Gamma_F \subset \mathcal{B}_F$, due to its coarse discretization. Afterwards, we find the local interface $\Gamma_L \subset \mathcal{B}_L$ by projecting Γ_F to \mathcal{B}_L . Finally, it is trivial that $\Gamma_G := \Gamma_F$, because \mathcal{B}_F and \mathcal{B}_G are in the same discretization space.

The edge $E_{F,i}^q \in \Gamma_F$ is on the interface if

$$E_{F,i}^q \in \Gamma_F \text{ if } \nexists i, j : E_{F,i}^q = E_{F,j}^r, \quad \text{for } q, r = (1, 2, 3, 4), \quad (2.91)$$

which means if an edge $E_{F,i}^q$ is shared between two elements in \mathcal{B}_F , it is not on the interface (inner edge) and if it belongs only to one element, then it must also belong to interface (outer edge). As a result, we define the fictitious interface as $\Gamma_F = \bigcup_{i,q} E_{F,i}^q$, hence $\Gamma_L = \bigcup_{i,k} E_{L,i}^q$ with $E_{L,i}^q := \mathcal{P}E_{F,i}^q$.

- **Interpolating the old solution at t^n from the global to the local mesh**

Given a continuous function $\mathbf{u}_G^{\text{adapt}}$ that is \mathbf{u}_G in $\mathcal{B}_G^{\text{adapt}}$, we define the linear interpolation operator $\pi : \mathcal{B}_G^{\text{adapt}} \rightarrow \mathcal{B}_L^{\text{adapt}}$ to $\mathbf{u}_G^{\text{adapt}}$ by

$$\mathbf{u}_{L,n}^{\text{adapt}}(\mathbf{x}) := \pi \mathbf{u}_{G,n}^{\text{adapt}} = \mathbf{N}_u^G(\mathbf{x}) \hat{\mathbf{u}}_{G,n}^{\text{adapt}} \quad \text{for } \mathbf{x} \in \mathcal{B}_L^{\text{adapt}}. \quad (2.92)$$

where $\mathbf{N}_u^G(\mathbf{x})$ is defined in Appendix A. Hence, $\mathbf{u}_{L,n}^{\text{new}} := \mathbf{u}_{L,n} \cup \mathbf{u}_{L,n}^{\text{adapt}}$.

2.4.2. Corrector step. We introduce a corrector step in which the computation is rerun on the newly determined local mesh. To this end, we compute Global-Local solutions until the checking criterion in Algorithm 2.2 is not satisfied (**No**). That means we could not find additional local edges on the interface such that $d_L(\mathbf{x}_L) < \text{TOL}_d$ on Γ_L holds.

Let us write Algorithm 3.3 in the following abstract form

$$\mathbf{s}_n = \text{GL}(\mathbf{s}_{n-1}), \quad (2.93)$$

with $\mathbf{s} = (\mathbf{u}_G, \mathbf{u}_L, d_L, \mathbf{u}_\Gamma, \lambda_C, \lambda_L)$. We define an intermediate solution \mathbf{s}_{n-1}^j at fixed t^n such that the corrector step for adaptive scheme reads,

$$\mathbf{s}_{n-1}^j = \text{GL}(\mathbf{s}_{n-1}). \quad (2.94)$$

Perform Algorithm 2.2, if the *checking criterion* in step 1 is satisfied. But, if this is not the case, then the corrector step is fulfilled, thus set $\mathbf{s}_{n-1}^j =: \mathbf{s}_n$ and stop; else $j + 1 \rightarrow j$.

2.4.3. The final predictor-corrector scheme. The aforementioned predictor-corrector adaptivity procedure is summarized in Algorithm 2.3. Fig. 3.3 depicts one

Algorithm 2.3: *Predictor-corrector steps for the adaptive procedure.*

Let $0 < \text{TOL}_d < 1$ be given. For the $d_L := d_{L,n} \in \mathcal{B}_L$, find corresponding $e_G \in \mathcal{B}_G$ which have to be refined using the following steps:

1. Compute the intermediate solution by $\mathbf{s}_{n-1}^j = \text{GL}(\mathbf{s}_{n-1})$,
2. perform Algorithm 2.2 if *Checking criterion* is satisfied (**Yes**),
3. if *checking criterion* in Algorithm 2.2 is not satisfied, then the corrector step is fulfilled, thus set $\mathbf{s}_{n-1}^j =: \mathbf{s}_n$ and stop; else $j + 1 \rightarrow j$.

iteration of the predictor-corrector steps for the adaptive procedure which is illustrated in Algorithm 2.3.

We notice that for the brutal fracture behavior, where a complete failure happens in one load increment, Algorithm 2.3 has an important effect. This is mainly because the corrector step is performed until there is no nodal point on the interface such that $d_L(\mathbf{x}_L) < \text{TOL}_d$ holds. If this is fulfilled, the adaptivity procedure stops and goes to the next load increment. Thus brutal fracture can be observed in the next time step. This is illustrated in the numerical example of the Section 2.5.

The performance of Algorithm 2.2 and Algorithm 2.3 is depicted in Fig. 2.8 and Fig. 2.9. This example refers to the isotropic single-edge notch under tension. The numerical setup is given in [224]. By applying predictor-corrector steps, we will have a more regularized fracture surface. This is observed for instance in Fig. 2.9 step 58, step 60 and step 62 (right figures). But that is not the case, if we only apply predictor step. For instance in Fig. 2.8, at step 58, after the predictor step (in the absence of the corrector stage). Here we do not have a regularized fracture surface. It will be regularized in the next load increment which is shown in step 59. That is also observed in steps 60 and 63 in Fig. 2.8, as well. To compare these effects on the global level, we refer to the load-displacement curve in Fig. 2.12a. It was observed that the corrector procedure applied to the predictor step improved the Global-Local results.

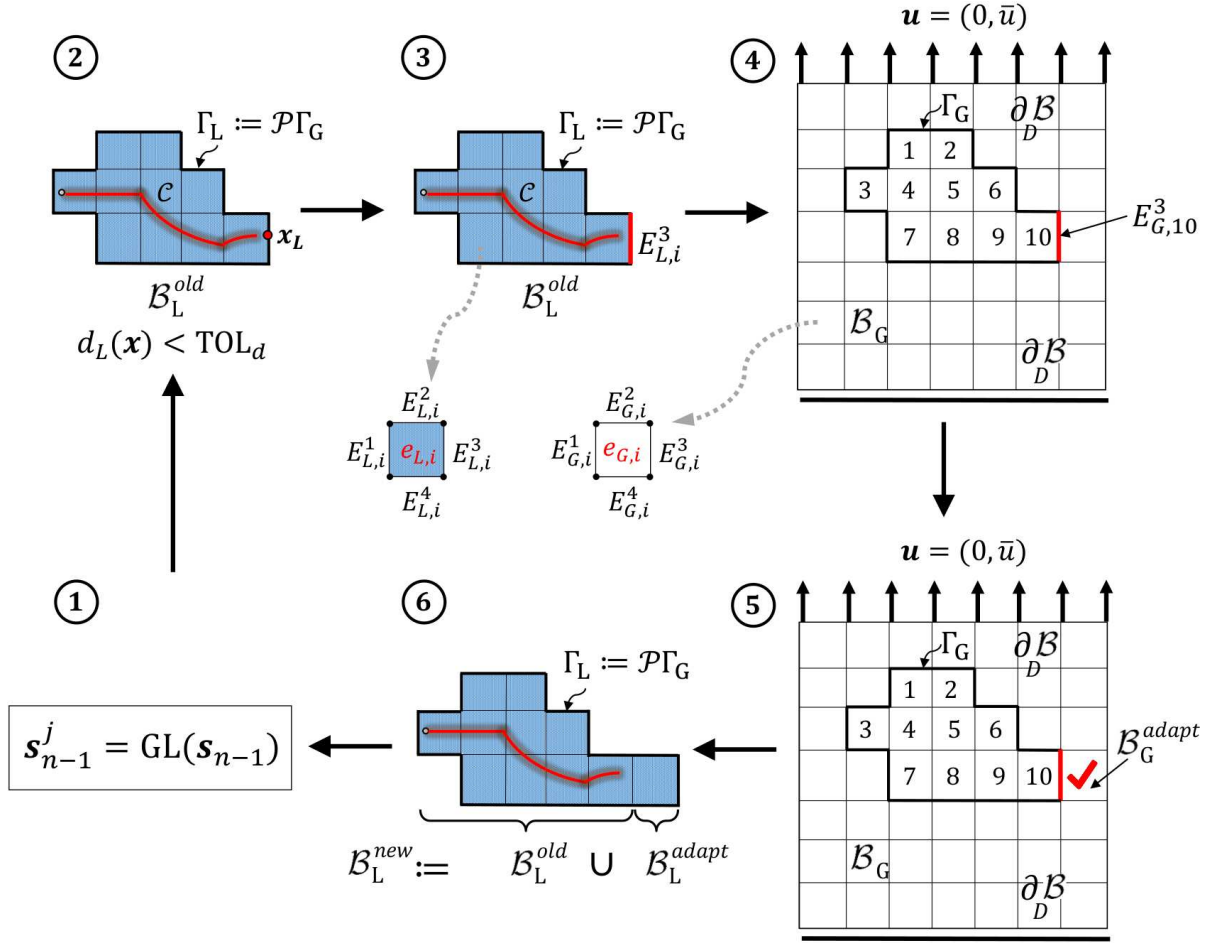


Figure 2.7: Explanation of the predictor-corrector adaptive scheme.

2.4.4. Homogenized phase-field solution on the global level. We determine the coarse representation of the crack phase-field. Here we denote $(\mathbf{u}_{G,n}, \mathbf{u}_{L,n}, d_{L,n}, \mathbf{u}_{\Gamma,n}, \lambda_{C,n}, \lambda_{L,n})$ to be the converged solution of the Global-Local approach. We emphasize that the computation of the global phase-field d_G is a post-processing step. The *homogenized global crack phase-field* solution can be determined based on the following ways.

(a) **Global crack phase-field solution.** We solve the crack phase-field given in (2.29) after having obtained the converged global solution by

$$d_G = \operatorname{argmin}_{d_G \in W} [-g'(d_{G+})\mathcal{H}(\mathbf{u}_{G,n}; \mathbf{M}_G) - l_G \delta_d \cdot \gamma_l], \quad (2.95)$$

with,

$$l_G := l_L \frac{h_G}{h_L} \quad \text{and} \quad \mathbf{M}_G := \mathbf{M}_L. \quad (2.96)$$

where \mathcal{H} is described by (2.35) and formulated on the global level. The last condition in (2.96)₂ holds because we assumed the structural tensor at the global level inclined with identical angle as the local level. This holds in the case of the transverse isotropic setting.

(b) **Homogeneous crack phase-field solution.** Assume that at the global level the transition zone of the crack phase-field vanishes. That results in a free isotropic and

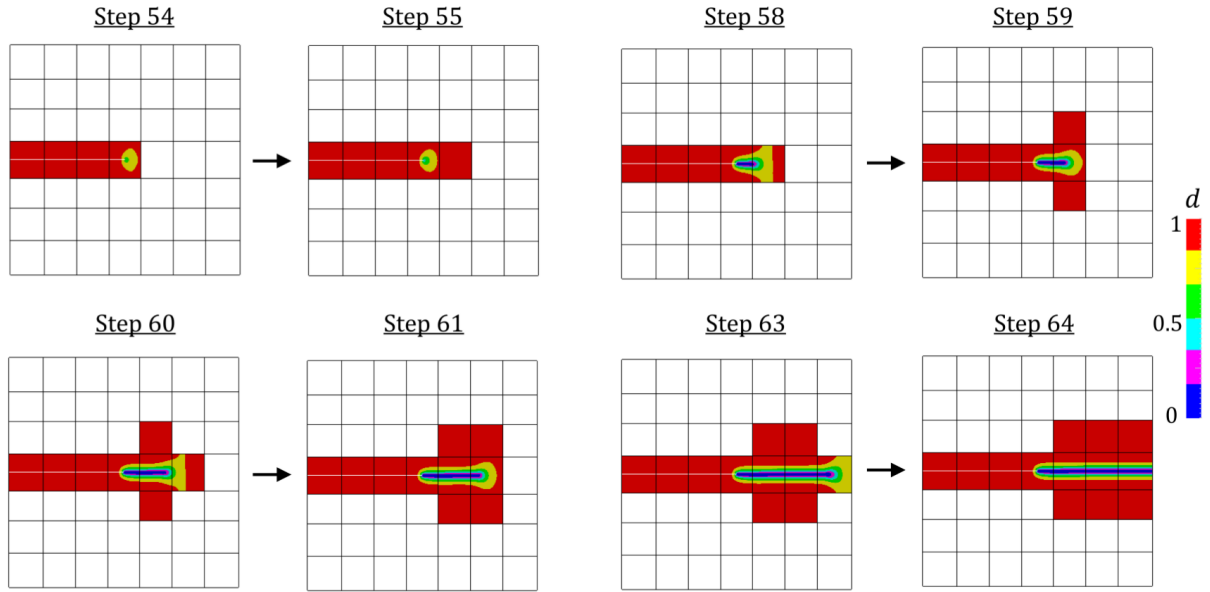


Figure 2.8: Global-Local approach augmented with the predictor adaptive scheme given in Algorithm 2.2; Fracture of isotropic single-edge-notched plate under tension per loading steps.

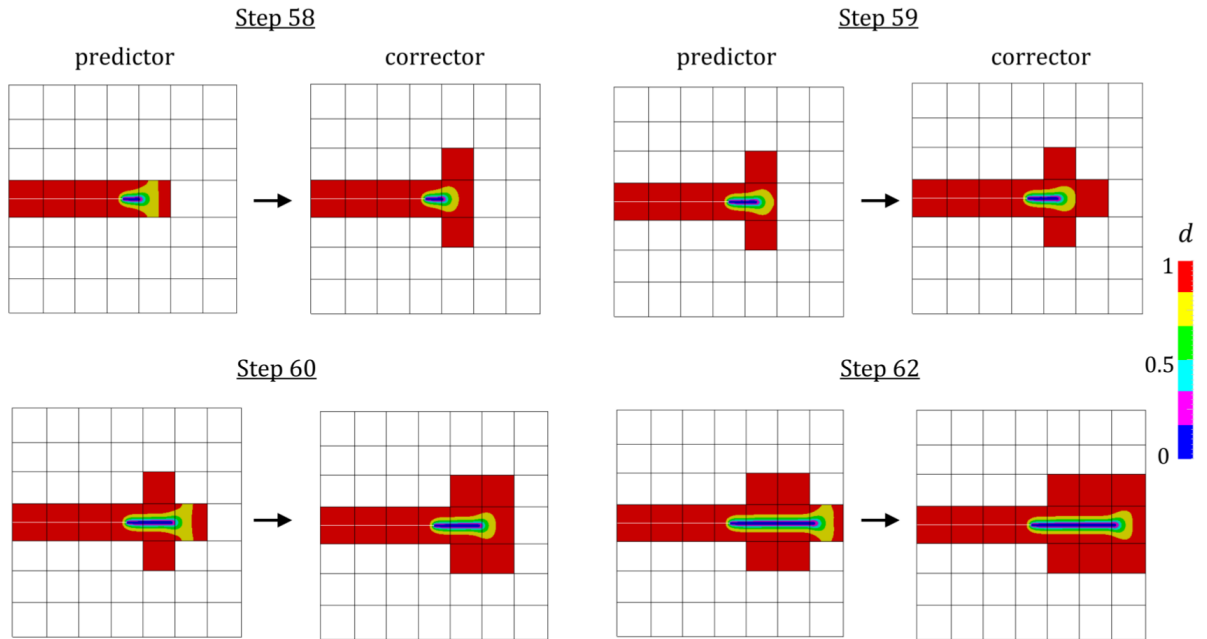


Figure 2.9: Global-Local approach augmented with the predictor-corrector adaptive scheme indicated in Algorithm 2.3; Fracture of isotropic single-edge-notched plate under tension per loading steps.

anisotropic Laplacian operator $\Delta(\bullet) = 0$ in (2.29). Hence, the second and third terms in (2.37) become zero. Following that Eq. 2.29 at the quasi-static stationary state is restated by

$$d_G = \frac{1}{1 + 2(1 - \kappa)\mathcal{H}(\mathbf{u}_{G,n}; \mathbf{M}_G)} \in [0, 1], \quad (2.97)$$

such that if $\mathcal{H} \rightarrow \infty$ then $d_G = 0$ and for $\mathcal{H} \rightarrow 0$ then $d_G = 1$ holds. The homogeneous crack phase-field solution d_G in (2.97) is independent of the l_G but the global crack phase-field solution in (2.95) depends on l_G . At the global level we do not have any given imperfection (e.g. notch shaped). That is located *only* at the local level. However, (2.95) or (2.97) still provides the desired crack direction because of $\mathcal{H}(\mathbf{u}_{G,n}; \mathbf{M}_G)$. This is due to the fact that $\mathbf{u}_{G,n}$ is determined based on the given $\mathbf{u}_\Gamma^{k, \frac{1}{2}}$ which is upscaled from local level, see (\tilde{C}_4) . As a result, the crack driving force at the global level is the *true projection* of the constitutive non-linearity at the local level. That is variationally consistent and resulting from the upscaling procedure (i.e. information which is transformed from the local level to the global scale).

2.5. Numerical Examples

The section presents the performance of the proposed adaptive Global-Local approach applied to the phase-field modeling of anisotropic brittle fracture. We consider four numerical model problems. The first example deals with an isotropic single-edge-notched shear test in which we set the directional tensor to be zero. The next three examples deal with transverse isotropic setting with different directional tensors.

2.5.1. Goals of the computations. For comparison purposes, we compute quantitative and qualitative single scale and Global-Local resolutions. In detail, we investigate:

- Crack patterns on the local scale at the complete fracture state in order to evaluate the down-scaling procedure (i.e. transition of external loading increments from the global scale to the local level);
- Load-displacement curves to evaluate the up-scaling procedure during the Global-Local coupling approach (i.e. transition of local non-linearity and heterogeneity responses to the global level);
- Investigations of the thermodynamically consistency between the single scale strain-energy and its Global-Local energy functional;
- Efficiency of the overall response resulting from the predictor-corrector adaptive scheme;
- Effect of the given threshold phase-field value in the adaptive process for the derivation of the fracture zone;
- Evaluating the homogenized phase-field solution at the global level, when the Global-Local scheme is in the converged state.

The outlined constitutive formulation is considered to be a canonically consistent and robust scheme for capturing the non-linearities on the lower level and its projection on to the global level.

2.5.2. Geometry, data and solution procedures. As a setup for the numerical investigations, we use:

- **Geometries and parameters:** In the first two examples, a boundary value problem applied to the square plate is shown in Fig. 2.10. We set $A = 0.5 \text{ mm}$ hence $\mathcal{B} = (0, 1)^2 \text{ mm}^2$ that includes a predefined single notch from the left edge to the body center, as depicted in Fig. 2.10. The predefined crack is in the $y = A$ plane and is restricted in $0 \leq |\mathcal{C}| \leq l_0$ and we set $l_0 = A = 0.5$. As a loading setup, we set the initial values for displacement and phase-field as $\mathbf{u}_0 := 0 \in \mathcal{B}$ and $d_0 := 1 \in \mathcal{B}_C$ and \mathcal{B}_L . The finite element discretization is explained in Section 2.3. Details of the last two examples are accordingly given.
- **Material parameters:** In the first two examples, the constitutive parameters for the isotropic and transversely isotropic material are the same as in [225] and given as $\lambda = 121.15 \text{ kN/mm}^2$, $\mu = 80.77 \text{ kN/mm}^2$. Griffith's critical elastic energy release rate is set as $G_c = 2.7 \times 10^{-3} \text{ kN/mm}$. In the first example, the preferred fiber direction is set to zero $\mathbf{a} = 0$ which represents the standard isotropic setting. Whereas, the three other examples represent transversely isotropic behavior that is characterized by the symmetric second-order structural tensor $\mathbf{M} = \mathbf{a} \otimes \mathbf{a}$. For a given angle ϕ of the preferred fiber direction, the normal vector is defined as $\mathbf{a} := [\cos(\phi) \quad \sin(\phi)]^T$. For the second example, the preferred fiber direction is given by the structural director \mathbf{a} which is inclined by $\theta = +30^\circ$ and $\theta = -30^\circ$ with respect to the x -axis of a fixed Cartesian coordinate system. Additionally, the anisotropy penalty-like parameters for the deformation part and fracture contribution are set to $\alpha = \chi = 50$ and $\Xi = 0$. All material properties are fixed for the following numerical examples, unless indicated otherwise.
- **Model parameters:** The phase-field parameters are chosen as $\kappa = 10^{-10}$ and $l = 2h$. The threshold value for the Global-Local predictor-corrector mesh refinement scheme is $\text{TOL}_d = 0.85$. This threshold value TOL_d is a fixed value except for the compression cases in which we use a different TOL_d .

- **Solution of the nonlinear problems:**

An alternate minimization scheme is used for solving the local boundary value problem indicated in Algorithm 3.3. Thus, we alternately solve for d_L by fixing \mathbf{u}_L and then solving for $(\mathbf{u}_L, \mathbf{u}_\Gamma, \mathbf{m}\lambda_L)$ by fixing d_L until convergence is reached. An iterative Newton solver is used in which the linear equation systems are solved with a generalized minimal residual method. The stopping criterion of the single scale and local Newton methods is $\text{To1}_{\text{N-R}} = 10^{-10}$. Specifically, the relative residual norm is given by $\text{Residual} : \|\mathbf{m}F(\mathbf{m}x_{k+1})\| \leq \text{To1}_{\text{N-R}} \|\mathbf{m}F(\mathbf{m}x_k)\|$. Here, $\mathbf{m}F$ refers to the residual of the equilibrium equation of the nonlinear single scale and local boundary value problems.

- **Software:**

The implementation is based on MATLAB R2018b [216] and FORTRAN 90 [82]. The user elements including the constitutive modeling at each Gaussian quadrature points are written in FORTRAN 90. The general framework for the Global-Local approach is implemented in MATLAB as a parent/main program such that all subprograms in FORTRAN 90 are called as a MEX-FILE.

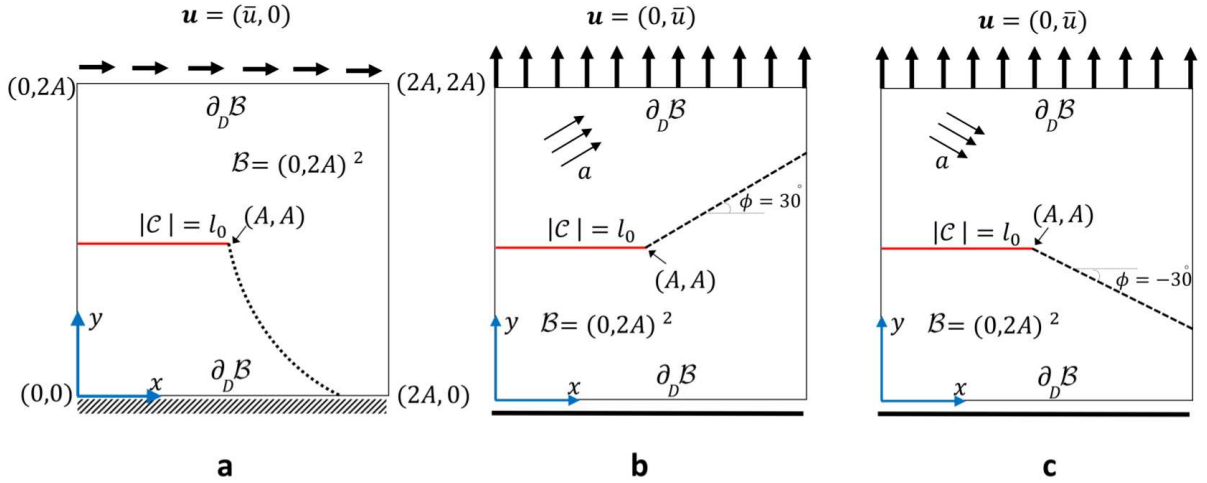


Figure 2.10: Geometry and loading setup for the single-edge-notched shear test in (a) and tensile test with the structural director \mathbf{a} inclined under an angle $\phi = +30$ in (b) and $\phi = -30$ in (c) with respect to the x -axis.

2.5.3. Example 1: Isotropic single-edge-notched shear test. In this example, attention is restricted to pure isotropic crack-propagation by letting $\mathbf{a} = 0$. In this setting, we consider a shear test such that fracture response exhibits a curved surface. The numerical computation is performed by applying a monotonic displacement $\bar{u} = 5 \times 10^{-5}$ in horizontal direction at the top boundary of the specimen.

An important aspect that has to be verified at the local level is the fracture state. Thus, we look at the crack phase field pattern at the local scale to investigate the transition of external loading increments (i.e. the down-scaling procedure) from the global domain to the local level. The Global-Local adaptive scheme to capture the curved surface is evaluated for different TOL_d . Hereby, TOL_d leads to different fracture zones and hence different local domains. Four different values of $\text{TOL}_d := (0.9, 0.85, 0.80, 0.70)$ are considered. Fig. 2.11 shows the evolution of the local domains for different TOL_d . The global mesh is only used to show a clear representation for the evolution of the local domain. Since global and local domains are performed independently, and therefore we deal with a two-scale finite element algorithm.

By comparing e.g. the first and fourth row in Fig. 2.11, it is trivial that a smaller value of the TOL_d yields a narrow fracture zone. Hence, if $\text{TOL}_{d_1} < \text{TOL}_{d_2}$ then $|\mathcal{B}_{L,1}| < |\mathcal{B}_{L,2}|$. The resultant narrow local domain due to the adaptivity approach in Fig. 2.11 demonstrates the great efficiency of the proposed method.

The above observation plays an important role by constraining the diffusivity zone of the crack phase-field in a narrow fracture region. Whereas in the standard single scale phase field modeling, the fracture zone is spread over more areas and hence a wider diffusive zone. Thus, by the Global-Local approach we limit the effect of diffusivity on the local level and not in the entire domain.

The influence of local effects (non-linear constitutive responses) on the global scale are described based on the load-displacement response, depicted in Fig. 2.12b. These curves are in a good agreement with the single scale solution. As it is expected the Global-Local approach with a higher value of the $\text{TOL}_d = 0.90$ is in very good agreement with the single

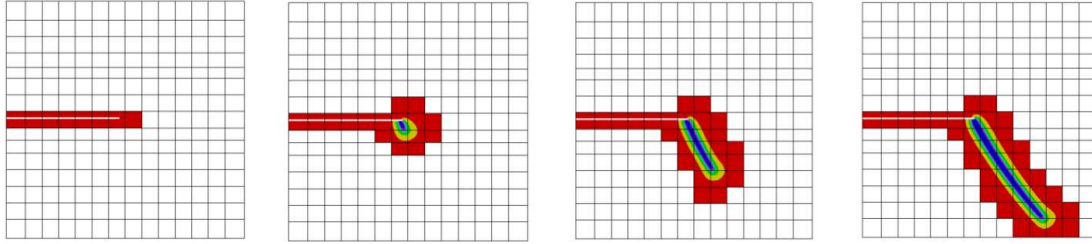
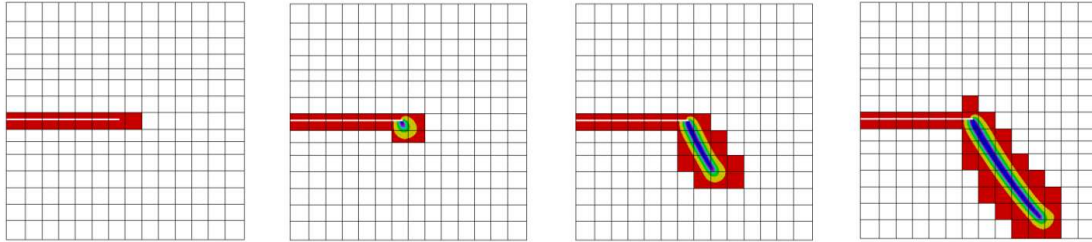
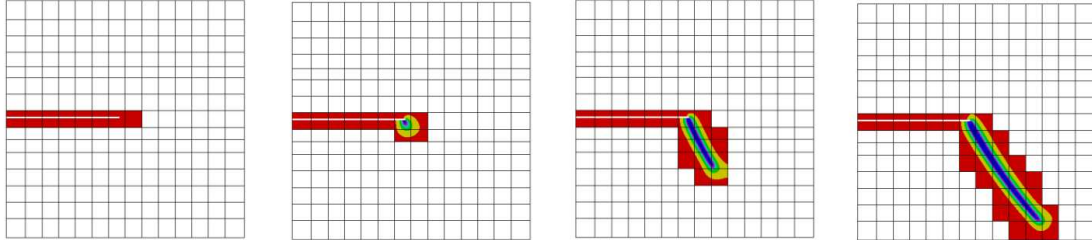
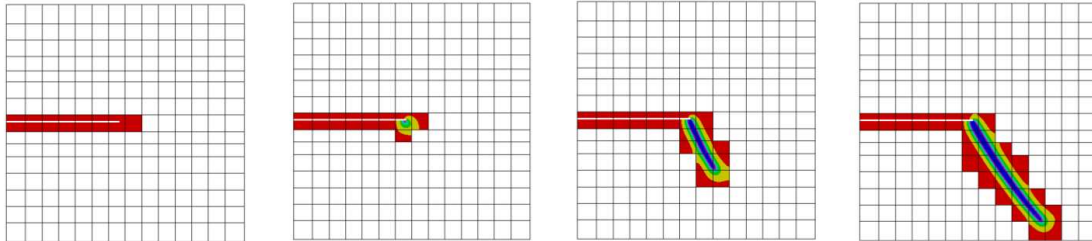
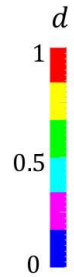
$TOL_d = 0.9$  **$TOL_d = 0.85$**  **$TOL_d = 0.80$**  **$TOL_d = 0.70$** **a****b****c****d**

Figure 2.11: Example 1. Evolution of the local domain for different threshold values of TOL_d and four deformation states up to final failure, (a) $\bar{u} = 0.0058 \text{ mm}$ (b) $\bar{u} = 0.0103 \text{ mm}$ (c) $\bar{u} = 0.0117 \text{ mm}$ (d) $\bar{u} = 0.0180 \text{ mm}$.

scale solution. That is mainly because within single scale phase-field modeling, we deal with a wider diffusivity zone and hence more elements with fracture state are involved.

The use of adaptivity leads to a narrow fracture zone and hence to a reduction of degrees of freedom. That is shown in Fig. 2.13a for different values of TOL_d . It turns out that a smaller values of TOL_d lead to a reduction of the active degrees of freedom and the computational time. At every jump which appears in Fig. 2.13a the predictor-corrector adaptive scheme is applied to the Global-Local scheme hence the number of degrees of freedom is increased.

More specifically, we show that the adaptive scheme applied to the Global-Local ap-

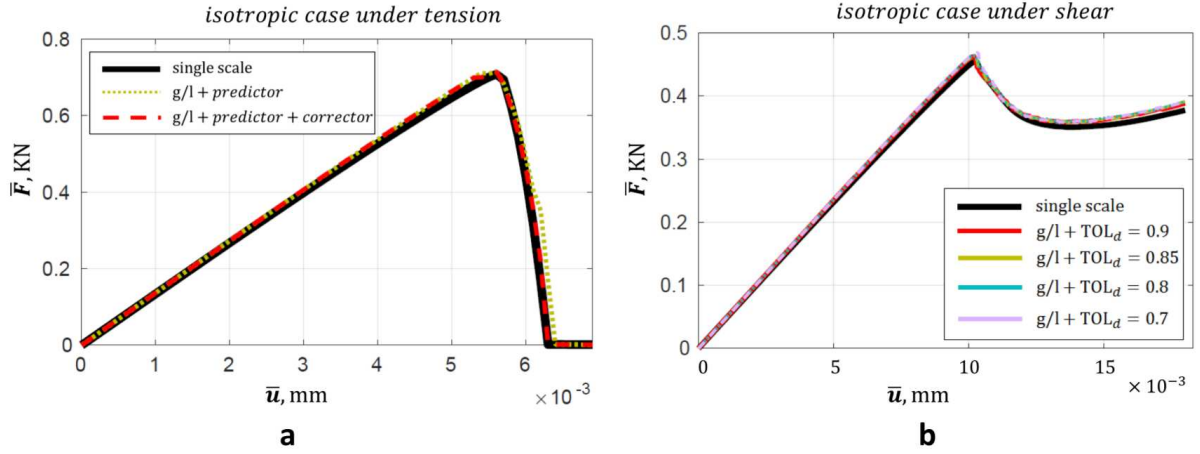


Figure 2.12: Load-displacement curves for the isotropic single-edge-notched test, (a) Example in Section 2.4, specimen under tension test and (b) Example 1, shear test based on Global-Local approach with different TOL_d versus single scale.

proach *considerably* reduces the computational cost in comparison with the single scale solution, as indicated in Fig. 2.13b. Note that, at load step $\bar{u} = 10 \times 10^{-3}$ (the loading point where the fracture initiates) a higher computational time is observed, see Fig. 2.13. That is due to the alternate minimization approach used for solving the variational phase-field formulation which needs more iteration at cracking to reach the equilibrium state.

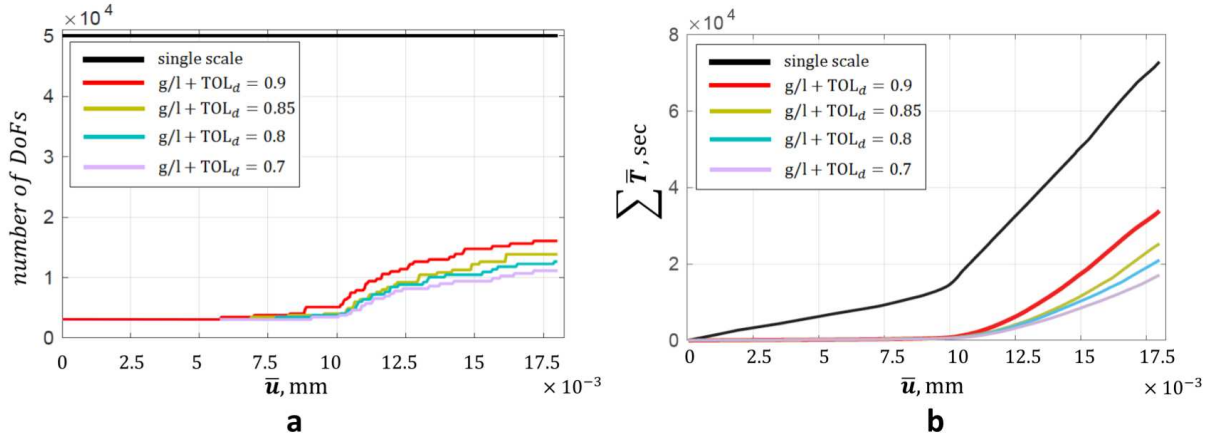


Figure 2.13: Example 1. Isotropic single-edge-notched shear test. (a) Number of degrees of freedom which have to be solved for and (b) Time-displacement curves in terms of the accumulated time.

We now aim to investigate the energy response when solving a problem as single scale problem and as Global-Local. Recall, the consistency of the energy functional (departing point of the Global-Local approximation)

$$\mathcal{E}(u, d; M) \equiv \tilde{\mathcal{E}}(u_G, u_L, d_L, u_\Gamma, \lambda_C, \lambda_L; M),$$

between the single scale and the Global-Local functional indicated in Formulation 2.2 and (2.58), respectively. We investigate this approximation by means of the evolution of the

total stored elastic strain energy plotted in Fig. 2.14a and the dissipated fracture energy shown in Fig. 2.14b during load increments. These Global-Local simulation results show very good agreement with the single scale scheme yet with its efficiency in time shown in Fig. 2.13b.

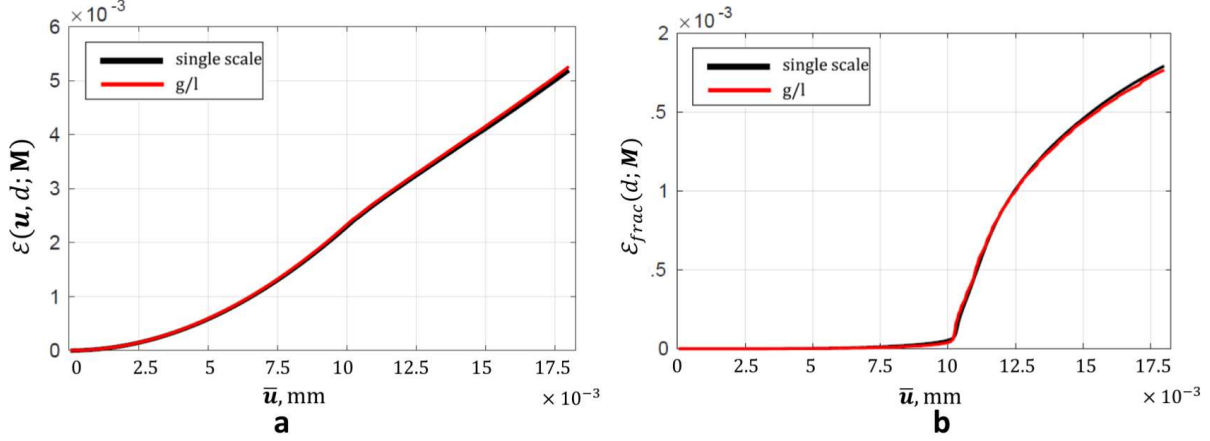


Figure 2.14: Example 1. Comparison of the energy response between the single scale domain and the Global-Local scheme for (a) the total free-energy functional and (b) the dissipated fracture energy.

At the converged Global-Local state, we obtain the following updated fields: $(\mathbf{u}_{G,n}, \mathbf{u}_{L,n}, d_{L,n}, \mathbf{u}_{\Gamma,n}, \lambda_{C,n}, \lambda_{L,n})$. Based on that, the homogenized global phase-field solution at the complete failure state is illustrated in Fig. 2.15 for different values of TOL_d . We emphasize that in the global level there is no pre-defined crack (i.e. globally there is no notch). However, it is interesting to note that the homogenized global phase-field solution is able to capture the crack direction which is indeed a consistent projection of the local response. Figure 2.15a provides the global phase-field solution by means of (2.95) at the converged Global-Local state. Accordingly, Fig. 2.15b provides the homogeneous phase-field solution based on (2.97). Note that, the homogenized global phase-field is slightly affected by TOL_d .

2.5.4. Example 2: Analysis of transversely isotropic single-edge-notched tension test. The second example deals with transversely isotropic material responses under tension. It is based on different fiber directions given by the structural director \mathbf{a} which is inclined under an angle ϕ with respect to the x -axis of a fixed Cartesian coordinate system. The numerical simulation is performed by applying a monotonic displacement $\bar{\mathbf{u}} = 5 \times 10^{-5}$ in vertical direction at the top of the specimen with a linearly increasing displacement. This loading setting is applied to the rest of numerical examples.

Fiber direction of $\phi = +30^\circ$. Here we investigate the transversely isotropic single-edge-notched tension test based on the fiber direction angle $\phi = +30^\circ$. We apply the Global-Local approach as follows:

- **Case a.** *Without* non-matching discrete interface and *without* adaptive scheme (a pre-defined local domain),

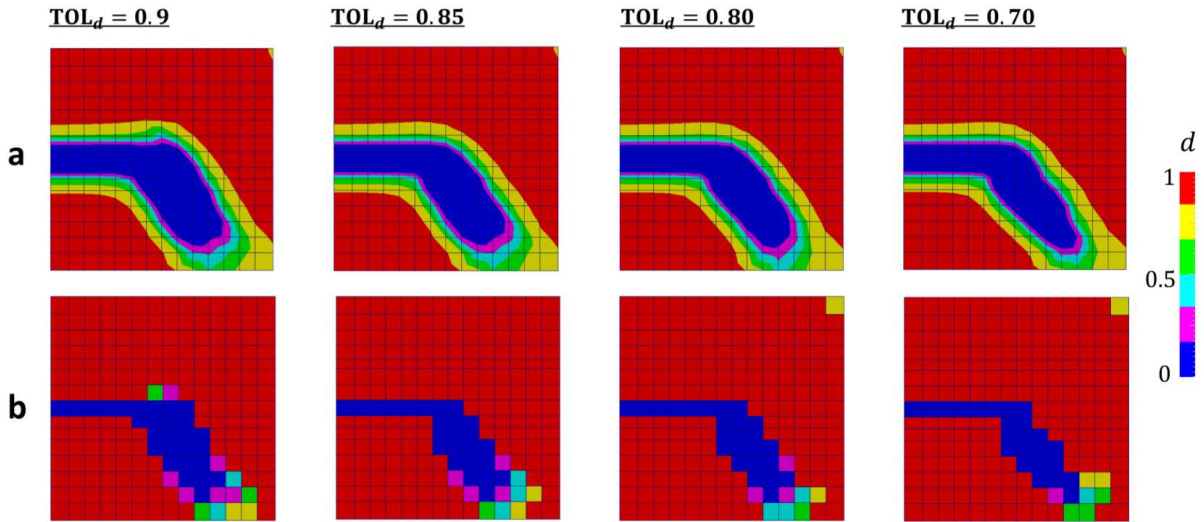


Figure 2.15: Example 1. Homogenized global crack phase-field solution for the isotropic single-edge-notched shear test (a) Global crack phase-field (b) Homogeneous crack phase-field solution at $\bar{u} = 0.0180 \text{ mm}$ for different TOL_d .

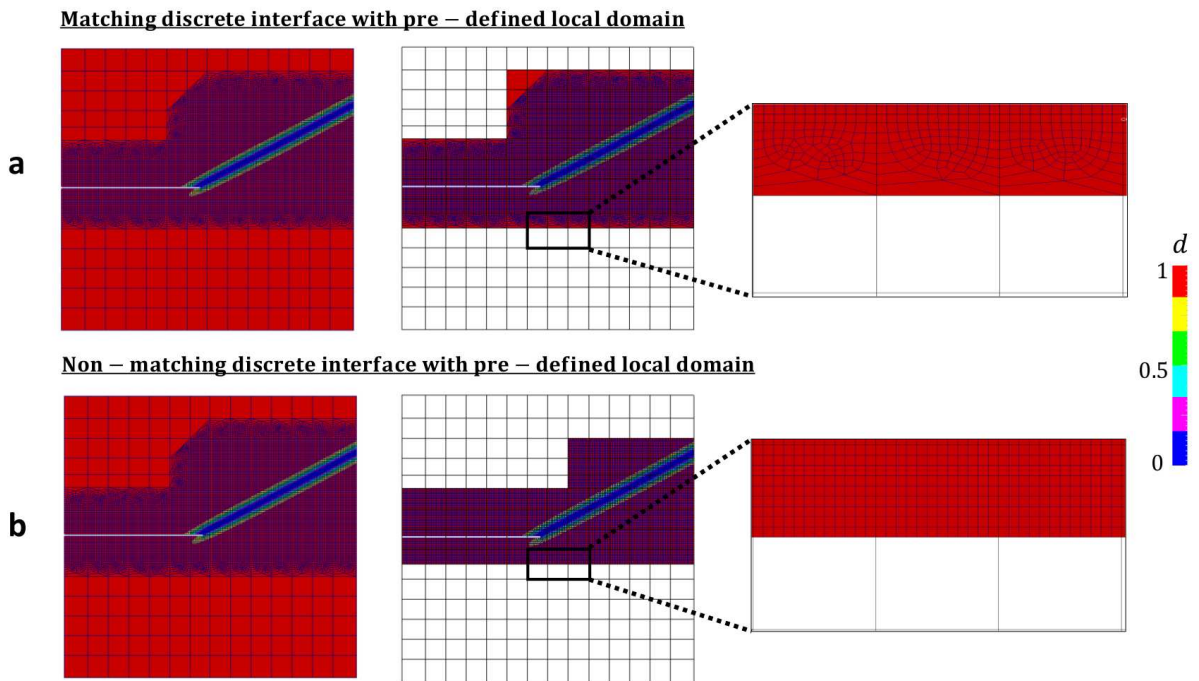


Figure 2.16: Example 2. Transversely isotropic single-edge-notched tension with $\phi = +30^\circ$. Complete fracture state at $\bar{u} = 0.010 \text{ mm}$ for (a) matching discrete interface (Case a) $\Gamma_G = \Gamma_L$ and (b) non-matching discrete interface $\Gamma_G \neq \Gamma_L$ with predefined local domain (Case b).

In this case, see Fig. 2.16a, we aim to evaluate the Proposition 1 such that $\mathcal{B} = \mathcal{B}_C \cup \Gamma \cup \mathcal{B}_L$. Here, the local domain is predefined and no adaptivity is applied. Also, the discrete interface between the global and local domains are one to one such that $\Gamma_G = \Gamma_L$ (see Fig. 2.16a last column). It is clear that the two finite element meshes used for Global-

Local approach represent "precisely" the same as a single scale domain. Hence, we expect an identical Global-Local response compared with the single scale solutions (see Remark 1 in Section 2.3.6). The complete fracture state is shown in Fig. 2.16a. Accordingly, a comparison of the load-displacement curves of the proposed formulation is demonstrated in Fig. 2.17a and shows a very good agreement compared with the single scale problem.

Remark 7: Note that this case is similar to the work of GERASIMOV ET AL. [143] if Robin-type boundary conditions are not taken into account (i.e. Global-Local approach based on Dirichlet-Neumann type boundary conditions), as sketched in Fig. 2.6a. Therein, the corresponding cumulative computational time is higher compared with the reference single scale solution (see Figure 10 in [143]), due to the slow convergence of the Global-Local procedure. That motivated the introduction of the Robin-type boundary conditions, resulting in a reduction of the computational cost, see Fig. 2.13b.

- **Case b.** With non-matching discrete interface and *without* adaptive scheme (a pre-defined local domain).

In the second case, we assume $\mathcal{B} \neq \mathcal{B}_C \cup \Gamma \cup \mathcal{B}_L$ and that the local domain is pre-defined hence no adaptivity is applied. Furthermore, the discrete interface between global and local domains are non-matching such that $\Gamma_G \neq \Gamma_L$ (see Fig. 2.16b last column). This removes one restriction applied in **Case a**, that is the matching discrete interface criteria.

The complete fracture state is shown in Fig. 2.16b. Compared with the first case, by the non-matching discrete interface, we are able to have an arbitrary mesh at the local domain (including interface) without any given interface conditions (and to avoid having distorted mesh between fine and coarse discretizations). The interface conditions refer to the identical discretization space for Γ_L and Γ_G , see Remark 3.1. The importance can be observed when the fracture reaches the interface, see e.g. Fig. 2.11.

The resulting load-displacement curve in Fig. 2.17b has a very good agreement when compared with the single scale problem.

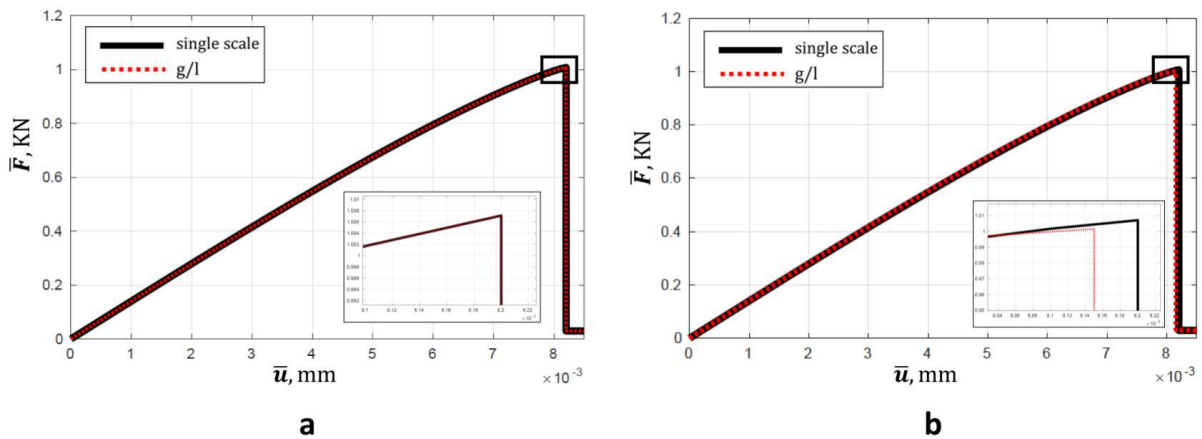


Figure 2.17: Example 2. Transversely isotropic single-edge-notched tension with $\phi = +30^\circ$. Comparison of the load-displacement curve between single scale problem and Global-Local formulation. (a) Matching discrete interface with $\mathcal{B} = \mathcal{B}_C \cup \Gamma \cup \mathcal{B}_L$ (**Case a**) and (b) non-matching discrete interface with $\mathcal{B} \neq \mathcal{B}_C \cup \Gamma \cup \mathcal{B}_L$ (**Case b**).

- **Case c.** *With* non-matching discrete interface and *with* adaptive scheme.

In the third case, we consider a non-matching discrete interface along with an adaptive scheme. This case removes all restrictions applied in **Case a** (matching interface and predefined local domain).

Fig. 2.18 illustrates the evolution of the crack phase-field along with the local domain and the corresponding Global-Local interface. The local domain and its coupling interface must be computed at each stage. The second row of Fig. 2.18 presents the local mesh evolution such that the non-matching discrete interface between global and local mesh is examined. To evaluate the solution related to the local to global transition, the load-

Local crack phase – field

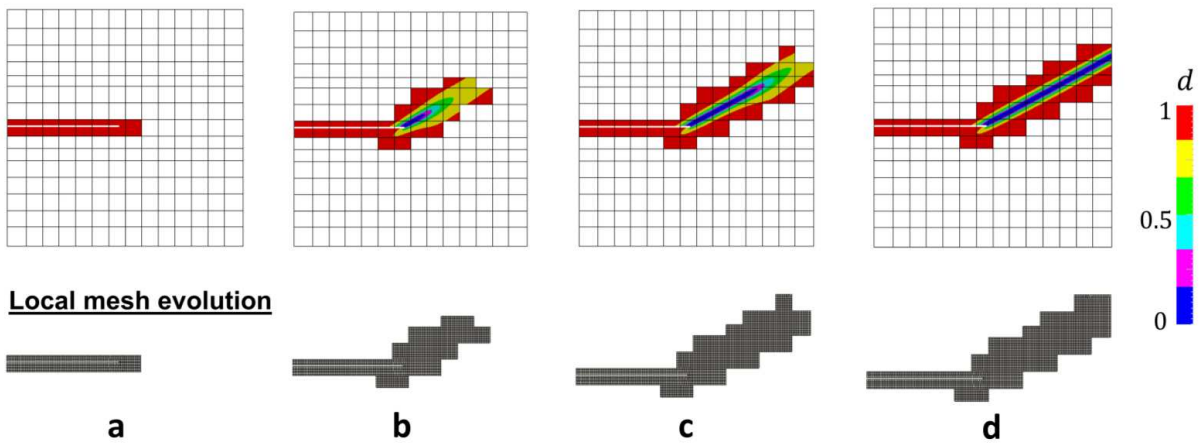


Figure 2.18: Example 2. Transversely isotropic single-edge-notched tension with $\phi = +30^\circ$. First row indicates the local crack phase-field resolution and second row represents the evolution of the local domain per time for different deformation states as follows: (a) $\bar{u} = 0.0030 \text{ mm}$ (b) $\bar{u} = 0.0088 \text{ mm}$ (c) $\bar{u} = 0.0092 \text{ mm}$ and (d) $\bar{u} = 0.010 \text{ mm}$.

displacement curve is shown in Fig. 2.19a. Since the single scale problem produces a very diffusive transition zone for the phase-field, more elements are involved (this is not the case in the sharp crack limit). This results in a small difference in the load-displacement curves between the Global-Local formulations and the reference single scale. Fig. 2.19b illustrates a reduction of the number of degrees of freedom.

The Global-Local approach, besides its feasibility for having two ad-hoc finite element models for the global and local domain, enables computations with legacy codes. Additionally, the reduction of unknowns leads to a reduction of the computational time. To illustrate the time efficiency, the simulation time ratio between single scale and the Global-Local approach are shown in Fig. 2.20a. It can be observed that in average, the Global-Local formulations perform 12 times faster. Furthermore, Fig. 2.20b demonstrates the corresponding accumulative computational time, which underlines the efficiency of the predictor-corrector adaptive scheme.

Fig. 2.21a presents the total elastic strain energy per load increments. The resulting Global-Local curve is in a very good agreement with the single scale approach.

Accordingly, the homogenized global phase-field solutions for different fracture states are depicted in Fig. 2.22. First and second row of Fig. 2.22 are based on approach (a)

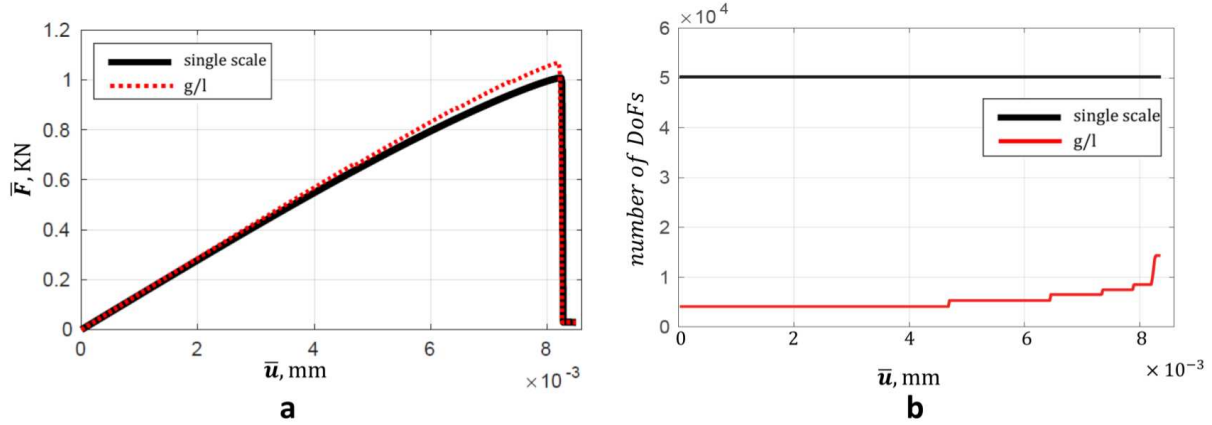


Figure 2.19: Example 2. Transversely isotropic single-edge-notched tension with $\phi = +30^\circ$. (a) Comparison of the load-displacement curve; (b) Number of degrees of freedom.

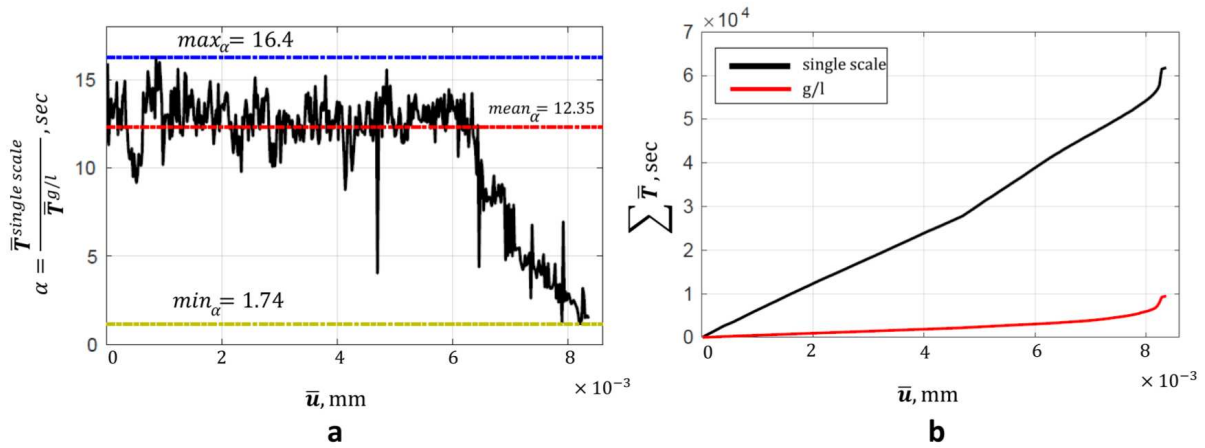


Figure 2.20: Example 2. Transversely isotropic single-edge-notched tension with $\phi = +30^\circ$. (a) Time ratio between the computed single scale and the Global-Local time per loading steps and (b) accumulated time-displacement curves.

and (b) outlined in section 2.4. For comparison purposes, the single scale resolution is also plotted in the third row of Fig. 2.22. It is observed that, the homogenized phase-field solution in the case of the anisotropic setting, is able to capture the crack direction. The global phase-field solution is affected by the global element size and also TOL_d (local scale).

Fiber direction of $\phi = -30^\circ$. This numerical example illustrates the transversely isotropic single-edge-notched tension test with $\phi = -30^\circ$. The crack phase-field resolution has a brutal fracture response in which a complete failure happens in one load increment. Thus the post-peak behavior is almost vertical, see Fig. 2.24. The aim of this numerical example is to show the capability of the Global-Local approach to capture such a brutal fracture behavior. This is mainly possible due to the introduction of the corrector step in the adaptive scheme described in Section 2.4.

Next, we investigate the effect of the TOL_d in the case of the brutal fracture behavior, by setting $\text{TOL}_d = (0.90, 0.80)$, as illustrated in Fig. 2.23. Similar as before, different TOL_d lead to different fracture zones and hence different local domains. The crack paths for

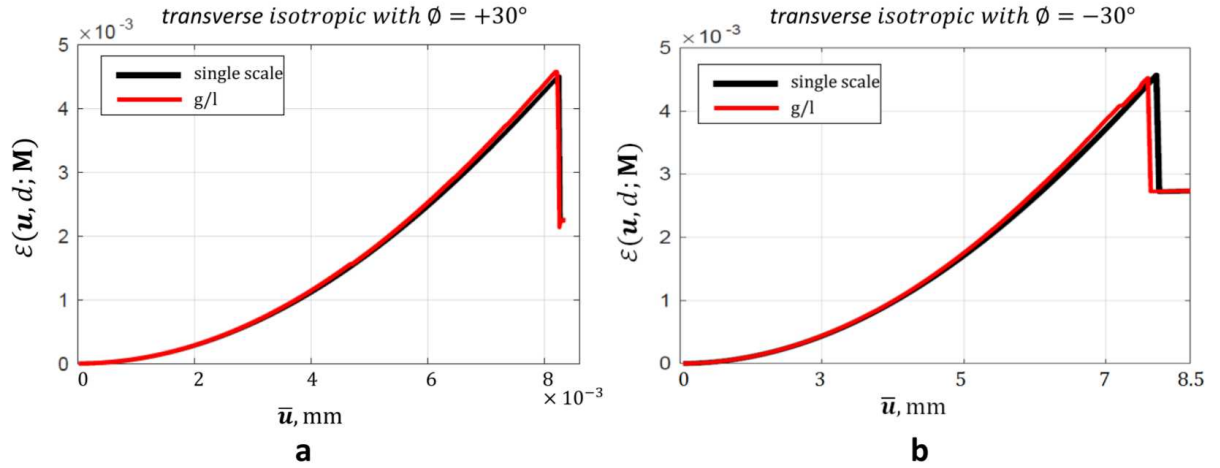


Figure 2.21: Example 2. Transversely isotropic single-edge-notched tension test. Comparison of the total energy functional between single scale domain and Global-Local scheme for fiber direction with $\phi = +30^\circ$ in (a) and fiber direction with $\phi = -30^\circ$ in (b).

both $\text{TOL}_d = 0.90$ and $\text{TOL}_d = 0.80$ are identical, yet with $\text{TOL}_d = 0.80$ a more narrow fracture zone is observed (hence a reduction of computational time).

A comparison of the load-displacement curves are shown in Fig. 2.24a. The effect of TOL_d on the load-displacement curve with zoom-in to the framed region of the left plot is shown in Fig. 2.24b. Despite of its brutal fracture behavior, the load-displacement curve with the higher value of $\text{TOL}_d = 0.90$ has a good agreement when compared with a single scale solution. Following the approximation between the single scale and the Global-Local modeling, Fig. 2.21b presents a very good agreement in the total elastic strain energy of both schemes during the load increments.

Figure 2.25 describes the efficiency of the proposed Global-Local approach. Here the accumulative computational time is plotted in Fig. 2.25a and the number of unknowns are plotted in Fig. 2.25b versus the displacement and compared with the single scale domain. At each jump in Fig. 2.25b, the predictor-corrector adaptive scheme is active and applied on the Global-Local scheme which increases the number of degrees of freedoms.

The homogenized global phase-field solution for this numerical setting is indicated in Fig. 2.26a at the complete fracture state. The single scale resolution is indicated in third row of Fig. 2.26b. It is evident that the homogenized phase-field solution is able to (i) capture the initial crack of the notch plate located at the local level and accordingly, (ii) the evolution of the fracture state which follows the preferred fiber direction.

2.5.5. Example 3: Investigation of transversely isotropic heterogeneous L-shaped panel test. The third model problem is concerned with anisotropic brittle fracture of a heterogeneous L-shaped panel test. The homogeneous isotropic counterpart setting for this benchmark problem has been reported by many authors, see e.g. [218, 305, 24, 316]. We demonstrate the performance of the Global-Local approach to predict crack propagation without any given initial crack region. In this case the initial local domain needs to be determined based on the critical stress state at the global level as outlined in Fig 2.27c. To increase the order of complexity, a heterogeneous structure is considered

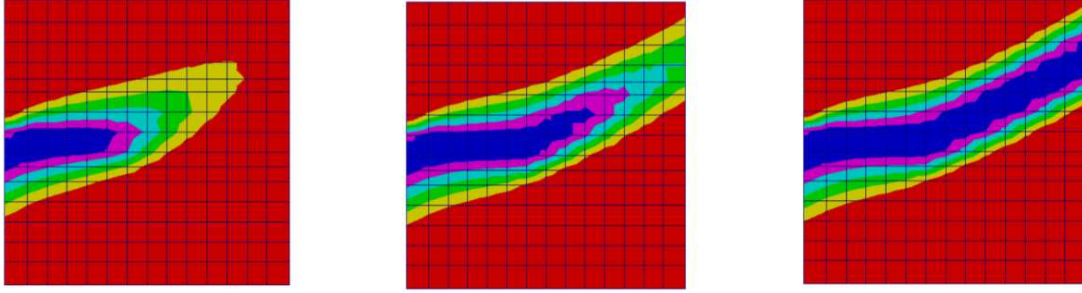
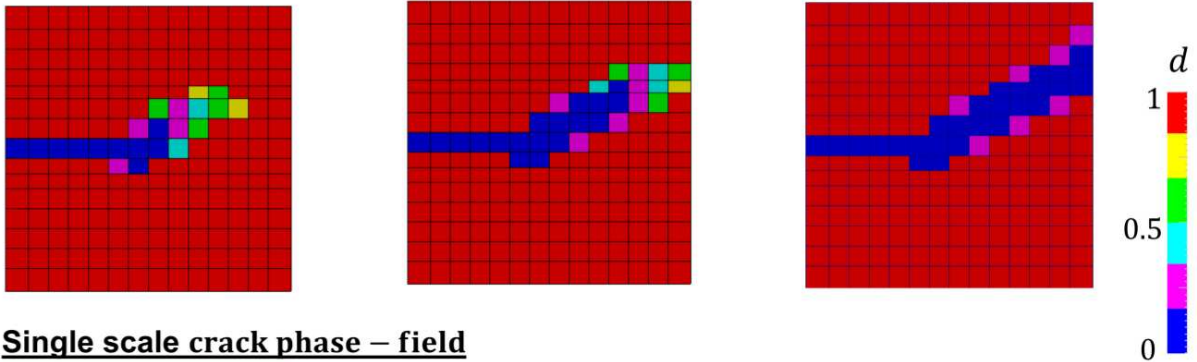
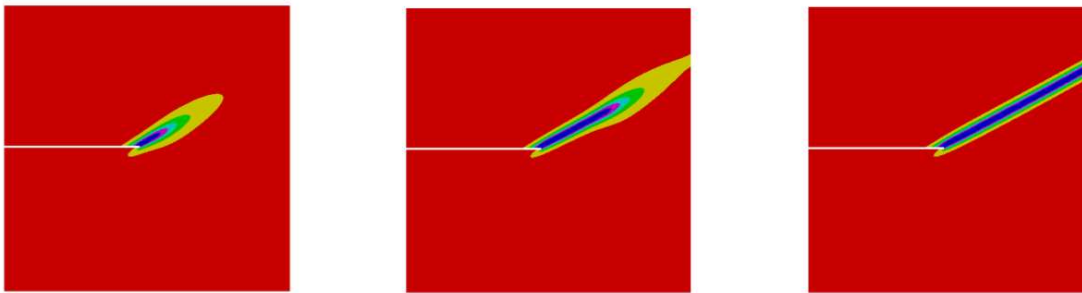
Global crack phase – field**Homogenous crack phase – field solution****Single scale crack phase – field****a****b****c**

Figure 2.22: Example 2. Homogenized global crack phase-field solution for $\phi = +30$. First row: the global crack phase-field; Second row: the homogeneous solution; Third row: single scale phase field solution per loading step for different deformations states as: (a) $\bar{\mathbf{u}} = 0.0088 \text{ mm}$ (b) $\bar{\mathbf{u}} = 0.0092 \text{ mm}$ and (c) $\bar{\mathbf{u}} = 0.010 \text{ mm}$.

by means of randomly distributed hard inclusions as plotted in Fig 2.27b. Furthermore transversely isotropic material behavior is assumed. The structural director \mathbf{a} is inclined under $\phi = -15^\circ$.

Geometry and loading conditions are depicted in Fig. 2.27a. The size of the specimen is chosen to be: $A = B = 250 \text{ mm}$ and $H = 30 \text{ mm}$. The bottom edge of the specimen is fixed in both directions and a vertical displacement is applied until final failure, see Fig. 2.27a. One third of the specimen is covered by hard inclusions, as shown in Fig. 2.27b. Here, crack propagation is expected. The remaining parts of the domain are supposed to be homogeneous, but affected by the transversely isotropic behavior.

The material parameters used in the simulation are the same as in [305] and set as:

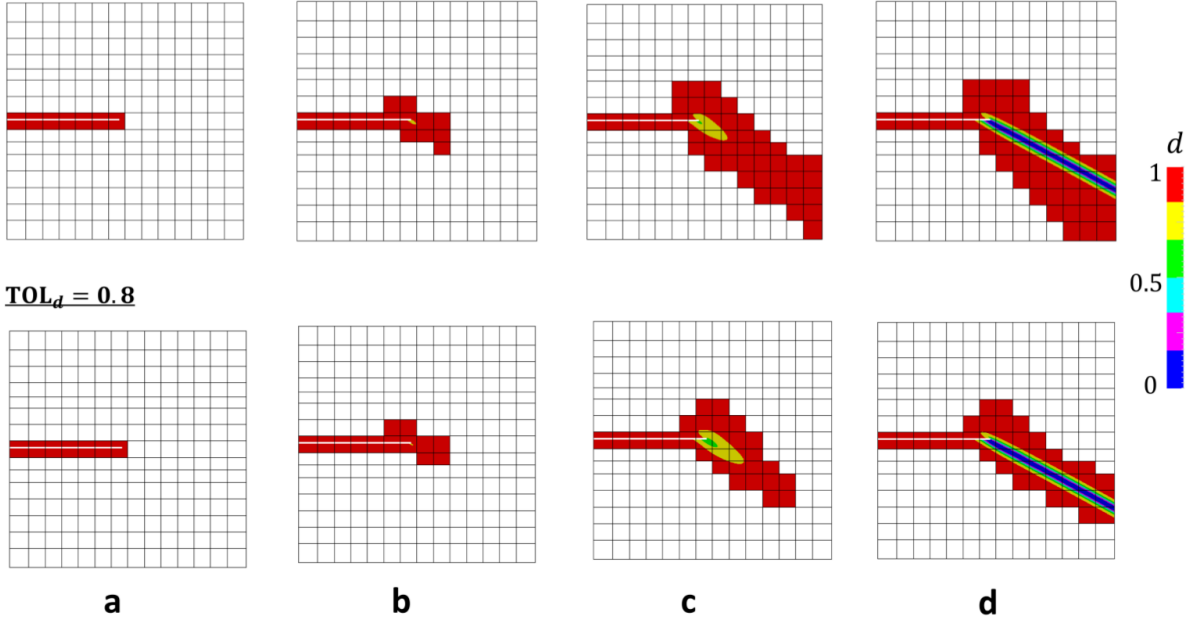
TOL_d = 0.9

Figure 2.23: Example 2. Fracture of transversely isotropic single-edge-notched plate under tension for $\phi = -30^\circ$. Resulting, local crack phase-field by Global-Local adaptive scheme indicated in; First row with $\text{TOL}_d = 0.90$; Second row with $\text{TOL}_d = 0.80$ per loading steps at (a) $\bar{u} = 0.0030 \text{ mm}$ (b) $\bar{u} = 0.0062 \text{ mm}$ (c) $\bar{u} = 0.0078 \text{ mm}$ (d) $\bar{u} = 0.0085 \text{ mm}$.

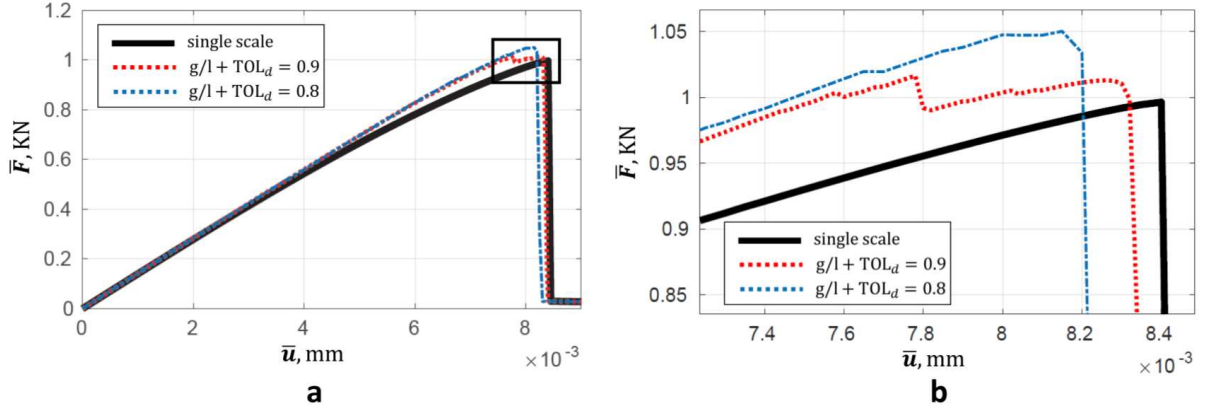


Figure 2.24: Example 2. Effect of different TOL_d on Global-Local approach by (a) Comparison of the load-displacement curve; (b) Zooming into the framed region of the left plot.

$\lambda = 6.16 \text{ kN/mm}^2$, $\mu = 10.95 \text{ kN/mm}^2$, $G_c = 9 \times 10^{-5} \text{ kN/mm}$, $\alpha = \chi = 50$ and $\Xi = 0$. The dimensionless mismatch ratio is denoted by $m = E_{inclusion}/E_{matrix}$ (here, E refers to Young's modulus) and set as $m = 10$. Thus, we deal with $E_{matrix} = 25.85 \text{ kN/mm}^2$ and $E_{inclusion} = 258.5 \text{ kN/mm}^2$.

In order to determine an initial fictitious domain, which has to be used for the Global-Local approach, an idea of the phase-field formulation with threshold state is considered. Here, a critical stress state on the global level is employed by extending the critical stress value of the isotropic phase-field formulation in [62] to an anisotropic heterogeneous

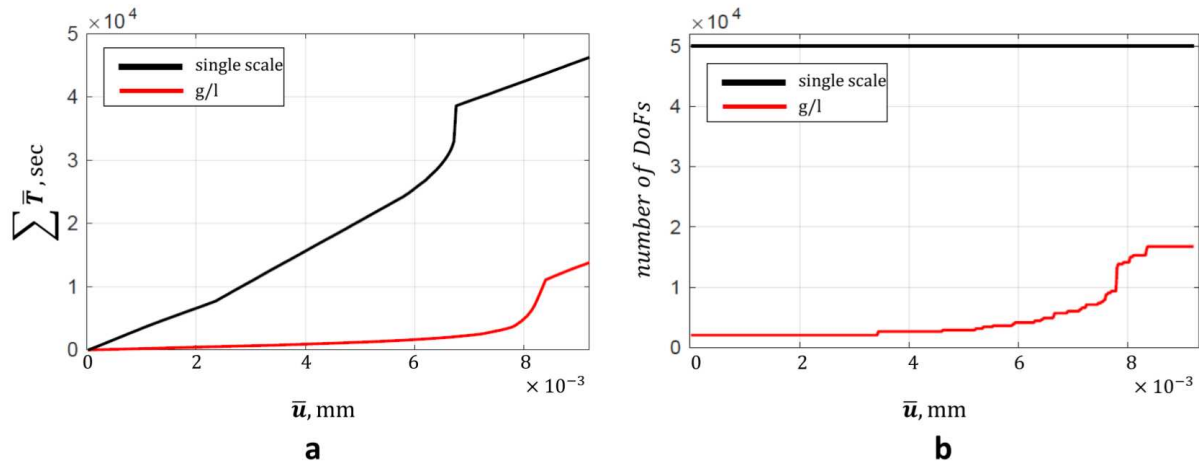


Figure 2.25: Example 2. Time efficiency for the transversely isotropic single-edge-notched tension test (a) Time-displacement curves in terms of the accumulated time; (b) Number of degrees of freedom.

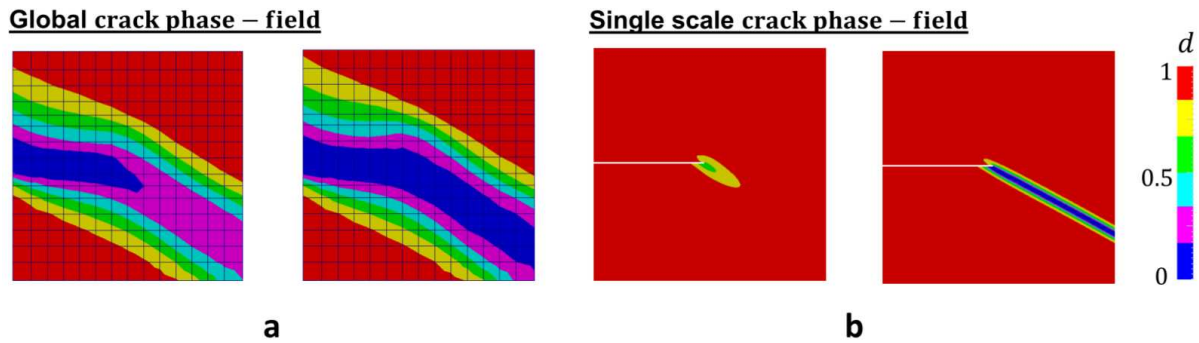


Figure 2.26: Example 2. Homogenized global crack phase-field solution for $\phi = -30^\circ$. (a) Global crack phase-field and (b) single scale solution for two deformation states: $\bar{u} = 0.0078 \text{ mm}$ and $\bar{u} = 0.0085 \text{ mm}$.

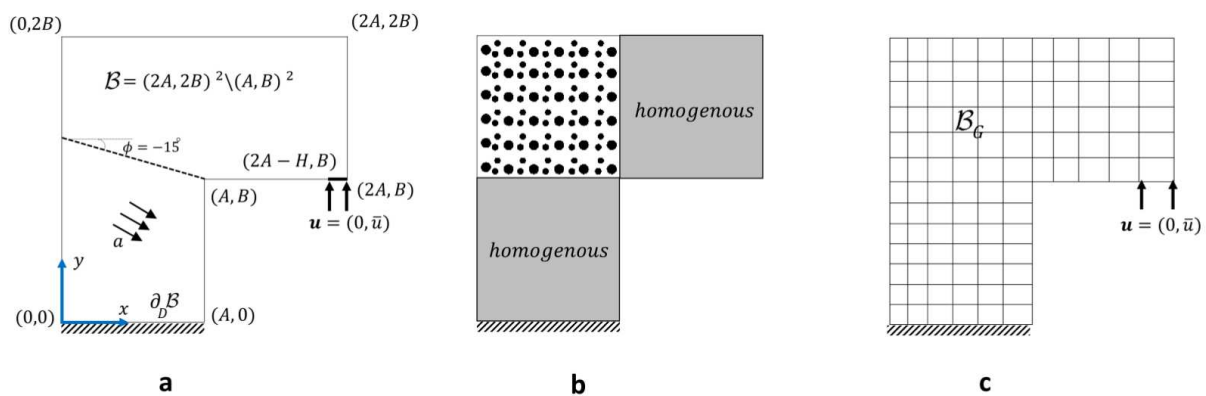


Figure 2.27: Example 3. Heterogeneous L-shaped panel test. (a) Geometry and loading setup with a structural director \mathbf{a} inclined under an angle $\phi = -15$ (b) partitioning of domain into the heterogeneity and homogeneity counterparts and (c) global finite element mesh without potential fictitious zones.

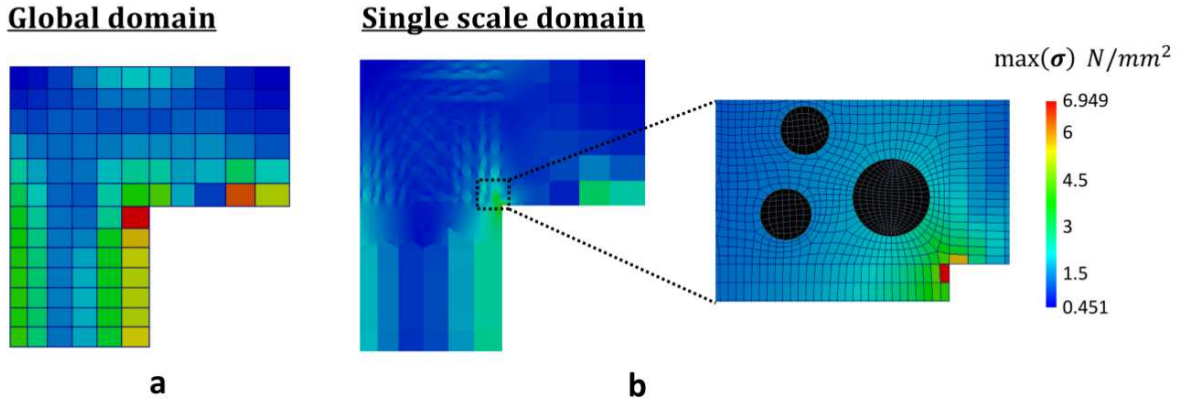


Figure 2.28: Example 3. Maximum stress state in the heterogeneous L-shaped panel test. (a) Global stress state and (b) single scale stress state.

setting. Hence, the critical values for the stress and corresponding strain, are obtained as

$$\varepsilon_c = \frac{\sqrt{3}}{3} \sqrt{\frac{G_c}{l(\chi a^4 + \bar{E})}} \quad \text{and} \quad \sigma_c = \frac{3\sqrt{3}}{16} \sqrt{\frac{G_c(\chi a^4 + \bar{E})}{l}}. \quad (2.98)$$

This result is based on (2.35) and (2.97) where $a = \sin(\phi)$, see [299]. The effective Young's modulus \bar{E} for the heterogeneous domain is defined as

$$\bar{E} := \frac{E_{Voigt} + E_{Reuss}}{2}$$

with

$$E_{Voigt} := \frac{1}{V} \int_{\mathcal{B}} E \, d\mathbf{x}, \quad \text{and} \quad E_{Reuss}^{-1} := \frac{1}{V} \int_{\mathcal{B}} E^{-1} \, d\mathbf{x}.$$

For $\chi = 0$ in (2.98) the isotropic case of [62] is recovered. The critical stress state increases as l decreases. Additionally, if the length scale l goes to 0 in the limit, the crack nucleation stress tends to infinity. This is in agreement with Griffith's theory, which allows to have crack nucleation in stress singularities. Then, the critical stresses based on the effective Young's modulus $\bar{E} = 36.136 \text{ kN/mm}^2$ yields $\sigma_c = 9.2603 \text{ N/mm}^2$ with the Voigt average $E_{Voigt} = 44.423 \text{ kN/mm}^2$ and the Reuss average $E_{Reuss} = 27.850 \text{ kN/mm}^2$.

Figure 2.28 shows the maximum stress state distribution of the heterogeneous L-shaped panel test. Here, the maximum stress is observed in the corner point of the specimen where the singularities are located. Hence, this is the potential candidate for the local domain. The Global-Local approach is then started after the stress state on the global domain reaches 75% of σ_c . This percentage of the critical stress is chosen to be on the safe side when starting the Global-Local formulations.

The evolution of the local crack phase-field with the corresponding mesh is depicted in Fig. 2.29 for different deformation stages. Specifically, the second row in Fig. 2.29 corresponds to the deformations $\bar{\mathbf{u}} = 0.324 \text{ mm}$, $\bar{\mathbf{u}} = 0.333 \text{ mm}$ and $\bar{\mathbf{u}} = 0.58 \text{ mm}$, respectively. Due to the existing hard/stiff inclusions, the crack phase-field propagates around the inclusions. The resulting crack pattern indicated in Fig. 2.29 demonstrates an excellent agreement with the single scale simulation, with the advantage that the Global-Local approach requires significantly less degrees of freedom.

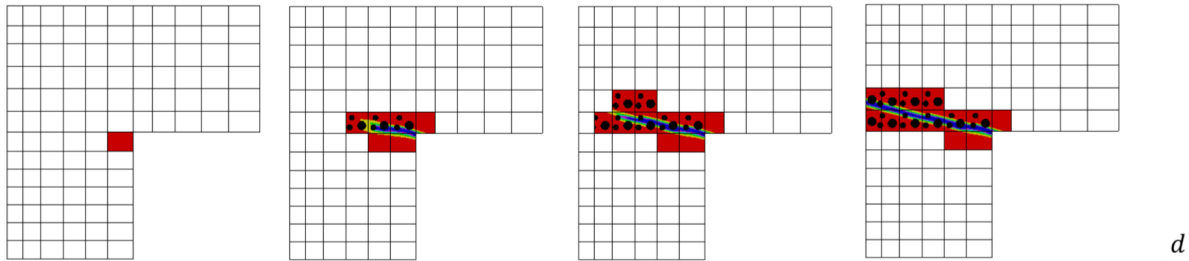
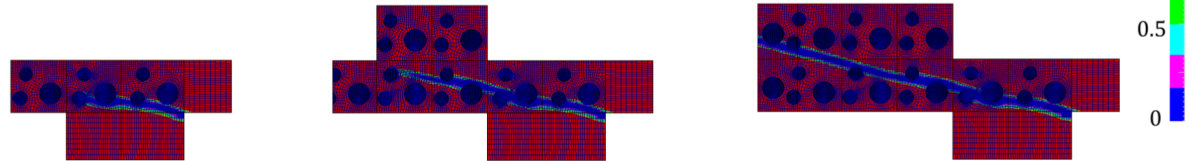
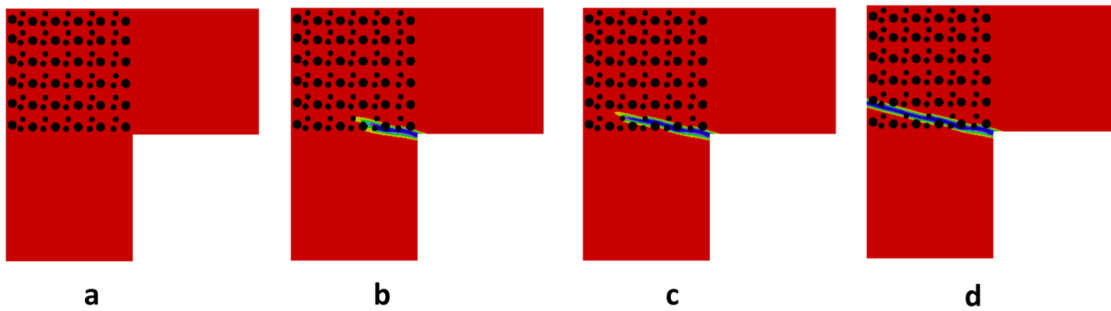
Local crack phase – field**Zoom – in local crack phase – field****Single scale crack phase – field**

Figure 2.29: Example 3. Crack phase-field pattern for the transversely isotropic heterogeneous L-shaped panel test with fiber direction angle of $\phi = -15^\circ$. First row: local crack phase-field based on the adaptive scheme; Second row: mesh evolution for local domain by considering the influence of inclusions; Third row: resulting single scale phase-field solution at (a) $\bar{u} = 0.15 \text{ mm}$, (b) $\bar{u} = 0.324 \text{ mm}$, (c) $\bar{u} = 0.333 \text{ mm}$ and (d) $\bar{u} = 0.58 \text{ mm}$.

A comparison of the load-displacement curves is shown in Fig. 2.30a. Therein, a good agreement of the Global-Local approach with the single scale solution was observed for the heterogeneous L-shaped panel test. Figure 2.30b illustrates the efficiency of the Global-Local approach. Here the accumulative computational time is reduced by a factor of eight.

2.5.6. Example 4: Investigation of transversely isotropic double-edge-notched tension. The last example is concerned with the capability of the proposed Global-Local approach for handling *coalescence* and *merging* of *crack paths* in the local domains. Specifically, the following numerical test aims to illustrate the effects of the double notch shaped specimen. Here crack-initiation and curved-crack-propagation, representing a mixed-mode fracture, are predicted with a Global-Local formulation. Additionally a transversely isotropic material behavior given by the structural director \mathbf{a} that is inclined under $\phi = -15^\circ$ is assumed.

The geometrical setup and the loading conditions of the notched specimen is depicted

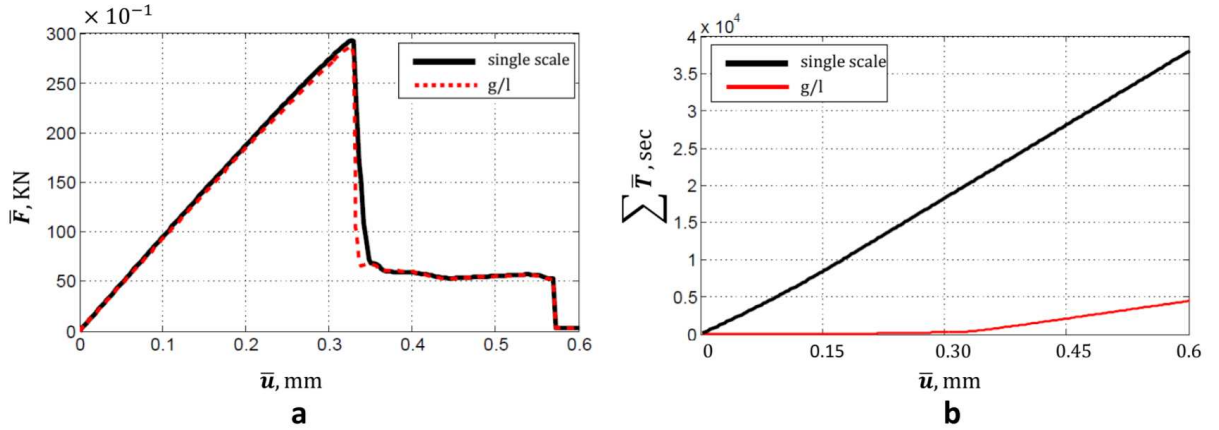


Figure 2.30: Example 3. Heterogeneous L-shaped panel test. (a) Comparison of the load-displacement curves and (b) accumulated time-displacement curves.

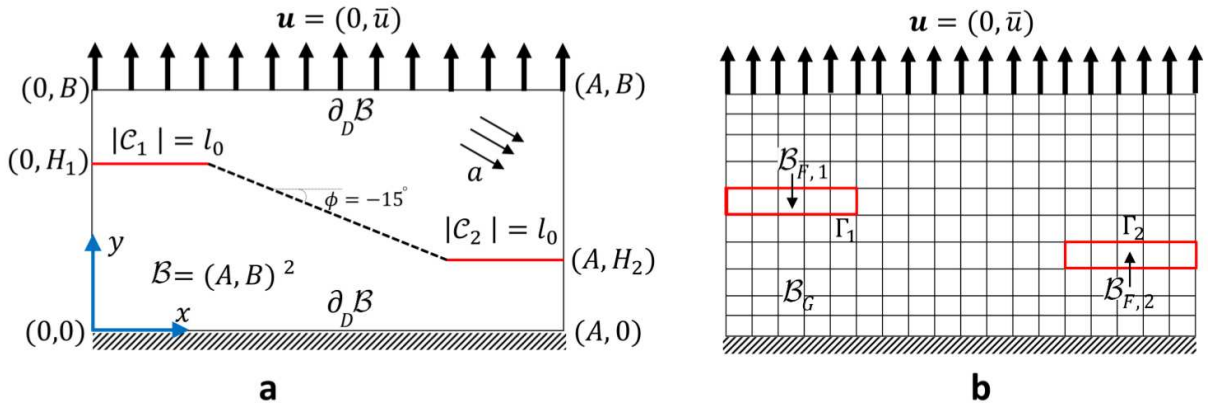


Figure 2.31: Example 4. Double-edge-notched tensile test. (a) Geometry and loading setup with a structural director \mathbf{a} inclined under an angle $\phi = -15$ and (b) global finite element mesh with two potential fictitious zone $\mathcal{B}_{F,1}$ and $\mathcal{B}_{F,2}$.

in Fig. 2.31a. The bottom edge of the plate is fixed in the x and y directions. A vertical displacement is applied at the top edge until final failure. We set $A = 20 \text{ mm}$ and $B = 10 \text{ mm}$ hence $\mathcal{B} = (20, 10)^2 \text{ mm}^2$. For the double-edge-notches, let $H_1 = 5.5 \text{ mm}$ and $H_2 = 3.5 \text{ mm}$ with the predefined crack length of $l_0 = 5 \text{ mm}$, see Fig. 2.31a. The material parameters used in the simulation are the same as in [6] and set as: $\lambda = 12 \text{ kN/mm}^2$, $\mu = 8 \text{ kN/mm}^2$, $G_c = 1 \times 10^{-3} \text{ kN/mm}$, $\alpha = \chi = 50$ and $\Xi = 0$.

The global finite element mesh includes two potential fictitious zones $\mathcal{B}_{F,1}$ and $\mathcal{B}_{F,2}$ with the interfaces Γ_1 and Γ_2 shown in Fig, 2.31b.

The evolution of the crack phase-field resulting from the local domain along with its mesh evolution are indicated in Fig. 2.32 for different deformation stages up to final failure. The single scale crack phase-field simulation is shown in Fig. 2.32 in the third row. At the loading step $\bar{u} = 0.0143 \text{ mm}$ the coalescence and merging of the two local domains are observed. Furthermore, a considerable reduction of the unknowns versus the single scale problem, can be clearly noticed due to the very narrow \mathcal{B}_L in Fig. 2.32.

These results demonstrate the feasibility/efficiency of using the proposed adaptive

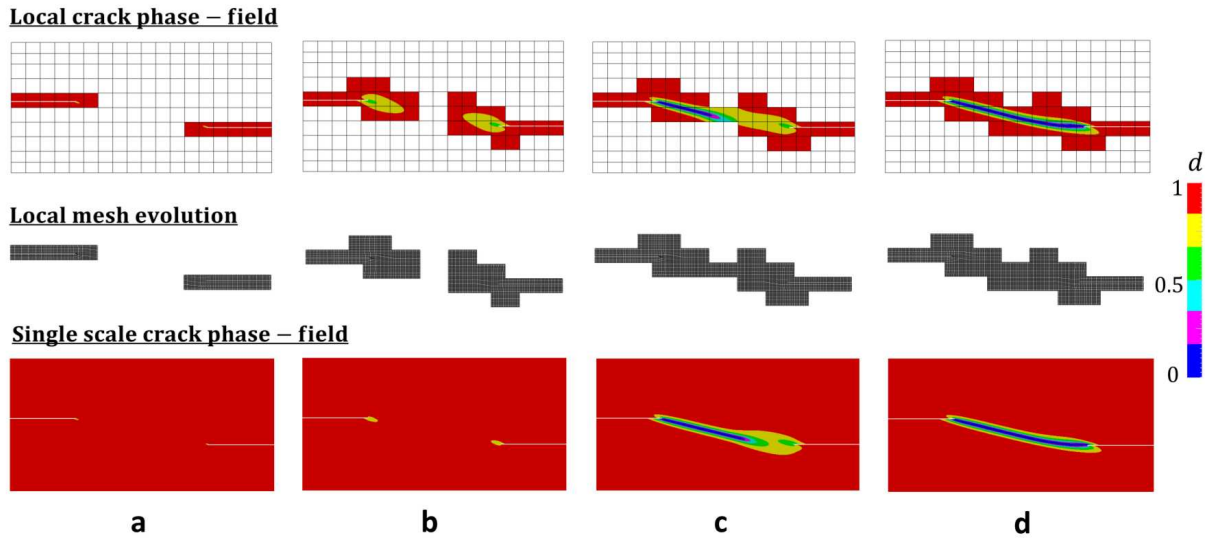


Figure 2.32: Example 4. Crack phase-field pattern for transversely isotropic double-edge-notched plate under tension with fiber direction angle of $\phi = -15^\circ$. First row: local crack phase-field based on the adaptive scheme; Second row: mesh evolution for local domain; Third row: resulting single scale phase-field solution at (a) $\bar{u} = 0.01 \text{ mm}$, (b) $\bar{u} = 0.0122 \text{ mm}$, (c) $\bar{u} = 0.0143 \text{ mm}$ and (d) $\bar{u} = 0.0145 \text{ mm}$.

Global-Local approach for different local domains and more complicated structures.

3. Global-Local approach for hydraulic fracture in poroelastic media

In this chapter, phase-field modeling of hydraulic fractures in porous media is extended towards a global-local approach. Therein, the failure behavior is solely analyzed in a (small) local domain. In the surrounding medium, a simplified and linearized system of equations is solved. Both domains are coupled by Robin-type interface conditions. The fracture(s) inside the local domain are allowed to propagate and consequently both subdomains change within time. Here, a predictor-corrector strategy is adopted in which the local domain is dynamically adjusted to the current fracture pattern. The resulting framework is algorithmically described in detail and substantiated with some numerical tests. The discussion in this chapter is based on the recent work of ALDAKHEEL ET AL. [17].

3.1. Introduction

In recent years, several pressurized [69, 242, 240, 313, 162, 163, 290, 257] and fluid-filled [239, 317, 196, 235, 234, 115, 160, 12, 200, 310, 198, 75, 199, 88, 161, 318, 15] phase-field fracture formulations have been proposed in the literature. These studies range from modeling of pressurized and fluid-filled fractures, mathematical analysis, numerical modeling and simulations up to high-performance parallel computations. Recently various extensions towards multiphysics phase-field fracture in porous media have been proposed in which various phenomena couple as for instance proppant [198], two-phase flow formulations [197] or given temperature variations [257]. All these examples demonstrate the potential of phase-field for crack propagation.

Phase-field fracture is a regularized approach, which has advantages and shortcomings. The first advantage is a continuum description based on first physical principles to determine the unknown crack path [134, 67, 230] and the computation of curvilinear and complex crack patterns. The model allows for nucleation, branching, merging and post-processing of certain quantities such that stress intensity factors become redundant. Therefore, easy handling of fracture networks in possibly and highly heterogeneous media can be treated. The formulation being described in a variational framework allows finite element discretizations and corresponding analyses. The mathematical model permits any dimension, thus phase-field fracture applies conveniently to three-dimensional simulations. On the energy level, the formulation is non-convex constituting a challenge for both theory and design of numerical algorithms. A second challenge is the computational cost. Various solutions have been proposed so far; namely staggered approaches (alternating minimization) [66, 73, 74], stabilized staggered techniques [72], quasi-monolithic approaches [162] (possibly with sub-iterations [213]), or fully monolithic approaches [142, 316, 315]. Adaptive mesh refinement was proposed to reduce the computational costs [73, 162, 35, 314]. A related technique that has the potential to treat large-scale problems is a global-local technique proposed in [143, 138]. Recently this was extended to a framework in which the local domain is dynamically updated according to the propagating fracture path [258]. The need for such framework can be found in multiscale porous media applications [94, 95] or in which a localized fracture occurs in a (big) reservoir [317].

The last two references are the motivation for the present work. Here, we extend the adaptive global-local phase-field fracture approach [258] to porous media applications

with hydraulic fractures. We first extend our model towards large strain formulations, in line with [4, 10, 108, 238]. Previous studies only concentrated on small strain applications. Then, the coupled multiphysics fracture framework is carefully derived. Both subdomains will be coupled via Robin-type interface conditions, see [258]. This leads to Lagrange multiplier formulations that are demanding from a mathematical point of view as well as in the implementation, see for example [321, 322, 320, 284]. A future rigorous numerical analysis of our global-local approach can be achieved with similar methodologies as used in [145, 144]. In particular, our formulation can deal with non-matching grids at the interface, which is very interesting for cases towards practical field problems as mentioned in [317] in which possibly various programming codes must be coupled. On the fine-scale level all (nonlinear) equations are solved. On the global level, only coarse representations of the pressure and crack phase-field are considered. As mentioned in the previous descriptions and references such multiphysics fracture formulations are challenging from a mathematical and numerical point of view. For these reasons, we concentrate in this work on careful algorithmic descriptions including supporting numerical simulations. Here, our emphasis is on results, demonstrating the computational convergence properties of our proposed numerical schemes. A rigorous numerical analysis must be left for future work.

The outline of this chapter is as follows: In Section 3.2, the governing equations are described. Then, in Section 3.3, the extension to a global-local formulation for pressurized fractures is derived. Therein, the Robin-type interface conditions are carefully discussed. This is followed by the final global-local algorithm. Afterward, we also discuss the dynamic choice of the local domains with the help of a predictor-corrector scheme. In Section 3.4 some numerical tests are carried out in order to substantiate our algorithmic developments.

3.2. Phase-field modeling of hydraulic fracture

This section outlines a theory of the variational phase-field fracture model in poroelastic media undergoing finite strains. This type of modeling is so-called hydraulic fracturing or fracking process. Three governing equations are used to describe the constitutive formulations for the mechanical deformation, fluid pressure and the crack phase-field. Strong and variational formulations of the coupled multi-physics problem are further introduced. Additionally, the framework is algorithmically described, resulting in the so-called *single-scale domain* formulations.

3.2.1. Governing equations. Let us $\mathcal{B} \in \mathcal{R}^\delta$ to be a solid in the Lagrangian (reference) configuration with dimension $\delta = 2, 3$ in space and time $t \in \mathcal{T} = [0, T]$ and $\partial\mathcal{B}$ is the surface boundary. Let assume Neumann conditions on $\partial_N\mathcal{B} := \Gamma_N \cup \mathcal{C}$, where Γ_N denotes the outer domain boundary and additionally Dirichlet boundary conditions on $\partial_D\mathcal{B}$. The sharp crack surface $\mathcal{C} \in \mathcal{R}^{\delta-1}$ is illustrated as a red color curve in Fig. 3.1.

The boundary-value-problem BVP described here is the coupled multi-field problem for the fluid-saturated porous media of the fracturing material. Fluid-saturated porous media is formulated based on coupled three-field problem. Hence, three unknown solution fields at material points $\mathbf{X} \in \mathcal{B}$ described by the deformation map $\varphi(\mathbf{X}, t)$ of the solid, the fluid pressure field $p(\mathbf{X}, t)$ and the crack phase-field $d(\mathbf{X}, t)$ defined as

$$\varphi : \begin{cases} \mathcal{B} \times \mathcal{T} \rightarrow \mathcal{R}^\delta \\ (\mathbf{X}, t) \mapsto \mathbf{x} = \varphi(\mathbf{X}, t) \end{cases}, \quad p : \begin{cases} \mathcal{B} \times \mathcal{T} \rightarrow \mathcal{R} \\ (\mathbf{X}, t) \mapsto p(\mathbf{X}, t) \end{cases}, \quad d : \begin{cases} \mathcal{B} \times \mathcal{T} \rightarrow [0, 1] \\ (\mathbf{X}, t) \mapsto d(\mathbf{X}, t) \end{cases}, \quad (3.1)$$

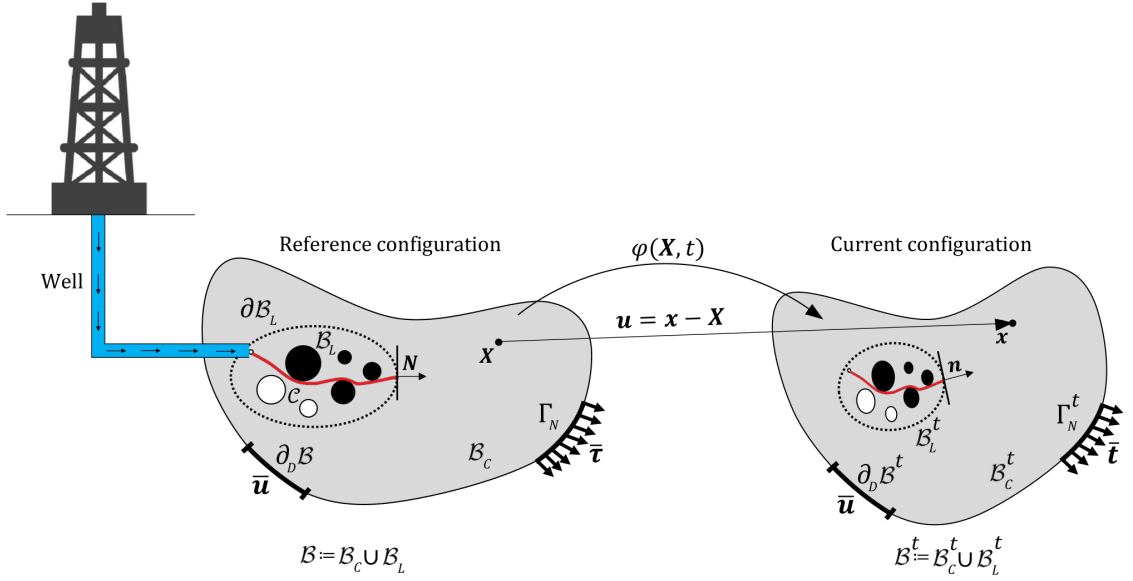


Figure 3.1: The unfractured domain indicates by \mathcal{B}_C . The red curved crack surface lives in the local domain \mathcal{B}_L . The entire domain is a close subset as $\mathcal{B} := \mathcal{B}_C \cup \mathcal{B}_L$ which includes unfractured and fractured states. The fracture boundary is $\partial\mathcal{B}_L$ and the outer boundary of the domain is $\partial\mathcal{B}$. Blue color refer to the injected fluid through the well drilling and injection.

with $\dot{d} \geq 0$. The location of the material point in the deformed configuration is depicted as $\mathbf{x} = \mathbf{X} + \mathbf{u}(\mathbf{X}, t)$ where $\mathbf{u}(\mathbf{X}, t)$ is the displacement field. Following Fig. 3.1 at the undeformed configuration, the crack phase-field $d(\mathbf{X}, t) = 0$ (light gray color) and $d(\mathbf{X}, t) = 1$ (red color) are referred to the unfractured and fully fractured state of the material, respectively. The sharp fracture surface \mathcal{C} is approximated in $\mathcal{B}_L \subset \mathcal{B}$ the so-called *local domain*. The unbroken sub-domain with no fracture is denoted by *complementary domain* $\mathcal{B}_C := \mathcal{B} \setminus \mathcal{B}_L \subset \mathcal{B}$, such that $\mathcal{B}_C \cup \mathcal{B}_L =: \mathcal{B}$ and $\mathcal{B}_C \cap \mathcal{B}_L = \emptyset$. We note that a region \mathcal{B}_L where the regularized crack phase-field is approximated is strongly related to the choice of the phase-field diffusivity parameter $l > 0$ (or so-called regularization parameter).

The material deformation gradient of the solid denoted by $\mathbf{F}(\mathbf{X}) := \nabla\varphi(\mathbf{X}, t) = \text{Grad}\varphi$ with the Jacobian $J := \det[\mathbf{F}] > 0$ and the right Cauchy-Green tensor $\mathbf{C} = \mathbf{F}^T \mathbf{F}$. The geometry is enforced by prescribed deformations $\bar{\mathbf{u}}$ and additionally prescribed traction vector $\bar{\boldsymbol{\tau}}$ at the surface $\partial\mathcal{B}$ of the undeformed configuration, which are defined by the time-dependent Dirichlet- and Neumann type conditions

$$\varphi = \bar{\varphi}(\mathbf{X}, t) \text{ on } \partial_D\mathcal{B} \quad \text{and} \quad \mathbf{P}\mathbf{N} = \bar{\boldsymbol{\tau}}(\mathbf{X}, t) \text{ on } \partial_N\mathcal{B}, \quad (3.2)$$

here \mathbf{N} is the material outward unit normal vector in the undeformed reference configuration such that two-point first Piola-Kirchhoff stress tensor $\mathbf{P}(\mathbf{F}, p, d)$ is the thermodynamic dual to \mathbf{F} . The global mechanical form of the equilibrium equation for the solid body is represented through *first* partial differential equation PDE for the multi-field problem as

$$\text{Div } \mathbf{P}(\mathbf{F}, p, d) + \bar{\mathbf{b}} = \mathbf{0}, \quad (3.3)$$

such that dynamic motion is neglected, i.e. quasi-static response, and also we denote $\bar{\mathbf{b}}$ as a prescribed body force.

To formulate the constitutive equation for the poromechanics, let us to move forward with a *biphasic* fully saturated porous material, which includes of a pore fluid (i.e. fluid phase) and a solid matrix (i.e. solid phase) within bulk material. A local volume element denoted by dV in the undeformed reference configuration can be additively decomposed into a fluid portion dV_F and a solid portion dV_S . Thus, the volume fraction is introduced via $n_\alpha := dV_\alpha/dV$, where $\alpha = \{S, F\}$. With respect to the fully saturated porous medium the *saturation condition* reads

$$\sum_{\alpha} n_{\alpha} = n_F + n_S = 1, \quad (3.4)$$

where $n_F(\mathbf{X}, t)$ represents the porosity, i.e. the volume occupied by the fluid is *same as* the pore volume. Note that in the *fracture region* where

$$d = 1 \quad \text{yields} \quad n_S = 0 \quad \text{and} \quad n_F = 1. \quad (3.5)$$

The volume fraction in the porous media, i.e. n_α , depends on the physical density (i.e. material, effective, intrinsic) $\rho_{\alpha R}$ to the partial density ρ_α through

$$\rho_\alpha = n_\alpha \rho_{\alpha R} \quad \text{with} \quad \rho_{\alpha R} := dm_\alpha/dV_\alpha \quad \text{and} \quad \rho_\alpha := dm_\alpha/dV, \quad (3.6)$$

where dm_α is the mass of the phase α . Thus, the overall density can be expressed as $\rho = \sum_{\alpha} n_\alpha \rho_{\alpha R}$. A comprehensive theoretical and applications review on the porous materials are provided in the works [58, 93, 99, 114, 283, 214]. The fluid volume fraction (porosity) n_F is linked to the fluid volume ratio θ (fluid content) per unit volume of the undeformed reference configuration \mathcal{B} via

$$n_F = n_{F,0} + \theta, \quad (3.7)$$

for constant fluid material density, where $n_{F,0}$ is the initial porosity. In the constitutive modeling θ describes the *first local internal* variable (history field). The evolution equation for the fluid volume ratio $\dot{\theta} = \dot{n}_F$ is derived by means of the fluid pressure field p . Prescribed Dirichlet- and Neumann boundary conditions for the pressure are described by

$$p = \bar{p}(\mathbf{X}, t) \quad \text{on} \quad \partial_D \mathcal{B} \quad \text{and} \quad \mathcal{F} \cdot \mathbf{N} = \bar{f}(\mathbf{X}, t) \quad \text{on} \quad \partial_N \mathcal{B}, \quad (3.8)$$

through the material fluid volume flux vector \mathcal{F} in the reference configuration, the imposed fluid pressure \bar{p} on the boundary surface and also fluid transport \bar{f} on the Neumann boundary surface. Because fluid-filled equation is a time dependent problem, the initial condition needs to be set for the fluid volume ratio and hence by $\theta(\mathbf{X}, t_0) = 0$ yields $n_F = n_{F,0}$ in \mathcal{B} . Furthermore, the fluid flux vector in (4.9) is described through to the negative direction of the material gradient of the fluid pressure ∇p through the permeability, based on Darcy-type fluid transport theory by

$$\mathcal{F} := -\mathbf{K}(\mathbf{F}, d) \nabla p, \quad (3.9)$$

here the second-order permeability tensor given by anisotropic second-order tensor \mathbf{K} which described based on the material deformation gradient \mathbf{F} and the crack phase-field d . To consider the effect of the fracture on the fluid contribution, permeability tensor

is decomposed into a *Darcy-type flow for an unfractured porous medium* \mathbf{K}_{Darcy} and a *Poiseuille-type flow in a fully fractured material* \mathbf{K}_{crack} defined as

$$\begin{aligned}\mathbf{K}(\mathbf{F}, d) &= \mathbf{K}_{Darcy}(\mathbf{F}) + d^\zeta \mathbf{K}_{frac}(\mathbf{F}), \\ \mathbf{K}_{Darcy}(\mathbf{F}) &= \frac{K}{\eta_F} J \mathbf{C}^{-1}, \\ \mathbf{K}_{frac}(\mathbf{F}) &= K_c \omega^2 J [\mathbf{C}^{-1} - \mathbf{C}^{-1} \mathcal{N} \otimes \mathbf{C}^{-1} \mathcal{N}],\end{aligned}\quad (3.10)$$

as outlined in [15, 234]. Here, $\mathcal{N} = \nabla d / |\nabla d|$ is the material outward normal to the crack surface, K is the isotropic intrinsic permeability of the pore space, K_c is the spatial permeability for the fracture state, η_F is the dynamic fluid viscosity and $\zeta \geq 1$ is a permeability transition exponent. Following [234], let us now to approximate the crack opening displacement ω (crack aperture) through $\omega = (\lambda_\perp - 1)h_e$ in terms of the stretch orthogonal to the crack surface $\lambda_\perp^2 = \nabla d \cdot \nabla d / \nabla d \cdot \mathbf{C}^{-1} \cdot \nabla d$ and the characteristic element length h_e . Characteristic element length, typically set as a minimum discretized element size, i.e. diameter of an element, in the fractured region.

The conservation of the fluid mass which reflects the *second* PDE within hydraulic fracturing setting reads

$$\dot{n}_F - \bar{r}_F + \text{Div}[\mathcal{F}] = 0, \quad (3.11)$$

with a given/imposed fluid source \bar{r}_F per unit volume of the initial configuration \mathcal{B} , which describes the injection process in hydraulic fracturing.

Within regularized fracture framework, a sharp-crack surface topology denoted by \mathcal{C} to ensure the continuity of the crack field is further regularized by the smeared crack surface functional shown by \mathcal{C}_l thus $\mathcal{C} \rightarrow \mathcal{C}_l$ as outlined in [6, 14], hence we have

$$\mathcal{C}_l(d) = \int_{\mathcal{B}} \gamma_l(d, \nabla d) dV \quad \text{with} \quad \gamma_l(d, \nabla d) = \frac{1}{2l} d^2 + \frac{l}{2} |\nabla d|^2, \quad (3.12)$$

in terms of the regularized crack surface density function denoted by γ_l per unit volume of the solid and the regularization parameter l , so-called length scale, which governs the fracture diffusivity. Hence, the crack phase-field d can be derived by the minimization of diffusive crack surface $\mathcal{C}_l(d)$ by

$$d = \text{Arg}\{\inf_d \mathcal{C}_l(d)\} \quad \text{with} \quad d = 1 \text{ on } \mathcal{C} \subset \mathcal{B}, \quad (3.13)$$

The outcome Euler-Lagrange differential equation is $d - l^2 \Delta d = 0$ in \mathcal{B} augmented with the homogeneous Neumann-type boundary condition that is $\nabla d \cdot \mathbf{N} = 0$ on $\partial \mathcal{B}$. Let us consider the smeared crack phase-field functional given in (4.13) to ensure the fracture Kuhn-Tucker conditions [10, 230]. To do so, the constitutive functions response by means of the a global evolution equation of regularized crack surface reads

$$\frac{d}{dt} \mathcal{C}_l(d) := \frac{1}{l} \int_{\mathcal{B}} [(1-d)\mathcal{H} - \eta \dot{d}] \dot{d} dV \geq 0. \quad (3.14)$$

Here, artificial/numerical material parameter denoted by $\eta \geq 0$ is used to characterizes the viscosity term of the crack propagation. The maximum absolute value for the crack

driving state function denoted by D is defined by the crack driving force \mathcal{H} which reads

$$\mathcal{H} = \max_{s \in [0, t]} D(\mathbf{x}, s) \geq 0, \quad (3.15)$$

that accounts for the irreversibility of the crack phase-field evolution by filtering out a maximum value of D . That is referred to the *second local history variable*. The local evolution of the crack phase-field equation in the given domain \mathcal{B} resulting from (6.10) augmented with its homogeneous Neumann type boundary condition, i.e. $\nabla d \cdot \mathbf{N} = 0$ on $\partial\mathcal{B}$ yields

$$[d - l^2 \Delta d] + \eta \dot{d} + (d - 1)\mathcal{H} = 0, \quad (3.16)$$

which states the *third* PDE for the coupled problem.

3.2.2. Constitutive functions. The coupled multi-physics boundary value problem is formulated through three primary fields (i.e. unknown solution fields) to illustrate the hydro-poro-elasticity of fluid-saturated porous media in the fracturing material by

$$\text{Global Primary Fields : } \mathfrak{U} := \{\boldsymbol{\varphi}, p, d\}, \quad (3.17)$$

the mechanical deformation map $\boldsymbol{\varphi}$, the pressure field p and the crack phase-field $0 \leq d \leq 1$. Note, for the numerical implementation standpoint, to guarantee $0 \leq d \leq 1$ holds, we project $d > 1$ to 1 and also $d < 0$ to 0 to avoid unphysical crack phase-field solution [257]. The constitutive formulations for the hydraulic phase-field fracture are written in terms of the following set

$$\text{Constitutive State Variables : } \boldsymbol{\mathfrak{C}} := \{\mathbf{F}, \theta, d, \nabla d\}, \quad (3.18)$$

which shows the response of the poro-elasticity material modeling with a first-order gradient damage model. A pseudo-energy density function denoted by $W(\boldsymbol{\mathfrak{C}})$ for the poroelastic media per unit volume reads

$$W(\boldsymbol{\mathfrak{C}}) = W_{elas}(\mathbf{F}, d) + W_{fluid}(\mathbf{F}, \theta) + W_{frac}(d, \nabla d). \quad (3.19)$$

Here, modified elastic density function W_{elas} which is degraded elastic response resulting from the fracture state, a fluid density function contribution W_{fluid} and fracture density function denoted by W_{frac} which contain the accumulated dissipative energy are accordingly used. The elastic density function is formulated through a Neo-Hookean strain energy function for a compressible isotropic elastic solid

$$W_{elas}(\mathbf{F}, d) = g(d) \psi_{elas}(\mathbf{F}) \quad \text{with} \quad \psi_{elas}(\mathbf{F}) = \frac{\mu}{2} \left[(\mathbf{F} : \mathbf{F} - 3) + \frac{2}{\beta} (J^{-\beta} - 1) \right], \quad (3.20)$$

such that the shear modulus μ and the parameter $\beta := \beta(\nu) = 2\nu/(1 - 2\nu)$ with the Poisson number $\nu < 0.5$ are used. The quadratic function $g(d) = (1 - d)^2 + \kappa$ formulates the transition between the intact region and the fracture region such that

- In the intact region, i.e. $d = 0$, yields $W_{elas}(\mathbf{F}, d) \approx \psi_{elas}(\mathbf{F})$,
- In the exact fracture region, i.e. $d = 1$, yields $W_{elas}(\mathbf{F}, d) \approx 0$.

Here, $\kappa \ll 1$ is chosen by sufficiently small quantity to provide numerically stabilization response. Additionally, $g(d)$ from an physical standpoint describe the degradation of the elastic energy function of the bulk material due to fracture response. It interpolates between the unfractured state denoted by $d = 0$ and the fully fractured phase/state indicated by $d = 1$ such that following constraints

$$g(0) = 1, \quad g(1) = 0, \quad g'(d) \leq 0 \quad \text{and} \quad g'(1) = 0, \quad (3.21)$$

are ensured. The fluid density function is postulated takes the following form

$$W_{fluid}(\mathbf{F}, \theta) = \frac{M}{2} \left[B^2(J-1)^2 - 2\theta B(J-1) + \theta^2 \right], \quad (3.22)$$

based on the given fluid coefficient including which includes Biot's coefficient B and Biot's modulus M . By considering the Coleman-Noll inequality condition in thermodynamics, the fluid pressure p and the two-point first Piola-Kirchhoff stress tensor \mathbf{P} are derived from the first order derivative of the pseudo-energy density function W given in (6.15) by

$$\begin{aligned} p(\mathbf{F}, \theta) &:= \frac{\partial W}{\partial \theta} = \theta M - MB(J-1), \\ \mathbf{P}(\mathbf{F}, p, d) &:= \frac{\partial W}{\partial \mathbf{F}} = g(d)\mathbf{P}_{eff}(\mathbf{F}) - BpJ\mathbf{F}^{-T} \quad \text{with} \quad \mathbf{P}_{eff} = \mu[\mathbf{F} - J^{-\beta}\mathbf{F}^{-T}], \end{aligned} \quad (3.23)$$

for the isotropic solid material. Here, the second-order material stress tensor \mathbf{P} is further decomposed in a additive manner into the effective stress tensor \mathbf{P}_{eff} and additionally a pressure part. This additive decomposition is written based on the classical Terzaghi split, as outlined in [300, 98]. Using the pressure definition in (4.24)₁ and the second PDE in (4.12) along with (3.7), thus the conservation of mass takes the following form

$$\boxed{\frac{\dot{p}}{M} + B\dot{J} - \bar{r}_F + \text{Div}[\mathcal{F}] = 0,} \quad (3.24)$$

hence, now fluid-filled PDE formulated by means of the fluid pressure p and not fluid volume fraction (porosity) and additionally the deformation map $\boldsymbol{\varphi}$. The fracture contribution of pseudo-energy density given in (6.15) takes the following explicit form

$$W_{frac}(d, \nabla d) = [1 - g(d)] \psi_c + 2\psi_c l \gamma_l(d, \nabla d), \quad (3.25)$$

where $\psi_c > 0$ is so-called a critical fracture density energy. Critical elasticity density function depends on the critical effective stress σ_c or the Griffith's energy release rate G_c , as outlined in [6]

$$\psi_c = \frac{\sigma_c^2}{2E} = \frac{3}{8l\sqrt{2}}G_c. \quad (3.26)$$

By taking the variational derivative $\delta_d W$ of (6.15), the third PDE in the rate-independent setting by considering some more algebra reads as follows

$$\boxed{2\psi_c[d - l^2\Delta d] + 2(d-1)\mathcal{H} = 0,} \quad (3.27)$$

through the history field \mathcal{H} , used in (6.11). Following that, the positive crack driving state function D reads

$$D := \left\langle \psi_{elas}(\mathbf{F}(\mathbf{X}, s)) - \psi_c \right\rangle_+ \geq 0. \quad (3.28)$$

Here, the Macaulay bracket defined through $\langle x \rangle_+ := (x + |x|)/2$ is used such that the *local irreversibility* condition (positivity of the fracture dissipation) to avoid crack healing process and thus $\dot{d} \geq 0$ is ensured.

3.2.3. Variational formulations derived for the coupled multi-field problem.

The primary fields \mathbf{u} given in (6.13) for the coupled poro-elastic media of the fracturing material is governed by three PDEs in (6.7), (4.25) and (6.12) in a strong form setting. Here, three PDEs is governed in a time increment $[t_n, t_{n+1}]$ such that time step $\Delta t = t_{n+1} - t_n > 0$ holds. Next, three test functions with respect to the deformation $\delta\varphi(\mathbf{X}) \in \mathbf{m}V_\varphi := \{\mathbf{H}^1(\mathcal{B})^\delta : \delta\varphi = \mathbf{0} \text{ on } \partial_D\mathcal{B}\}$, fluid pressure $\delta p(\mathbf{X}) \in V_p := \{H^1(\mathcal{B}) : \delta p = 0 \text{ on } \partial_D\mathcal{B}\}$ and crack phase-field $\delta d(\mathbf{X}) \in V_d := \{H^1(\mathcal{B})\}$ are defined. The variational formulations with respect to the three PDEs for the coupled poro-elastic media of the fracturing material are derived by

$$\begin{aligned} G_\varphi(\mathbf{u}, \delta\varphi) &= \int_{\mathcal{B}} \left[\mathbf{P} : \nabla \delta\varphi - \bar{\mathbf{b}} \cdot \delta\varphi \right] dV - \int_{\partial_N\mathcal{B}} \bar{\boldsymbol{\tau}} \cdot \delta\varphi dA = 0, \\ G_p(\mathbf{u}, \delta p) &= \int_{\mathcal{B}} \left[\left(\frac{1}{M}(p - p_n) + B(J - J_n) - \Delta t \bar{r}_F \right) \delta p + (\Delta t \mathbf{K} \nabla p) \cdot \nabla \delta p \right] dV \\ &\quad + \int_{\partial_N\mathcal{B}} \bar{f} \delta p dA = 0, \\ G_d(\mathbf{u}, \delta d) &= \int_{\mathcal{B}} \left[\left(2\psi_c d + 2(d - 1)\mathcal{H} \right) \delta d + 2\psi_c l^2 \nabla d \cdot \nabla \delta d \right] dV = 0. \end{aligned} \quad (3.29)$$

Thus, the fully coupled variational multi-field problem to describe hydraulic fractures in porous media is formulated in (4.34). Following (4.34), the compact variational form for the hydraulic phase-field brittle fractures in porous media reads

$$G_{\mathbf{u}}(\mathbf{u}, \delta\mathbf{u}) = G_\varphi(\mathbf{u}, \delta\varphi) + G_p(\mathbf{u}, \delta p) + G_d(\mathbf{u}, \delta d) = 0 \quad \forall (\delta\varphi, \delta p, \delta d) \in (V_\varphi, V_p, V_d).$$

(3.30)

Next, we use (4.34) as a departure point for the Global-Local approach in Section 3.3.

3.3. Extension Towards Global-Local Formulations

The above introduced system of equations (4.34) for the coupled problem of poroelasticity at fracture will be solved using the Global-Local (GL) method in this section. GL formulation is rooted in the domain decomposition approach, see [146]. In comparison with already existing GL papers, this contribution represents an initial work to the use of GL approach at *large deformations* for solving hydraulic fracture mechanics problems numerically. The main objective here is to introduce an adoption of the hydraulic phase-field fracture formulation in poroelastic media within legacy codes which can be further employed for the industrial applications. To this end, the material body \mathcal{B} is decomposed

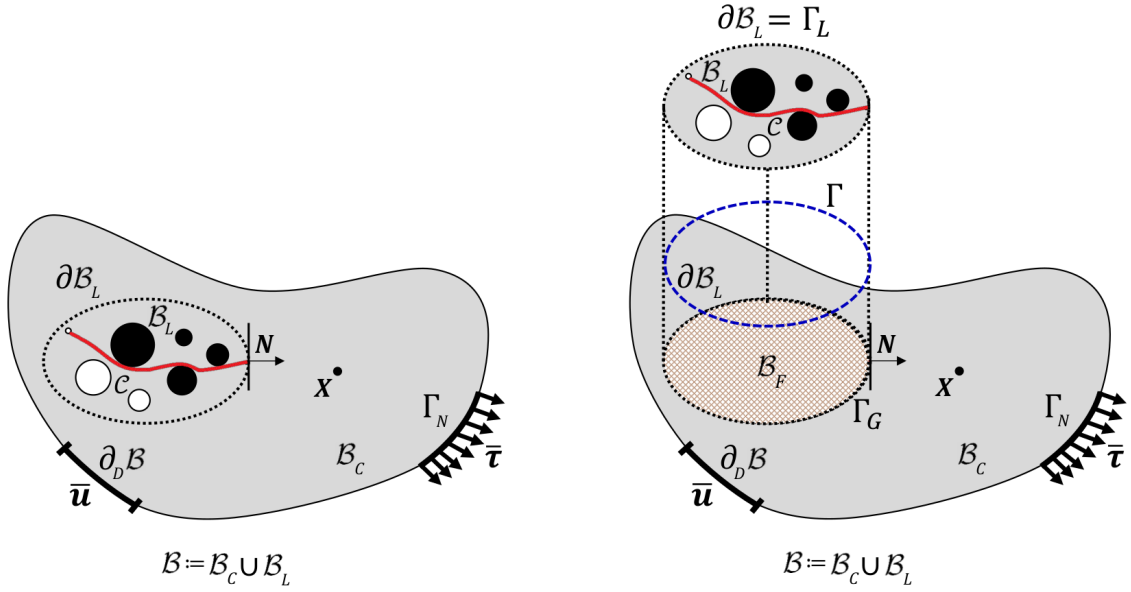


Figure 3.2: Description of the Global-Local setting. Left: Configuration and loading setup of the single-scale boundary value problem. Right: Global-Local Configuration, by means of the fictitious domain \mathcal{B}_F through filling the gap between \mathcal{B}_C and \mathcal{B}_L with a same constitutive modeling and discretization of \mathcal{B}_C such that its unification is so-called global domain $\mathcal{B}_G := \mathcal{B}_C \cup \Gamma_G \cup \mathcal{B}_F$.

into a global domain \mathcal{B}_G representing a poro-elastic media and a local domain \mathcal{B}_L reflecting the hydraulic fracturing (fracking) region. The global domain $\mathcal{B}_G := \mathcal{B}_C \cup \mathcal{B}_f \cup \Gamma_G$ is further split into a complementary domain \mathcal{B}_C corresponds to the intact area, a fictitious domain \mathcal{B}_f depicts a coarse representation of the local domain (in terms of the discretization) within the global domain and an interface Γ_G between the unfractured and the fractured domains. Hereby, the fictitious domain \mathcal{B}_f is defined as a prolongation of complementary domain towards \mathcal{B} . Hence it recovers the space of \mathcal{B} that is obtained by removing local domain from its continuum scale, see Fig. 3.2. As a result, same constitutive modeling and space discretization are used for both \mathcal{B}_f and \mathcal{B}_C , yielding $h_f := h_C$. The external loads are applied on \mathcal{B}_C and hence \mathcal{B}_L is assumed to be free from external loads.

At the interface Γ , the global $\Gamma_G \subset \mathcal{B}_G$ and local interfaces $\Gamma_L \subset \mathcal{B}_L$ are defined, such that in the continuum setting we have $\Gamma = \Gamma_G = \Gamma_L$. Thus, the deformation map φ and the fluid pressure p for both global and local domains do exactly coincide in the strong sense at interface, yielding

$$\varphi_L(\mathbf{X}, t) \stackrel{!}{=} \varphi_G(\mathbf{X}, t) \quad \text{and} \quad p_L(\mathbf{X}, t) \stackrel{!}{=} p_G(\mathbf{X}, t) \quad \text{at} \quad \mathbf{X} \in \Gamma. \quad (3.31)$$

Note that in a discrete setting we might face the situation that $\Gamma \neq \Gamma_G \neq \Gamma_L$ due to the two different discretization scheme within \mathcal{B}_G and \mathcal{B}_L leads to $h \neq h_L \neq h_G$ on Γ .

Remark 1: The strong primal continuity condition for the deformation/pressure given in Eq. 3.31 is too restrictive from the computational standpoint [120]. To resolve the crack phase-field quantity, it is demanding $h_L \ll h_G$. However, if we assume $\varphi_L \stackrel{!}{=} \varphi_G$

and $p_L \stackrel{!}{=} p_G$ on Γ , this yields $\Gamma_L = \Gamma_G$ in a discretized setting hence $h_L = h_G$ on Γ which contradicts $h_L \ll h_G$.

Formulation: Continuity conditions at interface Following Remark 1, we modify Eq. 3.31 in a strong sense by introducing the deformation $\varphi_\Gamma(\mathbf{X}, t)$ and pressure $p_\Gamma(\mathbf{X}, t)$ interface and their corresponding traction forces $\{\lambda_L^\varphi, \lambda_C^\varphi\}$ and $\{\lambda_L^p, \lambda_C^p\}$ that are introduced as Lagrange multipliers. This results in a set of equations at the interface as,

$$\left\{ \begin{array}{ll} \varphi_L(\mathbf{X}, t) = \varphi_\Gamma(\mathbf{X}, t) & \text{at } \mathbf{X} \in \Gamma_L, \\ \varphi_G(\mathbf{X}, t) = \varphi_\Gamma(\mathbf{X}, t) & \text{at } \mathbf{X} \in \Gamma_G, \\ \lambda_L^\varphi(\mathbf{X}, t) + \lambda_C^\varphi(\mathbf{X}, t) = \mathbf{0} & \text{at } \mathbf{X} \in \Gamma, \end{array} \right. \quad \text{and} \quad \left\{ \begin{array}{ll} p_L(\mathbf{X}, t) = p_\Gamma(\mathbf{X}, t) & \text{at } \mathbf{X} \in \Gamma_L, \\ p_G(\mathbf{X}, t) = p_\Gamma(\mathbf{X}, t) & \text{at } \mathbf{X} \in \Gamma_G, \\ \lambda_L^p(\mathbf{X}, t) + \lambda_C^p(\mathbf{X}, t) = 0 & \text{at } \mathbf{X} \in \Gamma. \end{array} \right. \quad (3.32)$$

Accordingly, the *single-scale* deformation map $\varphi(\mathbf{X}, t)$ and fluid pressure field $p(\mathbf{X}, t)$ in Section 3.2 are decomposed as follows

$$\varphi(\mathbf{X}, t) = \left\{ \begin{array}{ll} \varphi_L(\mathbf{X}, t) & \text{for } \mathbf{X} \in \mathcal{B}_L, \\ \varphi_G(\mathbf{X}, t) & \text{for } \mathbf{X} \in \mathcal{B}_G, \\ \varphi_\Gamma(\mathbf{X}, t) & \text{for } \mathbf{X} \in \Gamma, \end{array} \right. \quad \text{and} \quad p(\mathbf{X}, t) = \left\{ \begin{array}{ll} p_L(\mathbf{X}, t) & \text{for } \mathbf{X} \in \mathcal{B}_L, \\ p_G(\mathbf{X}, t) & \text{for } \mathbf{X} \in \mathcal{B}_G, \\ p_\Gamma(\mathbf{X}, t) & \text{for } \mathbf{X} \in \Gamma. \end{array} \right. \quad (3.33)$$

The fracture state is only resolve within \mathcal{B}_L . Hence, a scalar-valued function $d_L(\mathbf{X}, t) : \mathcal{B}_L \rightarrow [0, 1]$ is introduced in the \mathcal{B}_L . Hence, *single-scale phase-field* d is further decomposed which takes the following representation

$$d(\mathbf{X}, t) := \left\{ \begin{array}{ll} d_L & \text{for } \mathbf{X} \in \mathcal{B}_L, \\ 0 & \text{for } \mathbf{X} \in \mathcal{B}_G. \end{array} \right. \quad (3.34)$$

Now, the multi-physics problem for the Global-Local approach is described through eleven primary fields to characterize the hydro-poro-elasticity of fluid-saturated porous media at finite strains by

$$\text{Extended Primary Fields : } \mathfrak{P} := \{\varphi_G, \varphi_L, p_G, p_L, d_L, \lambda_C^\varphi, \lambda_L^\varphi, \lambda_C^p, \lambda_L^p, \varphi_\Gamma, p_\Gamma\}. \quad (3.35)$$

3.3.1. Governing formulations for the Global-Local coupling system. Based on the above introduced decompositions and the weak formulations outlined in (4.34), this section describes the GL weak forms of the PDEs for the coupled problem. The

global weak formulations of the deformation and pressure field take the form

$$\begin{aligned}
G_{\varphi_G}(\mathfrak{P}, \delta\varphi_G) &:= \int_{\mathcal{B}_G} \mathbf{P}(\nabla\varphi_G, p_G, 0) : \nabla\delta\varphi_G dV - \int_{\mathcal{B}_f} \mathbf{P}(\nabla\varphi_G, p_G, 0) : \nabla\delta\varphi_G dV \\
&\quad - \int_{\Gamma_G} \boldsymbol{\lambda}_C^\varphi \cdot \delta\varphi_G dA - \int_{\Gamma_{N,G}} \bar{\boldsymbol{\tau}} \cdot \delta\varphi_G dA = 0, \\
G_{p_G}(\mathfrak{P}, \delta p_G) &:= \int_{\mathcal{B}_G} \left[\frac{1}{M}(p_G - p_{G,n}) + B(J(\nabla\varphi_G) - J_n(\nabla\varphi_G)) \right] \delta p_G dV \\
&\quad + \int_{\mathcal{B}_G} \left[(\Delta t \mathbf{K}(\nabla\varphi_G, 0) \nabla p_G) \cdot \nabla \delta p_G \right] dV \\
&\quad - \int_{\mathcal{B}_f} \left[\frac{1}{M}(p_G - p_{G,n}) + B(J(\nabla\varphi_G) - J_n(\nabla\varphi_G)) + \Delta t \bar{r}_F \right] \delta p_G dV \\
&\quad - \int_{\mathcal{B}_f} \left[(\Delta t \mathbf{K}(\nabla\varphi_G, 0) \nabla p_G) \cdot \nabla \delta p_G \right] dV \\
&\quad - \int_{\Gamma_G} \lambda_C^p \delta p_G dA + \int_{\Gamma_{N,G}} \bar{f} \delta p_G dA = 0,
\end{aligned} \tag{G}$$

where $\delta\varphi_G \in \{\mathbf{H}^1(\mathcal{B}_G)^\delta : \delta\varphi_G = \mathbf{0} \text{ on } \partial_D \mathcal{B}\}$ and $\delta p_G \in \{H^1(\mathcal{B}_G) : \delta p_G = 0 \text{ on } \partial_D \mathcal{B}\}$ are the global test functions. Note that the pressure injection process of hydraulic fracturing \bar{r}_F exists only in the fictitious domain \mathcal{B}_f . The local weak formulations assumes the form

$$\begin{aligned}
G_{\varphi_L}(\mathfrak{P}, \delta\varphi_L) &:= \int_{\mathcal{B}_L} \mathbf{P}(\nabla\varphi_L, p_L, d_L) : \nabla\delta\varphi_L dV - \int_{\Gamma_L} \boldsymbol{\lambda}_L^\varphi \cdot \delta\varphi_L dA = 0, \\
G_{p_L}(\mathfrak{P}, \delta p_L) &:= \int_{\mathcal{B}_L} \left[\frac{1}{M}(p_L - p_{L,n}) + B(J(\nabla\varphi_L) - J_n(\nabla\varphi_L)) \right] \delta p_L dV \\
&\quad + \int_{\mathcal{B}_L} \left[(\Delta t \mathbf{K}(\nabla\varphi_L, d_L) \nabla p_L) \cdot \nabla \delta p_L \right] dV - \int_{\Gamma_L} \lambda_L^p \delta p_L dA = 0 \\
G_{d_L}(\mathfrak{P}, \delta d_L) &:= \int_{\mathcal{B}_L} \left[(2\psi_c d_L + 2(d_L - 1) \mathcal{H}(\nabla\varphi_L)) \delta d_L + 2\psi_c l^2 \nabla d_L \cdot \nabla \delta d_L \right] dV = 0,
\end{aligned} \tag{L}$$

where $\delta\varphi_L \in \mathbf{H}^1(\mathcal{B}_L)$, $\delta p_L \in H^1(\mathcal{B}_L)$ and $\delta d_L \in H^1(\mathcal{B}_L)$ are the local test functions with respect to the local deformation φ_L , local fluid pressure p_L and local crack phase-field d_L , respectively.

Next, we derive the weak formulations for the deformation and pressure continuity at interface Γ introduced in Formulation 3.1 by using a standard Galerkin procedure

$$G_{\varphi_\Gamma}(\mathfrak{P}, \delta\varphi_\Gamma) := \int_{\Gamma} (\boldsymbol{\lambda}_C^\varphi + \boldsymbol{\lambda}_L^\varphi) \cdot \delta\varphi_\Gamma dA = 0, \tag{C1}$$

$$G_{\lambda_C^\varphi}(\mathfrak{P}, \delta\lambda_C^\varphi) := \int_{\Gamma} (\varphi_\Gamma - \varphi_G) \cdot \delta\lambda_C^\varphi dA = 0, \tag{C2}$$

$$G_{\lambda_L^\varphi}(\mathfrak{P}, \delta\lambda_L^\varphi) := \int_{\Gamma} (\varphi_\Gamma - \varphi_L) \cdot \delta\lambda_L^\varphi dA = 0, \tag{C3}$$

$$G_{p_\Gamma}(\mathfrak{P}, \delta p_\Gamma) := \int_{\Gamma} (\lambda_C^p + \lambda_L^p) \delta p_\Gamma dA = 0, \tag{C4}$$

$$G_{\lambda_C^p}(\mathfrak{P}, \delta\lambda_C^p) := \int_{\Gamma} (p_{\Gamma} - p_G) \delta\lambda_C^p \, dA = 0, \quad (\text{C}_5)$$

$$G_{\lambda_L^p}(\mathfrak{P}, \delta\lambda_L^p) := \int_{\Gamma} (p_{\Gamma} - p_L) \delta\lambda_L^p \, dA = 0, \quad (\text{C}_6)$$

herein $\delta\varphi_{\Gamma} \in \mathbf{H}^1(\Gamma)$; $\delta p_{\Gamma} \in H^1(\Gamma)$; $\delta\lambda_C^{\varphi}, \delta\lambda_L^{\varphi} \in \mathbf{L}^2(\Gamma)$ and $\delta\lambda_C^p, \delta\lambda_L^p \in L^2(\Gamma)$ are the corresponding test functions. Equations (G), (L) and (C1)–(C6) specify the entire system of the Global-Local formulation.

3.3.2. Standard Dirichlet-Neumann boundary conditions. Two different ways exist to solve for the upper introduced system of equations, i.e. monolithic or staggered schemes. In this contribution, we employed the staggered method in the sense of alternate minimization [244] to find the stationary solution of the (G), (L) along with (C₁) – (C₆), see [143] based on non-intrusive Global-Local coupling scheme. To this end, let $k \geq 0$ be the Global-Local iteration index. Hence, the non-intrusive iterative solution scheme for GL computational framework at a fixed loading step n is accordingly computed by:

- Local Dirichlet problem: Equations to be solved are (L), (C₃) and (C₆)
- Pre-processing global level: Employing equations (C₁) and (C₄),
- Global Neumann problem: Equations to be solved are (G),
- Post-processing global level: Solving the last two equations (C₂) and (C₅).

By using this procedure for solving the system of equation, we unfortunately faced two difficulties that have to be resolved. (i) Because of the stiffness difference between local and fictitious domains, an acceleration/relaxation techniques must be utilized, as discussed in [143, 258]. (ii) Demanding an iterative GL scheme due to the imbalanced quantities of the deformation and pressure fields at the interface as

$$\int_{\Gamma} (\varphi_{\Gamma}^k - \varphi_L^k) \cdot \delta\lambda_L^{\varphi} \, dA \neq 0 \quad \text{and} \quad \int_{\Gamma} (p_{\Gamma}^k - p_L^k) \delta\lambda_L^p \, dA \neq 0, \quad (3.36)$$

These two difficulties have motivated us to develop alternative coupling conditions that resolve those challenges, which will be discussed next.

3.3.3. Robin-type boundary conditions. The aforementioned difficulties in the Global-Local formulation can be resolved using the Robin-type boundary conditions. As an outcome: (a) The stiff local response at the global level is relaxed; (b) the resolution of (3.36) is improved and (c) the computational time is remarkably reduced. The starting point for the construction of Robin-type boundary conditions are the coupling equations denoted in (C₁) – (C₆) arise from the continuity conditions at the interface in a strong sense. Those introduce the boundary conditions which have to be apply to the global and local domains for the consistent two-way coupling.

Robin-type boundary conditions at the local level.

Finite deformation. For the mechanical deformation field at the local level, a new coupling term is introduced as a combination of (C₁) and (C₂)

$$G_{\varphi_{\Gamma}}(\mathfrak{P}, \delta\varphi_{\Gamma}) + A_L^{\varphi} G_{\lambda_C^{\varphi}}(\mathfrak{P}, \delta\lambda_C^{\varphi}) = \int_{\Gamma} (\lambda_C^{\varphi} + \lambda_L^{\varphi}) \cdot \delta\varphi_{\Gamma} \, dA + A_L^{\varphi} \int_{\Gamma} (\varphi_{\Gamma} - \varphi_G) \cdot \delta\lambda_C^{\varphi} \, dA = 0 \quad (3.37)$$

Hence, for an iteration k (3.37) leads to

$$\int_{\Gamma} (\boldsymbol{\lambda}_C^{\varphi, k-1} + \boldsymbol{\lambda}_L^{\varphi, k}) \cdot \delta \boldsymbol{\varphi}_{\Gamma} \, dA + A_L^{\varphi} \int_{\Gamma} (\boldsymbol{\varphi}_{\Gamma}^{k, \frac{1}{2}} - \boldsymbol{\varphi}_G^{k-1}) \cdot \delta \boldsymbol{\lambda}_C^{\varphi} \, dA = 0. \quad (3.38)$$

Herein, A_L^{φ} is a local augmented stiffness matrix for the deformation which imposed along interface to permit a regularization of the local Jacobian matrix. By means of (3.38) at iteration k , the local system of equations for the mechanical problem at the interface (C₁) – (C₃) results in the following modified boundary conditions

$$\int_{\Gamma} \boldsymbol{\lambda}_L^{\varphi, k} \cdot \delta \boldsymbol{\varphi}_{\Gamma} \, dA + A_L^{\varphi} \int_{\Gamma} \boldsymbol{\varphi}_{\Gamma}^{k, \frac{1}{2}} \cdot \delta \boldsymbol{\lambda}_C^{\varphi} \, dA = \boldsymbol{\Lambda}_L^{\varphi, k-1}, \quad (\tilde{C}_1)$$

$$\int_{\Gamma} (\boldsymbol{\varphi}_{\Gamma}^{k, \frac{1}{2}} - \boldsymbol{\varphi}_L^k) \cdot \delta \boldsymbol{\lambda}_L^{\varphi} \, dA = 0, \quad (\tilde{C}_2)$$

with

$$\boldsymbol{\Lambda}_L^{\varphi, k-1} := \boldsymbol{\Lambda}_L(\boldsymbol{\lambda}_C^{\varphi, k-1}, \boldsymbol{\varphi}_G^{k-1}; A_L^{\varphi}) = A_L^{\varphi} \int_{\Gamma} \boldsymbol{\varphi}_G^{k-1} \cdot \delta \boldsymbol{\lambda}_C^{\varphi} \, dA - \int_{\Gamma} \boldsymbol{\lambda}_C^{\varphi, k-1} \cdot \delta \boldsymbol{\varphi}_{\Gamma} \, dA. \quad (3.39)$$

Fluid pressure. Analogously to the coupling terms for the deformation introduced above, we modify the local system of equations for the pressure field at the interface (C₄) – (C₆). It results in the following modified boundary conditions

$$\int_{\Gamma} \lambda_L^{p, k} \delta p_{\Gamma} \, dA + A_L^p \int_{\Gamma} p_{\Gamma}^{k, \frac{1}{2}} \delta \lambda_C^p \, dA = \Lambda_L^{p, k-1}, \quad (\tilde{C}_3)$$

$$\int_{\Gamma} (p_{\Gamma}^{k, \frac{1}{2}} - p_L^k) \delta \lambda_L^p \, dA = 0, \quad (\tilde{C}_4)$$

with

$$\Lambda_L^{p, k-1} := \Lambda_L(\lambda_C^{p, k-1}, p_G^{k-1}; A_L^p) = A_L^p \int_{\Gamma} p_G^{k-1} \delta \lambda_C^p \, dA - \int_{\Gamma} \lambda_C^{p, k-1} \delta p_{\Gamma} \, dA. \quad (3.40)$$

Together with (L), the local system of equations is solved for $(\boldsymbol{\varphi}_L^k, p_L^k, \boldsymbol{\lambda}_L^{\varphi, k}, \lambda_L^{p, k}, \boldsymbol{\varphi}_{\Gamma}^{k, \frac{1}{2}}, p_{\Gamma}^{k, \frac{1}{2}})$ for the given local Robin-type parameters $(\boldsymbol{\Lambda}_L^{\varphi, k-1}, \Lambda_L^{p, k-1}, A_L^{\varphi}, A_L^p)$.

Remark 2: *In the numerical implementation, the current local fields are computed based on the old global variables as history fields, see (3.38). Hereby, the deformation $\boldsymbol{\varphi}_{\Gamma}$ and fluid pressure p_{Γ} at the interface are updated at iteration $(k, \frac{1}{2})$. This choice is essential for the construction of the Robin-type boundary conditions. Note that, we proved in previous work that $\mathbf{u}_{\Gamma}^{(k, \frac{1}{2})} = \mathbf{u}_{\Gamma}^k$ with $\boldsymbol{\varphi} := \mathbf{u} + \mathbf{X}$ where \mathbf{X} is a fixed initial configuration, see [258]. With this prove at interface the continuity conditions are satisfied yielding a well posed problem and accelerate the convergence results. Note that other coupling conditions at the interface, i.e. updating the deformation and pressure at iteration k in (\tilde{C}_2) and (\tilde{C}_4) gives ill-posed problem due to the imposition of both Neumann and Dirichlet boundary conditions at same time at Γ .*

Robin-type boundary conditions at the global level.

Finite deformation. Accordingly, the new coupling boundary condition to be imposed at the global level is formulated by means of (C₁) and (C₃) for the mechanical deformation as

$$G_{\varphi_\Gamma}(\mathfrak{P}, \delta\varphi_\Gamma) + A_G^\varphi G_{\lambda_L^\varphi}(\mathfrak{P}, \delta\lambda_L^\varphi) = \int_\Gamma (\lambda_C^\varphi + \lambda_L^\varphi) \cdot \delta\varphi_\Gamma \, dA + A_G^\varphi \int_\Gamma (\varphi_\Gamma - \varphi_L) \cdot \delta\lambda_L^\varphi \, dA = 0, \quad (3.41)$$

such that for the iteration k (3.41) leads to

$$\int_\Gamma (\lambda_C^{\varphi,k} + \lambda_L^{\varphi,k}) \cdot \delta\varphi_\Gamma \, dA + A_G^\varphi \int_\Gamma (\varphi_\Gamma^k - \varphi_L^k) \cdot \delta\lambda_L^\varphi \, dA = 0, \quad (3.42)$$

where, A_G^φ is a global augmented stiffness matrix for the deformation imposed to the interface. By means of the (3.42), the Robin-type boundary condition at the global level follows

$$\int_\Gamma \lambda_C^{\varphi,k} \cdot \delta\varphi_\Gamma \, dA + A_G^\varphi \int_\Gamma \varphi_\Gamma^k \cdot \delta\lambda_L^\varphi \, dA = \Lambda_G^{\varphi,k}, \quad (\tilde{C}_5)$$

$$\int_\Gamma (\varphi_\Gamma^{k,\frac{1}{2}} - \varphi_G^k) \cdot \delta\lambda_C^\varphi \, dA = 0, \quad (\tilde{C}_6)$$

with

$$\Lambda_G^{\varphi,k} := \Lambda_G(\lambda_L^{\varphi,k}, \varphi_L^k; A_G^\varphi) = A_G^\varphi \int_\Gamma \varphi_L^k \cdot \delta\lambda_L^\varphi \, dA - \int_\Gamma \lambda_L^{\varphi,k} \cdot \delta\varphi_\Gamma \, dA. \quad (3.43)$$

Fluid pressure. Following the same procedure as above, the Robin-type boundary condition at the global level for the pressure field yields

$$\int_\Gamma \lambda_C^{p,k} \delta p_\Gamma \, dA + A_G^p \int_\Gamma p_\Gamma^k \delta\lambda_L^p \, dA = \Lambda_G^{p,k}, \quad (\tilde{C}_7)$$

$$\int_\Gamma (p_\Gamma^{k,\frac{1}{2}} - p_G^k) \delta\lambda_C^p \, dA = 0, \quad (\tilde{C}_8)$$

with

$$\Lambda_G^{p,k} := \Lambda_G(\lambda_L^{p,k}, p_L^k; A_G^p) = A_G^p \int_\Gamma p_L^k \delta\lambda_L^p \, dA - \int_\Gamma \lambda_L^{p,k} \delta p_\Gamma \, dA. \quad (3.44)$$

Together with (G), the global system of equations has to be solved for $(\varphi_G^k, p_G^k, \lambda_C^{\varphi,k}, \lambda_C^{p,k}, \varphi_\Gamma^k, p_\Gamma^k)$ for a given $(\Lambda_G^{\varphi,k}, \Lambda_G^{p,k}, A_G^\varphi, A_G^p, \varphi_\Gamma^{k,\frac{1}{2}}, p_\Gamma^{k,\frac{1}{2}})$. Here, $(A_G^\varphi, A_G^p, \Lambda_G^{\varphi,k}, \Lambda_G^{p,k})$ stand for global Robin-type parameters.

By means of the new coupling boundary conditions introduced in $(\tilde{C}_1) - (\tilde{C}_8)$ the imbalanced quantities in the Global-Local iterative framework are derived which read

$$\int_\Gamma (\varphi_\Gamma^k - \varphi_\Gamma^{k,\frac{1}{2}}) \cdot \delta\lambda_L^\varphi \, dA \neq 0 \quad \text{and} \quad \int_\Gamma (p_\Gamma^k - p_\Gamma^{k,\frac{1}{2}}) \delta\lambda_L^p \, dA \neq 0 \quad (3.45)$$

For the specific Robin-type boundary conditions, equation (3.45) can be resolved such that this term does not produce any accumulative error in the Global-Local iterative procedure,

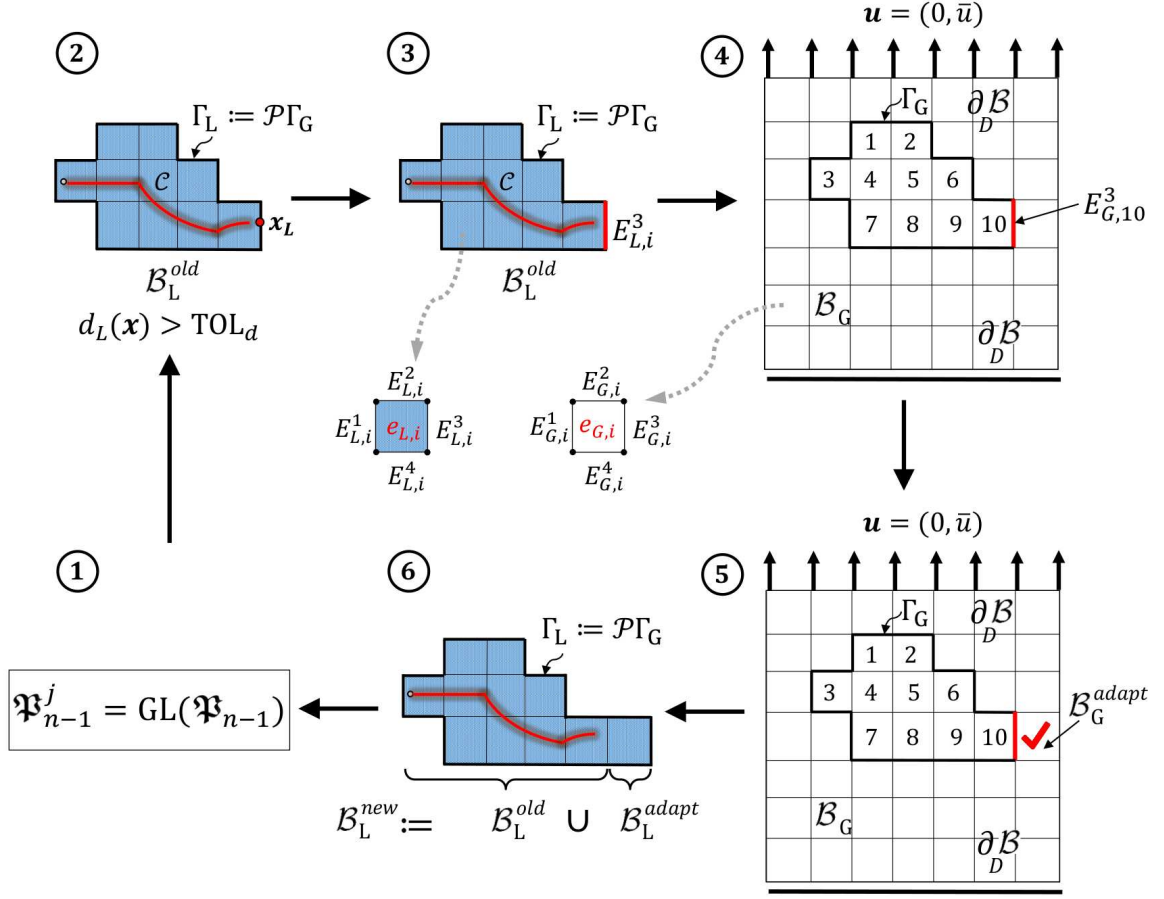


Figure 3.3: Description of the predictor-corrector mesh adaptivity scheme, introduced in [258].

see [258]. Thus, based on our recent work [258], the global and local augmented stiffness matrices \$(\mathbb{A}_G, \mathbb{A}_L)\$ for both, the deformation and pressure fields, within the Robin-type boundary conditions are given by

$$\boxed{\mathbb{A}_G = \mathbf{L}_L^T \mathbf{T}_L^{-T} \mathbf{S}_L \quad \text{and} \quad \mathbb{A}_L := \mathbf{S}_C.} \quad (3.46)$$

\mathbb{A}_G and \mathbb{A}_L can be seen as augmented stiffness matrices regularize the Jacobian stiffness matrix at the global and local levels, respectively. For details on the derivation of those matrices, we refer the interested reader to [258].

Remark 3: Note that the choice of the coupling equations \$(C_1) - (C_6)\$ at the local and global level for the Robin-type boundary conditions are the outcome of precise investigation of different combinations. However other choices are also possible, but one needs to adapt/derive the imbalance equations in (3.45) accordingly.

The detailed Global-Local scheme augmented with Robin-type boundary conditions is depicted in Algorithm 3.3. Basically, this type of formulation illustrates a generic two-scale finite element models to resolve the full non-linearities within the domain interest, i.e. \mathcal{B}_L and not necessarily entire domain.

Predictor-Corrector mesh adaptivity. To further reduce the computational time, an adaptive Global-Local approach is used. To this end, a predictor-Corrector mesh adaptivity is performed at t_n in Algorithm 3.3 [258]. By the adaptivity procedure, i.e. *dynamic allocation* of a local state, we mean: (a) to determine which global elements need to be refined; (b) to create the new fictitious and local domain, see Fig. 3.3; (c) to determine a new local interface; (d) to interpolate the old global solution. For details regarding the predictor-corrector adaptive scheme applied to the Global-Local formulation, we refer the interested reader to [162, 258] and Algorithm 2-3 therein.

3.4. Numerical Examples

This section demonstrates the performance of the proposed adaptive Global-Local approach applied to the phase-field modeling of hydraulic fracture in fluid-saturated porous media. Two numerical model problems for the GL formulations are investigated. A considerable reduction of the computational cost (up to 100 times) is observed in comparison with the single-scale solution. The material parameters used in both examples are listed in Table 6.1 and based on [234, 336]. For the numerical simulation all variables in both, the global and local domains, are discretized by bilinear quadrilateral $Q1$ finite elements.

3.4.1. Hydraulically induced crack driven by fluid volume injection. In the first numerical example, a boundary value problem applied to the square plate is shown in Fig. 3.4(a). We set $A = 40 \text{ m}$ hence $\mathcal{B} = (0, 80)^2 \text{ m}^2$ that includes a predefined single notch \mathcal{C}_1 of length 8 m in the body center with $a = (36, 40) \text{ m}$ and $b = (44, 40) \text{ m}$, as depicted in Fig. 3.4(a). A constant fluid flow of $\bar{f} = 0.002 \text{ m}^2/\text{s}$ is injected in \mathcal{C}_1 . At the boundary $\partial_D \mathcal{B}$, all the displacements are fixed in both directions and the fluid pressure is set to zero. Fluid injection \bar{f} continues until failure for $T = 49 \text{ s}$ with time step $\Delta t = 0.1 \text{ s}$ during the simulation.

We start our analysis by illustrating the single-scale results for different deformations states up to final failure related to Fig. 3.4(a). The vertical displacement u_y (first row), fluid pressure p (second row) and crack phase-field d (third row) evolutions are demonstrated in Figure 3.6 for four time steps [$t = 1.8; 6.5; 20; 48.5 \text{ s}$]. The crack initiates at the notch-tips due to fluid pressure increase until a threshold energy ψ_c is reached. Thereafter, the crack propagates horizontally in two directions towards the boundaries. In the

Table 3.1: Material parameters used in the numerical examples based on [234, 336].

No.	Parameter	Name	Value	Unit
1.	E	Young's modulus	15.96	GPa
2.	ν	Poisson's ratio	0.2	–
3.	M	Biot's modulus	12.5	GPa
4.	B	Biot's coefficient	0.79	–
5.	K	Intrinsic permeability	2×10^{-14}	m^2
6.	K_c	Spatial permeability in fracture	83.3	$\text{m}^3\text{s}/\text{kg}$
7.	ζ	Permeability transition exponent	50	–
8.	η_F	Dynamic fluid viscosity	1×10^{-3}	$\text{kg}/(\text{m}\cdot\text{s})$
9.	σ_c	Critical effective stress	0.005	GPa

Table 3.2: Example1. Time and degrees of freedoms comparison between the single-scale and GL problems for different reservoir's size.

Size of reservoir	Accumulated time, <i>sec.</i>			Total Degrees of freedoms	
	single-scale	g/l	ratio	single-scale	g/l
Small	1.9752e+04	849.0794	23.2632	87723	18315
Medium	6.2474e+04	862.3567	72.4453	171366	18665
Large	1.0559e+05	887.2200	119.0169	256035	19109

fractured zone, p is almost constant due to the increased permeability inside the crack. Whereas, low fluid pressure in the surrounding is observed due the chosen small time-step in comparison with the permeability of the porous medium, as outlined in [234]. The fluid pressure drops down while the crack propagates further as shown in Figure 3.6 (second row, middle states). Then, p increases again due to the prescribed fixed boundary conditions $\partial_D \mathcal{B}$, see Fig. 3.6 (second row, last state).

Next the performance of the Global-Local approach related to Fig. 3.4(a) is investigated. To this end, the evolution of the vertical displacement u_y (first row), fluid pressure

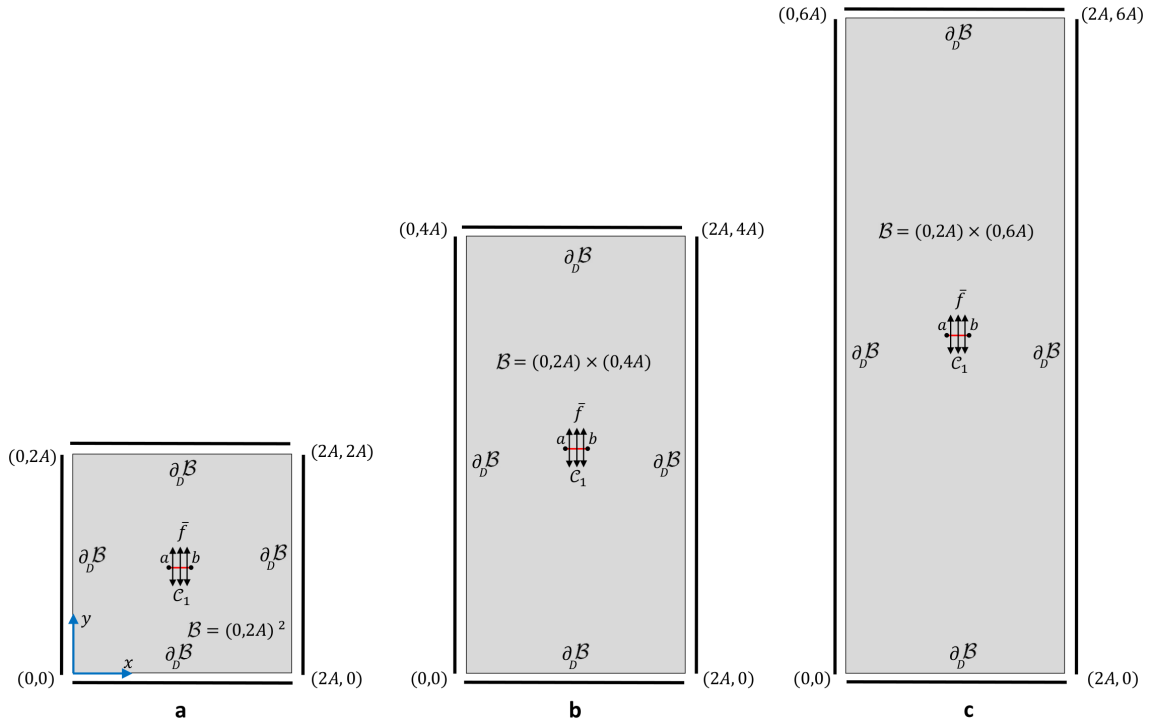


Figure 3.4: Example 1. Hydraulically induced crack driven by fluid volume injection. Three different geometries with their boundary conditions and described crack phase-field d as a Dirichlet boundary conditions at $t = 0$ s. (a) Small size specimen with $\mathcal{B} = (0, 80) \times (0, 80) \text{ m}^2$ such that $a = (36, 40) \text{ m}$ and $b = (44, 40) \text{ m}$ to compare the GL results with standard reference works e.g. [234]. Medium size with $\mathcal{B} = (0, 80) \times (0, 160) \text{ m}^2$ such that $a = (36, 80) \text{ m}$ and $b = (44, 80) \text{ m}$ in (b) and large size structure with $\mathcal{B} = (0, 80) \times (0, 240) \text{ m}^2$ such that $a = (36, 120) \text{ m}$ and $b = (44, 120) \text{ m}$ in (c) to illustrate the efficient performance of the Global-Local approach.

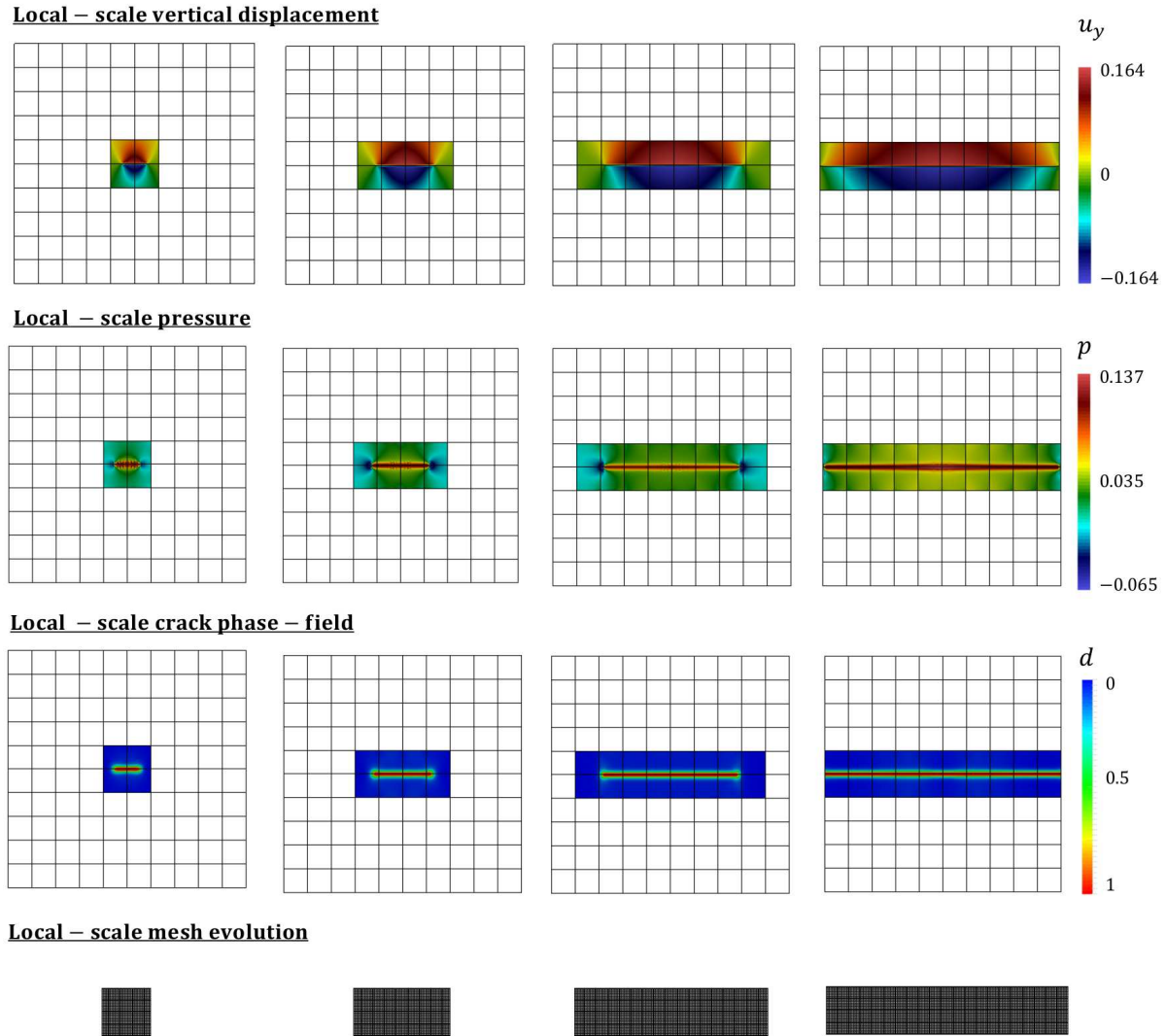


Figure 3.5: Example 1. Local-scale results of the hydraulically induced crack driven by fluid volume injection. Evolution of the vertical displacement u_y (first row), fluid pressure p (second row), crack phase-field d (third row) and local domain (fourth row) for different fluid injection time steps at $[t = 1.8; 6.5; 20; 48.5 \text{ s}]$ up to final failure.

p (second row), crack phase-field d (third row) and local domain (fourth row) for different fluid injection time steps $t = 1.8; 6.5; 20; 48.5 \text{ s}$ are demonstrated in Fig. 3.5 for the local-scale and in Fig. 3.7 for the homogenized global scale. Hereby, even with less number of elements at the global domain the overall response is qualitatively in a good agreement with the single-scale domain.

Figure 3.8a describes the maximum injected fluid pressure within the crack region versus the fluid injection time. For a comparison purpose, the Global-Local and single-scale solutions are both provided related to Fig. 3.4(a). The results obtained from Global-Local formulation are in a good agreement with the single-scale solution. Furthermore, it is noted that the injected fluid pressure increases within the crack region before it reaches to the peak point. Thereafter, as expected a drop of the fluid pressure is observed.

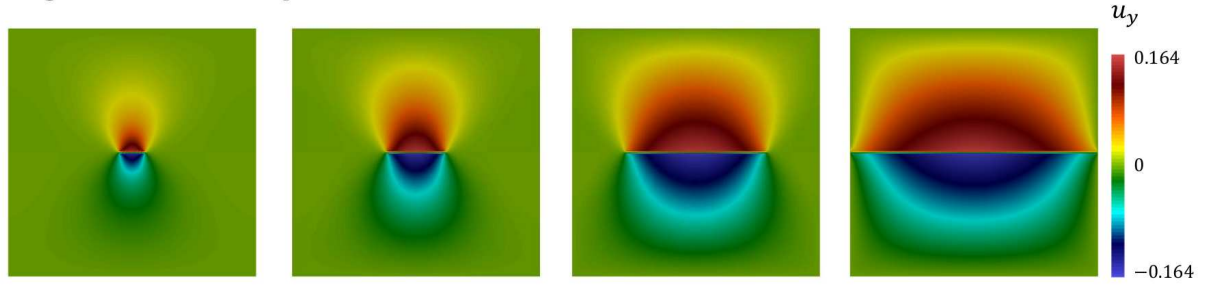
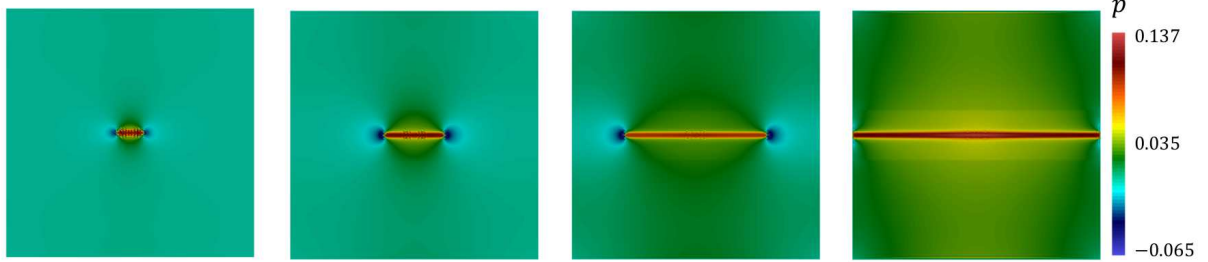
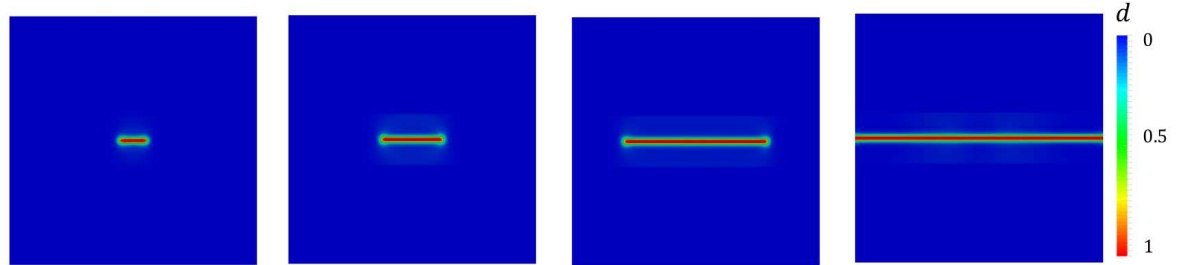
Single – scale vertical displacement**Single – scale pressure****Single – scale crack phase – field**

Figure 3.6: Example 1. Single-scale results of the hydraulically induced crack driven by fluid volume injection. Evolution of the vertical displacement u_y (first row), fluid pressure p (second row) and crack phase-field d (third row) for different deformation stages up to final failure at $[t = 1.8; 6.5; 20; 48.5 \text{ s}]$.

To illustrate the efficiency of the predictor-corrector adaptive scheme, we plot in 3.8b the corresponding accumulative computational time and in Fig. 3.9a the total number of unknowns (local and global problems) versus the fluid injection time and compared with the single-scale problem. It can be observed that the total accumulated time for the Global-Local formulations took 849 s whereas the single-scale simulation took 19752 s. Hence, Global-Local formulations performs 23.3 times faster for the small size specimen in Fig. 3.4(a).

Furthermore, for each jump in Fig. 3.9a, the predictor-corrector adaptive scheme is active and applied on the Global-Local scheme which increases the number of degrees of freedoms. At the complete failure state of Fig. 3.4(a), i.e. $t = 48.5 \text{ s}$, the total number of local nodes, elements and the degrees of freedoms are 5985, 5780 and 17955, respectively for the Global-Local formulations. Whereas for the single-scale the number of nodes, elements and the degrees of freedoms are 29241, 28900 and 87723, respectively. Hence, the Global-Local approach leads to significantly less degrees of freedom, as shown in Fig. 3.9a versus single-scale model.

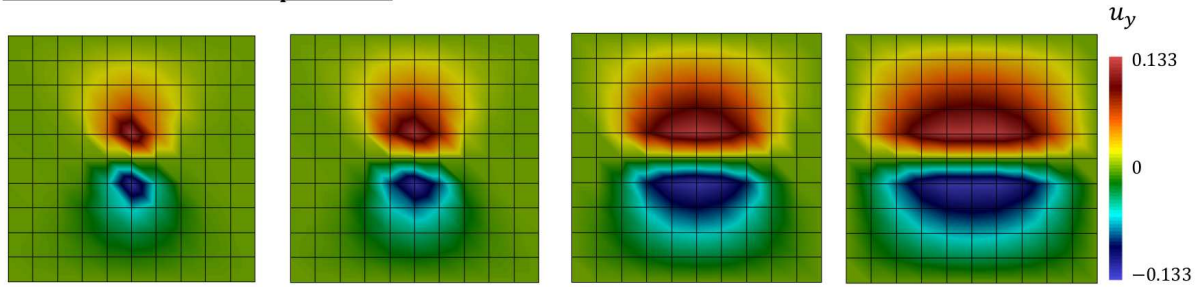
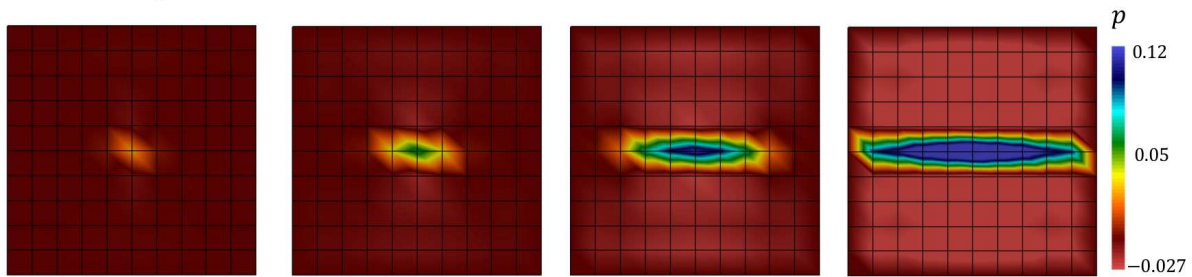
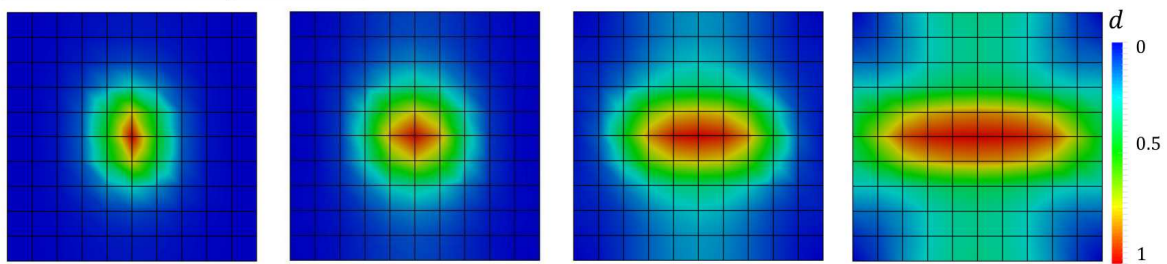
Global – scale vertical displacement**Global – scale pressure****Global – scale crack phase – field**

Figure 3.7: Example 1. Global-scale results of the hydraulically induced crack driven by fluid volume injection. Evolution of the vertical displacement u_y (first row), fluid pressure p (second row) and crack phase-field d (third row) for different deformation stages up to final failure at $t = 1.8; 6.5; 20; 48.5$ s.

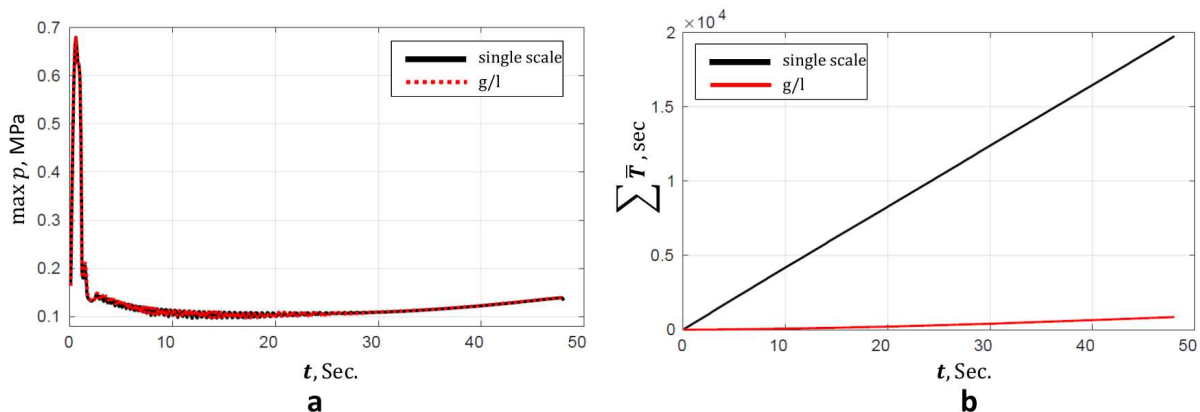


Figure 3.8: Example 1. Hydraulically induced crack driven by fluid volume injection. (a) Fluid pressure p within the crack region versus injection time; and (b) computational time-injection time curves in terms of the accumulated time.

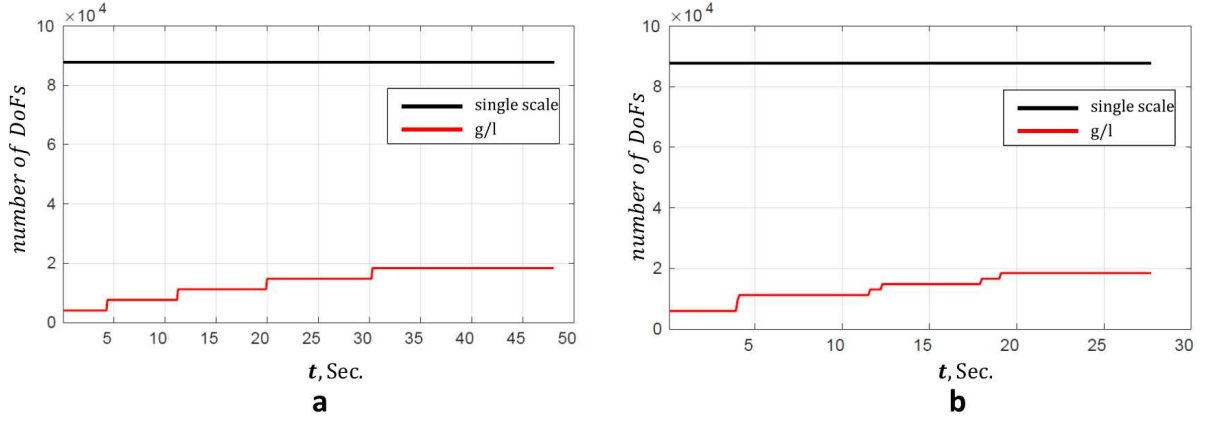


Figure 3.9: Number of degrees of freedom for the single scale problem and Global-Local formulation. (a) Example 1; and (b) Example 2.

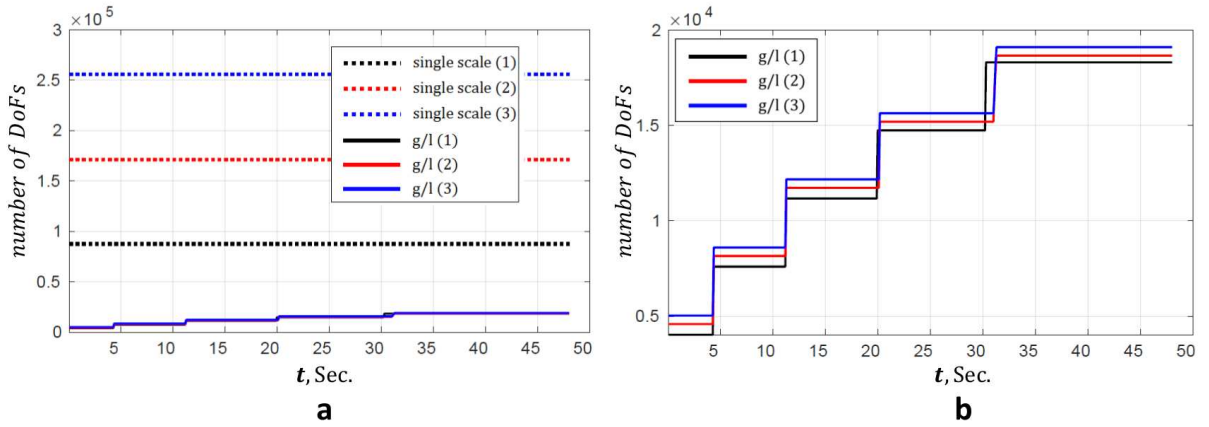


Figure 3.10: Example 1. Degrees of freedom DoFs comparison between the single scale problem and the Global-Local formulation for three different reservoir's size in (a). For better illustration of the GL performance, a zoom of the corresponding DoFs is depicted in (b).

For precise description of the efficient computations using the Global-Local technique, the above analyzed geometry is further extended to two larger scale structure as shown in Fig. 3.4(b)-(c). To this end, three different geometries having same local domain (heterogeneity/fracture patterns) are compared to demonstrate the powerful performance of the proposed Global-Local method. The geometrical configuration set for small size specimen with $\mathcal{B} = (0, 80) \times (0, 80) m^2$ such that $a = (36, 40) m$ and $b = (44, 40) m$. Medium size with $\mathcal{B} = (0, 80) \times (0, 160) m^2$ such that $a = (36, 80) m$ and $b = (44, 80) m$ in Fig. 3.4(b) and large size structure with $\mathcal{B} = (0, 80) \times (0, 240) m^2$ such that $a = (36, 120) m$ and $b = (44, 120) m$ in Fig. 3.4(c).

The outcome results are depicted in Fig 3.10 and Fig 3.11, representing the accumulated time and degrees of freedoms comparison between the single-scale and GL problems for three different reservoir's size (small, medium and large). As a summary, Table 3.2 compares all results related to Fig. 3.4. These results evidently highlight the potential of the Global-Local approach to treat large-scale problems.

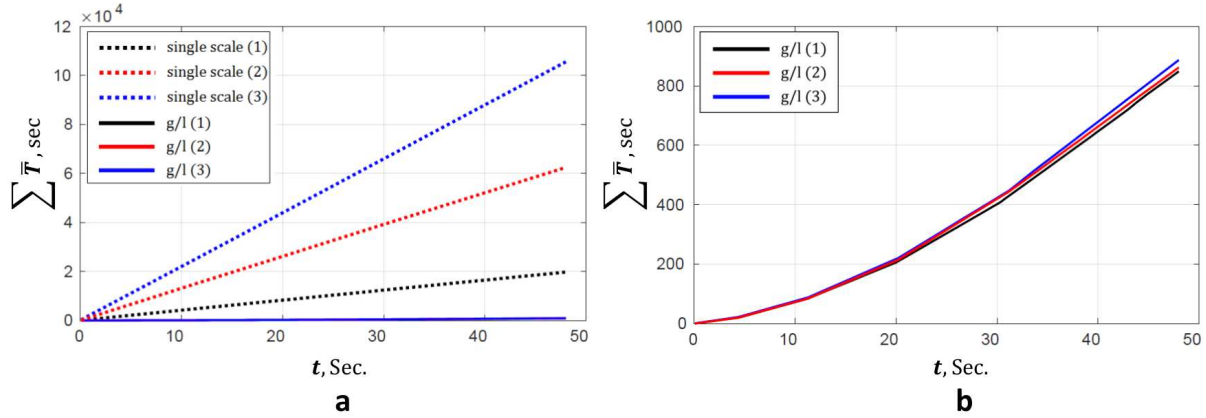


Figure 3.11: Example 1. Accumulated real computational time comparison between the single scale problem and the Global-Local formulation for three different reservoir's size in (a). For better illustration of the GL performance, a zoom of the corresponding computational-injection time curves is depicted in (b).

3.4.2. Joining of two cracks driven by fluid volume injection. The second example is concerned with the capability of the proposed GL approach for handling *coalescence* and *merging* of *crack paths* in the local domains. Crack-initiation and curved-crack-propagation, representing a mixed-mode fracture, are predicted with a Global-Local formulation.

The geometrical setup and the loading conditions of the specimen is similar to the benchmark problem of [313] and depicted in Fig. 3.12. We keep all parameters and loading as in the previous example. The first crack \mathcal{C}_1 is located near the middle of the domain with coordinates $a = (28, 40)$ and $b = (36, 40)$. The second crack \mathcal{C}_2 is vertically-oriented at $n = (50, 44)$ and $m = (50, 36)$ with a distance of 14 m from \mathcal{C}_1 . A constant fluid flow of $\bar{f} = 0.002 \text{ m}^2/\text{s}$ is injected in \mathcal{C}_1 and \mathcal{C}_2 as sketched in Fig. 3.12. At the boundary $\partial_D \mathcal{B}$, all the displacements are fixed in both directions and the fluid pressure is set to zero. Fluid injection \bar{f} continues until failure for $T = 28 \text{ s}$ with time step $\Delta t = 0.1 \text{ s}$ during the simulation. The total number of elements for the single-scale problem is 28900 elements and for Global domain is 100 elements. The number of elements for the local

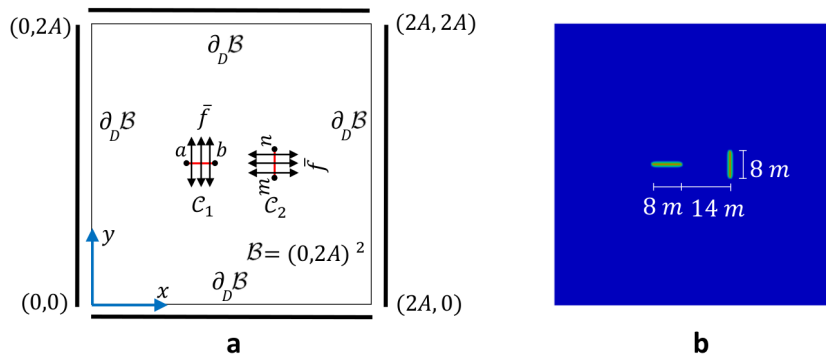


Figure 3.12: Example 2: Joining of two cracks driven by fluid volume injection. (a) Geometry and boundary conditions; and (b) described crack phase-field d as a Dirichlet boundary conditions at $t = 0 \text{ s}$.

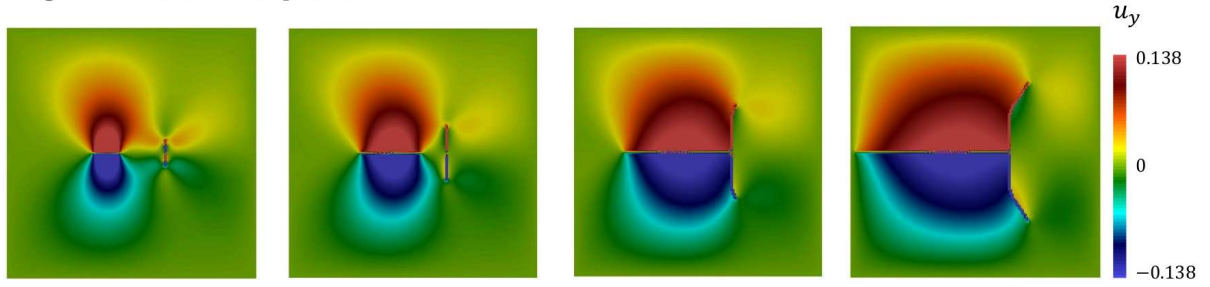
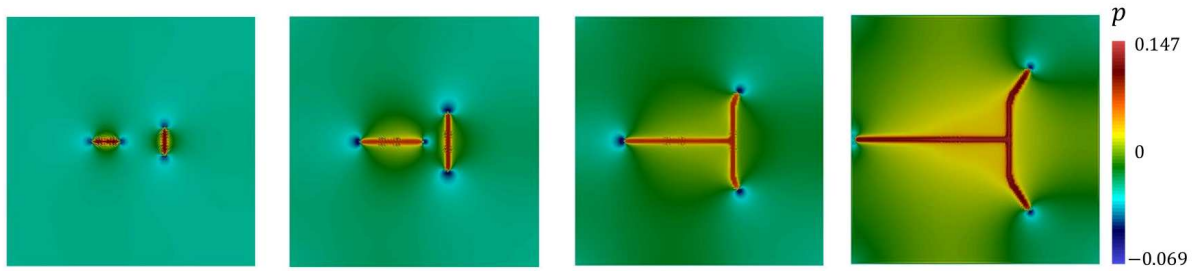
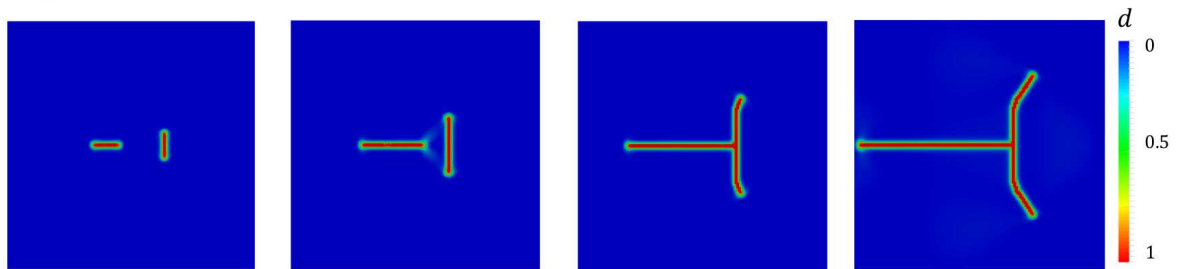
Single – scale vertical displacement**Single – scale pressure****Single – scale crack phase – field**

Figure 3.13: Example 2. Single-scale results of the joining cracks driven by fluid volume injection. Evolution of the vertical displacement u_y (first row), fluid pressure p (second row) and crack phase-field d (third row) for different deformation stages up to final failure at $[t = 1.8; 6.5; 13.5; 27.7 \text{ s}]$.

domain is determined based on predictor-corrector mesh adaptivity.

Figure 3.13 shows the evolutions of the fluid pressure p (first row) and the crack phase-field d (second row) for the single-scale problem at different times $[t = 1.8; 6.5; 13.5; 27.7 \text{ s}]$. Here the crack propagates from the notches. We again observe nearly constant fluid pressure in the fractured area ($d = 1$), whereas outside the crack zone p is much lower, see 3.12 (first row).

The local-scale results with the corresponding mesh are depicted in Fig. 3.14 for different fluid injection stages. Hereby, the vertical displacement u_y (first row), fluid pressure p (second row), crack phase-field d (third row) and local domain (fourth row) evolutions of the Global-Local formulation are demonstrated in Fig. 3.14 for four time steps $[t = 1.8; 6.5; 13.5; 27.7 \text{ s}]$. It is remarkably observed that the Global-Local approach augmented with predictor-corrector mesh adaptivity leads to the optimum number of elements to be used for the simulation, hence reducing additional cost. Additionally, note that extending the reservoir domain will significantly increase the computational cost for the single-scale problem (due to increase the number of elements) but this will not

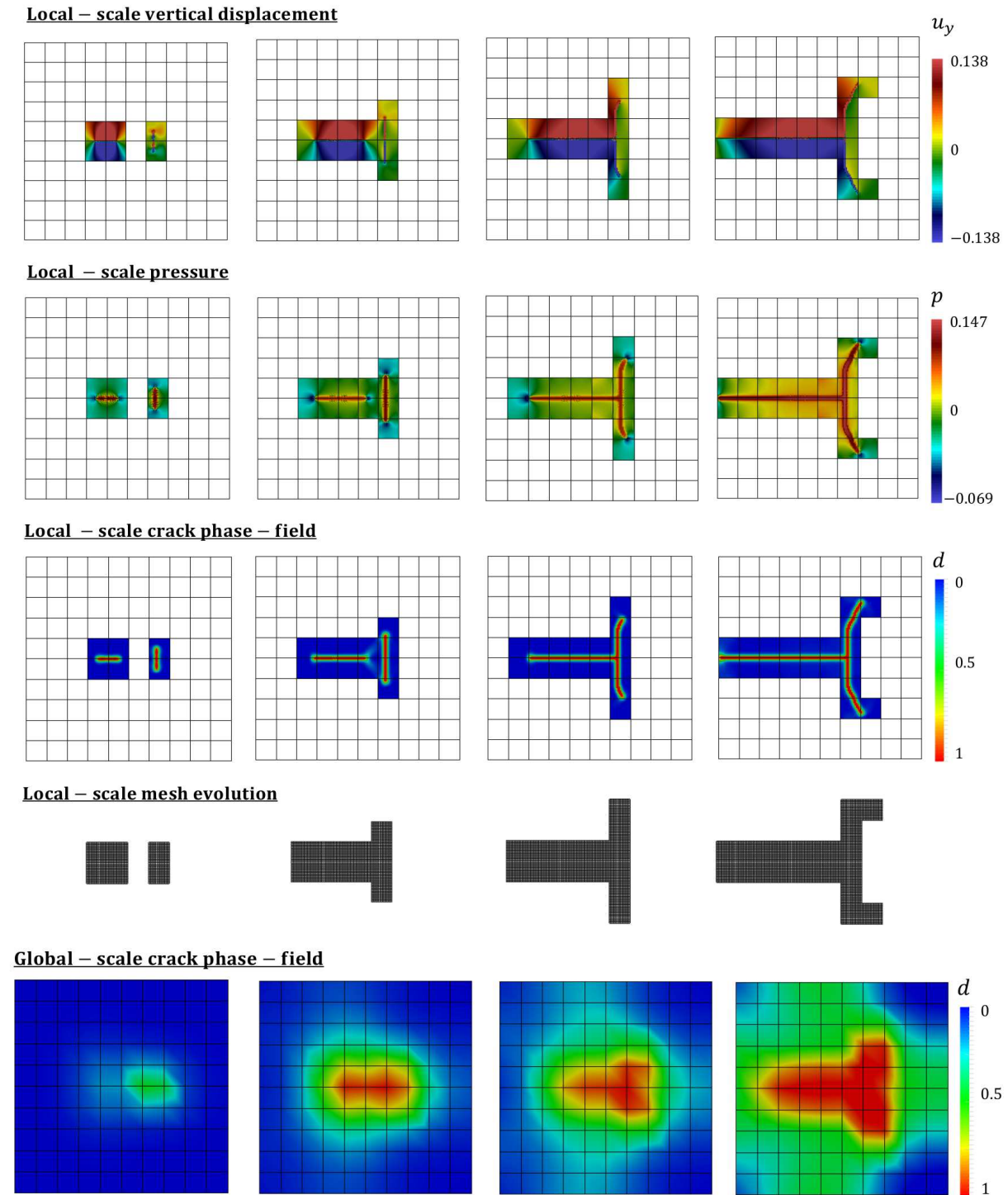


Figure 3.14: Example 2. Global-Local scale results of the joining cracks driven by fluid volume injection. Evolution of the vertical displacement u_y (first row), fluid pressure p (second row), local crack phase-field d (third row), local domain (fourth row) and global phase-field (fifth row) for different deformation stages up to final failure at $[t = 1.8; 6.5; 13.5; 27.7 \text{ s}]$.

change the computational cost for Global-Local formulation, thus applicable for the real large structure, as documented in Table 3.2. Therefore, localize effect (crack phase-field)

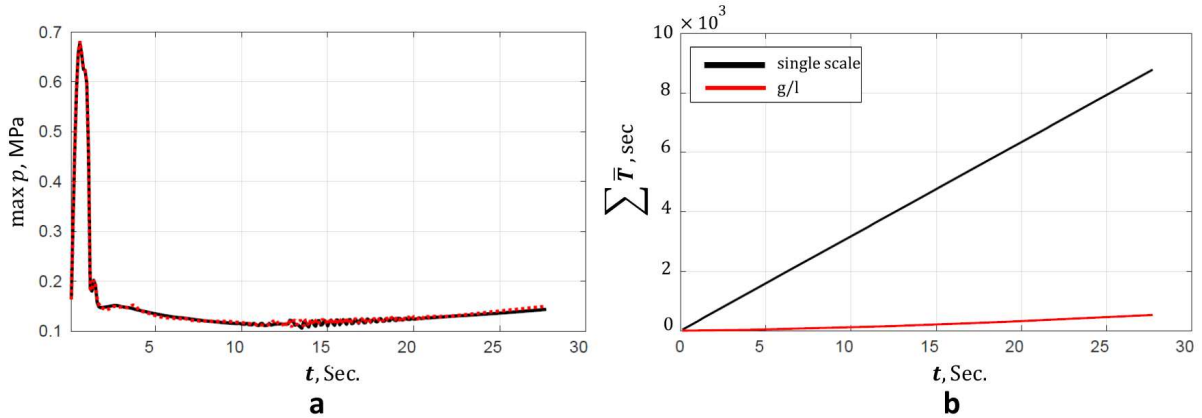


Figure 3.15: Example 2. Joining of two cracks driven by fluid volume injection. (a) Fluid pressure p within the crack region versus injection time; and (b) computational time-injection time curves in terms of the accumulated time.

which increase the computational cost is only considered within local domain and hence globally reduce the computational time. Another advantage of using the GL formulation is its capability of capturing the crack initiation and propagation at the homogenized global scale even with less number of elements as illustrated in Fig. 3.14 (fifth row).

Next, the maximum injected fluid pressure within the crack region is analyzed versus the fluid injection time in Figure 3.15a. The results obtained from Global-Local formulation are in a good agreement with the single scale solution. Figure 3.15b represents the corresponding accumulative computational time (i.e. CPU simulation time), per injection fluid time. In this study, we observed that the total accumulated time for the GL approach took 529 s whereas the single-scale problem took 8784 s. Hence, Global-Local formulations performs 16.6 times faster.

Finally, Fig. 3.9b demonstrates the total number of degrees of freedoms versus the fluid injection time for GL scheme and the single-scale problem. At the complete failure state, i.e. $t = 27.7$ sec, the total number of local nodes, elements and the degrees of freedoms for the GL method are 6036, 5780 and 18108, respectively. Whereas for the single-scale formulation the number of nodes, elements and the degrees of freedoms are 29241, 28900 and 87723, respectively. Thus the Global-Local approach requires significantly less degrees of freedom.

Algorithm 3.3: Global-Local iterative scheme combined with Robin-type BCs.**Input:** loading data $(\bar{\varphi}_n, \bar{p}_n)$ on $\partial_D \mathcal{B}$;solution $\mathfrak{P}_{n-1} := (\varphi_{G,n-1}, p_{G,n-1}, \varphi_{L,n-1}, p_{L,n-1}, d_{L,n-1}, \varphi_{\Gamma,n-1}, p_{\Gamma,n-1}, \lambda_{C,n-1}^\varphi, \lambda_{L,n-1}^\varphi, \lambda_{C,n-1}^p, \lambda_{L,n-1}^p)$ and $\mathcal{H}_{L,n-1}$ from step $n-1$.**Global-Local iteration** $k \geq 1$:Local boundary value problem:

- given $\mathbb{A}_L^\varphi, \mathbb{A}_L^p, \Lambda_L^{\varphi,k-1}, \Lambda_L^{p,k-1}, \mathcal{H}_{L,n-1}$; solve

$$\text{phase-field part: } \int_{\mathcal{B}_L} \left[(2\psi_c d_L + 2(d_L - 1) \mathcal{H}(\nabla \varphi_L)) \delta d_L + 2\psi_c l^2 \nabla d_L \cdot \nabla \delta d_L \right] dV = 0,$$

mechanical part:

$$\left\{ \begin{array}{l} \int_{\mathcal{B}_L} \mathbf{P}(\nabla \varphi_L, p_L, d_L) : \nabla \delta \varphi_L dV - \int_{\Gamma_L} \lambda_L^\varphi \cdot \delta \varphi_G dA = 0, \\ \int_{\Gamma} \lambda_L^\varphi \cdot \delta \varphi_\Gamma dA + \mathbb{A}_L^\varphi \int_{\Gamma} \varphi_\Gamma \cdot \delta \lambda_C^\varphi dA = \Lambda_L^{\varphi,k-1} \quad \text{and} \quad \int_{\Gamma} (\varphi_\Gamma - \varphi_L) \cdot \delta \lambda_L^\varphi dA = 0, \end{array} \right.$$

fluid pressure:

$$\left\{ \begin{array}{l} \int_{\mathcal{B}_L} \left[\frac{1}{M} (p_L - p_{L,n}) + B \left(J(\nabla \varphi_L) - J_n(\nabla \varphi_L) \right) \right] \delta p_L dV \\ + \int_{\mathcal{B}_L} \left[(\Delta t \mathbf{K}(\nabla \varphi_L, d_L) \nabla p_L) \cdot \nabla \delta p_L \right] dV - \int_{\Gamma_L} \lambda_L^p \delta p_L dA = 0, \\ \int_{\Gamma} \lambda_L^p \delta p_\Gamma dA + \mathbb{A}_L^p \int_{\Gamma} p_\Gamma \delta \lambda_C^p dA = \Lambda_L^{p,k-1} \quad \text{and} \quad \int_{\Gamma} (p_\Gamma - p_L) \delta \lambda_L^p dA = 0, \end{array} \right.$$

$$\text{set } (\varphi_L, p_L, d_L, \varphi_\Gamma, p_\Gamma, \lambda_L^\varphi, \lambda_L^p) := (\varphi_L^k, p_L^k, d_L^k, \varphi_\Gamma^{k, \frac{1}{2}}, p_\Gamma^{k, \frac{1}{2}}, \lambda_L^{\varphi,k}, \lambda_L^{p,k}),$$

- given $(\varphi_L^k, p_L^k, \lambda_L^{\varphi,k}, \lambda_L^{p,k}; \mathbb{A}_G^\varphi, \mathbb{A}_G^p)$, set

$$\Lambda_G^{\varphi,k} = \mathbb{A}_G^\varphi \int_{\Gamma} \varphi_L^k \cdot \delta \lambda_C^\varphi dA - \int_{\Gamma} \lambda_L^{\varphi,k} \cdot \delta \varphi_\Gamma dA; \quad \Lambda_G^{p,k} = \mathbb{A}_G^p \int_{\Gamma} p_L^k \delta \lambda_C^p dA - \int_{\Gamma} \lambda_L^{p,k} \delta p_\Gamma dA.$$

Global boundary value problem:

- given $\mathbb{A}_G^\varphi, \mathbb{A}_G^p, \Lambda_G^{\varphi,k}, \Lambda_G^{p,k}, \varphi_\Gamma^{k, \frac{1}{2}}, p_\Gamma^{k, \frac{1}{2}}$, solve

mechanical part:

$$\left\{ \begin{array}{l} \int_{\mathcal{B}_G} \mathbf{P}(\nabla \varphi_G, p_G, 0) : \nabla \delta \varphi_G dV - \int_{\mathcal{B}_f} \mathbf{P}(\nabla \varphi_G, p_G, 0) : \nabla \delta \varphi_G dV \\ - \int_{\Gamma} \lambda_C^\varphi \cdot \delta \varphi_G dA - \int_{\Gamma_N} \bar{\tau} \cdot \delta \varphi_G dA = 0, \\ \int_{\Gamma} \lambda_C^\varphi \cdot \delta \varphi_\Gamma dA + \mathbb{A}_G^\varphi \int_{\Gamma} \varphi_\Gamma \cdot \delta \lambda_L^\varphi dA = \Lambda_G^{\varphi,k} \quad \text{and} \quad \int_{\Gamma} (\varphi_\Gamma^{k, \frac{1}{2}} - \varphi_G) \cdot \delta \lambda_C^\varphi dA = 0, \end{array} \right.$$

fluid pressure:

$$\left\{ \begin{array}{l} \int_{\mathcal{B}_G} \left[\frac{1}{M} (p_G - p_{G,n}) + B \left(J(\nabla \varphi_G) - J_n(\nabla \varphi_G) \right) \right] \delta p_G dV - \int_{\Gamma} \lambda_C^p \delta p_G dA \\ + \int_{\mathcal{B}_G} \left[(\Delta t \mathbf{K}(\nabla \varphi_G) \nabla p_G) \cdot \nabla \delta p_G \right] dV - \int_{\mathcal{B}_f} \left[\frac{1}{M} (p_G - p_{G,n}) + B \left(J(\nabla \varphi_G) \right. \right. \\ \left. \left. - J_n(\nabla \varphi_G) \right) \right] \delta p_G dV - \int_{\mathcal{B}_f} \left[(\Delta t \mathbf{K}(\nabla \varphi_G) \nabla p_G) \cdot \nabla \delta p_G + \Delta t \bar{r}_F \right] dV + \int_{\Gamma_N} \bar{f} \delta p_G dA = 0, \\ \int_{\Gamma} \lambda_C^p \delta p_\Gamma dA + \mathbb{A}_G^p \int_{\Gamma} p_\Gamma \delta \lambda_L^p dA = \Lambda_G^{p,k} \quad \text{and} \quad \int_{\Gamma} (p_\Gamma^{k, \frac{1}{2}} - p_G) \delta \lambda_C^p dA = 0, \end{array} \right.$$

$$\text{set } (\varphi_G, p_G, \varphi_\Gamma, p_\Gamma, \lambda_C^\varphi, \lambda_C^p) := (\varphi_G^k, p_G^k, \varphi_\Gamma^k, p_\Gamma^k, \lambda_C^{\varphi,k}, \lambda_C^{p,k}),$$

- given $(\varphi_G^k, p_G^k, \lambda_C^{\varphi,k}, \lambda_C^{p,k}; \mathbb{A}_L^\varphi, \mathbb{A}_L^p)$, set

$$\Lambda_L^{\varphi,k} = \mathbb{A}_L^\varphi \int_{\Gamma} \varphi_G^k \cdot \delta \lambda_C^\varphi dA - \int_{\Gamma} \lambda_C^{\varphi,k} \cdot \delta \mathbf{m}_u \Gamma dA \quad \text{and} \quad \Lambda_L^{p,k} = \mathbb{A}_L^p \int_{\Gamma} p_G^k \delta \lambda_C^p dA - \int_{\Gamma} \lambda_C^{p,k} \delta p_\Gamma dA.$$

- if fulfilled, set $\mathfrak{P}^k := \mathfrak{P}_n$ and stop;
else $k+1 \rightarrow k$.

Output: solution \mathfrak{P}_n and $\mathcal{H}_{L,n}$.

4. A microscale model for failure in poro-elasto-plastic media

This chapter provides a micromechanical framework for modeling water-induced failure mechanisms of concrete in an experimental-virtual lab. The complicated geometry and content of concrete at a lower scale can be detected by a computed tomography (micro-CT) scan. Based on the experimental observations, we developed a constitutive model for the coupled problem of fluid-saturated heterogeneous porous media at fracture. The poro-plasticity model is additively decomposed into *reversible-elastic* and *irreversible-plastic* parts. The governing formulations are based on an energetic response function and a dissipated work due to plasticity (Drucker-Prager model), fluid transport (Darcy's law) and fracture (phase-field method) for the multiphysics problem. The model performance is demonstrated through some representative examples in 2D, representing an idealized microstructure of concrete. The contents of this chapter is based on the following publication ALDAKHEEL [12].

4.1. Introduction

Concrete is one of the most cost-efficient and durable construction materials in the world. Its range of applications has been enlarged widely in recent decades. Hence, nowadays the computational mechanics of concrete has become a very active research field with various geotechnical engineering applications. Within a multiscale point of view, concrete is considered as an over-complex system of solid skeletons (e.g. cement paste and stones), fluid bulk phases (e.g. water), pores with a high degree of heterogeneity. At the macroscopic level (m) it consists of a homogeneous material, whereas on the mesoscale (mm) various stone (aggregates) sizes distributed in a matrix of cement paste and surrounded by an interfacial transition zone (ITZ) are observed. On the microlevel (μm), this matrix is further decomposed into hydrated and unreacted phases, water/air pores (capillary/gel pores) whereas at the nanoscale (nm) these phases have complicated structure (Figure 4.1).

A great number of macro-meso-micro-nano-mechanically motivated approaches exist in the literature to model concrete failure behavior, see for example [319, 217, 282, 78, 334, 291, 264, 153, 180, 306, 208, 103, 346, 281, 137] and the citations therein. This work focuses on analyzing the concrete fracture processes at the *microscale* leading to accurate material descriptions and a better understanding of the failure mechanism at the macroscale. Consequently, a micromechanical formulation of a fully saturated porous media at fracture is developed within this contribution. Hence various effects must be considered for investigating failure response at the microlevel, i.e. modeling the two solid skeletons (hydrated cement paste and unhydrated clinker particles), fluid bulk phases (water/air) and their interaction, see [269, 263].

Several efforts can be found in the literature to study the fracture mechanism of concrete microstructure. In this regard, [282] developed a lattice model for simulating the micromechanical failure analysis of concrete. Hereby, the material is modeled as a lattice of brittle-breaking beam elements. Their fracture law was extremely simple with few parameters. Here, upon exceeding the maximum strength of a beam element, it will be removed from the mesh. [172] proposed a continuum thermodynamical approach for studying microstructure effects on the nonlinear fracture behavior of concrete. An idealized 2D random multi-cracked granular composite was considered numerically at the microscale. Moreover, viscoelasticity and kinetic energy effects were further investigated.

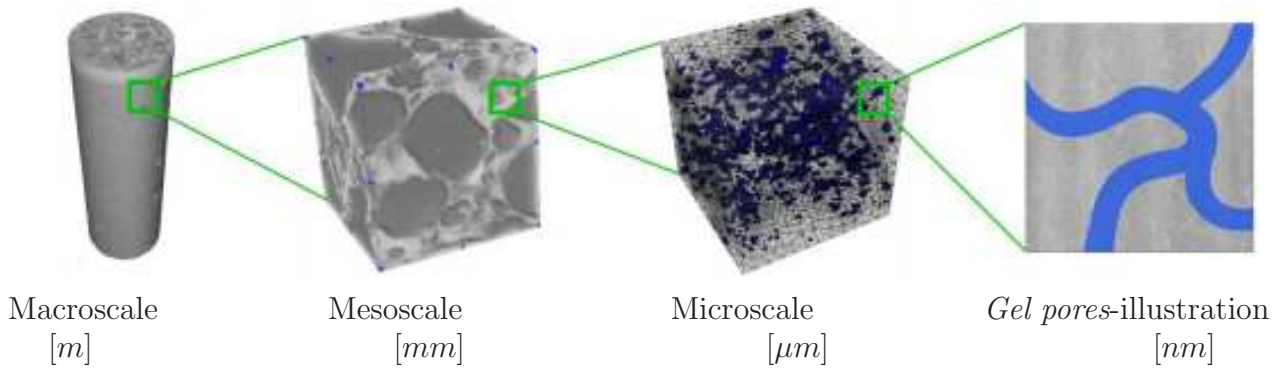


Figure 4.1: Representation of the various scales in concrete from the macrostructure to the nanostructure level.

In [152] a computational homogenization of hardened cement paste (HCP) was introduced including a thermomechanically coupled finite element model. Their model is capable of describing damage due to frost using results obtained from the microstructural analysis. The microscopic investigations were performed for different moistures, temperatures and micro-structures hence a temperature-moisture-damage correlation was obtained. [209] introduces an experimental procedure for micromechanical testing of consecutive layers in cement paste. The obtained properties were used directly as an input for numerical simulation of fracture behavior of cement paste at the microlevel. Recently [156] investigated issues on the characterization of cement paste microstructures from μ -CT and virtual experiment framework for evaluating mechanical properties. Thereby, a crack phase-field model for simulating crack propagation was used to evaluate the stiffness and tensile strength of cement paste microstructures and the evaluated properties were linked to the proposed characterization parameters.

Most of the above-mentioned approaches are based on dry geometries (Dried case D) which are stored and tested in the air to analyze concrete damage processes. However, specimens that are submerged in water (directly after the concreting process and during testing), representing a water-saturated concrete structure (Wet case W), have a significantly lower failure resistance than dry specimens. This phenomenon was recognized in the past (e.g. in offshore vs. onshore wind turbines), but how the moisture content in the concrete microstructure influences its resistance against fracture is still unknown. This has motivated [303] to study the influence of water-induced damage mechanisms on fatigue deterioration of high-strength concrete. A numerical model based on those experimental data was developed in [15]. This was achieved by employing a phase-field approach for hydraulic fracture in poro-elastic media. The outcome results stemmed out from the DFG-Priority Program SPP 2020 "Cyclic Damage Processes in High-Performance Concretes in the Experimental Virtual Lab". Herein, the constitutive formulations based on the assumption that the solid skeleton (matrix) at the micro-level is homogeneous and solely consists of cement paste. Furthermore, no inelastic material behavior is considered in the modeling. Such a choice neglects the experimentally observed plastic deformations and the two solid phases at the microscale. The goal of this work is to present a theoretical and a computationally efficient framework for modeling concrete microscopic failure in poro-elasto-plastic media based on experimental observations.

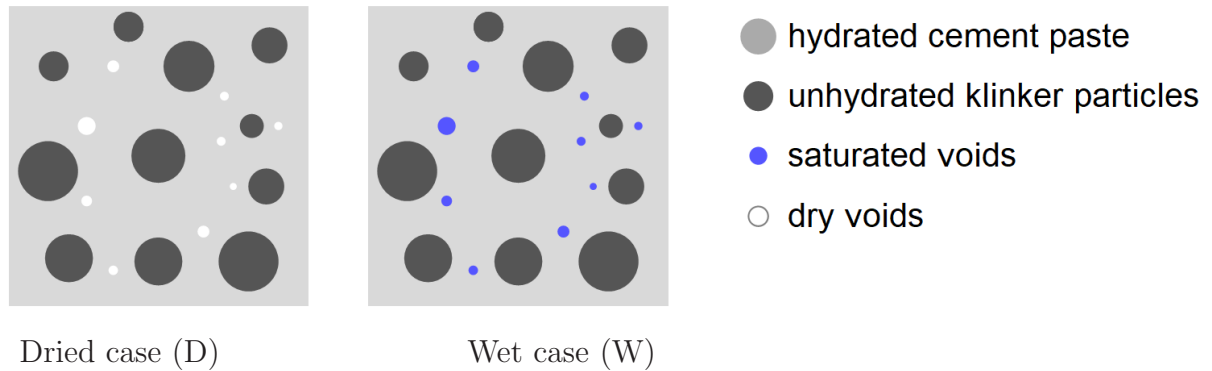


Figure 4.2: Definition of the concrete idealized microstructure.

The simulation of fracture processes in porous media at the micrometer length-scale is achieved by utilizing the continuum phase-field method PFM, which is based on the regularization of sharp crack discontinuities. This avoids the use of complex discretization methods for crack discontinuities and can account for multi-branched cracks within the solid skeleton. In recent years, several brittle [188, 162, 259, 270, 6, 285, 258, 160, 79, 295, 80, 119, 17] and ductile [10, 22, 64, 19, 4, 110, 86, 108, 8, 190, 118, 186, 253, 104] phase-field fracture formulations have been proposed in the literature. These studies range from the modeling of 2D/3D small and large strain deformations, variational formulations, multi-scale/physics problems, mathematical analysis, different decompositions and discretization techniques with many applications in science and engineering. All these examples and the citation therein demonstrate the potential of phase-field for crack propagation. Regarding the plastic deformations, a modified associated Drucker-Prager-type DP yield criterion function suitable for a wide range of applications in geotechnical and civil engineering is developed in line with [5, 112, 178, 34]. To eliminate the singularity at the peak of the cone, an additional term in the yield function is introduced which based on a constant perturbation-type parameter, see [193, 5]. For the modeling of fluid transport at the microscale, we assume laminar flow described by the Stokes equation which can be linked to Darcy’s law in porous media. A review on the foundations and applications of porous materials can be seen in the pioneering works [58, 93, 99, 114, 283, 214]. The coupling between those porous-media models and the DP elasto-plasticity formulations at failure are based on an energetic and a dissipative response functions for plasticity, fluid flow and fracture. On the computational side, a robust and efficient monolithic scheme is employed in the numerical implementation to compute the unknowns (*displacement, fluid pressure and crack phase-field*) using the software tool ACEFEM, see [184].

The Chapter is organized as follows: Section 4.2 outlines the experimental observations. In Section 4.3 the governing equations for the coupled problem are described. Next, the weak formulations are derived in Section 4.4. Finally, some numerical tests are carried out to substantiate our algorithmic developments in Section 4.5.

4.2. Experimental investigation and geometrical set-up

The motivation behind this work emerges from the experimental observations of [303] under the DFG-Priority Program SPP 2020 ”*Cyclic Damage Processes in High-Performance Concretes in the Experimental-Virtual Lab*”. Hence, we focus in the presented contribution on the numerical aspects at the micro-scale based on detailed microstructural data.

To this end, a micro-computed tomography (μ -CT) scan has been conducted, as shown in Figure 4.1. For comparison purposes, two different storage conditions are utilized in this study:

- Dried case (D): it contains test specimens, that dried at 105 ± 5 °C in a drying chamber to a constant mass.
- Wet case (W): it represents a water-saturated concrete structure. The test specimens are permanently (directly after the concreting process and during testing) submerged in water.

At the microscale, we distinguish between two types of pores in the concrete (W) specimen, visualized in blue color in Figure 4.2 as

- *Capillary pores*: It ranges between ($30nm - 100\mu m$) and developed because of stoichiometrically unnecessary water. For bigger capillary pores water can evaporate (depends on boundary conditions).
- *Gel pores*: It ranges between ($0.1nm - 30nm$) and arises from the chemistry of the hydration process. A graphical interpretation of the gel pores at the nanoscale level are given in Figure 4.1.

These CT-scan (.stl file) data are then transferred into a virtual element (**VEM**) mesh [332, 170] or a finite element (FEM) mesh [345, 323] for numerical analysis. Material properties of the matrix are obtained through nano-indentation techniques at the Institute of Continuum Mechanics IKM. For more details on the experimental set-up, we refer the interested reader to [303, 339].

Note that, our emphasis in this chapter is on results (i) *demonstrating the constitutive framework* and (ii) *highlighting the influence of water-induced damage mechanics* of our proposed concrete model at the microscale. Thus, the formulation performance will be demonstrated utilizing some representative examples in two-dimensional case representing an idealized microstructure of concrete, as plotted in Figure 4.2. A rigorous numerical analysis in 3D must be left for future work.

4.3. Governing equations for the multi-field problem

This section outlines a theory of fracture in poro-elasto-plastic media under fully saturated conditions. The constitutive formulations are based on three governing equations for the mechanical deformation, fluid pressure and the crack phase-field. Strong and weak formulations of the multi-physics problem are introduced.

4.3.1. Basic kinematics and constitutive formulation. Consider $\mathcal{B} \in \mathcal{R}^\delta$ to be a material body and denote $\partial\mathcal{B}$ as its boundary with dimension $\delta = 2, 3$ in space and time $t \in \mathcal{T} = [0, T]$. We assume Dirichlet boundary conditions on $\partial_D\mathcal{B}$ and Neumann conditions on $\partial_N\mathcal{B}$, as illustrated in Figure 4.3. The concrete microscopic boundary value problem for the coupled problem of fluid-saturated heterogeneous porous media at fracture is a coupled three-field problem. It is characterized at material points $\mathbf{x} \in \mathcal{B}$

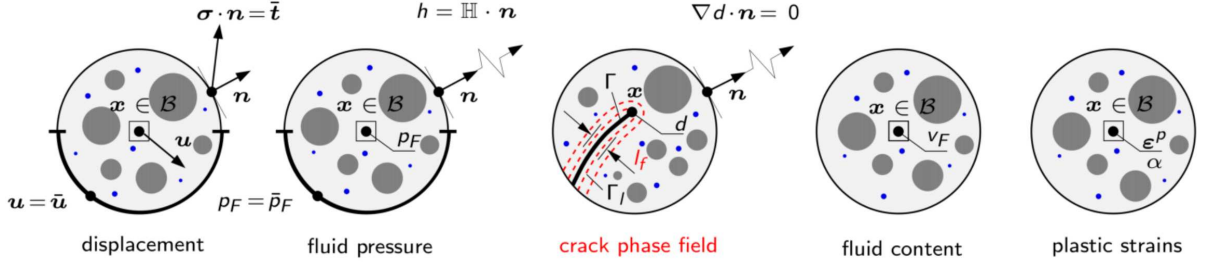


Figure 4.3: Primary fields and boundary conditions for the concrete specimen at the microstructure. Light gray color refers to the hydrated cement paste, dark gray color stands for the unhydrated clinker particles, blue color depicts the water and red color represents the regularized crack.

by the displacement field of the solid \mathbf{u} , the pressure field p_F and the crack phase-field d defined as

$$\mathbf{u} : \begin{cases} \mathcal{B} \times \mathcal{T} \rightarrow \mathcal{R}^\delta \\ (\mathbf{x}, t) \mapsto \mathbf{u}(\mathbf{x}, t) \end{cases} \quad ; \quad p_F : \begin{cases} \mathcal{B} \times \mathcal{T} \rightarrow \mathcal{R} \\ (\mathbf{x}, t) \mapsto p_F(\mathbf{x}, t) \end{cases} \quad ; \quad d : \begin{cases} \mathcal{B} \times \mathcal{T} \rightarrow [0, 1] \\ (\mathbf{x}, t) \mapsto d(\mathbf{x}, t) \end{cases}, \quad (4.1)$$

with $d \geq 0$ where $d(\mathbf{x}, t) = 0$ represents the unbroken state of the solid matrix (light gray regions) and $d(\mathbf{x}, t) = 1$ refers to the fully fractured solid matrix (red region), as sketched in Figure 4.3.

The gradient of the displacement field defines the symmetric strain tensor of the solid skeleton as

$$\boldsymbol{\varepsilon} = \text{sym}[\nabla \mathbf{u}] := \frac{1}{2}[\nabla \mathbf{u} + \nabla \mathbf{u}^T]. \quad (4.2)$$

The solid is loaded by prescribed deformations and external traction on the boundary, defined by time-dependent Dirichlet- and Neumann conditions

$$\mathbf{u} = \bar{\mathbf{u}}(\mathbf{x}, t) \text{ on } \partial_D \mathcal{B} \quad \text{and} \quad \boldsymbol{\sigma} \cdot \mathbf{n} = \bar{\mathbf{t}}(\mathbf{x}, t) \text{ on } \partial_N \mathcal{B}, \quad (4.3)$$

where \mathbf{n} is the outward unit normal vector and $\bar{\mathbf{t}}$ is the prescribed traction vector at the solid surface $\partial \mathcal{B}$. The stress tensor $\boldsymbol{\sigma}$ is the thermodynamic dual to $\boldsymbol{\varepsilon}$. To account for plastic deformations with isotropic hardening/softening response, we define the symmetric plastic strain tensor $\boldsymbol{\varepsilon}^p$ and the equivalent plastic strain α as

$$\boldsymbol{\varepsilon}^p : \begin{cases} \mathcal{B} \times \mathcal{T} \rightarrow \mathcal{R}^6 \\ (\mathbf{x}, t) \mapsto \boldsymbol{\varepsilon}^p(\mathbf{x}, t) \end{cases} \quad ; \quad \alpha : \begin{cases} \mathcal{B} \times \mathcal{T} \rightarrow \mathcal{R} \\ (\mathbf{x}, t) \mapsto \alpha(\mathbf{x}, t) \end{cases} \quad (4.4)$$

with

$$\boldsymbol{\varepsilon}^p(\mathbf{x}, 0) = \mathbf{0} \quad \text{and} \quad \alpha(\mathbf{x}, 0) = 0, \quad (4.5)$$

representing the *first* and the *second local internal variables* (history fields) of the solid, as plotted in Figure 4.3. In small strain setting, the elastic strain tensor is obtained in an additive format from the total strain $\boldsymbol{\varepsilon}$ and the plastic strain tensor $\boldsymbol{\varepsilon}^p$, yields

$$\boldsymbol{\varepsilon}^e = \boldsymbol{\varepsilon} - \boldsymbol{\varepsilon}^p. \quad (4.6)$$

Remark 1:

Regarding the concrete solid skeleton at the microscale, only the hydrated cement paste undergoes elastic-plastic-fracture deformations. Whereas the unhydrated clinker particles are stiff, i.e. almost two to three times stiffer than the hydrated phase, as experimentally documented in [106]. Hence the unhydrated phase is modeled as an elastic material. Furthermore, no interfacial transition zone (ITZ) is observed between those phases in contrast to the mesoscale case.

The solid skeleton has to satisfy the equation of equilibrium, representing the *first* partial differential equation PDE for the coupled problem as

$$\boxed{\operatorname{div} \boldsymbol{\sigma} + \bar{\mathbf{b}} = \mathbf{0}} \quad (4.7)$$

where dynamic effects are neglected and $\bar{\mathbf{b}}$ is the given body force.

For the constitutive modeling of poro-mechanics, the fluid pressure p_F in (4.1)₂ derives the evolution of the fluid volume ratio v_F which is defined as

$$v_F : \begin{cases} \mathcal{B} \times \mathcal{T} \rightarrow \mathcal{R} \\ (\mathbf{x}, t) \mapsto v_F(\mathbf{x}, t) \end{cases} \quad (4.8)$$

herein, the fluid volume ratio describes the *third local internal* variable, as demonstrated in Figure 4.3. The boundary conditions for the pressure are determined as follows

$$p_F = \bar{p}_F(\mathbf{x}, t) \text{ on } \partial_D \mathcal{B} \quad \text{and} \quad \mathbb{H} \cdot \mathbf{n} = h(\mathbf{x}, t) \text{ on } \partial_N \mathcal{B}, \quad (4.9)$$

in terms of the fluid volume flux vector \mathbb{H} , the prescribed fluid pressure \bar{p}_F and the fluid transport h . The initial condition for the fluid volume ratio is set $v_F(\mathbf{x}, 0) = n_F$ equal to the initial porosity in \mathcal{B} .

Remark 2:

For the initial condition of the fluid content in such a closed system, we assume two water sources at the microscale:

- Capillary pores (saturated voids),
- Water in the gel pores as a homogenized quantity by zooming further in the hydrated cement paste, see Figure 4.1.

The fluid flux vector in (4.9)₂ is linked to the negative gradient of the fluid pressure via the permeability, according to Darcy-type fluid transport as

$$\mathbb{H} := -\mathbf{k}(\boldsymbol{\varepsilon}, d) \nabla p_F, \quad (4.10)$$

where the permeability tensor \mathbf{k} depends on the total strain $\boldsymbol{\varepsilon}$ and the crack phase-field d . It is decomposed into a *Darcy-type flow for an unbroken porous medium* \mathbf{k}_{Darcy} and a *Poiseuille-type flow in a fully fractured material* \mathbf{k}_{frac} defined as

$$\mathbf{k}(\boldsymbol{\varepsilon}, d) = \mathbf{k}_{Darcy} + d^\zeta \mathbf{k}_{frac}(\boldsymbol{\varepsilon}) \quad \text{with} \quad \mathbf{k}_{Darcy} = \frac{k}{\eta_F} \mathbf{1} \quad \text{and} \quad \mathbf{k}_{frac} = k_c \omega^2 [\mathbf{1} - \mathbf{N} \otimes \mathbf{N}] \quad (4.11)$$

as outlined in [15, 236, 161], where k is the intrinsic permeability in an isotropic pore space, $\mathbf{N} = \nabla d / \|\nabla d\|$ is the unit normal to the crack surface Γ , η_F is the dynamic fluid viscosity, $\zeta \geq 1$ is a permeability transition exponent, k_c is the spatial permeability in fracture and $\mathbf{1}$ is the identity tensor. An estimation for the crack width is provided by $\omega = (\mathbf{N} \cdot \boldsymbol{\varepsilon} \mathbf{N}) h_e$ in terms of the characteristic element length h_e . The fluid has to satisfy the balance of fluid mass, reflecting the *second* PDE for the coupled problem as

$$\dot{v}_F + \text{div}[\mathbb{H}] = 0 \quad (4.12)$$

where fluid sources describing the injection processes are neglected at this level.

For the phase-field problem, a sharp-crack surface topology $\Gamma \rightarrow \Gamma_l$ is regularized by the crack surface functional as outlined in [14, 258]

$$\Gamma_l(d) = \int_{\mathcal{B}} \gamma_l(d, \nabla d) dv \quad \text{with} \quad \gamma_l(d, \nabla d) = \frac{1}{2l_f} d^2 + \frac{l_f}{2} \|\nabla d\|^2, \quad (4.13)$$

based on the crack surface density function γ_l per unit volume of the solid and the fracture length scale parameter l_f that governs the regularization, as plotted in Figure 4.3. To describe a purely geometric approach to phase-field fracture, the regularized crack phase-field d is obtained by a minimization principle of diffusive crack topology

$$d = \text{Arg} \left\{ \inf_d \Gamma_l(d) \right\} \quad \text{with} \quad d = 1 \text{ on } \Gamma \subset \mathcal{B}, \quad (4.14)$$

yielding $d - l_f^2 \Delta d = 0$ in \mathcal{B} along with the Neumann-type boundary condition $\nabla d \cdot \mathbf{n} = 0$ on $\partial\mathcal{B}$. Evolution of the regularized crack surface functional (4.13) can be driven by the constitutive functions as outlined in [10], postulating a global evolution equation of regularized crack surface as

$$\frac{d}{dt} \Gamma_l(d) =: \frac{1}{l_f} \int_{\mathcal{B}} [(1-d)\mathcal{H} - \eta_c \dot{d}] \dot{d} dv \geq 0, \quad (4.15)$$

where $\eta_c \geq 0$ is a material parameter that characterizes the artificial/numerical viscosity of the crack propagation. The crack driving force

$$\mathcal{H} = \max_{s \in [0, t]} D(\mathbf{x}, s) \geq 0, \quad (4.16)$$

is introduced as the *fourth local history variable* that accounts for the irreversibility of the phase-field evolution by filtering out a maximum value of what is known as the crack driving state function D . Then the evolution statement (6.10) provides the local equation for the evolution of the crack phase-field in the domain \mathcal{B} along with its homogeneous Neumann boundary condition as

$$[d - l_f^2 \Delta d] + \eta_c \dot{d} + (d-1)\mathcal{H} = 0 \quad (4.17)$$

with $\nabla d \cdot \mathbf{n} = 0$ on $\partial\mathcal{B}$. It represents the *third* PDE for the coupled problem.

4.3.2. Energetic response function. The multiphysics problem is based on three primary fields to characterize the poro-elasto-plasticity of fluid-saturated porous media at fracture as

$$\text{Global Primary Fields : } \mathfrak{U} := \{\mathbf{u}, p_F, d\} , \quad (4.18)$$

the displacement field \mathbf{u} , the fluid pressure field p_F and the crack phase-field d . The constitutive approach to water-induced failure mechanics for concrete focuses on the set

$$\text{Constitutive State Variables : } \mathfrak{C} := \{\boldsymbol{\varepsilon}, \boldsymbol{\varepsilon}^p, \alpha, v_F, d, \nabla d\} , \quad (4.19)$$

reflecting a combination of poro-elasto-plasticity with a first-order gradient damage modeling. It is based on the definition of a pseudo-energy density per unit volume contains the sum

$$W(\mathfrak{C}) = W_{ep}(\boldsymbol{\varepsilon}, \boldsymbol{\varepsilon}^p, \alpha, d) + W_{fluid}(\boldsymbol{\varepsilon}, v_F) + W_{frac}(d, \nabla d) \quad (4.20)$$

of a degrading elastic-plastic part W_{ep} and a contribution due to fluid W_{fluid} and fracture W_{frac} that contain the accumulated dissipative energy. The elastic-plastic contribution is modeled with an isotropic Hookean strain energy function as

$$W_{ep}(\boldsymbol{\varepsilon}, \boldsymbol{\varepsilon}^p, \alpha, d) = g(d) \psi_{ep}(\boldsymbol{\varepsilon}, \boldsymbol{\varepsilon}^p, \alpha) , \quad (4.21)$$

with

$$\psi_{ep}(\boldsymbol{\varepsilon}, \boldsymbol{\varepsilon}^p, \alpha) = \frac{\lambda}{2} \text{tr}[\boldsymbol{\varepsilon} - \boldsymbol{\varepsilon}^p]^2 + \mu(\boldsymbol{\varepsilon} - \boldsymbol{\varepsilon}^p) : (\boldsymbol{\varepsilon} - \boldsymbol{\varepsilon}^p) + \sigma_y \alpha + \frac{H}{2} \alpha^2 , \quad (4.22)$$

in terms of the two Lamé constants λ and μ , the hardening modulus H and the solid yield stress σ_y . The degradation function $g(d) = (1 - d)^2$ models the degradation of the elastic-plastic energy of the solid due to fracture. It interpolates between the unbroken response for $d = 0$ and the fully broken state at $d = 1$ by satisfying the constraints $g(0) = 1$, $g(1) = 0$, $g'(d) \leq 0$ and $g'(1) = 0$. The fluid contribution is assumed to have the form

$$W_{fluid}(\boldsymbol{\varepsilon}, v_F) = \frac{M}{2} \left[B^2 \text{tr}[\boldsymbol{\varepsilon}]^2 - 2 B v_F \text{tr}[\boldsymbol{\varepsilon}] + v_F^2 \right] , \quad (4.23)$$

in terms of the Biot's coefficient B and Biot's modulus M . Following the Coleman-Noll procedure, the fluid pressure p_F , the Cauchy stress tensor $\boldsymbol{\sigma}$ and the hardening driving force q are obtained from the pseudo-energy density function W in (6.15) for isotropic material behavior as

$$\begin{aligned} p_F(\boldsymbol{\varepsilon}, v_F) &:= \frac{\partial W}{\partial v_F} = M v_F - M B \text{tr}[\boldsymbol{\varepsilon}] , \\ \boldsymbol{\sigma}(\boldsymbol{\varepsilon}^e, p_F, d) &:= \frac{\partial W}{\partial \boldsymbol{\varepsilon}^e} = g(d) \boldsymbol{\sigma}_{eff}(\boldsymbol{\varepsilon}^e) - B p_F \mathbf{1} \quad \text{with} \quad \boldsymbol{\sigma}_{eff} = \lambda \text{tr}[\boldsymbol{\varepsilon}^e] \mathbf{1} + 2 \mu \boldsymbol{\varepsilon}^e \quad (4.24) \\ q(\alpha, d) &:= -\frac{\partial W}{\partial \alpha} = g(d) \tilde{q}(\alpha) \quad \text{with} \quad \tilde{q}(\alpha) = -[\sigma_y + H\alpha] , \end{aligned}$$

where the stress tensor is additively decomposed into an effective part $\boldsymbol{\sigma}_{eff}$ and a pressure part according to the classical Terzaghi split, as outlined in [300, 98]. Using the pressure

definition in (4.24)₁ and the second PDE in (4.12), the balance of mass is modified as follows

$$\frac{\dot{p}_F}{M} + B \operatorname{tr}[\dot{\boldsymbol{\varepsilon}}] + \operatorname{div}[\mathbb{H}] = 0, \quad (4.25)$$

which now depends on the fluid pressure p_F and the displacement \mathbf{u} .

The fracture part of pseudo-energy density (6.15) is modeled by

$$W_{frac}(d, \nabla d) = [1 - g(d)] \psi_c + 2\psi_c l_f \gamma_l(d, \nabla d), \quad (4.26)$$

where $\psi_c > 0$ is a critical fracture energy. It is defined in terms of the critical effective stress σ_c

$$\psi_c = \frac{\sigma_c^2}{2E_{cement}}, \quad (4.27)$$

as outlined in [6], where E_{cement} is the Young's modulus for the hydrated cement paste. By taking the variational derivative $\delta_d W$ of (6.15) with respect to d along with some manipulation as documented in [8], the third PDE in (6.12) yields for the rate-independent setting as follows

$$2\psi_c[d - l_f^2 \Delta d] + 2(d - 1)\mathcal{H} = 0, \quad (4.28)$$

in terms of the history field \mathcal{H} , introduced in (6.11). The crack driving state function D is defined by

$$D := \left\langle \psi_{ep}(\boldsymbol{\varepsilon}_+^e, \alpha) - \psi_c \right\rangle_+ \geq 0, \quad (4.29)$$

with the Macaulay bracket $\langle x \rangle_+ := (x + \|x\|)/2$, that ensures the irreversibility of the crack evolution. Note that only the tensile/positive part of the *elastic* energy in (6.16) is considered for computing the crack driving force. It is defined in terms of the positive strain tensor $\boldsymbol{\varepsilon}_+^e := \sum_{a=1}^3 \langle \varepsilon_a^e \rangle_+ \mathbf{n}_a \otimes \mathbf{n}_a$. Here, $\{\varepsilon_a^e\}_{a=1..3}$ are the principal elastic strains and $\{\mathbf{n}_a\}_{a=1..3}$ are the principal strain directions.

4.3.3. Plastic Dissipation. The elastic-plastic model requires additionally the formulation of a yield function, a hardening law and an evolution equation for the plastic variables. The yield function restricts the elastic region. To this end, a modified associated Drucker-Prager-type DP yield criterion function is developed within this contribution, in line with [112, 178, 34]. To overcome the singularity at the peak of the cone in Figure 4.4, an additional term in the yield function is introduced, see [193, 5], that based on a constant perturbation-type parameter, yields

$$\widehat{\Phi}_{plastic}(\boldsymbol{\sigma}_{eff}, \tilde{q}) = \sqrt{\|\operatorname{dev}[\boldsymbol{\sigma}_{eff}]\|^2 + P_\phi^2} + \beta_\phi \left(\frac{1}{3} \operatorname{tr}[\boldsymbol{\sigma}_{eff}] - P_0 \right) + \sqrt{\frac{2}{3}} \tilde{q} \quad (4.30)$$

governed by the additional term P_ϕ which provides a *smoothing-out of the peak* of the Drucker-Prager cone. It is defined as

$$P_\phi := \beta_\phi S \quad \text{with} \quad \beta_\phi = \frac{6 \sin \chi}{3 \pm \sin \chi}, \quad S = P_0^* - P_0 \quad \text{and} \quad P_0 = C \cot \chi \quad (4.31)$$

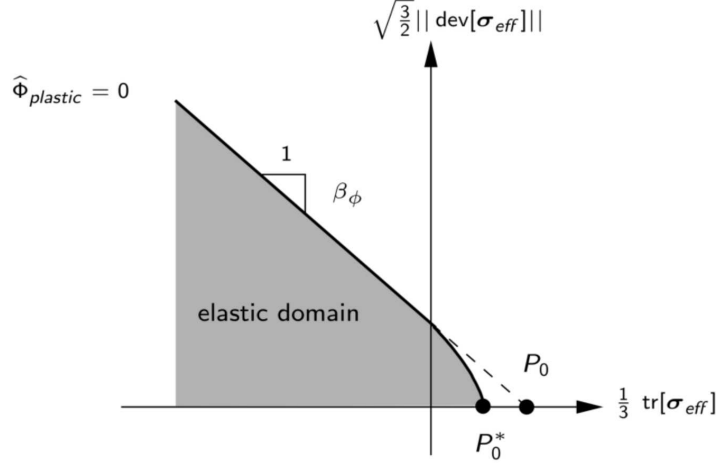


Figure 4.4: Visualization of the modified associated Drucker-Prager-type yield criterion function.

with the perturbation parameter S , the yield slope β_ϕ and the peak position P_0 in terms of the *friction angle* χ and cohesion C . A graphical interpretation of the modified associated Drucker-Prager yield criterion surface is given in Figure 4.4. The plastic flow rule of the solid skeleton takes the associate form

$$\dot{\boldsymbol{\varepsilon}}^p = \lambda_p \boldsymbol{\mathfrak{N}} \quad \text{with} \quad \boldsymbol{\mathfrak{N}} := \partial_{\boldsymbol{\sigma}_{eff}} \widehat{\Phi}_{plastic}(\boldsymbol{\sigma}_{eff}, \tilde{q}) = \frac{\text{dev}[\boldsymbol{\sigma}_{eff}]}{\sqrt{\|\text{dev}[\boldsymbol{\sigma}_{eff}]\|^2 + P_\phi^2}} + \frac{1}{3} \beta_\phi \mathbf{1}, \quad (4.32)$$

and the evolution of the equivalent plastic strain is derived as

$$\dot{\alpha} = \lambda_p \partial_{\tilde{q}} \widehat{\Phi}_{plastic}(\boldsymbol{\sigma}_{eff}, \tilde{q}) = \sqrt{\frac{2}{3}} \lambda_p \quad (4.33)$$

in terms of the plastic Lagrange multiplier λ_p that describes the amount of the plastic flow. For further details on the algorithmic treatment of the plastic history variables $\{\boldsymbol{\varepsilon}^p, \alpha\}$, we refer to the works [5, 112, 178, 34, 193].

4.4. Weak formulations for the coupled problem

The update of the primary fields $\boldsymbol{\mathfrak{U}}$ in (6.13) in a typical time increment $[t_n, t_{n+1}]$ with time step $\Delta t > 0$ is governed by three PDEs in (6.7), (4.25) and (6.12) in a strong form setting. Next, we define three test functions for the displacement $\delta \boldsymbol{u}(\boldsymbol{x}) \in \{\boldsymbol{H}^1(\mathcal{B})^\delta : \delta \boldsymbol{u} = \mathbf{0} \text{ on } \partial_D \mathcal{B}\}$, fluid pressure $\delta p_F(\boldsymbol{x}) \in \{\boldsymbol{H}^1(\mathcal{B}) : \delta p_F = 0 \text{ on } \partial_D \mathcal{B}\}$ and crack phase-field $\delta d(\boldsymbol{x}) \in \boldsymbol{H}^1(\mathcal{B})$. The weak formulations for the above introduced three PDEs of the coupled poro-elasto-plastic media problem at fracture are derived from a standard Galerkin procedure as

$$\begin{aligned} G_u(\boldsymbol{\mathfrak{U}}, \delta \boldsymbol{u}) &= \int_{\mathcal{B}} \left[\boldsymbol{\sigma} : \nabla \delta \boldsymbol{u} - \bar{\boldsymbol{b}} \cdot \delta \boldsymbol{u} \right] dv - \int_{\partial_{NB}} \bar{\boldsymbol{t}} \cdot \delta \boldsymbol{u} da = 0, \\ G_{p_F}(\boldsymbol{\mathfrak{U}}, \delta p_F) &= \int_{\mathcal{B}} \left[\left(\frac{1}{M} (p_F - p_{F,n}) + B (\text{tr}[\boldsymbol{\varepsilon}] - \text{tr}[\boldsymbol{\varepsilon}_n]) \right) \delta p_F + (\Delta t \boldsymbol{k} \nabla p_F) \cdot \nabla \delta p_F \right] dv \\ &\quad + \int_{\partial_{NB}} h \delta p_F da = 0, \\ G_d(\boldsymbol{\mathfrak{U}}, \delta d) &= \int_{\mathcal{B}} \left[\left(2\psi_c d + 2(d-1)\mathcal{H} \right) \delta d + 2\psi_c l_f^2 \nabla d \cdot \nabla \delta d \right] dv = 0, \end{aligned} \quad (4.34)$$

where $p_{F,n}$ represents the fluid pressure at time t_n . This set of equations fully describes the constitutive model.

Remark 3:

In a small strain setting, the total strain tensor is additively decomposed into an elastic and a plastic part, see (4.6). Similarly, the scalar fluid volume ratio v_F can also be decomposed into reversible-elastic v_F^e and irreversible-plastic v_F^p parts, according to [34], yields

$$v_F = v_F^e + v_F^p .$$

Evolution of those history fields are defined as:

$$\dot{v}_F^e = \frac{1}{M} \dot{p}_F + B \operatorname{tr}[\dot{\boldsymbol{\epsilon}}^e] \quad \text{and} \quad \dot{v}_F^p = B \operatorname{tr}[\dot{\boldsymbol{\epsilon}}^p] .$$

This decomposition will be further investigated in future works.

4.5. Representative numerical example

This section demonstrates the performance of the proposed phase-field model for water-induced damage mechanics in poro-elasto-plastic media. Two different cases are analyzed and compared as explained in Section 4.3. As a geometrical setup, we consider a boundary value problem applied to the square plate as shown in Figure 4.2. It represents an idealized microstructure of the concrete specimen in two-dimensional setting.

The size of the square specimen is chosen to be $L = 100 \mu\text{m}$. Unhydrated clinker particles demonstrated as big circles (ranging between $4.0 - 10.0 \mu\text{m}$) with the dark gray

Table 4.1: Material parameters used in the numerical examples.

No.	Parameter	Name	Value	Unit
1.	E_{cement}	Young's modulus for hydrated phase	20.0	GPa
2.	E_{clinker}	Young's modulus for unhydrated phase	3×20.0	GPa
3.	ν	Poisson's ratio	0.2	–
4.	β_ϕ	Yield slope	0.95	–
5.	S	Perturbation parameter	1×10^{-3}	MPa
6.	P_0	Cone peak position	0.002	MPa
7.	H	Hardening modulus	0.35	MPa
8.	σ_y	Solid yield stress	5.0	MPa
9.	M	Biot's modulus	100	MPa
10.	B	Biot's coefficient	1.0	–
11.	k	Intrinsic permeability	1×10^{-16}	m^2
12.	k_c	Spatial permeability in fracture	10.0	$\text{m}^3\text{s}/\text{kg}$
13.	ζ	Permeability transition exponent	50	–
14.	η_F	Dynamic fluid viscosity	1×10^{-6}	$\text{kg}/(\text{m}\cdot\text{s})$
15.	η_c	Fracture viscosity	1×10^{-6}	GPa
16.	l_f	Fracture length scale	0.50	μm
17.	σ_c	Critical effective stress	0.14	MPa

color in Figure 4.2. Small blue/white circles (ranges between $1.2 - 3.0 \mu\text{m}$) refer to the saturated/dry pores. The circles are arbitrarily distributed inside the hydrated cement paste (plotted in light gray color). We fix the bottom edge of the plate and apply a compression load at the top edge until the plate is fully broken. Material properties of the concrete solid phases are obtained through nano-indentation techniques. Other material parameters used in the simulation are listed in Table 6.1.

For the finite element simulation, all variables are discretized by quadratic shape functions. Similar results have been observed using the recently developed **virtual element method** (VEM) with 8 noded quadrilateral elements Q2S, representing a *first-order* VEM, see [8, 7]. Furthermore, the computations are performed by using a nested Newton-Raphson algorithm. Load stepping is applied when necessary. Since all formulations are linearized in a consistent manner using ACEGEN see [184], quadratic convergence is achieved within a load step.

The key goal of this investigation is to illustrate the water effects on concrete failure at the microscopic length scale. To this end, we compare the idealized concrete specimen under two different environments.

4.5.1. Dried case (D). reduced to standard phase-field modeling of ductile fracture in the heterogeneous microstructure. For the numerical implementation, two primary fields are solved, namely the displacement field \mathbf{u} and the crack phase-field d .

Figure 4.5 illustrates the equivalent plastic strain α (first row) and the crack phase-field d (second row) evolutions for different deformation states up to final failure $\{\bar{u} = 0; 0.0064; 0.0076; 0.0082 \mu\text{m}\}$. We observe an accumulation of α around the stiff clinker particles and the pores until a threshold energy ψ_c is reached. Thereafter the crack phase-field d initiates around the heterogeneous regions where the maximum equivalent plastic strain is concentrated. Then it propagates in random directions inside the hydrated cement paste (plotted in light gray color) and joins other cracks till final rupture as shown

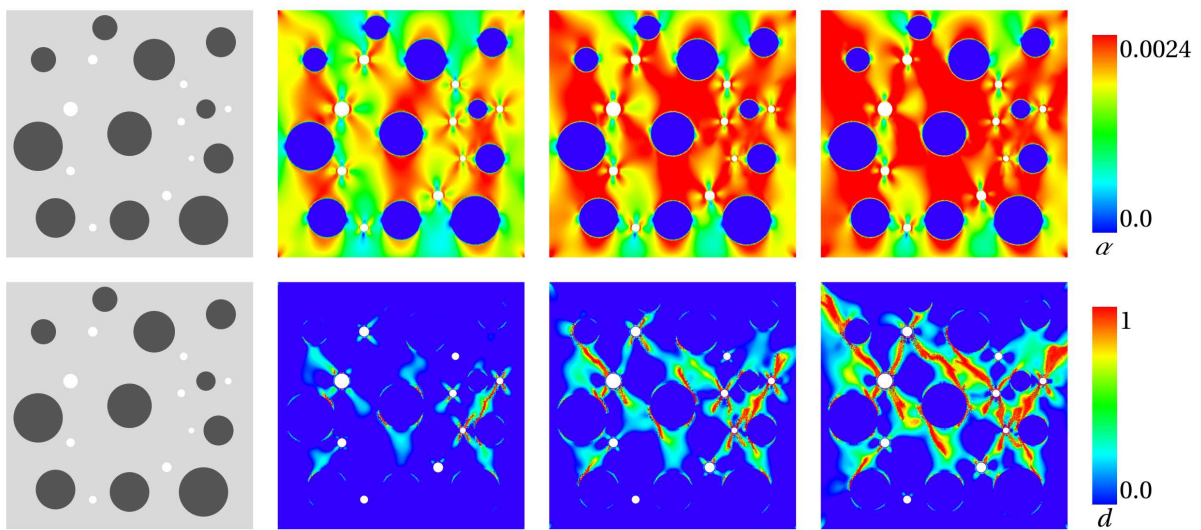


Figure 4.5: Compression test for the idealized microstructure of *dry concrete*: Evolution of equivalent plastic strain α (first row) and crack phase-field d (second row) for different deformation states up to final failure $\{\bar{u} = 0; 0.0064; 0.0076; 0.0082 \mu\text{m}\}$.

in Figure 4.5 (second row).

4.5.2. Wet case (W). The second model problem is concerned with analyzing the concrete failure phenomena of an idealized microstructure geometry underwater (wet environment). To this end, the fracture phase-field formulations are extended towards fluid-saturated heterogeneous porous media at microscale as discussed in Section 4.3. In this case, all the pores are assumed to be filled with the water phase (i.e. partially saturated condition with mixed air/water pores is excluded).

The evolution of the equivalent plastic strain α (first row), the crack phase-field d (second row) and the fluid pressure p_F (third row) are depicted in Figure 4.6. The plasticity starts to accumulate around the stiff unhydrated clinker particles and the fluid pressure increases from the saturated pores. Then, the crack initiates in the plastic zones when the elastic-plastic energies reach a critical value. As expected, the fluid pressure drops in the fractured areas as shown in Figure 4.6 (third row).

Next, we compare the load-displacement curves of the dried and wet concrete specimens in Figure 4.7(a). It has been demonstrated that concrete tested underwater shows earlier damage behavior compared to the dry case. This is due to the water influences which is in good agreement with the experimental observation in [303, 302]. For a better understanding of the water effects, we plot in Figure 4.7(b) the averaged fluid pressure evolution with load in the saturated pores until the final rupture. We notice an accumu-

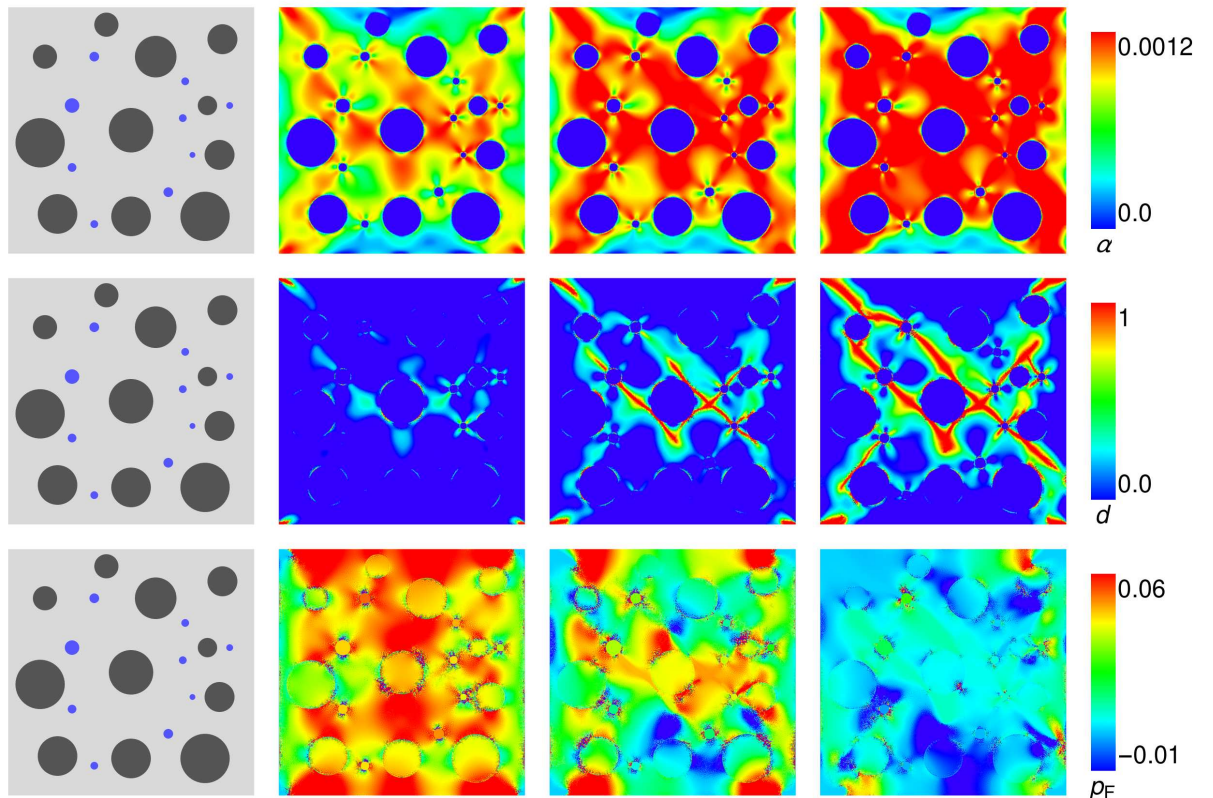


Figure 4.6: Compression test for the idealized microstructure of *wet concrete*: Evolution of equivalent plastic strain α (first row), crack phase-field d (second row) and fluid pressure p_F (third row) for different deformation states up to final failure $\{\bar{u} = 0; 0.0030; 0.0036; 0.0044 \mu\text{m}\}$.

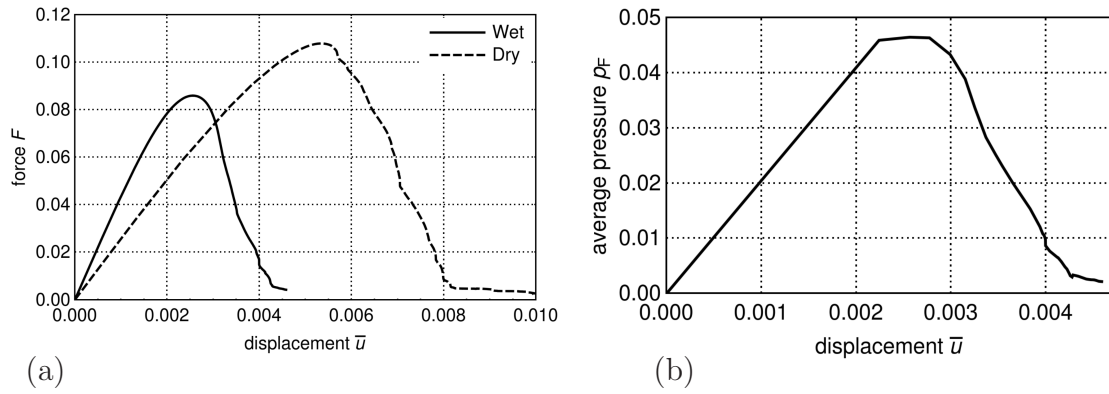


Figure 4.7: Compression test for the idealized microstructure of concrete: (a) Load [N] - displacement [μm] comparison between the dry and wet cases; and (b) the average pressure [MPa] in the wet pores.

lation of p_F in the saturated pores until fracture initiation, then the pressure drops in those areas, as outlined in Figure 4.6 (third row).

— Part II —

Advanced Virtual Element Method

5. 2D Virtual elements for phase-field modeling of brittle fracture

This chapter addresses an efficient low order *virtual element method* (VEM) for the phase-field modeling of isotropic brittle fracture. The discussion in this chapter is based on the recent work of ALDAKHEEL ET AL. [6].

Virtual elements were introduced in the last decade and applied to various problems in solid mechanics. The phase-field approach regularizes sharp crack surfaces within a pure continuum setting by a specific gradient damage modeling with constitutive terms rooted in fracture mechanics, see MIEHE ET AL. [225, 230]. In the presented contribution, we propose a rigorous variational-based framework for the phase-field modeling of brittle fracture in elastic solids undergoing small strains. The key goal here, is the extension towards the recently developed virtual element formulation due to the flexible choice of nodes number in an element which can be changed easily during the simulation process, as outlined in WRIGGERS ET AL. [328, 329]. To this end, the *potential density* is formulated in terms of suitable polynomial functions, instead of computing the unknown shape functions for complicated element geometries, e.g. arbitrary convex or concave polygonal elements. An important aspect of this work is the introduction of an incremental minimization principle, with a novel construction of the *stabilization density* for the coupled multi-field problem. On the computational side, a robust and efficient *monolithic scheme* is employed using the software tool ACEFEM program in the numerical implementation to compute the unknowns (displacement and crack phase-field), see KORELC & WRIGGERS [184]. The performance of the formulation is underlined by means of representative examples.

5.1. Introduction

The finite element method (FEM) is a well established tool for solving a wide range of boundary value problems in science and engineering, see e.g. BATHE [43], ZIENKIEWICZ ET AL. [345] and WRIGGERS [323]. However in recent years different methods like the isogeometric analysis outlined in Hughes et al. [174, 92] and the virtual element method proposed in BEIRÃO DA VEIGA ET AL. [46] were introduced as tools that bring some new features to the numerical solution of problems in solid mechanics. The virtual element method is a generalization of the finite element method, which has inspired from modern *mimetic finite difference schemes*, rooted in the pioneering work of BREZZI ET AL. [71]. It has proven to be a competitive discretization scheme for meshes with irregularly shaped elements that can even become non-convex. Furthermore, VEM allows exploration of features such as flexibility with regard to mesh generation and choice of element shapes, e.g. use very general polygonal and polyhedral meshes. In this regard, a stabilization procedure is required in the virtual element method, as described in CANGIANI ET AL. [77] for linear Poisson problems. So far applications of virtual elements have been devoted to linear elastic deformations in GAIN ET AL. [135] and ARTIOLI ET AL. [36], contact problems in WRIGGERS ET AL. [328], 3D finite elasto-plastic deformations in HUDOBIVNIK ET AL. [169], anisotropic materials at finite strains in WRIGGERS ET AL. [330, 331], 2D magnetostatic problems in BEIRÃO DA VEIGA ET AL. [48], inelastic solids in TAYLOR & ARTIOLI [298] and hyperelastic materials at finite deformations in CHI ET AL. [85] and WRIGGERS ET AL. [329]. In this contribution, we examine the efficiency of the VEM for predicting the failure mechanisms in solids due to crack initiation and propagation.

The structure of the VEM typically comprises a term in the weak formulation or the

potential density functional in which the displacement field \mathbf{u} and the fracture phase-field d , being sought are replaced by their projection: \mathbf{u}_Π and d_Π onto a polynomial space. This results in a rank-deficient structure, therefore it is necessary to add a stabilization term to the formulation, see BEIRÃO DA VEIGA ET AL. [46], BEIRÃO DA VEIGA ET AL. [47] and CHI ET AL. [85], where in the latter the scalar stabilization parameter of the linear case was replaced by one that depends on the fourth-order elasticity tensor.

A new stabilization technique for VEM was recently developed in WRIGGERS ET AL. [329] who use a technique that was first described in NADLER & RUBIN [249], generalized in BOERNER ET AL. [60] and simplified in KRYSL [187] in the context of hexahedral finite elements. The essence of the method is the addition of the positive semi-definite potential density function $\pi(\nabla_s \mathbf{u}_\Pi, d_\Pi, \nabla d_\Pi)$ to a positive-definite potential $\hat{\pi}(\nabla_s \mathbf{u}, d, \nabla d)$ which is evaluated using full quadrature. For consistency the subtraction of a term involving $\hat{\pi}(\nabla_s \mathbf{u}_\Pi, d_\Pi, \nabla d_\Pi)$ as a function of the projected displacement and the phase-field is made.

This chapter represents an initial contribution to the use of the virtual element methodology for numerically solving *fracture-mechanics* problems. In contrast to the projection of the displacement field as the only global field being sought in most virtual element method applications up to now, this work further extends VEM towards *multi-physics problems*. For this purpose, the crack phase-field is also projected onto a polynomial space. The modeling of crack formation can be achieved in a convenient way by continuum phase-field approaches to fracture, which are based on the regularization of sharp crack discontinuities. Phase-field modeling of fracture has been attracting considerable attention in recent years due to its capability of capturing complex crack patterns in various problems in solid mechanics. Many efforts have been focused on the regularized modeling of Griffith-type brittle fracture in elastic solids. In this regard, MIEHE ET AL. [225] proposed a phase-field approach to fracture with a local irreversibility constraint on the crack phase-field. It incorporates regularized crack surface density functions as central constitutive objects, which is motivated in a descriptive format based on geometric considerations. Recent works on brittle fracture have been devoted to the dynamic case in BORDEN ET AL. [62], cohesive fracture in VERHOESEL & DE BORST [307], multiplicative decomposition of the deformation gradient into compressive-tensile parts in HESCH & WEINBERG [164], different choices of degradation functions in KUHN ET AL. [189] and SARGADO ET AL. [280], coupled thermo-mechanical and multi-physics problems at large strains in MIEHE ET AL. [231], a new fast hybrid formulation in AMBATI ET AL. [24], to model fracture of arterial walls with an emphasis on aortic tissues in GÜLTEKIN ET AL. [149], finite-deformation contact problems in HESCH ET AL. [165], emphasis on a possible formula for the length scale estimation in ZHANG ET AL. [341], anisotropic material behavior at small and large deformations in TEICHTMEISTER ET AL. [299], for the description of hydraulic fracturing in HEIDER & MARKERT [159] and EHLERS & LUO [115], to describe fatigue effects for brittle materials in ALESSI ET AL. [20], crack penetration or deflection at an interface in PAGGI & REINOSO [259] and material point method in KAKOURIS & TRIANTAFYLLOU [176]. Extensions of these models towards the phase-field modeling of ductile fracture can be achieved by coupling of gradient damage mechanics with models of elasto-plasticity, as proposed in the works of ALDAKHEEL ET AL. [4, 14], MIEHE ET AL. [230, 232, 237, 238], AMBATI ET AL. [23], BORDEN ET AL. [64], ALESSI ET AL. [19], DITTMANN ET AL. [107] and NA & SUN [248].

The goal of this work is to present a consistent variational-based framework for the

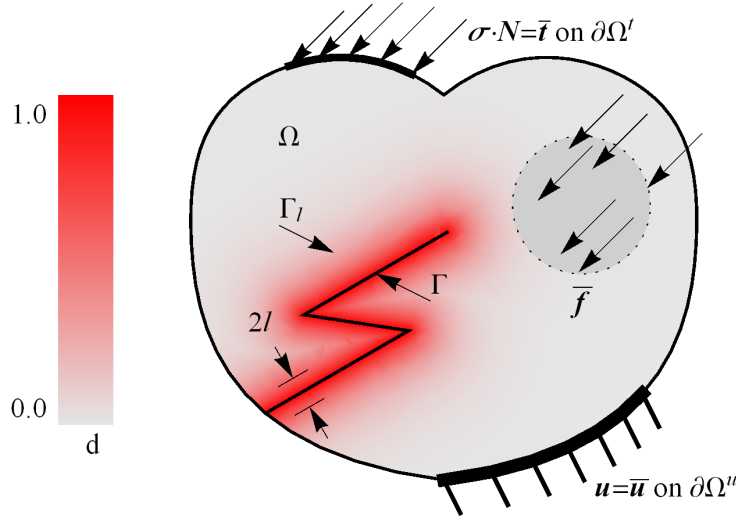


Figure 5.1: Solid with a regularized crack and boundary conditions.

phase-field modeling of brittle fracture using an efficient virtual element method. On the computational side, one may employ either a monolithic or a staggered algorithm to compute the unknowns, in which the displacement and the crack phase-field are computed simultaneously or alternatively, respectively. In this work, a robust and efficient monolithic scheme is employed in the numerical implementation using the software tool ACEFEM, see KORELC & WRIGGERS [184].

The chapter is organized as follows: Section 5.2 outlines the primary fields and constitutive state variables of the multi-field problem. Section 5.3 is devoted to the construction of a variational phase-field approach to brittle fracture in elastic solids. The development of the virtual element method is formulated in Section 5.4. Finally, Section 5.5 presents numerical results that demonstrate the modeling capabilities of the proposed approach. The formulation performs extremely well in benchmark tests involving regular, distorted and Voronoi meshes. For comparison purposes, results of the standard finite element method (FEM) are also demonstrated.

5.2. Basic kinematics at small strains

5.2.1. Displacement and crack phase-field. Let $\Omega \in \mathcal{R}^\delta$ with $\delta = 2, 3$ be a solid domain. The response of fracturing solid at material points $\mathbf{x} \in \Omega$ and time $t \in \mathcal{T} = [0, T]$ is described by the displacement field $\mathbf{u}(\mathbf{x}, t)$ and the crack phase-field $d(\mathbf{x}, t)$

$$\mathbf{u} : \begin{cases} \Omega \times \mathcal{T} \rightarrow \mathcal{R}^\delta \\ (\mathbf{x}, t) \mapsto \mathbf{u}(\mathbf{x}, t) \end{cases} \quad \text{and} \quad d : \begin{cases} \Omega \times \mathcal{T} \rightarrow [0, 1] \\ (\mathbf{x}, t) \mapsto d(\mathbf{x}, t) \end{cases} \quad \text{with} \quad \dot{d} \geq 0 \quad (5.1)$$

with $d(\mathbf{x}, t) = 0$ and $d(\mathbf{x}, t) = 1$ for the unbroken and the fully broken state of the material respectively, as depicted in Figure 5.1. The gradient of the displacement field defines the symmetric strain tensor of the geometrically linear theory

$$\boldsymbol{\varepsilon} = \nabla_s \mathbf{u} = \text{sym}[\nabla \mathbf{u}] := \frac{1}{2}[\nabla \mathbf{u} + \nabla \mathbf{u}^T]. \quad (5.2)$$

The time-dependent Dirichlet- and Neumann boundary conditions of the solid are defined as

$$\mathbf{u} = \bar{\mathbf{u}} \text{ on } \partial\Omega^u \quad \text{and} \quad \boldsymbol{\sigma} \cdot \mathbf{N} = \bar{\mathbf{t}} \text{ on } \partial\Omega^t \quad (5.3)$$

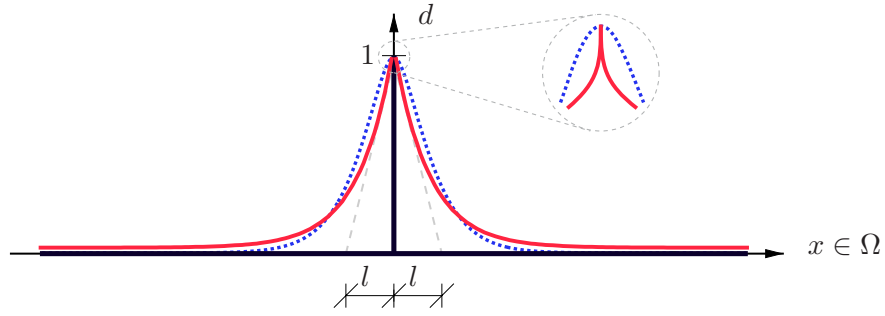


Figure 5.2: One dimensional cracked bar. Black thick line represents a sharp crack at $x = 0$. Red and blue lines represent diffusive crack modeling. For the red thick line: $\gamma_l = d^2/2l + l|\nabla d|^2/2$ with regularization profile $\exp[-|x|/l]$ satisfying $d(0) = 1$ and for the blue dotted line: $\gamma_l = d^2/2l + l|\nabla d|^2/4 + l^3(\Delta d)^2/32$ with regularization profile $\exp[-2|x|/l](1 + 2|x|/l)$ satisfying $d(0) = 1$ and $d'(0) = 0$.

with a prescribed displacement and external traction on the surface $\partial\Omega = \partial\Omega^u \cup \partial\Omega^t$ of the solid domain, where $\partial\Omega^u \cap \partial\Omega^t = \emptyset$. For the phase-field problem, a sharp-crack surface topology $\Gamma \rightarrow \Gamma_l$ is regularized by the crack surface functional as outlined in MIEHE ET AL. [225, 230]

$$\Gamma_l(d) = \int_{\Omega} \gamma_l(d, \nabla d) dV \quad \text{with} \quad \gamma_l(d, \nabla d) = \frac{1}{2l}d^2 + \frac{l}{2}|\nabla d|^2 \quad (5.4)$$

based on the crack surface density function γ_l per unit volume of the solid and the fracture length scale parameter that governs the regularization, as plotted in Figure 5.1. The function γ_l already appears in the approximation by AMBROSIO & TORTORELLI [25] of the MUMFORD & SHAH [247] functional of image segmentation. For vanishing fracture length scale $l \rightarrow 0$, the functional $\Gamma_l(d)$ converges to a sharp-crack topology Γ as schematically visualized in Figure 5.2 for a one dimensional cracked bar, which depicts in addition a possible higher order approximation suggested by BORDEN ET AL. [63] and DITTMANN ET AL. [107]. To describe a purely geometric approach to phase-field fracture, the regularized crack phase-field d is obtained by a *minimization principle of diffusive crack topology*

$$d = \text{Arg}\{\inf_d \Gamma_l(d)\} \quad \text{with} \quad d = 1 \text{ on } \Gamma \subset \Omega \quad (5.5)$$

yielding the Euler equation $d - l^2\Delta d = 0$ in Ω along with the Neumann-type boundary condition $\nabla d \cdot \mathbf{N} = 0$ on $\partial\Omega$, where \mathbf{N} is the outward normal on $\partial\Omega$. Figure 5.3 demonstrates a numerical solution for (5.5) in two-dimensional setting using an efficient virtual element method (VEM). The Γ -limit of the above variational principle gives for $l \rightarrow 0$ the sharp crack surface Γ , as plotted in Figure 5.3(d) for the VEM specimen with a voronoi mesh.

The above introduced variables will characterize the brittle failure response of a solid, based on the two *global primary fields*

$$\text{Global Primary Fields: } \mathfrak{U} := \{\mathbf{u}, d\}, \quad (5.6)$$

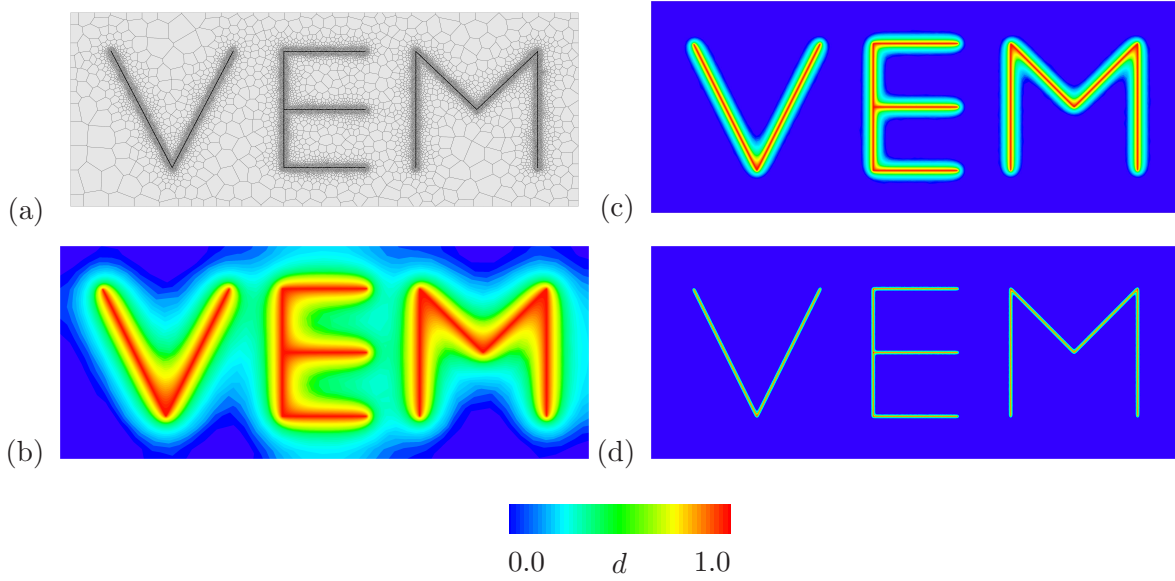


Figure 5.3: A purely geometric approach to phase-field fracture based on virtual element method (VEM). (a) Geometry and discretization of the specimen using *Voronoi meshes*. (b)–(d) Solutions of the variational problem (5.5) for a rectangular specimen Ω with a given VEM-shape for the sharp crack Γ , prescribed by the Dirichlet condition $d = 1$ on $\Gamma \subset \Omega$ for different fracture length scales $l^b > l^c > l^d$.

the displacement field \mathbf{u} and the crack phase-field d . The subsequent constitutive approach to the phase-field modeling of brittle fracture focuses on the set

$$\text{Constitutive State Variables: } \boldsymbol{\mathfrak{C}} := \{\boldsymbol{\varepsilon}, d, \nabla d\}, \quad (5.7)$$

reflecting a combination of elasticity with a first-order gradient damage modeling.

5.2.2. Constitutive evolution of crack phase-field. Following the recent works of MIEHE ET AL. [230], ALDAKHEEL [10] and ALDAKHEEL ET AL. [14], the evolution of the regularized crack surface functional is driven by the constitutive functions, postulating a global *evolution equation of regularized crack surface* as

$$\frac{d}{dt} \Gamma_l(d) = \int_{\Omega} \delta_d \gamma_l(d, \nabla d) \dot{d} dV := \frac{1}{l} \int_{\Omega} [(1-d)\mathcal{H} - \eta \dot{d}] \dot{d} dV \geq 0 \quad (5.8)$$

where $\eta \geq 0$ is a material parameter that characterizes the viscosity of the crack propagation. The crack driving force

$$\mathcal{H} = \max_{s \in [0, t]} D(\mathbf{x}, s) \geq 0, \quad (5.9)$$

is introduced that accounts on the irreversibility of the phase-field evolution by filtering out a maximum value of what is known as the *crack driving state function* D . Then the evolution statement (5.8) provides the local equation for the evolution of the crack phase-field in the domain Ω along with its homogeneous Neumann boundary condition as

$$\eta \dot{d} = (1-d)\mathcal{H} - [d - l^2 \Delta d] \quad \text{with} \quad \nabla d \cdot \mathbf{N} = 0 \quad \text{on} \quad \partial\Omega \quad (5.10)$$

5.3. Variational based phase-field approach to brittle fracture

In this section, we outline a variational approach to brittle fracture in elastic solids at small strains, in line with [10, 232].

5.3.1. Constitutive work density function. The constitutive work density function W is assumed to depend on the constitutive state variables \mathbf{C} introduced in (5.7). It consists of the sum

$$W(\mathbf{C}) = W_{bulk}(\boldsymbol{\varepsilon}, d) + W_{frac}(d, \nabla d) \quad (5.11)$$

of a degrading elastic bulk energy W_{bulk} and a contribution due to fracture W_{frac} , which contains the accumulated dissipative energy, as already suggested in ALDAKHEEL [10] and MIEHE ET AL. [232] for coupled gradient plasticity-damage problem. The elastic bulk contribution in (5.11) is assumed to be a quadratic function as

$$W_{bulk}(\boldsymbol{\varepsilon}, d) = g(d) \psi(\boldsymbol{\varepsilon}) \quad \text{with} \quad \psi(\boldsymbol{\varepsilon}) = \frac{\lambda}{2} \text{tr}^2[\boldsymbol{\varepsilon}] + \mu \text{tr}[\boldsymbol{\varepsilon}^2] \quad \text{and} \quad g(d) = (1 - d)^2, \quad (5.12)$$

where, $\lambda > 0$ and $\mu > 0$ are the elastic Lamé constants. $g(d)$ is a degradation function that models the degradation of the stored elastic energy of the solid due to fracture. It interpolates between the unbroken response for $d = 0$ and the fully broken state at $d = 1$ by satisfying the constraints $g(0) = 1$, $g(1) = 0$, $g'(d) \leq 0$ and $g'(1) = 0$. In order to enforce a crack evolution only in tension, the stored elastic energy of the solid is additively decomposed into a positive part $\tilde{\psi}^+$ due to tension and a negative part $\tilde{\psi}^-$ due to compression, outlined in the *pioneering work* of MIEHE ET AL. [225] as

$$W_{bulk}(\boldsymbol{\varepsilon}, d) = (1 - d)^2 \tilde{\psi}^+ + \tilde{\psi}^- \quad \text{with} \quad \tilde{\psi}^\pm = \frac{\lambda}{2} \langle \text{tr}[\boldsymbol{\varepsilon}] \rangle_\pm^2 + \mu \text{tr}[(\boldsymbol{\varepsilon}_\pm)^2] \quad (5.13)$$

in terms of the two ramp functions $\langle x \rangle_+ := (x + |x|)/2$ and $\langle x \rangle_- := (x - |x|)/2$ of \mathcal{R}_+ and \mathcal{R}_- , respectively, and the positive and negative strain tensors $\boldsymbol{\varepsilon}_+ := \sum_{a=1}^3 \langle \varepsilon_a \rangle_+ \mathbf{n}_a \otimes \mathbf{n}_a$ and $\boldsymbol{\varepsilon}_- := \boldsymbol{\varepsilon} - \boldsymbol{\varepsilon}_+$. $\{\varepsilon_a\}_{a=1..3}$ are the principal strains and $\{\mathbf{n}_a\}_{a=1..3}$ are the principal strain directions. The second term in (5.11) models the accumulated dissipation

$$W_{frac}(d, \nabla d) = [1 - g(d)] \psi_c + 2 \frac{\psi_c}{\zeta} l \gamma_l(d, \nabla d) \quad (5.14)$$

where, $\psi_c > 0$ is a critical fracture energy and ζ controls the post-critical range after crack initialization.

5.3.2. Dissipation potential function. The crack phase-field evolution \dot{d} is based on a dissipation potential related to a threshold function. This function is formulated in terms of an energetic driving force F^f and a dissipative resistance force R^f , defined as

$$F^f := -\partial_d W_{bulk} \quad \text{and} \quad R^f := \delta_d W_{frac} := \partial_d W_{frac} - \text{Div}[\partial_{\nabla d} W_{frac}] \quad (5.15)$$

A crack resistance domain associated with the crack propagation in the space of the crack driving force is defined by

$$\mathcal{E}_{frac} := \{ (F^f - R^f) \mid \phi^f(F^f - R^f) \leq 0 \} \quad \text{with} \quad \phi^f(F^f - R^f) = F^f - R^f \quad (5.16)$$

based on the crack threshold function ϕ^f . With this function at hand, a dissipation potential function can be constructed based on the standard concept of maximum dissipation. A rate-dependent dissipation potential function in a non-constrained manner is defined as

$$V(\dot{\mathbf{c}}) = \sup_{F^f - R^f} \left[(F^f - R^f) \dot{d} - V^*(F^f - R^f) \right] \quad \text{with} \quad V^*(F^f - R^f) = \frac{1}{2\eta} \langle \phi^f(F^f - R^f) \rangle_+^2, \quad (5.17)$$

based on the dual dissipation potential function. The necessary condition of the local optimization problem (5.17)₁ yields the crack phase-field evolution

$$\dot{d} = \lambda^f \partial_{F^f - R^f} \phi^f \quad \text{with} \quad \lambda^f := \frac{1}{\eta} \langle \phi^f(F^f - R^f) \rangle_+ \geq 0 \quad (5.18)$$

where the positiveness of the viscous constitutive function λ^f implies via (5.18) a monotonous growth $\dot{d} \geq 0$ of the fracture phase-field.

5.3.3. Variational principle for the two-field evolution problem. The rate-type minimization principle is governed by the global rate potential functional

$$\Pi(\dot{\mathbf{u}}) = \int_{\Omega} \pi(\dot{\mathbf{c}}) dV - \Pi_{ext}(\dot{\mathbf{u}}) \quad \text{with} \quad \Pi_{ext}(\dot{\mathbf{u}}) := \int_{\Omega} \bar{\mathbf{f}} \cdot \dot{\mathbf{u}} dV + \int_{\partial\Omega} \bar{\mathbf{t}} \cdot \dot{\mathbf{u}} dA \quad (5.19)$$

in terms of the constitutive rate potential density per unit volume

$$\pi(\dot{\mathbf{c}}) = \frac{d}{dt} W(\mathbf{c}) + V(\dot{\mathbf{c}}) \quad (5.20)$$

and the external load functional $\Pi_{ext}(\dot{\mathbf{u}})$, where $\bar{\mathbf{f}}$ is a given body force per unit volume of the solid and $\bar{\mathbf{t}}_N$ is a given traction field on the surface. The evolution of two primary fields is determined by the minimization principle

$$\{\dot{\mathbf{u}}, \dot{d}\} = \text{Arg} \left\{ \inf_{\dot{\mathbf{u}}, \dot{d}} \Pi(\dot{\mathbf{u}}) \right\}. \quad (5.21)$$

The combination of the global minimization principle (5.21) with the local maximum problem (5.17) for the definition of the dissipation potential V provides a mixed variational principle, that defines all equations of fracture in elastic solids. When introducing the mixed potential density

$$\pi^* = \frac{d}{dt} W + (F^f - R^f) \dot{d} - V^*, \quad (5.22)$$

the Euler equations of the variational principle for the quasi-static case, where inertia effects are neglected, appear in the form:

1. *Stress equilibrium* $\delta_{\dot{\mathbf{u}}} \pi^* \equiv \text{Div} [\partial_{\varepsilon} W] + \bar{\mathbf{f}} = \mathbf{0}$
2. *Fracture force* $\delta_{\dot{d}} \pi^* \equiv \partial_d W - \text{Div} [\partial_{\nabla d} W] + (F^f - R^f) = 0$ (5.23)
3. *Fracture phase-field* $\partial_{(F^f - R^f)} \pi^* \equiv \dot{d} - \partial_{(F^f - R^f)} V^* = 0$

along with Neumann-type boundary conditions of the form defined as

$$\partial_{\varepsilon} W \cdot \mathbf{N} = \bar{\mathbf{t}} \quad \text{on} \quad \partial\Omega^t \quad \text{and} \quad \nabla d \cdot \mathbf{N} = \mathbf{0} \quad \text{on} \quad \partial\Omega^{\nabla d} \quad (5.24)$$

5.3.4. Time-discrete incremental variational formulation. This section provides the time discretization of the above introduced rate type-variational formulation. Consider a discrete time interval $[t_n, t_{n+1}]$, where $\tau := t_{n+1} - t_n > 0$ denotes the step length. Next, we assume all fields variable at time t_n to be known. The aim is to determine all variables at the current discrete time t_{n+1} (fields without subscript) based on variational principle valid for the time increment under consideration. In particular,

$$\mathbf{e}^* := \{\boldsymbol{\varepsilon}, d, \nabla d, F^f - R^f\} \quad \text{and} \quad \mathbf{e}_n^* := \{\boldsymbol{\varepsilon}_n, d_n, \nabla d_n, F_n^f - R_n^f\} \quad (5.25)$$

denoted as the state variables at time t_{n+1} and time t_n , respectively. The incremental potential density functional for the coupled problem is defined as

$$\Pi^\tau(\boldsymbol{\mathfrak{U}}) = \int_{\Omega} \pi^\tau(\mathbf{e}) dV - \Pi_{ext}^\tau(\mathbf{u}) \quad \text{with} \quad \pi^\tau(\mathbf{e}) = \text{Algo} \left\{ \int_{t_n}^{t_{n+1}} \pi(\dot{\mathbf{e}}) dt \right\} \quad (5.26)$$

based on an *algorithmic approximation* of the incremental potential density per unit volume π^τ . Using a fully implicit Euler scheme and following same procedure as in (5.22), we end up with the incremental mixed potential density function

$$\pi^{*\tau}(\mathbf{e}^*) = W + (F^f - R^f)(d - d_n) - \tau V^* \quad (5.27)$$

based on the state variables \mathbf{e}^* at time t_{n+1} defined in (5.25). The development of the *virtual element* that handle phase-field brittle fracture in elastic solids can start from the particular form of the potential density functional, defined in (5.26). This has advantages when the code is automatically generated using the software tool ACEGEN, see KORELC & WRIGGERS [184]. Next, we define the governing partial differential equations describing the multi-field approach to phase-field-type crack propagation in elastic solids:

Balance of linear momentum. The first equation is the stress equilibrium for the quasi-static form of the balance of linear momentum defined as

$$\text{Div}[\boldsymbol{\sigma}] + \overline{\mathbf{f}} = \mathbf{0} . \quad (5.28)$$

The stress tensor is obtained from the potential W in (5.11) by

$$\boldsymbol{\sigma} := \partial_{\boldsymbol{\varepsilon}} W = (1 - d)^2 \tilde{\boldsymbol{\sigma}}_+ + \tilde{\boldsymbol{\sigma}}_- \quad \text{with} \quad \tilde{\boldsymbol{\sigma}}_{\pm} = \lambda \langle \text{tr}[\boldsymbol{\varepsilon}^e] \rangle_{\pm} \mathbf{1} + 2\mu \boldsymbol{\varepsilon}_{\pm} \quad (5.29)$$

where $\tilde{\boldsymbol{\sigma}}$ is the effective stress tensor dual to the strain tensor $\boldsymbol{\varepsilon}$.

The fracture phase-field equation. Equation (5.23)₂ determines the PDE for the fracture phase-field update equation. It defines the fracture driving force

$$F^f - R^f = 2(1 - d)[\tilde{\psi}^+(\boldsymbol{\varepsilon}) - \psi_c] - 2\frac{\psi_c}{\zeta}[d - l^2 \Delta d] . \quad (5.30)$$

This partial differential equation is accompanied by equation (5.23)₃ for the update of the crack phase-field, which reads

$$(d - d_n)/\tau = \lambda^f \partial_{(F^f - R^f)} \phi^f = \lambda^f . \quad (5.31)$$

For brevity, we introduce a modified viscosity of the crack propagation as

$$\eta^f := \frac{\zeta}{2\psi_c} \eta , \quad (5.32)$$

the combination of (5.30) and (5.31) characterizes a generalized Ginzburg-Landau- or Allen-Cahn-type equation for the update of the crack phase-field d

$$(d - d_n)/\tau = \frac{1}{\eta^f} \left\langle (1 - d) \zeta \left[\frac{\tilde{\psi}^+}{\psi_c} - 1 \right] - [d - l^2 \Delta d] \right\rangle_+ \quad (5.33)$$

where the Macaulay bracket ensures the irreversibility of the crack evolution. Following the recent works ALDAKHEEL [10], MIEHE ET AL. [238] and ALDAKHEEL ET AL. [14], (5.33) may be recast using (5.10) as

$$\eta^f (d - d_n)/\tau = (1 - d) \mathcal{H} - [d - l^2 \Delta d] \quad (5.34)$$

with the crack driving force \mathcal{H} , that accounts for the irreversibility of the phase-field evolution by filtering out the maximum value of the *crack driving state function* D . It is defined by

$$\mathcal{H} := \max_{s \in [0, t]} D(\mathbf{c}; s) \geq 0 \quad \text{with} \quad D := \zeta \left\langle \frac{\tilde{\psi}^+}{\psi_c} - 1 \right\rangle_+ \quad (5.35)$$

5.3.5. Crack driving state functions for different fracture criteria. The definition of the effective crack driving state function D allows a strong flexibility, with regard to alternative crack driving criteria. In the previous section, we constructed an energetic criterion with threshold based on the fracture contribution of the work density function. In the following, other examples are presented to complete specific definitions of the phase-field equation (5.34).

Stress-based criterion. To distinguish between energetic tensile and compressive parts of the elastic bulk energy, the effective stress tensor is decomposed into a positive and negative part

$$\tilde{\boldsymbol{\sigma}} = \tilde{\boldsymbol{\sigma}}^+ + \tilde{\boldsymbol{\sigma}}^- \quad \text{with} \quad \tilde{\boldsymbol{\sigma}}^\pm = \sum_{a=1}^3 \langle \tilde{\sigma}_a \rangle_\pm \mathbf{n}_a \otimes \mathbf{n}_a = \sum_{a=1}^3 \left[\lambda \langle \varepsilon_1 + \varepsilon_2 + \varepsilon_3 \rangle_\pm + 2\mu \langle \varepsilon_a \rangle_\pm \right] \mathbf{n}_a \otimes \mathbf{n}_a \quad (5.36)$$

for which the principal directions of the stress and strain tensor do coincide for isotropic materials. Based on this split, MIEHE ET AL. [231, 232] proposed a simplified stress-based brittle failure criterion for mixed tensile-compression stress modes, characterized by the threshold-type crack driving state function

$$D = \zeta \left\langle \sum_{a=1}^3 \left(\frac{\langle \tilde{\sigma}_a \rangle_+}{\sigma_c} \right)^2 - 1 \right\rangle_+ \quad (5.37)$$

with the critical fracture stress $\sigma_c > 0$. This models an isotropic failure surface in the principal effective stress space.

Energetic criterion without threshold. A strain criterion for brittle fracture without threshold was first proposed by MIEHE ET AL. [225] and results with a damage-type degradation at low stress levels. Such a criterion is based on the following fracture contribution to the work density function (5.11)

$$W_{frac}(d, \nabla d) = g_c \gamma_l(d, \nabla d) . \quad (5.38)$$

in terms of the crack surface density function γ_l . Here, g_c is the Griffith's critical energy release rate, that enters the formulation as the key material parameter on the side of fracture mechanics. Next, the fracture driving force takes the form

$$F^f - R^f = 2(1 - d)\tilde{\psi}^+(\boldsymbol{\varepsilon}) - \frac{g_c}{l}[d - l^2\Delta d]. \quad (5.39)$$

Following same procedure as the case with threshold in previous section, the crack driving state function D yields

$$D := \frac{2\tilde{\psi}^+}{g_c/l} \quad (5.40)$$

It is defined as the ratio between the locally stored positive effective elastic energy $\tilde{\psi}^+$ and the Griffith's critical energy release rate parameter g_c , which is smeared out over the fracture length scale l . The modified viscosity of the crack propagation η^f in (5.34) for this case reads

$$\eta^f := \frac{l}{g_c}\eta. \quad (5.41)$$

A relation between the above introduced fracture parameters: g_c , ψ_c and σ_c , can be deduced for the isotropic brittle fracture case, based on an analytical study of homogeneous and localized solutions of gradient damage models outlined in the works of PHAM ET AL. [268] and SICSIC & MARIGO [286] as

$$g_c = \frac{4}{3} w \psi_c \quad \text{and} \quad \sigma_c = \sqrt{2E\psi_c} \quad \text{with} \quad w = 2l\sqrt{2} \quad (5.42)$$

in terms of the Young's modulus E and the width of the crack band w .

5.4. Formulation of the virtual element method

Following the work of BREZZI ET AL. [71], the main idea of the virtual element method is a Galerkin projection of the unknowns onto a specific ansatz space. The domain Ω is partitioned into non-overlapping polygonal elements which need not to be convex and can have any arbitrary shape with different node numbers, as plotted in Figure 5.4 representing a *bird-like* element with vertices \boldsymbol{x}_I . Here a low-order approach is adopted, see WRIGGERS ET AL. [329] and WRIGGERS & HUDOBIVNIK [324], using linear ansatz functions where nodes are placed only at the vertices of the polygonal elements. Furthermore, the restriction of the element shape functions to the element boundaries are linear functions.

5.4.1. Ansatz functions for VEM. The virtual element method relies on the split of the ansatz space into a part $\boldsymbol{\mathfrak{U}}_\Pi$ representing the projected primary field defined in (5.6) and a remainder

$$\boldsymbol{\mathfrak{U}}^h = \boldsymbol{\mathfrak{U}}_\Pi^h + (\boldsymbol{\mathfrak{U}}^h - \boldsymbol{\mathfrak{U}}_\Pi^h) \quad \text{with} \quad \boldsymbol{\mathfrak{U}}_\Pi^h := \{\boldsymbol{u}_\Pi^h, d_\Pi^h\} \quad (5.43)$$

The projection $\boldsymbol{\mathfrak{U}}_\Pi^h$ is defined at element level by a linear ansatz function \mathbf{N}_Π as

$$\boldsymbol{\mathfrak{U}}_\Pi^h = \begin{bmatrix} u_{\Pi x} \\ u_{\Pi y} \\ d_\Pi \end{bmatrix} = \mathbf{a} \cdot \mathbf{N}_\Pi = \begin{bmatrix} a_1 & a_4 & a_7 \\ a_2 & a_5 & a_8 \\ a_3 & a_6 & a_9 \end{bmatrix} \begin{bmatrix} 1 \\ x \\ y \end{bmatrix} \quad (5.44)$$

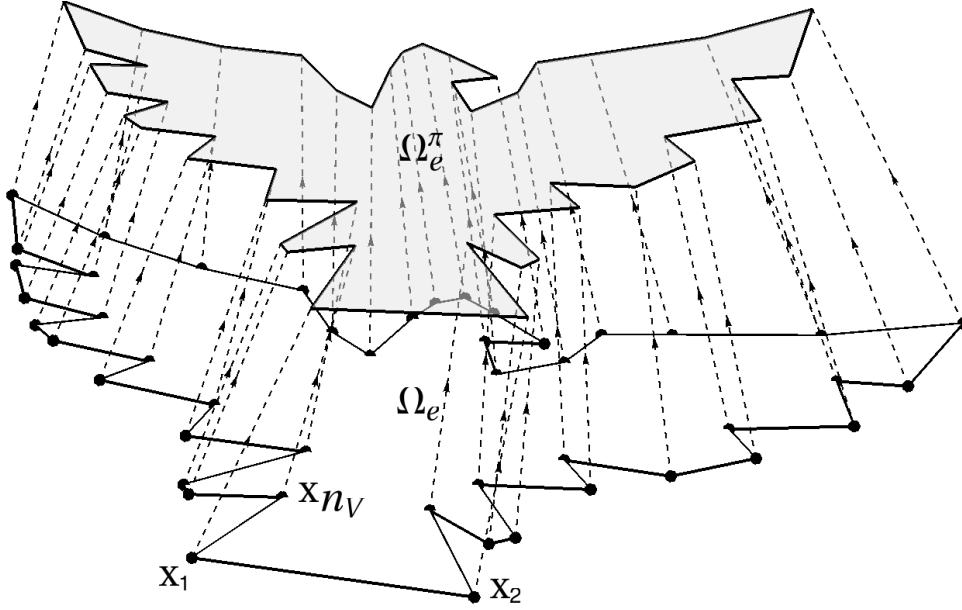


Figure 5.4: Polynomial basis function for the virtual element ansatz with vertices \mathbf{x}_I .

with the unknowns \mathbf{a} . The projection \mathfrak{U}_Π^h is now defined such that it satisfies

$$\int_{\Omega_e} \nabla \mathfrak{U}_\Pi^h dV \stackrel{!}{=} \int_{\Omega_e} \text{Grad } \mathfrak{U}^h dV \quad (5.45)$$

which yields, with the linear ansatz in (7.30) that $\nabla \mathfrak{U}_\Pi^h$ is constant,

$$\nabla \mathfrak{U}_\Pi^h|_e \stackrel{!}{=} \frac{1}{\Omega_e} \int_{\Omega_e} \text{Grad } \mathfrak{U}^h dV = \frac{1}{\Omega_e} \int_{\partial\Omega_e} \mathfrak{U}^h \otimes \mathbf{N} dA \quad (5.46)$$

where \mathbf{N} is the normal at the boundary $\partial\Omega_e$ of the domain Ω_e of a virtual element e , see Figure 5.5. Thus label $\square|_e$ represents element quantities that have constant value within an element e . A direct computation of the projected gradient yields with the linear ansatz in (7.30) the simple matrix form

$$\nabla \mathfrak{U}_\Pi^h|_e = \begin{bmatrix} \nabla u_{\Pi x} \\ \nabla u_{\Pi y} \\ \nabla d_\Pi \end{bmatrix} = \begin{bmatrix} a_4 & a_7 \\ a_5 & a_8 \\ a_6 & a_9 \end{bmatrix} \quad (5.47)$$

The boundary integral in (7.34) has to be evaluated. To this end, a linear ansatz for the primary fields along the element edges is introduced as

$$(\mathfrak{U}^h)_k = (1 - \xi_k) \mathfrak{U}_1 + \xi_k \mathfrak{U}_2 = M_{k1} \mathfrak{U}_1 + M_{k2} \mathfrak{U}_2 \quad \text{with } \xi_k = \frac{x_k}{L_k} \quad (5.48)$$

for a boundary segment k of the virtual element. The local nodes: 1–2 are chosen in counter-clockwise order and can be found in Figure 5.5. In (7.37) M_{k1} is the ansatz function along a segment k , related to node 1, ξ_k is the local dimensionless coordinate and \mathfrak{U}_1 is the nodal value at that node. The ansatz function M_{k2} is defined in the same way. From (7.34)–(7.37), the unknowns a_4 – a_9 can be computed from the normal vectors

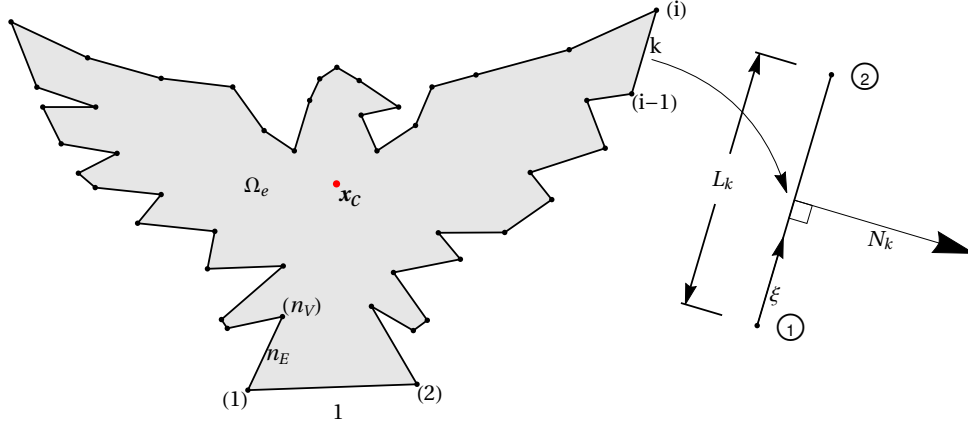


Figure 5.5: Virtual element with n_V nodes and local boundary segment of the bird-like polygonal element.

of the boundary segments in elements and nodal displacement as

$$\begin{bmatrix} a_4 & a_7 \\ a_5 & a_8 \\ a_6 & a_9 \end{bmatrix} = \frac{1}{\Omega_e} \int_{\partial\Omega_e} \mathbf{u}^h \otimes \mathbf{N} \, dA = \frac{1}{\Omega_e} \sum_{k=1}^{n_V} \int_{\partial\Omega_k} \begin{bmatrix} u_x(\mathbf{x})N_x & u_x(\mathbf{x})N_y \\ u_y(\mathbf{x})N_x & u_y(\mathbf{x})N_y \\ d(\mathbf{x})N_x & d(\mathbf{x})N_y \end{bmatrix} dA \quad (5.49)$$

where we have used $\mathbf{N} = \{N_x, N_y\}^T$ and $\mathbf{u} = \{u_x, u_y, d\}^T$, furthermore n_V is the number of element vertices which coincides with the number of segments (edges) of the element, for first order VEM. Note that the normal vector \mathbf{N} changes from segment to segment. In the 2D case it can be computed for a segment k as

$$\mathbf{N}_k = \begin{Bmatrix} N_x \\ N_y \end{Bmatrix}_k = \frac{1}{L_k} \begin{Bmatrix} y_1 - y_2 \\ x_2 - x_1 \end{Bmatrix}_k \quad (5.50)$$

with $\{x_i, y_i\}_{i=1,2}$ being the local coordinates of the two vertices of the segment k . The integral in (7.38) can be evaluated for the ansatz functions (7.37) exactly by using the trapezoidal or Gauss-Lobatto rule. By selecting the vertices as the Gauss-Lobatto points it is sufficient to know only the nodal values

$$\mathbf{u}_e = \{\mathbf{u}_1, \mathbf{u}_2, \dots, \mathbf{u}_{n_V}\} \quad (5.51)$$

at the n_V vertices V in Figure 5.5. Since the ansatz function in (7.37) fulfills the property $M_I(x_J) = \delta_{IJ}$ the actual form of the function M does not enter the evaluation of the boundary integrals which makes the evaluation extremely simple. Finally, by comparing (7.35) and (7.38) the unknowns a_4 to a_9 are obtained by inspection, for further details see e.g. WRIGGERS ET AL. [329]. The projection in (7.34) does not determine the ansatz \mathbf{u}_{Π}^h in (7.30) completely and has to be supplemented by a further condition to obtain the constants a_1 , a_2 and a_3 . For this purpose we adopt the condition that the sum of the nodal values of \mathbf{u}^h and of its projection \mathbf{u}_{Π}^h are equal. This yields for each element Ω_e

$$\frac{1}{n_V} \sum_{I=1}^{n_V} \mathbf{u}_{\Pi}^h(\mathbf{x}_I) = \frac{1}{n_V} \sum_{I=1}^{n_V} \mathbf{u}^h(\mathbf{x}_I) \quad (5.52)$$

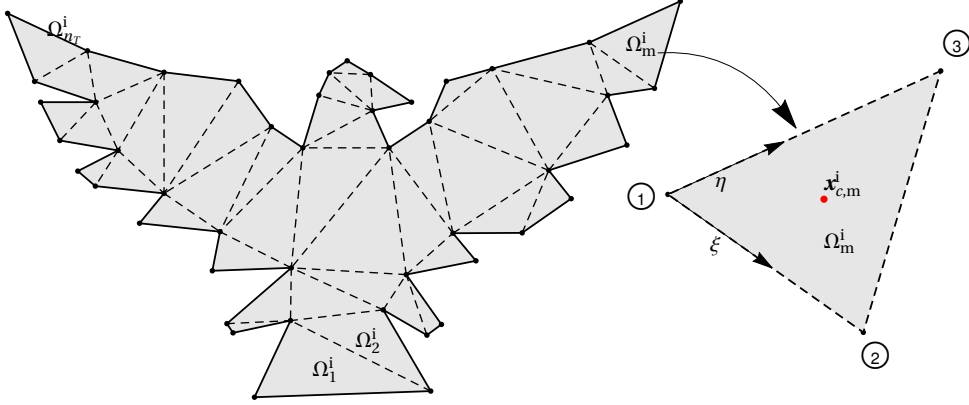


Figure 5.6: Internal triangular mesh of the bird-like polygonal element.

where \mathbf{x}_I are the coordinates of the nodal point I and the sum includes all boundary nodes. Substituting (7.30) and (7.37) in (6.38), results with the three unknowns a_1 , a_2 and a_3 as

$$\begin{bmatrix} a_1 \\ a_2 \\ a_3 \end{bmatrix} = \frac{1}{n_V} \sum_{I=1}^{n_V} [\mathbf{u}_I - \nabla \mathbf{u}_{\Pi I} \cdot \mathbf{x}_I] = \frac{1}{n_V} \sum_{I=1}^{n_V} \begin{bmatrix} u_{xI} - u_{x,x} x_I - u_{x,y} y_I \\ u_{yI} - u_{y,x} x_I - u_{y,y} y_I \\ d_I - d_{,x} x_I - d_{,y} y_I \end{bmatrix} \quad (5.53)$$

Thus, the ansatz function \mathbf{u}_{Π}^h of the virtual element is completely defined.

5.4.2. Construction of the virtual element. A virtual element is based only on the projection \mathbf{u}_{Π}^h of the displacement and fracture phase-field would lead to a rank deficient element once the number of vertices is greater than 3. Thus the formulation has to be stabilized like the classical one-point integrated elements developed by FLANAGAN & BELYTSCHKO [125], BELYTSCHKO & BINDEMAN [50], REESE ET AL. [276], REESE & WRIGGERS [275], MUELLER-HOEPPE ET AL. [246], KORELC ET AL. [185] and KRYSL [187]. In the following we will develop a virtual element for phase-field modeling of brittle fracture in isotropic elastic solids. To this end, the potential density functional defined in (5.26) can be rewritten by exploiting the split in (7.29). Thus we have, by summing up all element contributions for the n_e virtual elements

$$\Pi^\tau(\mathbf{u}) = \mathbf{A} \sum_{e=1}^{n_e} \Pi^\tau(\mathbf{u}_e) \quad \text{with} \quad \Pi^\tau(\mathbf{u}_e) = [\Pi_c^\tau(\mathbf{u}_{\Pi}^h)|_e + \Pi_{stab}^\tau(\mathbf{u}^h - \mathbf{u}_{\Pi}^h)|_e], \quad (5.54)$$

based on a constant part Π_c^τ and an associated stabilization term Π_{stab}^τ . Herein, the crack driving force \mathcal{H} is a local history variable evaluated *only once* at the element level and used in both parts of the potential density functional. The first part in (6.40)₂ can be computed as

$$\Pi_c^\tau(\mathbf{u}_{\Pi}^h)|_e = \int_{\Omega_e} \pi^\tau(\mathbf{e}_{\Pi}^h) dV - \int_{\Omega_e} \bar{\mathbf{f}} \cdot \mathbf{u}_{\Pi}^h dV - \int_{\partial\Omega_e} \bar{\mathbf{t}} \cdot \mathbf{u}_{\Pi}^h dA \quad \text{with} \quad \mathbf{e}_{\Pi}^h = \{\boldsymbol{\varepsilon}_{\Pi}^h, d_{\Pi}^h, \nabla d_{\Pi}^h\} \quad (5.55)$$

The projected strain tensor can be computed from the projected displacement as

$$\boldsymbol{\varepsilon}_{\Pi}^h = \frac{1}{2} [\nabla \mathbf{u}_{\Pi}^h + \nabla^T \mathbf{u}_{\Pi}^h]. \quad (5.56)$$

The primary fields \mathbf{u}_{Π}^h are linear functions and their gradient $\nabla \mathbf{u}_{\Pi}^h$ is constant over the area of the virtual element Ω_e , as a consequence, the potential π^τ is integrated by evaluating the function at the element centroid \mathbf{x}_c as shown in Figure 5.5 and multiplying it with domain size Ω_e analogous to the standard Gauss integration scheme in FEM

$$\int_{\Omega_e} \pi^\tau(\mathbf{e}_{\Pi}^h) dV = \pi^\tau(\mathbf{e}_{\Pi}^h)|_c \Omega_e \quad (5.57)$$

with the label $\square|_c$ refers to quantities evaluated at the element centroid \mathbf{x}_c . The potential density function $\pi^\tau(\mathbf{e}_{\Pi}^h)$ is still a nonlinear function with respect to the displacement and the crack phase-field nodal degrees of freedom.

Next, the stabilization potential has to be derived for the coupled problem based on the potential (5.26). Following the recent work of WRIGGERS ET AL. [329], we introduce a non-linear stabilization procedure, that takes the form

$$\Pi_{stab}^\tau(\mathbf{u}^h - \mathbf{u}_{\Pi}^h)|_e = \widehat{\Pi}^\tau(\mathbf{u}^h)|_e - \widehat{\Pi}^\tau(\mathbf{u}_{\Pi}^h)|_e \quad (5.58)$$

For the stabilization density function $\widehat{\pi}^\tau$, we propose a similar function to the original density function (5.26), however scaled by a constant value β as: $\widehat{\pi}^\tau = \beta \pi^\tau$. In (6.44), the stabilization with respect to the projected primary fields $\widehat{\Pi}^\tau(\mathbf{u}_{\Pi}^h)|_e$ can be then calculated as (6.43), yielding

$$\widehat{\Pi}^\tau(\mathbf{u}_{\Pi}^h)|_e = \beta \pi^\tau(\mathbf{e}_{\Pi}^h)|_c \Omega_e \quad (5.59)$$

The potential $\widehat{\Pi}^\tau(\mathbf{u}^h)|_e$ is computed by applying standard FEM procedure, i.e. by first discretizing the virtual element domain Ω_e into internal triangle element mesh consisting of $n_T = n_E - 2$ triangles as plotted in Figure 5.6 for the *bird-like* polygonal element. Then the integral over Ω_e is transformed into the sum of integrals over triangles. By using a linear ansatz for the primary fields \mathbf{u} , an approximation can be computed for the constitutive variables \mathbf{e} within each triangle Ω_m^i of the inscribed mesh, see WRIGGERS ET AL. [329]. This gives

$$\widehat{\Pi}^\tau(\mathbf{u}^h)|_e = \int_{\Omega_e} \widehat{\pi}^\tau(\mathbf{e}^h) dV = \beta \int_{\Omega_e} \pi^\tau(\mathbf{e}^h) dV = \beta \sum_i^{n_T} \Omega_e^i \pi^\tau(\mathbf{e}^h)|_c \quad (5.60)$$

where $\pi^\tau(\mathbf{e}^h)|_c$ is the potential density function evaluated at the triangle centroid \mathbf{x}_c^i and Ω_e^i is the area of the i^{th} triangle in the element e , as plotted in Figure 5.6.

To compute the stabilization parameter β , a connection to the bending problem was imposed regarding to the bulk energy as outlined in WRIGGERS & HUDOBIVNIK [324]. By limiting the element size Ω_e towards 0, the difference between the potentials of projected values $\widehat{\Pi}^\tau(\mathbf{u}_{\Pi}^h)$ and the true values $\widehat{\Pi}^\tau(\mathbf{u}^h)$ will also approach towards 0, thus stabilization will disappear in limit. Due to the finer mesh requirements of the fracture phase field problem compared with [324], the choice of β factor term is less relevant, since it is only relevant for coarse meshes. In this regard we propose a constant value for β taken from the interval:

$$0 < \beta \leq 1 \quad (5.61)$$

Note that for β approaching zero, the potential $\Pi^\tau(\mathbf{u}^h)$ in (6.40) will depend only on the projection part $\Pi_c^\tau(\mathbf{u}_\Pi^h)$, leading to rank deficiency. However when $\beta = 1$ the FEM results related to the internal mesh will be reproduced. A numerical study of the stabilization parameter influence on the load-deflection curves of the overall structural response will be investigated in Section 5.5.

All further derivations leading to the residual vector \mathbf{R}_e and the tangent matrix \mathbf{K}_e of the virtual element were performed with the symbolic tool ACEGEN. This yields for (6.40) along with the potentials (6.41) and (6.44)–(6.46) the following:

$$\mathbf{R}_e = \frac{\partial \Pi^\tau(\mathbf{u}_e)}{\partial \mathbf{u}_e} \quad \text{and} \quad \mathbf{K}_e = \frac{\partial \mathbf{R}_e}{\partial \mathbf{u}_e} \quad (5.62)$$

With these expressions at hand, we adopt a global Newton-Raphson algorithm for the coupled problem, resulting to the following linearized system

$$\mathbf{R} + \mathbf{K} \Delta \mathbf{u} = \mathbf{0} \quad \text{with} \quad \mathbf{R} = \bigwedge_{e=1}^{n_e} \mathbf{R}_e, \quad \mathbf{K} = \bigwedge_{e=1}^{n_e} \mathbf{K}_e \quad \text{and} \quad \mathbf{u} = \bigwedge_{e=1}^{n_e} \mathbf{u}_e \quad (5.63)$$

that determines at given global primary fields \mathbf{u} their linear increment $\Delta \mathbf{u}$ in a typical Newton-type iterative solution step. This system of nonlinear equations has to be solved in a nested algorithm, where the displacement and the crack phase-field are the global unknown variables.

5.5. Representative numerical examples

We now demonstrate the performance of the proposed virtual element formulation for the phase-field modeling of brittle fracture at small deformations by means of representative numerical examples. For comparison purposes, results of the standard finite element method (FEM) are also demonstrated. All computations are performed by using a nested Newton-Raphson algorithm. Load stepping is applied when necessary. Due to the fact that all formulations are linearized in a consistent manner using ACEGEN, quadratic convergence is achieved within a load step. In Section 5.5.1, we compare VEM and FEM results for the standard single-edge-notched tension test of MIEHE ET AL. [225]. Furthermore different studies will be discussed here to demonstrate the efficiency of the virtual element scheme for solving fracture-mechanics problems. Next, a symmetric three-point bending test is investigated in Section 5.5.2. Thereafter, a crack initiation and branching in a bi-material specimen is analyzed in Section 5.5.3. Finally, in Section 5.5.4, a tensile specimen with double notched or two holes, representing a mixed-mode fracture, is considered to demonstrate the performance of the proposed method for curved crack propagation.

5.5.1. Investigation of single-edge notched tension test. The first benchmark test considers a square plate with a horizontal notch placed at the middle height from the left outer surface to the center of the specimen. The geometrical setup and the loading conditions of the specimen are depicted in Figure 6.5(a). The size of the square specimen is chosen to be $L = 0.5$ mm. We fixed the bottom edge of the plate in y -direction and applied a vertical displacement at the top edge until the plate is fully broken. The material parameters used in the simulation are the same as in the reference work of MIEHE ET AL. [225]. The elastic parameters are chosen as $\lambda = 121.1538$ kN/mm² and

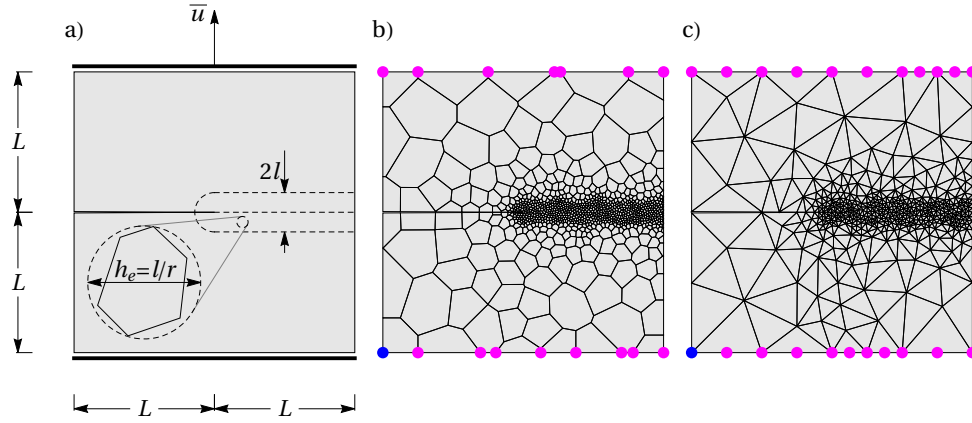


Figure 5.7: Single-edge notched tension test. a) Geometry and boundary conditions, b) VEM with Voronoi mesh and c) triangular finite element mesh.

$\mu = 80.7692 \text{ kN/mm}^2$, the viscosity of the crack propagation $\eta = 10^{-6} \text{ kNs/mm}^2$ and the critical energy release rate as $g_c = 2.7 \times 10^{-3} \text{ kN/mm}$. The specimen is discretized by using different virtual elements (VEM) in Figure 6.5(b) and finite element (FEM) formulations Figure 6.5(c). Here we use the following notations: VEM-VO with a Voronoi mesh ; VEM-T2 with 6 noded triangle representing a *first order* VEM (Note that: T2 in this case implies that, the triangle mesh used is the same as for the second order FEM and *not second order VEM*) ; FEM-T1 with linear triangle and FEM-T2 with quadratic triangle, to test the robustness of the virtual element formulation. A mesh refinement in the expected fracture zone is applied; this is based on the ratio $r := l/h_e$ between the mesh size h_e and the fracture length scale l , as sketched in Figure 6.5(a).

Figure 6.6 shows the contour plot of the fracture phase-field d simulated using the virtual element formulations with a Voronoi mesh, for two different length scales $l_1 = 0.0375 \text{ mm}$ and $l_2 = 0.0075 \text{ mm}$ with the same length/mesh ratio $r = 8$. The crack phase-field initiates at the notch-tip and propagates horizontally till separation, as outlined in MIEHE ET AL. [225]. To illustrate the length scale effect on the overall structural response, we plot in Figure 6.7 the load-displacement curves for four different elements and two length scales. For the smaller length scale parameter l , we observe: i) a higher peak force F as outlined in Figure 6.7(b) thereafter F drops to zero at cracking, ii) a sharp crack pattern is obtained as expected, see Figure 6.6(d)–(f). The VEM results are in a good agreement with the reference work [225]. Table 6.2 compares the different FEM and VEM discretization, related to the force-displacement F - u curves in Figure 6.7(a),

Table 5.1: A comparison between different FEM and VEM discretizations, related to F - u curves in Figure 6.7(a).

	FEM-T1	FEM-T2	VEM-T2	VEM-VO
Number of elements	37981	37981	37981	44473
Number of nodes	19040	76060	76060	88950
Number of degrees of freedom	57160	228155	228155	266831
Total Number of steps	804	1596	673	645
Total number of iterations	6286	13236	5737	5586
Average iterations/step	7.8	8.3	8.5	8.6

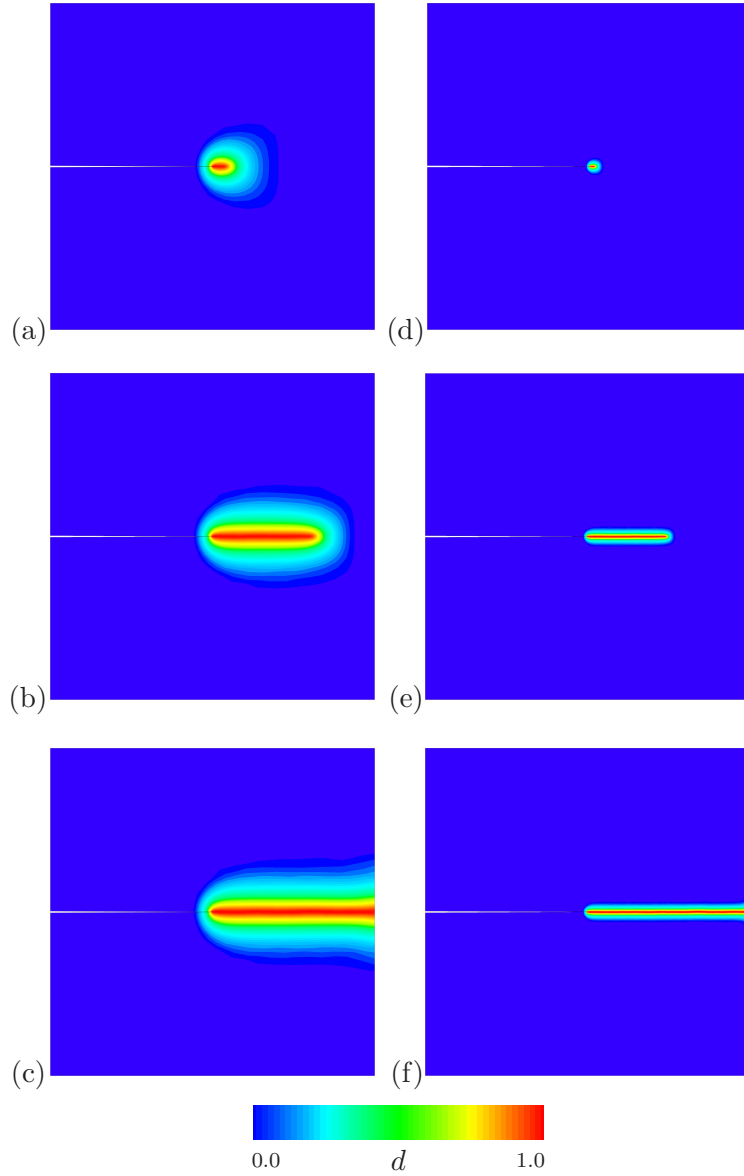


Figure 5.8: Single-edge notched tension test. Contour plots of the fracture phase-field d for two fracture length scales l and three different deformation states up to final rupture. (a)–(c) $l = 0.0375$ mm and (d)–(f) $l = 0.0075$ mm.

Table 5.2: Number of degrees of freedom for different FEM and VEM discretizations, related to the convergence study in Figure 5.10(b).

$r = l/h_e$	$\frac{1}{4}$	$\frac{1}{2}$	1	2	4	8	12	16
FEM-T1	142	264	542	1310	3759	12217	25706	43975
FEM-T2	521	993	2080	5116	14859	48629	102499	175505
VEM-T2	521	993	2080	5116	14859	48629	102499	175505
VEM-VO	378	886	1978	4265	16119	56599	98624	170130

with respect to robustness and efficiency.

Next, we investigate mesh objectivity and convergence of the virtual element formulations for the phase-field approach with respect to the mesh size. To this end, Figure 5.10(b)

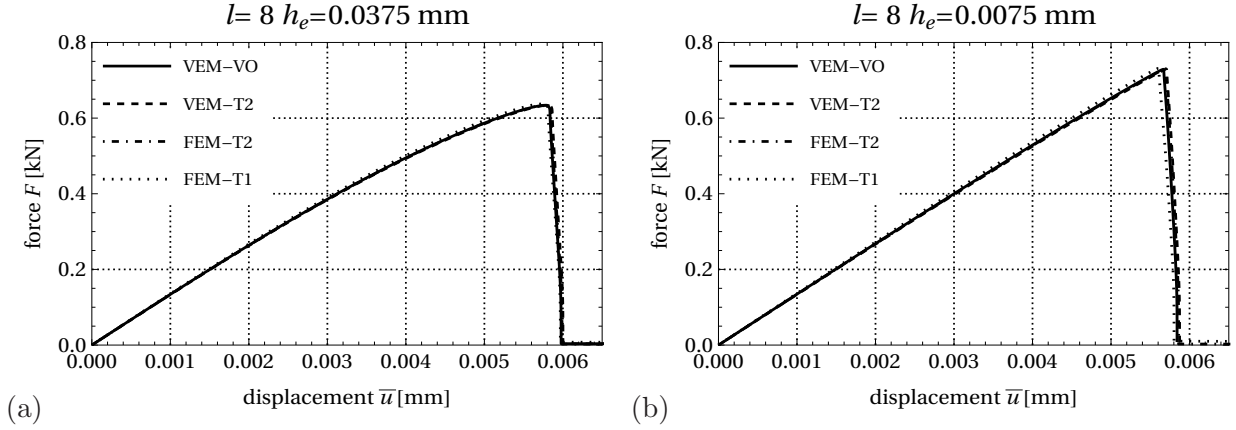


Figure 5.9: Load–displacement responses for single-edge notched tension test. A comparison between different VEM and FEM discretization for two different fracture length scales. (a) $l = 0.0375 \text{ mm}$ and (b) $l = 0.0075 \text{ mm}$.

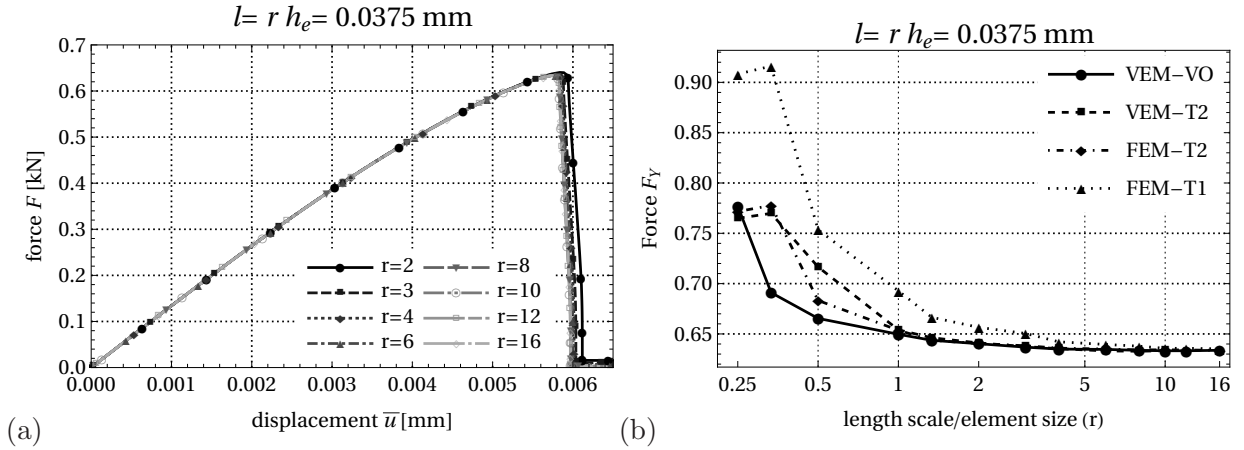


Figure 5.10: Single-edge notched tension test. a) Load–displacement response for VEM-Voronoi mesh, resulting with mesh objective results when $r = l/h_e \geq 2$. b) Convergence of the VEM and FEM results for the phase-field approach with respect to mesh size.

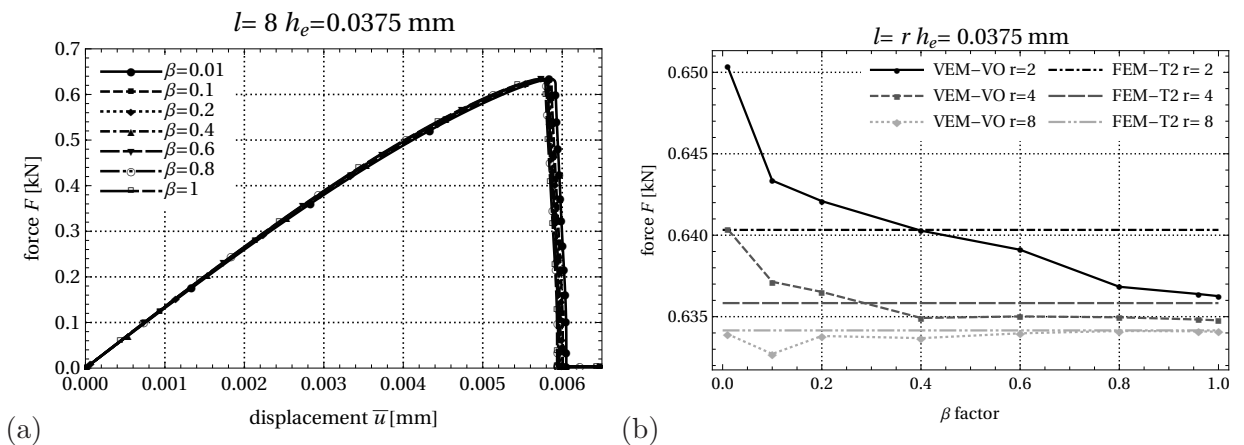


Figure 5.11: Single-edge notched tension test. a) A numerical study of the stabilization parameter influence on the load-deflection curves of the overall structural response for VEM with Voronoi mesh. b) Comparison of the FEM and VEM peak force results for different values of the stabilization parameter β and different mesh size l/h .

demonstrates the load versus the *logarithmically scaled* mesh size/length scale ratio r for four different element formulations at the crack initiation. A converged solution for the critical force at crack initiation can be obtained for mesh-size/length-scale ratio: $r \geq 2$. As a consequence *mesh objectivity* is achieved for $r \geq 2$ as illustrated in Figure 5.10(a) using VEM-VO with fixed length scale $l = 0.0375$ mm. Furthermore, Figure 5.10(b) shows that the virtual element method performance is comparable to using finite elements of higher order, e.g. FEM-T2. In this regard, Table 5.2 outlines a description of the number of degrees of freedom for different FEM and VEM discretizations related to the convergence study in Figure 5.10(b).

Finally, Figure 5.11 points out the influence of the stabilization parameter β on the load-deflection curves of the overall structural response. Note that, for $0 < \beta \leq 1$ the same $F-u$ results are obtained in Figure 5.11(a), using VEM-VO with the length scale $l = 8h_e = 0.0375$ mm. In order to check the convergence of the virtual element stabilization formulation, we plot in Figure 5.11(b) the load versus stabilization parameter for different mesh-size/length-scale ratio r and compare them with the FEM-T2 element. We observe that, by increasing r a better result close to the quadratic FEM is achieved. However, the difference in the critical force at crack initiation for all β is very small. As a consequence, we chose a value for the stabilization parameter as $\beta = 0.4$ in all the simulations, in which VEM coincide with FEM results.

5.5.2. Analysis of a three-point bending test. The second model problem is concerned with analyzing brittle fracture of three point bending test of a supported notched beam. The geometry and the loading of the specimen are given in Figure 5.12(a). The size of the specimen is chosen to be: $H = 2$ mm, $L = 4$ mm, $H_g = 0.4$ mm and $L_g = 0.2$ mm. The material parameters used in the simulation are the same as in the reference work

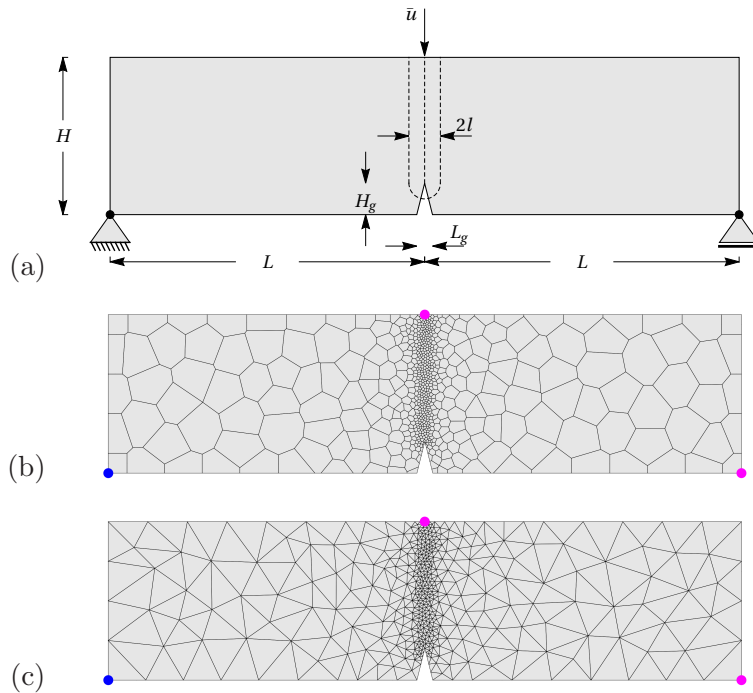


Figure 5.12: Three-point bending test. a) Geometry and boundary conditions, b) VEM with Voronoi mesh and c) triangular finite element mesh.

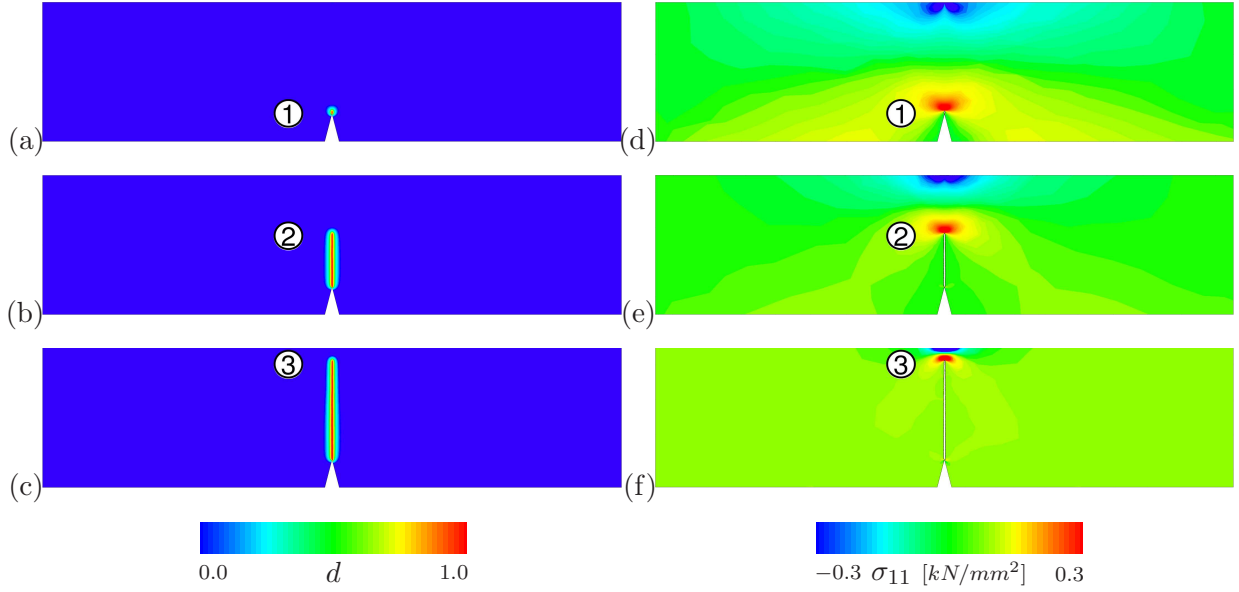


Figure 5.13: Three-point bending test. a) Contour plots of the fracture phase-field d in (a)–(c) and the normal stress σ_{11} during the crack evolution in (d)–(f).

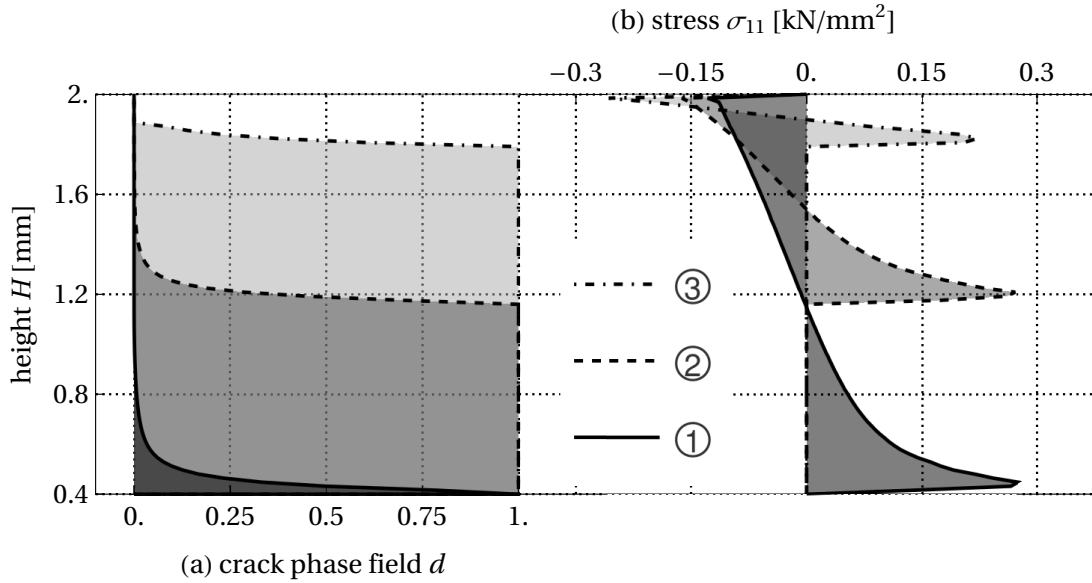


Figure 5.14: Three-point bending test. Evolution of the crack phase-field d in (a) and the stress σ_{11} in (b) for three different deformation states corresponding to the contour plots in Figure 5.13 at a cut in the center of the beam.

of MIEHE ET AL. [225]. The elastic parameters are chosen as $\lambda = 12.0 \text{ kN/mm}^2$ and $\mu = 8.0 \text{ kN/mm}^2$, the viscosity of the crack propagation $\eta = 10^{-6} \text{ kNs/mm}^2$, the critical energy release rate as $g_c = 5.0 \times 10^{-4} \text{ kN/mm}$ and the stabilization parameter as $\beta = 0.4$. Different element formulations are studied to illustrate the robustness of the proposed VEM. A mesh refinement in the expected fracture zone is applied, see Figure 5.12(b)–(c).

Figure 5.13 demonstrates contour plots of the fracture phase-field d and the normal stress σ_{11} simulated using VEM-VO with length scale parameter $l = 0.03 \text{ mm}$ and length/mesh ratio $r = 8$. The evolution of the phase-field and the normal stress at a cut

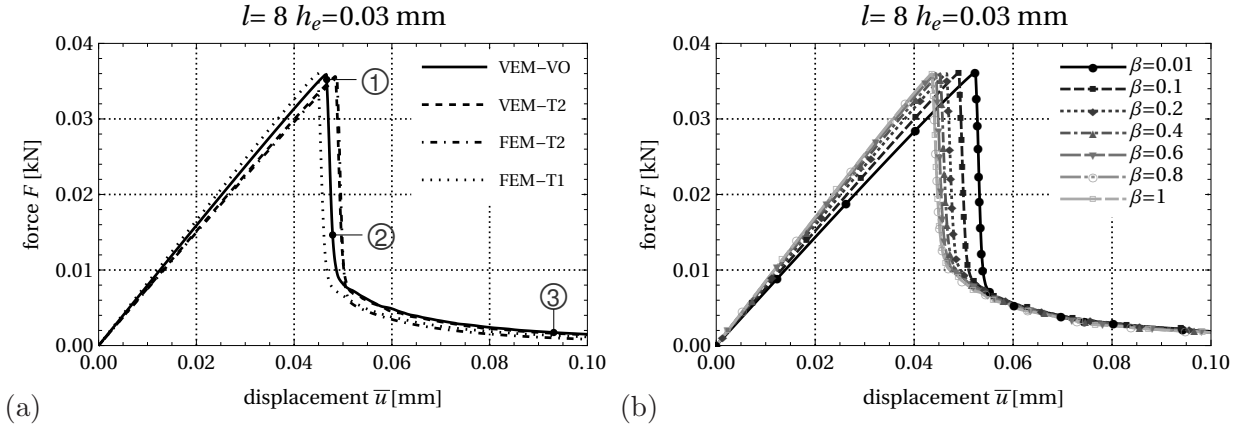


Figure 5.15: Load–displacement responses for three-point bending test. (a) Comparison between different VEM and FEM discretization and (b) numerical study of the stabilization parameter influence on the load-deflection curves of the overall structural response for VEM with Voronoi mesh.

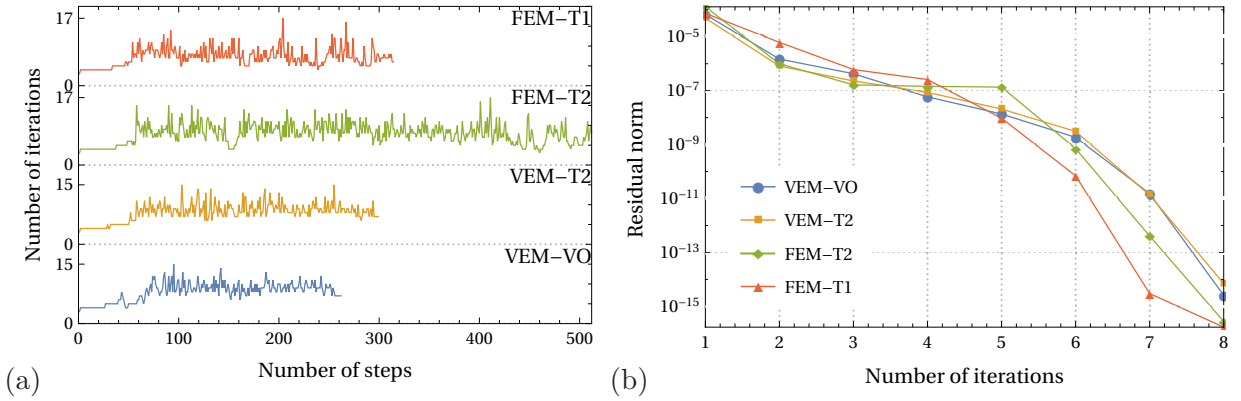


Figure 5.16: Convergence properties for three-point bending test. (a) Comparison between the total number of iterations in each time step of the different VEM and FEM discretization that required to achieve convergence and (b) the residual norm for the final time step versus the number of iterations needed to obtain convergence.

in the beam center for three different deformation states corresponding to Figure 5.13 is plotted in Figure 5.14. Tensile stresses are observed at the notch-tip when the beam is loaded, see Figure 5.13(d) and Figure 5.14(b). The crack starts to initiate in this tensile area and propagates straight to the load, resulting in a pure Mode-I failure of the beam as shown in Figure 5.13(c) and Figure 5.14(b). For visualization of crack surface, deformed regions with a crack phase-field $d \approx 1$ are not plotted in the stress distribution, see Figures 5.13(d)–(f).

Load-displacement curves of the overall structural response are plotted for different elements formulations of FEM and VEM for comparison purposes in Figure 5.15(a). Next, the influence of the stabilization parameter β is illustrated in Figure 5.15(b). As observed in the single-notch test above, for $0 < \beta \leq 1$ the same F - u results are obtained. Finally, Figure 5.16 illustrates the convergence properties for the different element formulations plotted in Figure 5.15(a). Note that we employed an efficient and robust monolithic scheme for all elements in the numerical implementations. Here, quadratic convergence for VEM and FEM discretization is achieved, see Figure 5.16(b). Furthermore, virtual

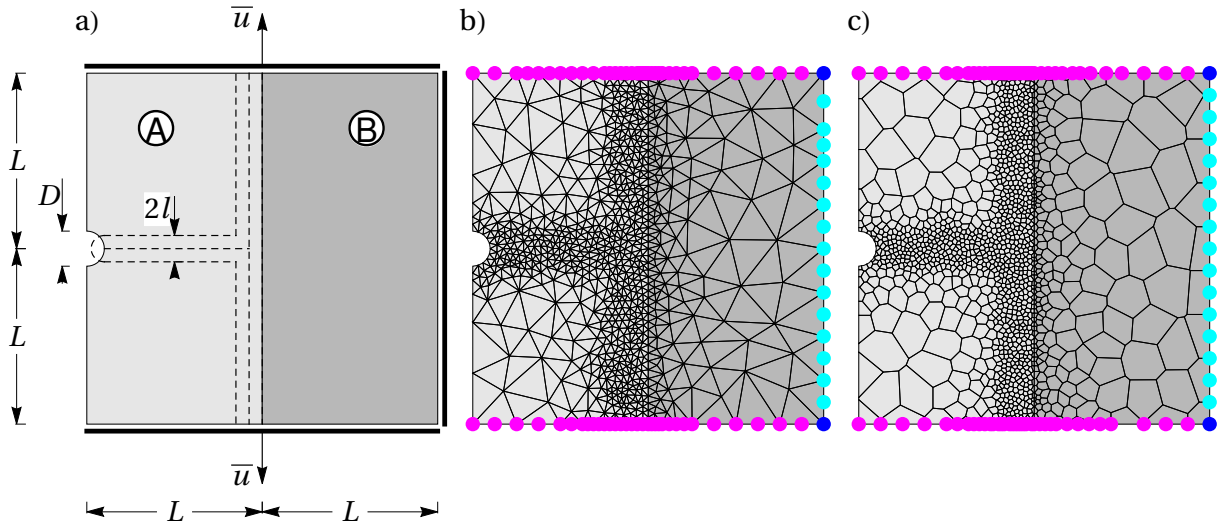


Figure 5.17: Bi-material specimen. a) Geometry and boundary conditions, b) triangular finite element mesh and c) VEM with Voronoi mesh.

elements required *fewer* steps and iterations for final convergence compared with finite element method, as shown in Figure 5.16(a). Thus here, VEM is more robust than FEM, however, this comes with extra computational costs.

5.5.3. Analysis of a crack in a Bi-Material plate. We model the fracture phenomena of a bi-material specimen under tensile loading as reported in the recent work of

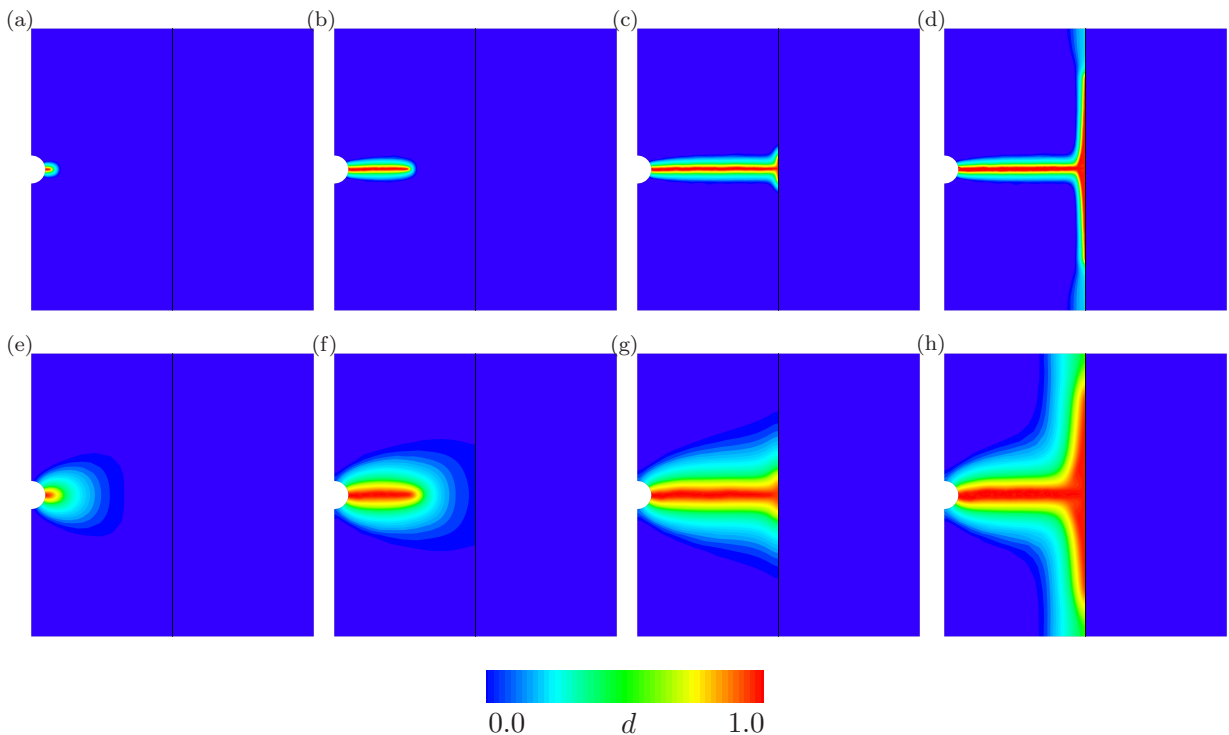


Figure 5.18: Bi-material specimen. Contour plots of the fracture phase-field d for two fracture length scales l and four different deformation states up to final rupture. (a)–(d) $l_1 = 1.25$ mm and (e)–(h) $l_2 = 5.0$ mm.

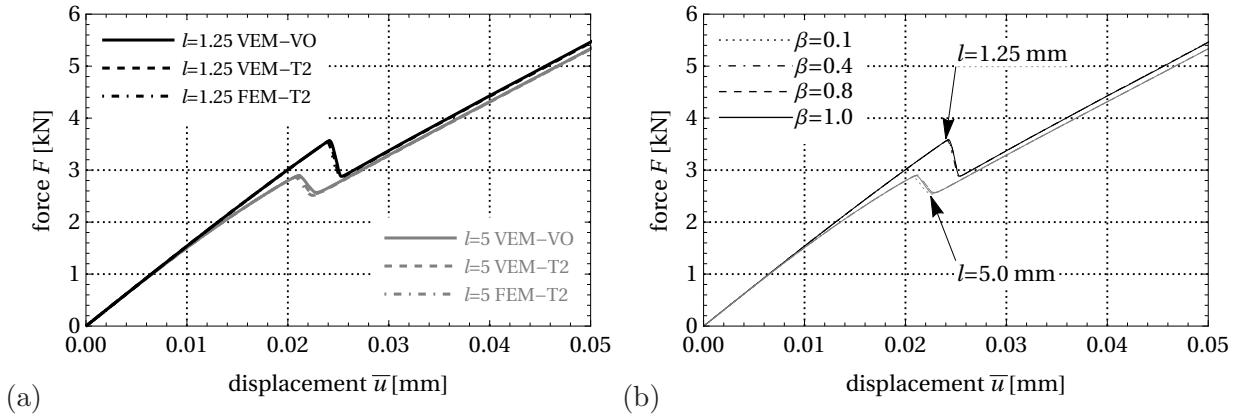


Figure 5.19: Load–displacement responses for the Bi-material test with two different fracture length scales. (a) A comparison between different VEM and FEM discretization and (b) numerical study of the stabilization parameter influence β for VEM with Voronoi mesh.

SARGADO ET AL. [280]. The aim here is to demonstrate crack phase-field initiation and branching. The geometrical setup and the loading conditions of the specimen are depicted in Figure 5.17(a). The size of the specimen is chosen to be: $L = 50$ mm and the diameter of notch is $D = 10$ mm. We fixed the right edge of the plate in x -direction and applied vertical displacement to the top and bottom edges until final failure. The material parameters used in the simulation are the same as in the reference work of SARGADO ET AL. [280]. B -material is stiffer than A -material and represents purely elastic material behavior without fracturing. Young's modulus is chosen for A -material as $E^A = 100$ kN/mm² and for B -material as $E^B = 200$ kN/mm², Poisson's ratio is set to $\nu = 0.2$, the viscosity of the crack propagation $\eta^A = 10^{-6}$ kNs/mm², the critical energy release rate for A -zone as

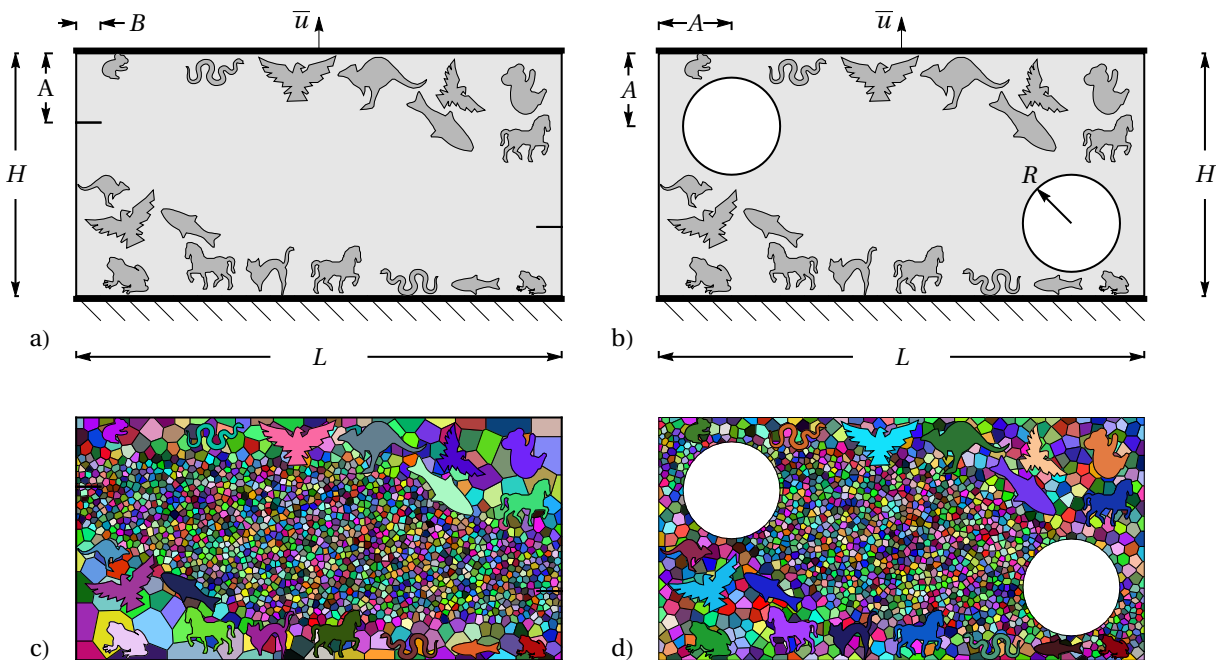


Figure 5.20: Tensile test with two notches or holes. a)-b) Geometry and boundary conditions. c)-d) VEM with Voronoi mesh.

$g_c^A = 10^{-4} \text{ kN/mm}$ and the stabilization parameter as $\beta = 0.4$. Different element formulations are studied to illustrate the robustness of the proposed VEM. A mesh refinement in the expected fracture zone is applied, see Figure 5.17(b)-(c).

Figure 5.18 shows the contour plot of the fracture phase-field d simulated using the virtual element formulations with a Voronoi mesh, for two different length scales $l_1 =$

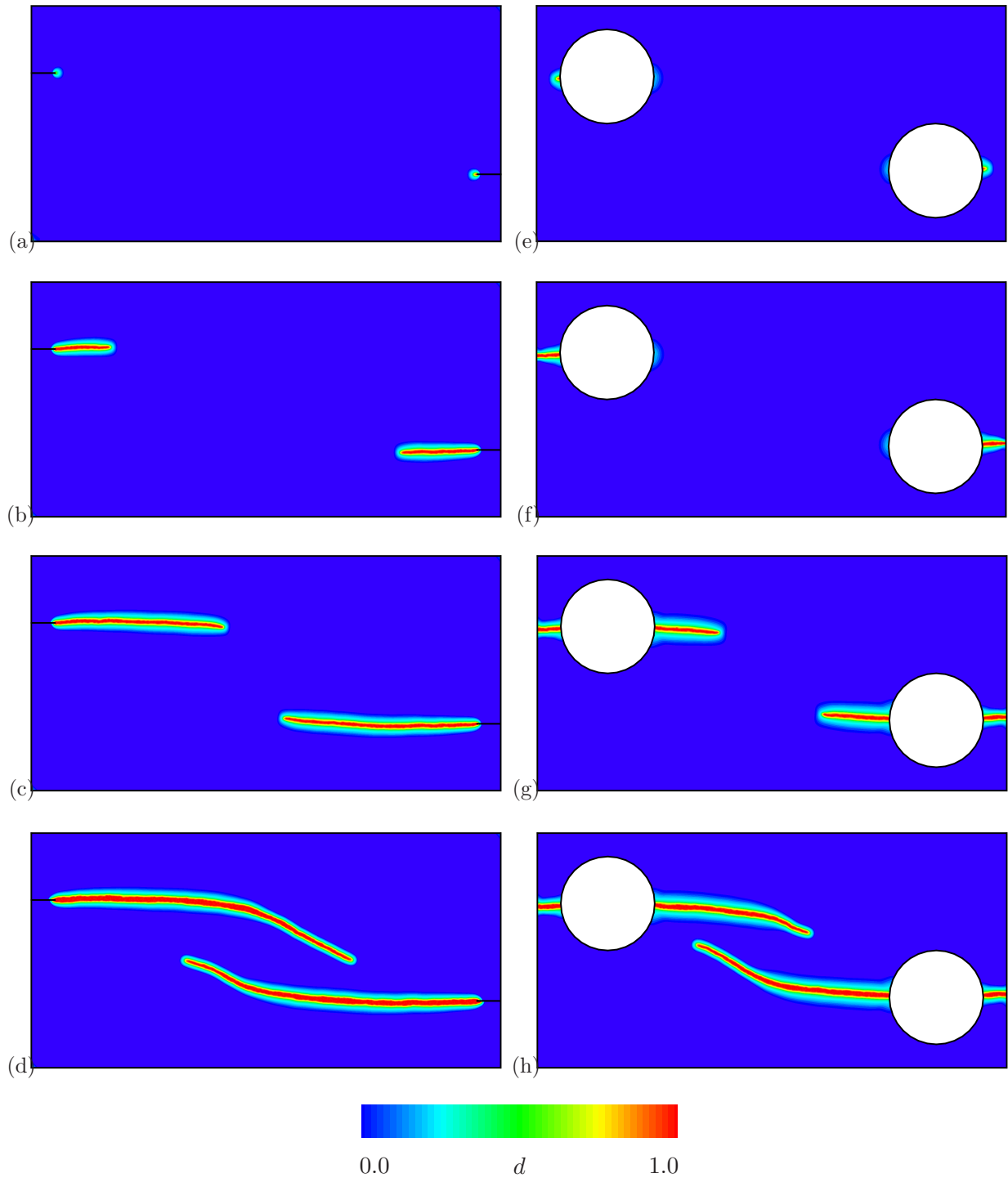


Figure 5.21: Tensile test with two notches or holes. Contour plots of the fracture phase-field d for the double edge notched specimen in (a)–(d) and for the two-holes specimen in (e)–(h).

1.25 mm and $l_2 = 5.0$ mm with same length/mesh ratio $r = 8$. The crack phase-field initiates at the notch-tip and propagates horizontally up to the interface between A- and B-zones. Thereafter it branches along the interfaces vertically till final failure, as documented in the work of SARGADO ET AL. [280]. A sharp crack pattern is obtained for the smaller length scale parameter l , as demonstrated in Figure 5.18(d).

Load-displacement curves for different length scales and elements formulations of FEM and VEM are displayed in Figure 5.19(a). All simulations show similar behavior before crack initiation. Thereafter, the force drops sharply at cracking to a lower level, which represents the residual forces of the undamaged B-zone of the specimen. Next, the influence of the stabilization parameter β is illustrated in Figure 5.19(b). As observed in the above two examples, for $0 < \beta \leq 1$ comparable F - u results are obtained.

5.5.4. Tensile test with two notches or holes. The last example is concerned with the capability and the flexible choice of the number of nodes in an element for VEM. To this end, a tension test of a double edge notched or two holes specimen is investigated. The purpose of this test is to illustrate the effects of the hole/notch shape on the crack-initiation and curved-crack-propagation, representing a mixed-mode fracture. The geometrical setup and the loading conditions of the notched specimen are depicted in Figure 5.20(a) and for the holes-specimen in Figure 5.20(b). The size of the specimen is chosen to be: $L = 20$ mm, $H = 10$ mm, $R = 2$ mm, $A = 3$ mm and $B = 1$ mm. We fixed the bottom edge of the plate in x - and y -directions, the top edge in x -direction and applied a vertical displacement at the top edge until final failure. The shear modulus is chosen as $\mu = 8.0$ kN/mm², Poisson's ratio $\nu = 0.3$, the viscosity of the crack propagation $\eta = 10^{-6}$ kNs/mm², the critical energy release rate as $g_c = 1.0 \times 10^{-3}$ kN/mm, the stabilization parameter as $\beta = 0.4$ and the fracture length scale parameter $l = 0.1$ mm.

Virtual element formulation with various animals-shaped Voronoi cells (bird, horse, snake, frog, koala, fish, kangaroo, ...) are employed in the undamaged zones, whereas we applied a mesh refinement with standard Voronoi mesh in the expected fracture zone having the length/mesh ratio $r = 8$, as outlined in Figure 5.20(c)-(d).

The crack phase-field initiates at the two notch-tip in Figure 5.21(a) or around the two holes in Figure 5.21(e). Thereafter, the left crack propagates towards the bottom surface while the right crack propagates towards the top surface, resulting with a mixed-mode fracture, see Figure 5.21(b)-(d) for the notched specimen and Figure 5.21(f)-(h) for the holes-specimen.

6. 2D Virtual elements for phase-field modeling of ductile fracture

An efficient low order virtual element method (VEM) for the phase field modeling of ductile fracture is outlined within this chapter. The recently developed VEM is a competitive discretization scheme for meshes with highly irregular shaped elements. The phase-field approach is a very powerful technique to simulate complex crack phenomena in multi-physical environments. The formulation in this contribution is based on a minimization of a pseudo-potential density functional for the coupled problem undergoing large strains. Main aspect of development is the extension towards the virtual element formulation due to its flexibility in dealing with complex shapes and arbitrary number of nodes. Two numerical examples illustrate the efficiency, accuracy and convergence properties of the proposed method. The recent publication of ALDAKHEEL ET AL. [8] serve as the basis for the content of this chapter.

6.1. Introduction

The virtual element method (VEM) has been developed over the last decade and applied to various problems in solid mechanics. It is a generalization of the finite element method (FEM) [43, 345, 323], which has been inspired from modern mimetic finite difference schemes [71]. VEM allows exploration of features such as flexibility with regard to mesh generation and choice of element shapes, e.g. the use of very general polygonal and polyhedral meshes. In this regard, a stabilization procedure is required in the virtual element method, as described in [77] for linear Poisson problems. Up to now applications of virtual elements have been devoted to linear elastic deformations in [135, 36], contact problems in [328], finite elasto-plastic deformations in [324, 169], anisotropic materials at finite strains in [330, 331], small strain isotropic damage in [96], inelastic solids in [298] and hyperelastic materials at finite deformations in [85, 329]. Recently, [6] propose an efficient virtual element scheme for the phase-field modeling of brittle fracture at small strains. This chapter extends VEM towards finite deformations ductile fracture using the phase-field approach.

The development of a virtual element methodology for solving fracture-mechanics problems numerically includes a projection step and a stabilization step. In the projection step, the deformation map $\boldsymbol{\varphi}$ and the fracture phase-field d which appear in the pseudo-potential density functional are replaced by their projection: $\boldsymbol{\varphi}_{\Pi}$ and d_{Π} onto a polynomial space. This results in a rank-deficient structure, therefore it is necessary to add a stabilization term to the formulation, see [46, 47, 85], where in the latter the scalar stabilization parameter of the linear case was replaced by one that depends on the fourth-order elasticity tensor. A new stabilization technique for VEM was recently developed in [329] who use a technique that was first described in [249], generalized in [60] and simplified in [187] in the context of hexahedral finite elements. The essence of the method is the addition of the pseudo-energy density function $W(\nabla\boldsymbol{\varphi}_{\Pi}, d_{\Pi}, \nabla d_{\Pi}, \mathbf{h})$ to a density function $\widehat{W}(\nabla\boldsymbol{\varphi}, d, \nabla d, \mathbf{h})$ which is evaluated using full quadrature. For consistency the subtraction of a term involving $\widehat{W}(\nabla\boldsymbol{\varphi}_{\Pi}, d_{\Pi}, \nabla d_{\Pi}, \mathbf{h})$ as a function of the projected deformation map and the crack phase-field is made. Here \mathbf{h} is the history field array for the plastic strain measures and the crack driving force. This history array is locally evaluated only once at the element level and used in all parts of the pseudo-energy density function.

In the presented work, we examine the efficiency of VEM for predicting ductile failure mechanisms in solids due to crack initiation and propagation. The modeling of crack formation can be achieved in a convenient way by continuum phase-field approaches to fracture, which are based on the regularization of sharp crack discontinuities. Phase-field modeling of fracture has been attracting considerable attention in recent years due to its capability of capturing complex crack patterns in various problems in solid mechanics. Many efforts have been focused on the regularized modeling of Griffith-type brittle fracture in elastic solids. In this regard, [225] proposed a phase field approach to fracture with a local irreversibility constraint on the crack phase field. It incorporates regularized crack surface density functions as central constitutive objects, which is motivated in a descriptive format based on geometric considerations. Recent works on brittle fracture have been devoted to the dynamic case in [62], cohesive fracture in [307], multiplicative decomposition of the deformation gradient into compressive-tensile parts in [164], different choices of degradation functions in [189], coupled thermo-mechanical and multi-physics problems at large strains in [231, 109], to model fracture of arterial walls with an emphasis on aortic tissues in [149], finite-deformation contact problems in [165], emphasis on a possible formula for the length scale estimation in [341], anisotropic material behavior at small and large deformations in [299, 59], for the description of hydraulic fracturing in [159, 115], to describe fatigue effects for brittle materials in [20], to the modeling of fracture in polymeric hydrogels in [61], for enhanced assumed strain shells at large deformations in [277] and the virtual element method in [6].

Extensions of these models towards the phase field modeling of ductile fracture can be achieved by coupling of gradient damage mechanics with models of elasto-plasticity. In this regard, [113] investigates a setting of brittle fracture in elastic-plastic solids. In [230], the modeling of dynamic fracture in the logarithmic Lagrangian strain space has been presented with emphasis on the brittle to ductile transition in thermo-elastic-plastic solids. The model suggested in [22] uses a characteristic degradation function that couples damage to plasticity in a multiplicative format. [64] proposes a mechanism for including a measure of stress triaxiality as a driving force for crack initiation and propagation. The coupling of gradient plasticity with gradient damage at finite strains is considered in [4, 10, 232, 238, 233, 237, 107, 108] based on a rigorous variational principle. In [18] a comparative study between different phase-field models of fracture coupled with plasticity is outlined. A coupled phase-field and plasticity modeling of geological materials is recently proposed by [86, 5]. Recently, [14] extend the phase field modeling of fracture towards porous finite plasticity to account for complex phenomena at the micro-scale, such as nucleation, growth and coalescence of micro-voids, as well as the final rupture at the macro-scale.

A minimization of a pseudo-potential density functional for the phase field modeling of ductile fracture is presented as a key goal of this work by using an efficient virtual element method. It is based on the definition of a pseudo-energy density per unit volume, that contains the sum of a degrading elastic-plastic part and a contribution due to fracture, in line with [10, 232, 230]. On the computational side, a robust and efficient monolithic scheme is employed in the numerical implementation to compute the unknowns (the deformation map and the crack phase-field) using the software tool ACEFEM, see [184].

The chapter is organized as follows: Section 6.2 outlines the governing equations for the phase-field approach to ductile fracture in elastic-plastic solids undergoing large de-

formations. The development of the virtual element method is formulated in Section 6.3. Finally, Section 6.4 presents numerical results that demonstrate the modeling capabilities of the proposed approach. The formulation performs extremely well in benchmark tests involving regular, distorted and Voronoi meshes. For purpose of comparison, results of the standard finite element method (FEM) are also demonstrated.

6.2. Governing equations for phase field ductile fracture

This section outlines a theory of fracture in elastic-plastic solids at large deformations. It is based on a minimization of a pseudo-potential energy for the coupled problem. To this end, let $\Omega \in \mathcal{R}^\delta$ with $\delta = 2, 3$ be the reference configuration of a solid domain. The response of fracturing solid at material points $\mathbf{X} \in \Omega$ and time $t \in \mathcal{T} = [0, T]$ is described by the deformation map $\varphi(\mathbf{X}, t)$ and the crack phase-field $d(\mathbf{X}, t)$ as

$$\varphi : \begin{cases} \Omega \times \mathcal{T} \rightarrow \mathcal{R}^\delta \\ (\mathbf{X}, t) \mapsto \mathbf{x} = \varphi(\mathbf{X}, t) = \mathbf{X} + \mathbf{u}(\mathbf{X}, t) \end{cases} \quad \text{and} \quad d : \begin{cases} \Omega \times \mathcal{T} \rightarrow [0, 1] \\ (\mathbf{X}, t) \mapsto d(\mathbf{X}, t) \end{cases} \quad (6.1)$$

with $d \geq 0$ where \mathbf{x} is the position of a material point in the deformed configuration and $\mathbf{u}(\mathbf{X}, t)$ is the displacement field. The crack phase-field $d(\mathbf{X}, t) = 0$ and $d(\mathbf{X}, t) = 1$ refer to the unbroken and fully broken state of the material respectively. The material deformation gradient is defined by $\mathbf{F} := \nabla \varphi_t(\mathbf{X}) = \text{Grad} \varphi$ with the Jacobian $J := \det[\mathbf{F}] > 0$. The solid is loaded by prescribed deformations and external traction on the boundary, defined by time-dependent Dirichlet- and Neumann conditions

$$\varphi = \bar{\varphi}(\mathbf{X}, t) \text{ on } \partial\Omega_\varphi \quad \text{and} \quad \mathbf{P}\mathbf{N} = \bar{\mathbf{t}}(\mathbf{X}, t) \text{ on } \partial\Omega_t \quad (6.2)$$

where \mathbf{N} is the outward unit normal vector on the surface $\partial\Omega = \partial\Omega_\varphi \cup \partial\Omega_t$ of the undeformed configuration. The first Piola-Kirchhoff stress tensor \mathbf{P} is the thermodynamic dual to \mathbf{F} . In finite strain plasticity, the deformation gradient is multiplicatively decomposed into an elastic and a plastic part as

$$\mathbf{F} = \mathbf{F}_e \mathbf{F}_p \quad \text{with} \quad J = J_e J_p = J_e = \det[\mathbf{F}_e] \quad \text{and} \quad J_p = \det[\mathbf{F}_p] = 1 \quad (6.3)$$

where the constraint of plastic incompressibility holds for the case of von Mises J_2 -plasticity. The elastic part of the right Cauchy-Green tensor $\mathbf{C} = \mathbf{F}^T \mathbf{F}$ can be computed as

$$\mathbf{C} = \mathbf{F}_p^T \mathbf{F}_e^T \mathbf{F}_e \mathbf{F}_p = \mathbf{F}_p^T \mathbf{C}_e \mathbf{F}_p \quad \text{yields} \quad \mathbf{C}_e = \mathbf{F}_p^{-T} \mathbf{C} \mathbf{F}_p^{-1}. \quad (6.4)$$

Furthermore, the elastic left Cauchy-Green tensor \mathbf{b}_e is defined as

$$\mathbf{b}_e = \mathbf{F}_e \mathbf{F}_e^T = \mathbf{F} \mathbf{C}_p^{-1} \mathbf{F}^T \quad \text{with} \quad \mathbf{C}_p = \mathbf{F}_p^T \mathbf{F}_p \quad (6.5)$$

where \mathbf{C}_p is the plastic part of the right Cauchy-Green tensor. To account for phenomenological hardening/softening response, we define the equivalent plastic strain variable by the evolution equation

$$\dot{\alpha} = \dot{\gamma} \quad \text{with} \quad \dot{\alpha} \geq 0. \quad (6.6)$$

as a local internal variable, where $\dot{\gamma} \geq 0$ is the plastic Lagrange multiplier. The hardening variable starts to evolve from the initial condition $\alpha(\mathbf{X}, 0) = \theta$.

The solid Ω has to satisfy the equation of equilibrium as

$$\text{Div } \mathbf{P} + \bar{\mathbf{f}} = \mathbf{0} \quad (6.7)$$

where dynamic effects are neglected and $\bar{\mathbf{f}}$ is the given body force.

For the phase-field problem, a sharp-crack surface topology $\Gamma \rightarrow \Gamma_l$ is regularized by the crack surface functional as outlined in [225, 230]

$$\Gamma_l(d) = \int_{\Omega} \gamma_l(d, \nabla d) dV \quad \text{with} \quad \gamma_l(d, \nabla d) = \frac{1}{2l}d^2 + \frac{l}{2}|\nabla d|^2 \quad (6.8)$$

based on the crack surface density function γ_l per unit volume of the solid and the fracture length scale parameter l that governs the regularization. To describe a purely geometric approach to phase-field fracture, the regularized crack phase-field d is obtained by a minimization principle of diffusive crack topology

$$d = \text{Arg}\{\inf_d \Gamma_l(d)\} \quad \text{with} \quad d = 1 \text{ on } \Gamma \subset \Omega \quad (6.9)$$

yielding the Euler equation $d - l^2\Delta d = 0$ in Ω along with the Neumann-type boundary condition $\nabla d \cdot \mathbf{N} = 0$ on $\partial\Omega$. Evolution of the regularized crack surface functional (6.8) can be driven by the constitutive functions as outlined in [230, 10, 14], postulating a global evolution equation of regularized crack surface as

$$\frac{d}{dt}\Gamma_l(d) = \int_{\Omega} \delta_d \gamma_l(d, \nabla d) \dot{d} dV := \frac{1}{l} \int_{\Omega} [(1-d)\mathcal{H} - \eta_f \dot{d}] \dot{d} dV \geq 0 \quad (6.10)$$

where $\eta_f \geq 0$ is a material parameter that characterizes the artificial/numerical viscosity of the crack propagation. The crack driving force

$$\mathcal{H} = \max_{s \in [0, t]} D(\mathbf{X}, s) \geq 0, \quad (6.11)$$

is introduced as a *local history variable* that accounts on the irreversibility of the phase-field evolution by filtering out a maximum value of what is known as the crack driving state function D . Then the evolution statement (6.10) provides the local equation for the evolution of the crack phase-field in the domain Ω along with its homogeneous Neumann boundary condition as

$$\eta_f \dot{d} = (1-d)\mathcal{H} - [d - l^2\Delta d] \quad \text{with} \quad \nabla d \cdot \mathbf{N} = 0 \quad \text{on} \quad \partial\Omega \quad (6.12)$$

The above introduced variables will characterize the ductile failure response of a solid, based on the two global primary fields

$$\text{Global Primary Fields : } \mathfrak{U} := \{\varphi, d\}, \quad (6.13)$$

the deformation map φ and the crack phase-field d . The constitutive approach to the phase-field modeling of ductile fracture focuses on the set

$$\text{Constitutive State Variables : } \mathfrak{C} := \{\mathbf{b}_e, \alpha, \mathcal{H}, d, \nabla d\}, \quad (6.14)$$

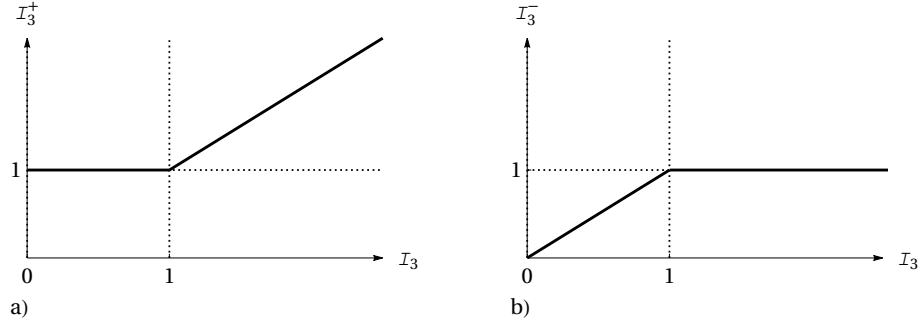


Figure 6.1: Third invariant decomposition. (a) Positive part defined as $I_3^+ := \max\{I_3, 1\}$ and (b) negative part defined as $I_3^- := \min\{I_3, 1\}$.

reflecting a combination of elasto-plasticity with a first-order gradient damage modeling. It is based on the definition of a pseudo-energy density per unit volume contains the sum

$$W(\mathbf{e}) = W_{elas}(\mathbf{b}_e, d) + W_{plas}(\alpha, d) + W_{frac}(\mathcal{H}, d, \nabla d) \quad (6.15)$$

of a degrading elastic W_{elas} and plastic energies W_{plas} and a contribution due to fracture W_{frac} , which contains the accumulated dissipative energy in line with [10, 232]. The elastic contribution is the Neo-Hookean strain energy function for a homogeneous compressible isotropic elastic material

$$\begin{aligned} W_{elas}(\mathbf{b}_e, d) &= g(d) [\psi_{vol}(\mathbf{b}_e) + \psi_{iso}(\mathbf{b}_e)] \quad \text{with} \\ \psi_{vol} &= \frac{\kappa}{4}(I_3 - 1 - \ln I_3) \\ \psi_{iso} &= \frac{\mu}{2}(I_3^{-1/3} I_1 - 3) \end{aligned} \quad (6.16)$$

in terms of the bulk modulus $\kappa > 0$, the shear modulus $\mu > 0$ and the invariants: $I_1 = \text{tr } \mathbf{b}_e$ and $I_3 = \det \mathbf{b}_e$. The plastic contribution is assumed to have the form

$$W_{plas}(\alpha, d) = g(d) \psi_p(\alpha) \quad \text{with} \quad \psi_p = Y_0 \alpha + \frac{H}{2} \alpha^2 + (Y_\infty - Y_0)(\alpha + \exp[-\delta\alpha]/\delta) \quad (6.17)$$

with the initial yield stress Y_0 , infinite yield stress $Y_\infty \geq Y_0$, the isotropic hardening modulus $H \geq 0$ and the saturation parameter δ .

The degradation function $g(d) = (1 - d)^2$ models the degradation of the elastic-plastic energy of the solid due to fracture. It interpolates between the unbroken response for $d = 0$ and the fully broken state at $d = 1$ by satisfying the constraints $g(0) = 1$, $g(1) = 0$, $g'(d) \leq 0$ and $g'(1) = 0$.

In order to enforce a crack evolution only in tension, the *volumetric* elastic energy is additively decomposed into a positive part ψ_{vol}^+ due to tension and a negative part ψ_{vol}^- due to compression, outlined in the pioneering work of [28] as

$$W_{elas}(\mathbf{b}_e, d) = g(d) [\psi_{vol}^+(\mathbf{b}_e) + \psi_{iso}(\mathbf{b}_e)] + \psi_{vol}^-(\mathbf{b}_e) \quad \text{with} \quad \psi_{vol}^\pm = \frac{\kappa}{4}(I_3^\pm - 1 - \ln I_3^\pm) \quad (6.18)$$

in terms of the positive I_3^+ and the negative I_3^- third invariant defined as

$$\begin{aligned} I_3^+ &:= \max\{I_3, 1\} = \langle I_3 - 1 \rangle_+ + 1 = \frac{1}{2} \left[(I_3 - 1) + |I_3 - 1| \right] + 1 \\ I_3^- &:= \min\{I_3, 1\} = \langle I_3 - 1 \rangle_- + 1 = \frac{1}{2} \left[(I_3 - 1) - |I_3 - 1| \right] + 1 \end{aligned} \quad (6.19)$$

as visualized in Figure 6.1. Following the Coleman-Noll procedure, the Kirchhoff stresses tensor $\boldsymbol{\tau}$ and the first Piola-Kirchoff stress tensor \mathbf{P} are obtained from the elastic strain energy function $W_{elas}(\mathbf{b}_e, d)$ in (6.18) for isotropic material behavior as

$$\boldsymbol{\tau} = 2\mathbf{b}_e \frac{\partial W_{elas}}{\partial \mathbf{b}_e} \quad \text{and} \quad \mathbf{P} = \boldsymbol{\tau} \mathbf{F}^{-T} \quad (6.20)$$

The fracture part of pseudo-energy density (6.15) takes the form

$$W_{frac}(\mathcal{H}, d, \nabla d) = 2 \frac{\psi_c}{\zeta} l \gamma_l(d, \nabla d) + \frac{\eta_f}{2 \Delta t} (d - d_n)^2 + g(d) \mathcal{H} \quad (6.21)$$

where $\Delta t := t - t_n > 0$ denotes the time step, $\psi_c > 0$ is a critical fracture energy and ζ controls the post-critical range after crack initialization. Following the recent works [10, 232, 237], the history field \mathcal{H} is defined by

$$\mathcal{H} := \max_{s \in [0, t]} D(\mathbf{b}_e, \alpha; s) \geq 0 \quad \text{with} \quad D := \left\langle \psi_{vol}^+ + \psi_{iso} + \psi_p - \psi_c \right\rangle_+ \quad (6.22)$$

with the Macaulay bracket $\langle x \rangle_+ := (x + |x|)/2$, that ensures the irreversibility of the crack evolution.

The finite elasto-plastic model requires additionally the formulation of a yield function, a hardening law and an evolution equation for the plastic variables. The yield function restricts the elastic region. By assuming J_2 -plasticity with nonlinear isotropic hardening the yield function has the form

$$\chi = \sqrt{3/2} |\mathbf{f}^p| - r^p \quad \text{with} \quad \mathbf{f}^p := \text{dev}[\boldsymbol{\tau}] = \boldsymbol{\tau} - \frac{1}{3} \text{tr}[\boldsymbol{\tau}] \mathbf{1} \quad \text{and} \quad r^p := \partial_\alpha W_{plas} \quad (6.23)$$

in terms of the deviatoric plastic driving force \mathbf{f}^p and the resistance force r^p . With the yield function at hand, we define the dual dissipation function for visco-plasticity according to Perzyna-type model as

$$\Phi^*(\mathbf{f}^p, r^p) = \frac{1}{2\eta_p} \left\langle \sqrt{3/2} |\mathbf{f}^p| - r^p \right\rangle_+^2 \quad (6.24)$$

with η_p being the viscosity parameter of the rate dependent plastic deformation. The evolution equations for the plastic variables are, see e.g. [323, 324, 288, 151]

$$-\frac{1}{2} \mathcal{L}_v \mathbf{b}_e = \dot{\gamma} \mathbf{n} \mathbf{b}_e \quad \text{with} \quad \mathbf{n} = \frac{\partial \chi}{\partial \mathbf{f}^p} \quad \text{and} \quad \dot{\alpha} = \dot{\gamma} := \frac{1}{\eta_p} \langle \chi \rangle_+, \quad (6.25)$$

where \mathcal{L}_v denotes the Lie derivative in time. The evolution equation (7.19)₁ can be recast with (7.4) in an alternative form

$$\dot{\mathbf{C}}_p^{-1} = -2 \dot{\gamma} \mathbf{F}^{-1} \mathbf{n} \mathbf{F} \mathbf{C}_p^{-1} \quad (6.26)$$

which will be used later for the algorithmic treatment of plasticity within the numerical solution algorithm, see e.g. [183]. The Kuhn-Tucker conditions for the elasto-plastic model are

$$\chi \leq 0 \quad , \quad \dot{\gamma} \geq 0 \quad \text{and} \quad \chi \dot{\gamma} = 0 \quad (6.27)$$

The development of the virtual element formulation for the phase-field ductile fracture in elastic-plastic solids can start from a pseudo potential density functional instead of using the weak form. This has advantages when the code is automatically generated using the software tool ACEGEN, see [184]. The pseudo potential density functional depends on the elastic and the fracture parts and *keeps* the plastic history variables and the crack driving force *constant* during the first variation. The pseudo potential density functional can then be written as

$$\Pi(\mathbf{u}, \mathbf{h}) = \int_{\Omega} W(\mathbf{e}) dV - \Pi_{ext}(\varphi) \quad \text{with} \quad \Pi_{ext}(\varphi) := \int_{\Omega} \bar{\mathbf{f}} \cdot \varphi dV + \int_{\partial\Omega_t} \bar{\mathbf{t}} \cdot \varphi dA \quad (6.28)$$

Here $\mathbf{h} := \{\mathbf{C}_p^{-1}, \alpha, \mathcal{H}\}$ is the history field array for the plastic strain measures and the crack driving force.

6.3. Formulation of the virtual element method

Following the work of [71], the main idea of the virtual element method is a Galerkin projection of the unknowns onto a specific ansatz space. The domain Ω is partitioned into non-overlapping polygonal elements which need not to be convex and can have any arbitrary shape with different node numbers, as plotted in Figure 6.2 representing a *horse-like* element with \mathbf{X}_I vertices. Here a low-order approach is adopted, see [329] and [324], using linear ansatz functions where nodes are placed only at the vertices of the polygonal elements. Furthermore, the restriction of the element shape functions to the element boundaries are linear functions.

6.3.1. Ansatz functions for VEM. The virtual element method relies on the split of the ansatz space into a part \mathbf{u}_{Π} representing the projected primary field defined in

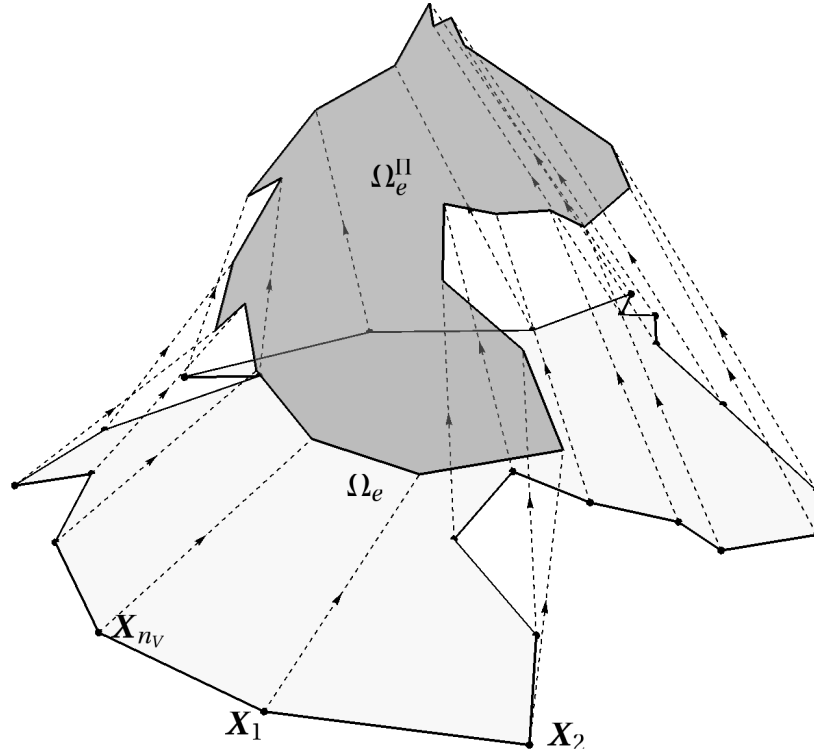


Figure 6.2: Polynomial basis function for the virtual element ansatz with vertices \mathbf{X}_I .

(6.13) and a remainder

$$\mathbf{u}^h = \mathbf{u}_{\Pi}^h + (\mathbf{u}^h - \mathbf{u}_{\Pi}^h) \quad \text{with} \quad \mathbf{u}_{\Pi}^h := \{\varphi_{\Pi}^h, d_{\Pi}^h\} \quad (6.29)$$

The projection \mathbf{u}_{Π}^h is defined at element level by a linear ansatz function \mathbf{N}_{Π} as

$$\mathbf{u}_{\Pi}^h = \begin{bmatrix} \varphi_{\Pi X} \\ \varphi_{\Pi Y} \\ d_{\Pi} \end{bmatrix} = \mathbf{a} \cdot \mathbf{N}_{\Pi} = \begin{bmatrix} a_1 & a_4 & a_7 \\ a_2 & a_5 & a_8 \\ a_3 & a_6 & a_9 \end{bmatrix} \begin{bmatrix} 1 \\ X \\ Y \end{bmatrix} \quad (6.30)$$

with the unknowns \mathbf{a} . The projection \mathbf{u}_{Π}^h is now defined such that it satisfies

$$\int_{\Omega_e} \nabla \mathbf{u}_{\Pi}^h dV \stackrel{!}{=} \int_{\Omega_e} \text{Grad} \mathbf{u}^h dV \quad (6.31)$$

which yields, with the linear ansatz in (7.30) that $\nabla \mathbf{u}_{\Pi}^h$ is constant as

$$\nabla \mathbf{u}_{\Pi}^h|_e \stackrel{!}{=} \frac{1}{\Omega_e} \int_{\Omega_e} \text{Grad} \mathbf{u}^h dV = \frac{1}{\Omega_e} \int_{\partial\Omega_e} \mathbf{u}^h \otimes \mathbf{N} dA \quad (6.32)$$

where \mathbf{N} is the normal at the boundary $\partial\Omega_e$ of the domain Ω_e of a virtual element e , see Figure 6.3. Thus label $\square|_e$ represents element quantities that have constant value within an element e . A direct computation of the projected gradient yields with the linear ansatz in (7.30) the simple matrix form

$$\nabla \mathbf{u}_{\Pi}^h|_e = \begin{bmatrix} \nabla \varphi_{\Pi X} \\ \nabla \varphi_{\Pi Y} \\ \nabla d_{\Pi} \end{bmatrix} = \begin{bmatrix} \varphi_{\Pi X,X} & \varphi_{\Pi X,Y} \\ \varphi_{\Pi Y,X} & \varphi_{\Pi Y,Y} \\ d_{\Pi,X} & d_{\Pi,Y} \end{bmatrix} = \begin{bmatrix} a_4 & a_7 \\ a_5 & a_8 \\ a_6 & a_9 \end{bmatrix} \quad (6.33)$$

The boundary integral in (7.34) has to be evaluated. To this end, a linear ansatz for the primary fields along the element edges is introduced as

$$(\mathbf{u}^h)_k = (1 - \xi_k) \mathbf{u}_1 + \xi_k \mathbf{u}_2 = M_{k1} \mathbf{u}_1 + M_{k2} \mathbf{u}_2 \quad \text{with} \quad \xi_k \in [0, 1] \quad (6.34)$$

for a boundary segment k of the virtual element. The local nodes: ①–② are chosen in counter-clockwise order and can be found in Figure 6.3. In (7.37) M_{k1} is the ansatz function along a segment k , related to node ①, ξ_k is the local dimensionless coordinate and \mathbf{u}_1 is the nodal value at that node. The ansatz function M_{k2} is defined in the same way. From (7.34)–(7.37), the unknowns a_4 – a_9 can be computed from the normal vectors of the boundary segments in elements and the nodal primary fields as

$$\begin{bmatrix} a_4 & a_7 \\ a_5 & a_8 \\ a_6 & a_9 \end{bmatrix} = \frac{1}{\Omega_e} \int_{\partial\Omega_e} \mathbf{u}^h \otimes \mathbf{N} dA = \frac{1}{\Omega_e} \sum_{k=1}^{n_V} \int_{\partial\Omega_k} \begin{bmatrix} \varphi_X(\mathbf{X})N_X & \varphi_X(\mathbf{X})N_Y \\ \varphi_Y(\mathbf{X})N_X & \varphi_Y(\mathbf{X})N_Y \\ d(\mathbf{X})N_X & d(\mathbf{X})N_Y \end{bmatrix} dA \quad (6.35)$$

where we have used $\mathbf{N} = \{N_X, N_Y\}^T$ and $\mathbf{u} = \{\varphi_X, \varphi_Y, d\}^T$, furthermore n_V is the number of element vertices which coincides with the number of segments (edges) of the element, for first order VEM. Note that the normal vector \mathbf{N} changes from segment to segment. In the 2D case it can be computed for a segment k as

$$\mathbf{N}_k = \begin{Bmatrix} N_X \\ N_Y \end{Bmatrix}_k = \frac{1}{L_k} \begin{Bmatrix} Y_1 - Y_2 \\ X_2 - X_1 \end{Bmatrix}_k \quad (6.36)$$

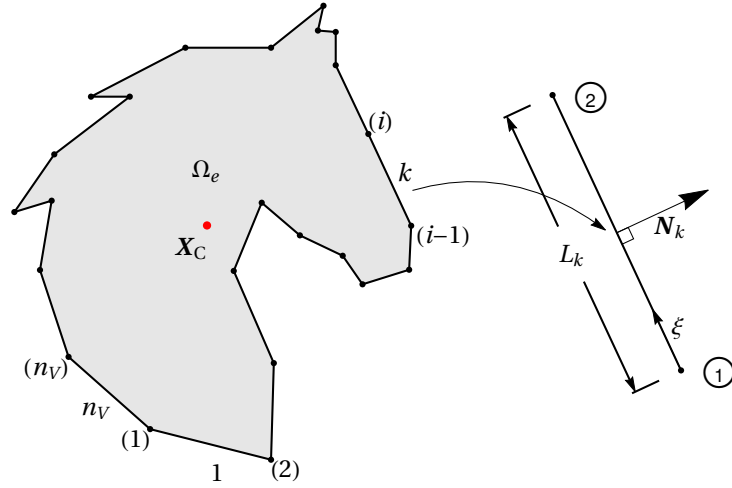


Figure 6.3: Virtual element with n_V nodes and local boundary segment of the horse-like polygonal element.

with $\{X_i, Y_i\}_{i=1,2}$ being the local coordinates of the two vertices of the segment k . The integral in (7.38) can be evaluated for the ansatz functions (7.37) exactly by using the trapezoidal or Gauss-Lobatto rule. By selecting the vertices as the Gauss-Lobatto points it is sufficient to know only the nodal values

$$\mathfrak{U}_e = \{\mathfrak{U}_1, \mathfrak{U}_2, \dots, \mathfrak{U}_{n_V}\} \quad (6.37)$$

at the n_V vertices V in Figure 6.3. Since the ansatz function in (7.37) fulfills the property $M_I(X_J) = \delta_{IJ}$ the actual form of the function M does not enter the evaluation of the boundary integrals which makes the evaluation extremely simple. Finally, by comparing (7.35) and (7.38) the unknowns a_4 to a_9 are obtained by inspection, for further details see e.g. [329]. The projection in (7.34) does not determine the ansatz \mathfrak{U}_Π^h in (7.30) completely and has to be supplemented by a further condition to obtain the constants a_1 , a_2 and a_3 . For this purpose we adopt the condition that the sum of the nodal values of \mathfrak{U}^h and of its projection \mathfrak{U}_Π^h are equal. This yields for each element Ω_e

$$\frac{1}{n_V} \sum_{I=1}^{n_V} \mathfrak{U}_\Pi^h(\mathbf{X}_I) = \frac{1}{n_V} \sum_{I=1}^{n_V} \mathfrak{U}^h(\mathbf{X}_I) \quad (6.38)$$

where \mathbf{X}_I are the coordinates of the nodal point I and the sum includes all boundary nodes. Substituting (7.30) and (7.37) in (6.38), results with the three unknowns a_1 , a_2 and a_3 as

$$\begin{bmatrix} a_1 \\ a_2 \\ a_3 \end{bmatrix} = \frac{1}{n_V} \sum_{I=1}^{n_V} [\mathfrak{U}_I - \nabla \mathfrak{U}_{\Pi I} \cdot \mathbf{X}_I] = \frac{1}{n_V} \sum_{I=1}^{n_V} \begin{bmatrix} \varphi_{XI} - \varphi_{\Pi X, X} X_I - \varphi_{\Pi X, Y} Y_I \\ \varphi_{YI} - \varphi_{\Pi Y, X} X_I - \varphi_{\Pi Y, Y} Y_I \\ d_I - d_{\Pi, X} X_I - d_{\Pi, Y} Y_I \end{bmatrix} \quad (6.39)$$

Thus, the ansatz function \mathfrak{U}_Π^h of the virtual element is completely defined.

6.3.2. Construction of the virtual element. The virtual element method relies on the projection \mathfrak{U}_Π^h of the deformation map and fracture phase-field. This was approximated in the last section by a first order polynomial leading to a gradient which has a

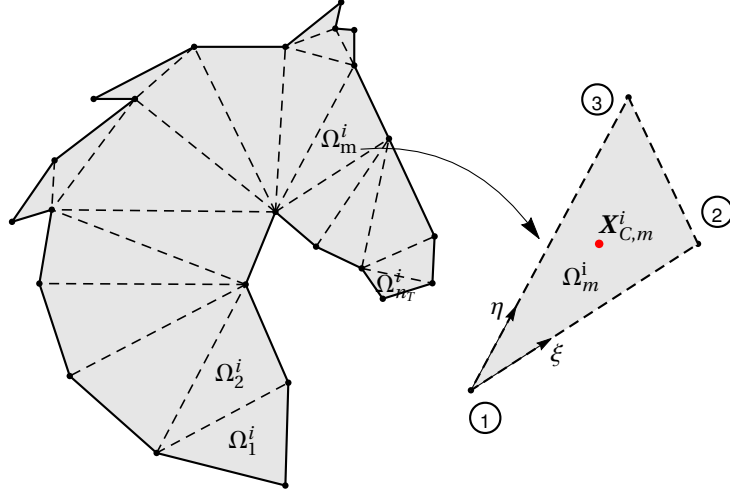


Figure 6.4: Internal triangular mesh of the horse-like polygonal element.

constant value. This is called consistency term, but it does not lead to a stable formulation once the number of vertices is greater than 3. Thus the formulation has to be stabilized like the classical one-point integrated elements developed by [125, 50, 276, 275, 246, 185, 187].

In the following development of the virtual element for the phase-field modeling of ductile fracture, the plastic variables and the crack driving force are computed from the consistency term. These variables are then used as given and fixed history values in the stabilization procedure.

To this end, the potential density functional defined in (6.28) can be rewritten by exploiting the split in (7.29). Thus we have, by summing up all element contributions for the n_e virtual elements

$$\Pi(\mathbf{u}, \mathbf{h}) = \bigwedge_{e=1}^{n_e} \Pi(\mathbf{u}_e, \mathbf{h}_e) \quad \text{with} \quad \Pi(\mathbf{u}_e, \mathbf{h}_e) = [\Pi_c(\mathbf{u}_\Pi^h, \mathbf{h})|_e + \Pi_{stab}(\mathbf{u}^h - \mathbf{u}_\Pi^h, \mathbf{h})|_e] , \quad (6.40)$$

based on a constant part Π_c and an associated stabilization term Π_{stab} . Here the history fields array \mathbf{h}_e are local variables evaluated *only once* at the element level and used in both parts of the potential density functional. A summary of the algorithmic treatment for the finite strain plasticity and the crack driving force is outlined in Box 6.1, for further details we refer to the work [324].

The first part in (6.40)₂ can be computed as

$$\Pi_c^\tau(\mathbf{u}_\Pi^h, \mathbf{h})|_e = \int_{\Omega_e} W(\mathbf{e}_\Pi^h) dV - \int_{\Omega_e} \bar{\mathbf{f}} \cdot \boldsymbol{\varphi}_\Pi^h dV - \int_{\partial\Omega_e} \bar{\mathbf{t}} \cdot \boldsymbol{\varphi}_\Pi^h dA , \quad (6.41)$$

with $\mathbf{e}_\Pi^h = \{\mathbf{b}_{e\Pi}^h, \alpha, \mathcal{H}, d_\Pi^h, \nabla d_\Pi^h\}$. The projected elastic left Cauchy-Green tensor $\mathbf{b}_{e\Pi}^h$ can be computed from the projected deformation map and the plastic part of the right Cauchy-Green tensor as

$$\mathbf{b}_{e\Pi}^h = \mathbf{F}_\Pi^h \mathbf{C}_p^{-1} \mathbf{F}_\Pi^{hT} \quad \text{with} \quad \mathbf{F}_\Pi^h = \nabla \boldsymbol{\varphi}_\Pi^h , \quad (6.42)$$

The primary fields \mathbf{u}_Π^h are linear functions and their gradient $\nabla \mathbf{u}_\Pi^h$ is constant over the area of the virtual element Ω_e , as a consequence, the pseudo-energy density per unit

volume W is integrated by evaluating the function at the element centroid \mathbf{X}_c as shown in Figure 6.3 and multiplying it with domain size Ω_e analogous to the standard Gauss integration scheme in FEM

$$\int_{\Omega_e} W(\boldsymbol{\epsilon}_{\Pi}^h) dV = W(\boldsymbol{\epsilon}_{\Pi}^h)|_c \Omega_e \quad (6.43)$$

with the label $\square|_c$ refers to quantities evaluated at the element centroid \mathbf{X}_c . The pseudo potential is still a nonlinear function with respect to the deformation map and the crack phase-field nodal degrees of freedom and the history field array.

Next, the stabilization potential has to be derived for the coupled problem based on the potential (6.28). Following the recent work of WRIGGERS ET AL. [329], we introduce a non-linear stabilization procedure, that takes the form

$$\Pi_{stab}(\boldsymbol{\mathfrak{U}}^h - \boldsymbol{\mathfrak{U}}_{\Pi}^h, \mathbf{h})|_e = \widehat{\Pi}(\boldsymbol{\mathfrak{U}}^h, \mathbf{h})|_e - \widehat{\Pi}(\boldsymbol{\mathfrak{U}}_{\Pi}^h, \mathbf{h})|_e \quad (6.44)$$

For the stabilization density function \widehat{W} , we propose a similar function to the original density function (6.28), however scaled by a constant value β as: $\widehat{W} = \beta W$. In (6.44), the stabilization with respect to the projected primary fields $\widehat{\Pi}^{\tau}(\boldsymbol{\mathfrak{U}}_{\Pi}^h, \mathbf{h})|_e$ can be then calculated as (6.43), yielding

$$\widehat{\Pi}(\boldsymbol{\mathfrak{U}}_{\Pi}^h, \mathbf{h})|_e = \beta W(\boldsymbol{\epsilon}_{\Pi}^h)|_c \Omega_e \quad (6.45)$$

Whereas, the potential $\widehat{\Pi}(\boldsymbol{\mathfrak{U}}^h, \mathbf{h})|_e$ is computed by applying standard FEM procedure, i.e. by first discretizing the virtual element domain Ω_e into internal triangle element mesh

Given: $\mathbf{F}_{\Pi}^h, d_{\Pi}, \mathbf{C}_{pn}^{-1}, \alpha_n, \mathcal{H}_n$	Find: $\mathbf{C}_p^{-1}, \alpha, \mathcal{H}$
$\mathbf{b}_{e\Pi}^h = \mathbf{F}_{\Pi}^h \mathbf{C}_{pn}^{-1} \mathbf{F}_{\Pi}^{hT}$	
$W_{elas}(\mathbf{b}_{e\Pi}^h, d_{\Pi}) = g(d_{\Pi}) [\psi_{vol}^+(\mathbf{b}_{e\Pi}^h) + \psi_{iso}(\mathbf{b}_{e\Pi}^h)] + \psi_{vol}^-(\mathbf{b}_{e\Pi}^h)$	
$W_{plas}(\alpha, d_{\Pi}) = g(d_{\Pi}) \psi_p(\alpha)$	
$\mathbf{f}^p := \text{dev}[\boldsymbol{\tau}] \quad \text{with} \quad \boldsymbol{\tau} = 2 \mathbf{b}_{e\Pi}^h \frac{\partial W_{elas}}{\partial \mathbf{b}_{e\Pi}^h}$	
$r^p = \partial_{\alpha} W_{plas}(\alpha, d_{\Pi})$	
$\chi(\mathbf{f}^p, r^p) = \sqrt{3/2} \mathbf{f}^p - r^p$	
$\mathbf{C}_p^{-1} = \mathbf{F}_{\Pi}^{h-1} \exp \left[-2(\alpha - \alpha_n) \sqrt{3/2} \frac{\mathbf{f}^p}{ \mathbf{f}^p } \right] \mathbf{F}_{\Pi}^h \mathbf{C}_{pn}^{-1}$	
$\alpha = \alpha_n + \Delta\gamma$	
$\Delta\gamma = \frac{\Delta t}{\eta_p} \left\langle \chi(\mathbf{f}^p, r^p) \right\rangle_+ \geq 0$	
$\mathcal{H} := \max D(\mathbf{b}_{e\Pi}^h, \alpha) \geq 0 \quad \text{with} \quad D := \left\langle \psi_{vol}^+ + \psi_{iso} + \psi_p - \psi_c \right\rangle_+$	

Box 6.1: Algorithmic treatment of the history field array for the plastic strain measures and the crack driving force.

consisting of $n_T = n_E - 2$ triangles as plotted in Figure 6.4 for the *horse-like* polygonal element. Then the integral over Ω_e is transformed into the sum of integrals over triangles. By using a linear ansatz for the primary fields \mathbf{u} , an approximation can be computed for the constitutive variables \mathbf{c} within each triangle Ω_m^i of the inscribed mesh, see WRIGGERS ET AL. [329]. This gives

$$\widehat{\Pi}(\mathbf{u}^h, \mathbf{h}) \Big|_e = \int_{\Omega_e} \widehat{W}(\mathbf{c}^h) dV = \beta \int_{\Omega_e} W(\mathbf{c}^h) dV = \beta \sum_i^{n_T} \Omega_e^i W(\mathbf{c}^h) \Big|_c \quad (6.46)$$

where $W(\mathbf{c}^h) \Big|_c$ is the potential density function evaluated at the triangle centroid \mathbf{X}_c^i and Ω_e^i is the area of the i^{th} triangle in the element e , as plotted in Figure 6.4.

To compute the stabilization parameter β , a connection to the bending problem was imposed regarding to the bulk energy as outlined in [324]. By limiting the element size Ω_e towards 0, the difference between the potentials of projected values $\widehat{\Pi}(\mathbf{u}_{\Pi}^h, \mathbf{h})$ and the true values $\widehat{\Pi}(\mathbf{u}^h, \mathbf{h})$ will also approach towards 0, thus stabilization will disappear in limit. Due to the finer mesh requirements of the fracture phase field problem compared with [324], the choice of β factor term is less relevant, since it is only relevant for coarse meshes. In this regard we propose a constant value for β taken from the interval:

$$0 < \beta \leq 1 \quad (6.47)$$

Note that for β approaching zero, the potential $\Pi(\mathbf{u}^h, \mathbf{h})$ in (6.40) will depend only on the projection part $\Pi_c(\mathbf{u}_{\Pi}^h, \mathbf{h})$, leading to rank deficiency. However when $\beta = 1$ the FEM results related to the internal mesh will be reproduced. Following our previous work on VEM for phase field brittle fracture [6], we chose a value for the stabilization parameter *at fracture* as $\beta = 0.4$ in all the simulations in Section 6.4, in which VEM coincide with FEM results. In case of a *pure elastic-plastic state*, the stabilization parameter follows the same procedure introduced in our previous works [169, 324] and takes the form

$$\beta = \min \left\{ 0.4, \frac{\sigma_{VM}}{E \alpha} \right\}, \quad (6.48)$$

where $\sigma_{VM} = \sqrt{3/2} |\mathbf{f}^p|$ is the von Mises stress, E is the Young's modulus and α is the equivalent plastic strain providing an approximation for the tangent of the hardening curve.

All further derivations leading to the residual vector \mathbf{R}_e and the tangent matrix \mathbf{K}_e of the virtual element were performed with the software tool ACEGEN. This yields for (6.40) along with the potentials (6.41) and (6.44)–(6.46) the following:

$$\mathbf{R}_e = \frac{\partial \Pi(\mathbf{u}_e, \mathbf{h}_e)}{\partial \mathbf{u}_e} \quad \text{and} \quad \mathbf{K}_e = \frac{\partial \mathbf{R}_e}{\partial \mathbf{u}_e} \quad (6.49)$$

where the history variables are treated as fixed fields in (6.49)₁, i.e. $\partial_{\mathbf{u}_e} \mathbf{h}_e = \mathbf{0}$. With these expressions at hand, we adopt a global Newton-Raphson algorithm for the coupled problem, resulting to the following linearized system

$$\mathbf{R} + \mathbf{K} \Delta \mathbf{u} = \mathbf{0} \quad \text{with} \quad \mathbf{R} = \bigwedge_{e=1}^{n_e} \mathbf{R}_e, \quad \mathbf{K} = \bigwedge_{e=1}^{n_e} \mathbf{K}_e \quad \text{and} \quad \mathbf{u} = \bigwedge_{e=1}^{n_e} \mathbf{u}_e \quad (6.50)$$

that determines at given global primary fields \mathbf{u} their linear increment $\Delta \mathbf{u}$ in a typical Newton-type iterative solution step. This system of nonlinear equations has to be solved in a nested algorithm, where the deformation map and the crack phase-field are the global unknown variables.

Table 6.1: Material parameters used in the numerical examples.

No.	Parameter	Name	Value	Unit
1.	E	Young's modulus	206.9	GPa
2.	ν	Poisson's ratio	0.29	–
3.	H	hardening parameter	0.13	GPa
4.	Y_0	initial yield stress	0.45	GPa
5.	Y_∞	infinite yield stress	0.45/1.165	GPa
6.	δ	saturation parameter	16.93	–
7.	ψ_c	critical fracture energy	0.025/2.0	GPa
8.	η_p	plastic viscosity	10^{-8}	GPa.s
9.	η_f	fracture viscosity	10^{-8}	GPa.s
10.	l	fracture length scale	0.008/0.02	mm
11.	ζ	fracture parameter	8.0/1.0	–

Table 6.2: A comparison between different FEM and VEM discretizations, related to F-U curves in Figure 6.7(a).

	VEM-VO	VEM-T2	FEM-T2	FEM-T1
Number of elements	12369	11109	11109	11109
Number of nodes	24744	22291	22290	5591
No. of equations	74195	66826	66826	16749
Number of steps	280	234	305	232
Total number of iterations	2372	1504	2610	1599
Average iterations/step	6.1134	5.76245	6.97861	6.07985

6.4. Representative numerical examples

We now demonstrate the performance of the proposed virtual element formulation for the phase-field modeling of ductile fracture at finite deformations by means of two representative numerical examples. For comparison purposes, results of the standard finite element method (FEM) are also demonstrated. All computations are performed by using a nested Newton-Raphson algorithm. Load stepping is applied when necessary. Due to the fact that all formulations are linearized in a consistent manner using ACEGEN, quadratic convergence is achieved within a load step. The material parameters used in this section are the same for all examples and given in Table 6.1. They are used by many authors in the literature as a reference for metals [287, 155, 10]. In the first example, we compare VEM and FEM results for the standard single-edge-notched shear test of [10, 238, 22]. Next, an axial stretch of a bar is investigated.

To illustrate the capability and the flexible choice of the number of nodes in an element for VEM, various animals-shaped Voronoi cells (bird, horse, snake, frog, koala, fish, kangaroo, ...) are employed in the undamaged as well as the damaged zones (i.e. an area of interest) for the virtual element formulation in the following subsections.

6.4.1. Single-edge notched shear test. The first benchmark test considers a square plate with a horizontal notch placed at the middle height from the left outer surface to the center of the specimen. The geometrical setup and the loading conditions of the specimen are depicted in Figure 6.5(a). The size of the square specimen is chosen

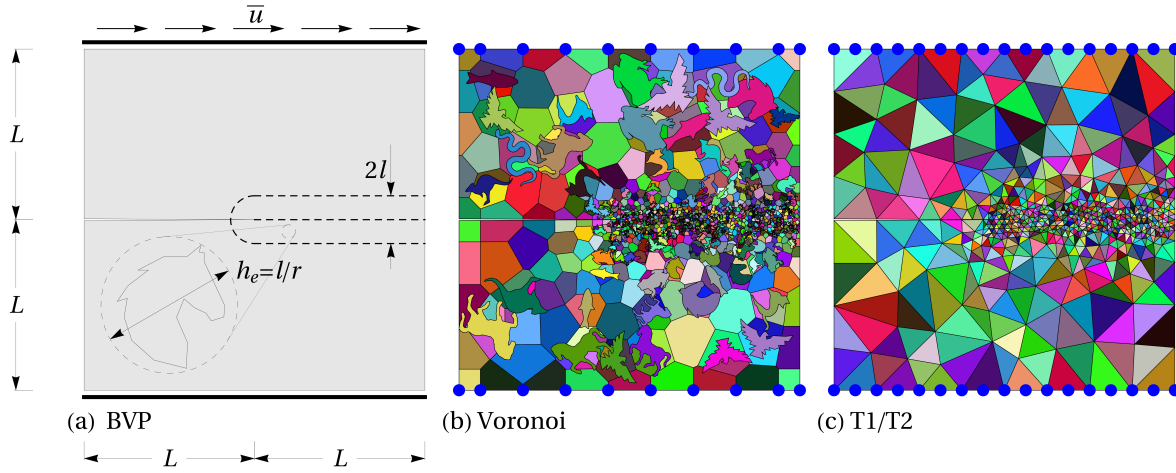


Figure 6.5: Single-edge notched shear test. a) Geometry and boundary conditions, b) VEM with Voronoi mesh and c) triangular finite element mesh.

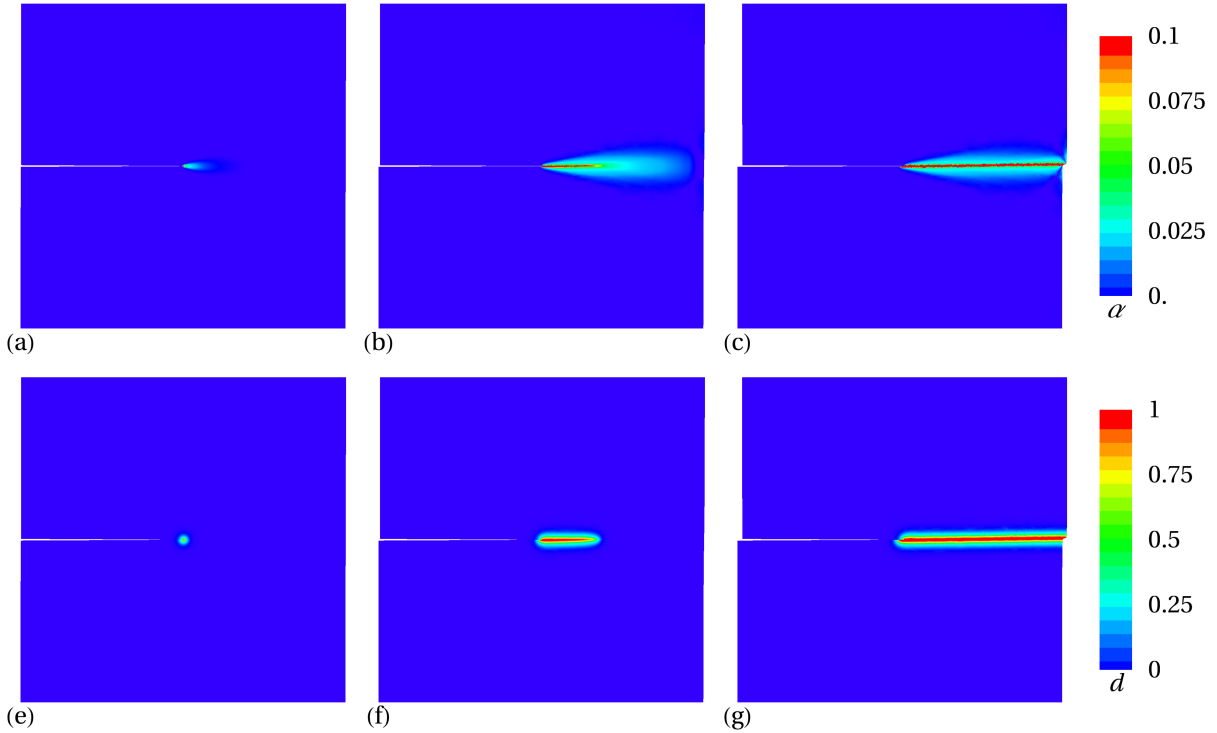


Figure 6.6: Single-edge notched shear test. Contour plots of the equivalent plastic strain α in (a)–(c) and the fracture phase-field d in (e)–(g) for three different deformation states up to final rupture.

to be $L = 0.5$ mm. We fixed the bottom edge of the plate and applied shear loading to the top edge until the plate is fully broken. The specimen is discretized by using different virtual elements (VEM) in Figure 6.5(b) and finite element (FEM) formulations Figure 6.5(c). Here we use the following notations: VEM-VO with a Voronoi mesh ; VEM-T2 with 6 noded triangle representing a *first order* VEM (Note that: T2 in this case implies that, the triangle mesh used is the same as for the second order FEM and *not second order VEM*) ; FEM-T1 with linear triangle and FEM-T2 with quadratic

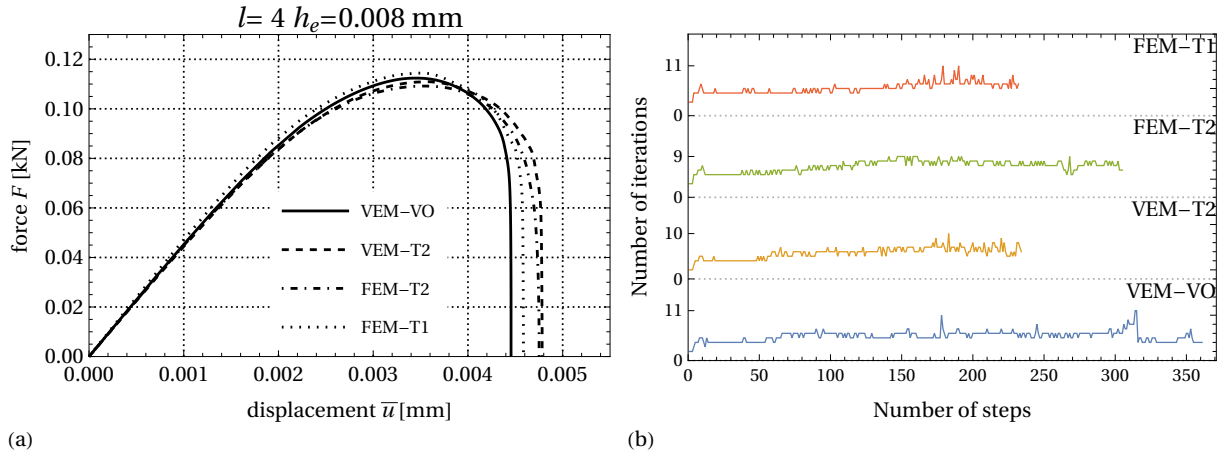


Figure 6.7: Single-edge notched shear test. (a) Load–displacement responses for different VEM and FEM discretization. (b) Comparison between the total number of iterations in each time step that required to achieve convergence for different discretization.

triangle, to test the robustness of the virtual element formulation. A mesh refinement in the expected fracture zone is applied, this is based on the ratio $r := l/h_e$ between the mesh size h_e and the fracture length scale l , as sketched in Figure 6.5(a).

The evolution of the crack phase field d in comparison to the evolution of the equivalent plastic strain α for three different deformation stages up to final rupture are depicted in Figure 6.6. This was achieved by using the virtual element formulations with various animals-shaped Voronoi cells, for fracture length scale $l = 0.008$ mm and the length/mesh ratio $r = 4$. The crack phase-field initiates at the notch-tip, see Figure 6.6(e), where the maximum equivalent plastic strain α is concentrated as shown in Figure 6.6(a). Thereafter, the crack propagates horizontally till separation in Figure 6.6(g), as outlined in [10, 238, 22].

Load-displacement curves of the overall structural response are plotted for different elements formulations of FEM and VEM for comparison purposes in Figure 6.7(a). The VEM results are in a good agreement with the reference works. Table 6.2 compares the different FEM and VEM discretization, related to F-U curves in Figure 6.7(a), with respect to robustness and efficiency. Figure 6.7(b) illustrates the convergence properties for the different element formulations plotted in Figure 6.7(a) at the final deformation state $\bar{u} = 0.0048$ mm. We observe that virtual elements required *fewer* steps and iterations for final convergence compared with finite element method of higher order. Thus here, VEM is more robust than FEM, however, this comes with extra computational costs.

6.4.2. Axial stretch of a bar. The second numerical example is concerned with analyzing the ductile failure behavior of a bar due to a prescribed displacement \bar{u} along axial direction at the right side. It is a standard benchmark problem of finite plasticity and has been analyzed by many authors, see [11, 229, 13, 288]. Experimental observation shows that a necking zone takes place before final ductile rupture. The localized plastic strains in the necking area and the subsequent ductile failure response will be used to test the robustness of the virtual element formulation. The geometrical setup and the boundary conditions of the bar with height $H = 2$ mm and length $L = 10$ mm are illustrated in Figure 6.8. To trigger localization and necking in the center of the bar,

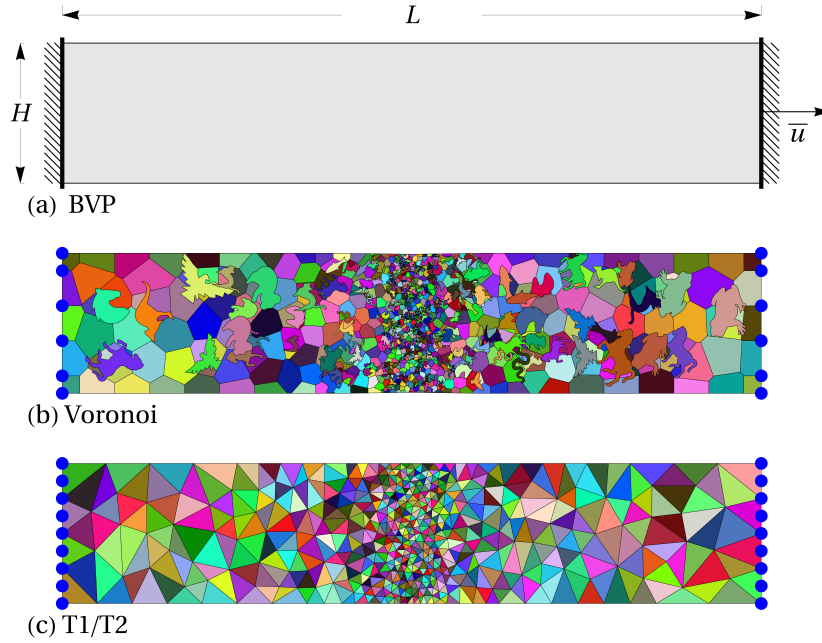


Figure 6.8: Axial stretch of a bar. a) Geometry and boundary conditions, b) VEM with Voronoi mesh and c) triangular finite element mesh.

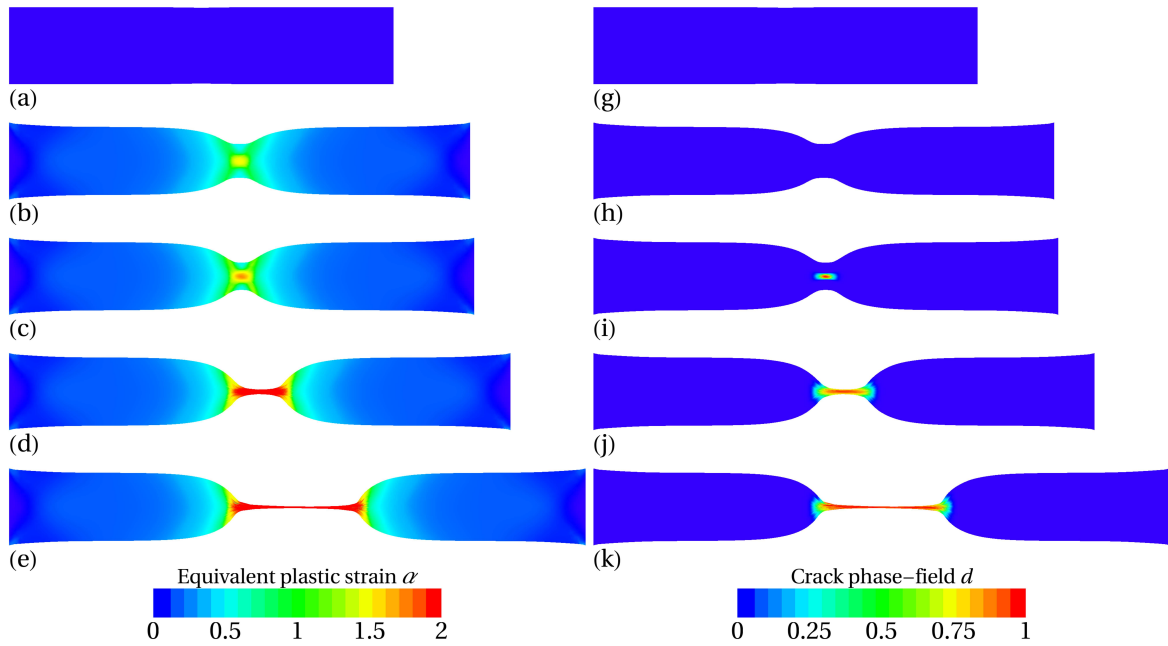


Figure 6.9: Axial stretch of a bar. Contour plots of the equivalent plastic strain α in (a)–(e) and the fracture phase-field d in (g)–(k) for five different deformation states up to final rupture.

a geometrical imperfection is introduced in the central zone. Here, a reduction of the specimen net section at the central zone is applied, in which the height at the center is chosen to be $H_c = 0.99 H$. At the left edge of the bar we applied a Dirichlet boundary condition of $\bar{\mathbf{u}} = \mathbf{0}$ and applied a horizontal displacement at the right edge that has the magnitude of 20 % of the bar length e.g. $\bar{u} = 0.2L$. A mesh refinement in the expected

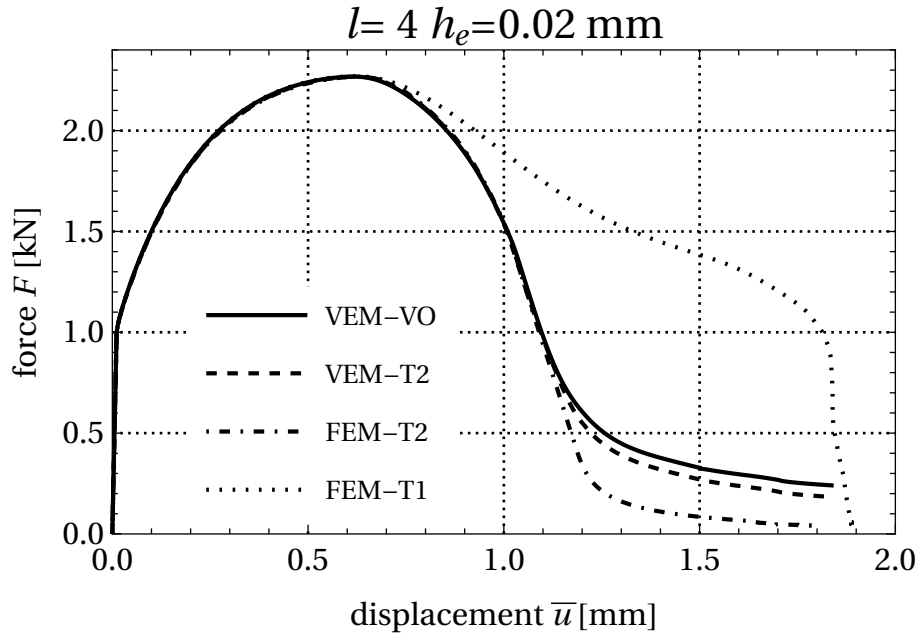


Figure 6.10: Axial stretch of a bar. Load–displacement responses for different VEM and FEM discretization.

fracture zone is applied for all VEM and FEM element formulations, see Figure 6.8(b)-(c).

Figure 6.9 shows the contour plots of the equivalent plastic strain α and the fracture phase field d simulated using the virtual element formulations with various animals-shaped Voronoi cells, for fracture length scale $l = 0.02 \text{ mm}$ and different deformation stages up to final failure. We observed a huge plastic deformation as a necking zone with concentration hardening in Figure 6.9(b)-(c) at the specimen center, resulting with crack initiation at center zone as demonstrated in Figure 6.9(i). Thereafter, the crack phase-field propagates outward following the equivalent plastic strain path till the complete failure as shown in Figure 6.9(j)-(k). Load-displacement curves for different elements formulations of FEM and VEM are displayed in Figure 6.10. All simulations show similar behavior before crack initiation. Thereafter, all elements show almost closer results, except the FEM-T1 which exhibit a stiffer response. As a consequence, the capability of VEM element with Voronoi mesh is comparable to using finite elements of higher order.

7. 3D Virtual elements for finite thermo-plasticity problems

In the previous analysis of the virtual element formulations (Chapter 5 and Chapter 6) *only* two-dimensional problems were considered for various engineering applications in solid mechanics. The successful application of the method to non-linear setting in 2D leads naturally to the question of its effectiveness and robustness in the *third* dimension under large deformations for coupled problems. This chapter is concerned with the extensions of the virtual element method to problems of 3D finite strain thermo-plasticity. Low-order formulations for problems in multi-dimensions, with elements being arbitrary shaped polyhedra, are considered. The formulation is based on minimization of a pseudo energy expression, with a generalization of a stabilization techniques. The resulting discretization scheme is investigated using different numerical examples that demonstrate efficiency, accuracy and convergence properties. For comparison purposes, results of the standard finite element method (FEM) are also demonstrated. The contents of this chapter is based on the following publications ALDAKHEEL ET AL. [7, 169].

7.1. Introduction

Heat treatment processes are a field of research with various engineering applications. This covers forming, machining and cutting of different components. For instance, heating of a steel bolt and cross wedge rolling are processes under thermo-mechanical loading conditions. These processes exhibit complex coupling phenomenon: i) the heat effects the mechanical response by thermal expansion and temperature dependent mechanical properties. ii) On the contrary, the mechanical load action on the thermal field leads to high-temperature distribution and heat dissipation. All applications in this area can significantly benefit from a precise predictive computational tool to model this coupling during and after the forming phases of products to improve the structural reliability.

A great number of pure phenomenological and micro-mechanically motivated approaches exists in literature for thermo-mechanical coupling. In this regard, [32, 33] developed several numerical concepts for the coupled processes based on the so-called natural formulation. [288, 327] investigated the coupled associative thermo-plasticity at finite strains, addressing in detail the numerical analysis aspects. A micro-mechanical approach for modeling the coupled thermo-crystal-plasticity can be found in [294, 83, 81]. A physical approach based on nonlinear rheological models was introduced in [205] to describe finite thermoviscoplasticity. [30, 226] outlined a constitutive model for finite thermo-visco-plastic behavior of amorphous glassy polymers and considered details of its numerical implementation. A variational formulation for the coupled multi-field problem is outlined in [76, 42] based on the works [337, 293].

Most of the approaches existing in the literature for solving thermo-mechanical problems are based on the finite element method (FEM) as a discretization scheme, see [323, 344]. However in recent years different methods were introduced as tools that bring some new features to the numerical analysis aspects of problems in solid and fluid mechanics, like the isogeometric analysis outlined in Hughes et al. [174, 92]. In this contribution a relatively new method, the virtual element method (VEM), will be presented as an alternative approach. The method was developed by F. Brezzi and coworkers [46]. Despite being only five years under development the application range in engineering of VEM has been enlarged such that it includes small/large strain formulations for inelastic re-

sponses. VEM is a competitive discretization scheme for meshes with highly irregular shaped elements. Recent works on virtual elements have been devoted to linear elastic deformations in [47, 135, 36], contact problems in [328], finite elasto-plastic deformations in [169], anisotropic materials in [330, 331, 273], small strain isotropic damage in [96], inelastic solids in [298], hyperelastic materials at finite deformations in [85, 329] and crack-propagation for 2D elastic solids at small strains in [175]. Recently, [6, 8] propose an efficient virtual element scheme for the phase-field modeling of brittle and ductile fracture.

This chapter extends VEM towards finite strain thermo-plasticity problems. Low-order formulations for problems in two and three dimensions are considered, with elements being arbitrary polygons or polyhedra. The various formulations considered are based on minimization of a pseudo energy, with a novel construction of the stabilization energy. In the mechanical part, the model problem of von Mises J_2 -plasticity is used in this paper which includes incompressibility of the plastic deformation and nonlinear isotropic hardening as discussed in [288, 169]. In the thermal part, we follow the investigations of [288, 10] that demonstrate the effect of temperature on the mechanical fields resulting in a thermal expansion and also the change of geometry during heat conduction.

The development of a virtual element typically includes a projection step and a stabilization step. In the projection step, the deformation φ_h and the temperature field T_h which appear in the weak formulation or energy functional are replaced by their projection: φ_Π and T_Π onto a polynomial space. This results in a rank-deficient structure, so that it is necessary to add a stabilization term to the formulation, see [46] and [47] which depends in the linear case on a scalar value computed from the elasticity tensor. In [85] the scalar stabilization parameter was replaced by one that computed using the deformation depending fourth-order elasticity tensor. A new stabilization techniques for the virtual element method was lately developed in [329] who use a technique that was first described in [249], generalized in [60] and simplified in [187] in the context of hexahedral finite elements. This stabilization is also applied in this work where some correction were needed in case of plastic deformations.

The chapter is organized as follows: Section 7.2 outlines the governing equations for finite strain thermo-elasto-plasticity. The development of the virtual element method is formulated in Section 7.3. Finally, a number of numerical tests are presented and discussed in Section 7.4. For comparison purposes, results of the standard finite element method (FEM) are also included.

7.2. Governing equations

This section summarize the theory of coupled thermo-plasticity at large deformations, see e.g. [327, 184, 288, 13].

7.2.1. Basic kinematics at finite strains. Let $\Omega \in \mathbb{R}^d$ with $d = 2, 3$ be the reference configuration of the solid as depicted in Figure 7.1 and $\varphi(\mathbf{X}, t)$ is the nonlinear deformation map at time $t \in \mathbb{R}_+$ and initial position \mathbf{X} defined as

$$\mathbf{x} = \varphi(\mathbf{X}, t) = \mathbf{X} + \mathbf{u}(\mathbf{X}, t) \quad (7.1)$$

where \mathbf{x} is the position of a material point in the deformed configuration and $\mathbf{u}(\mathbf{X}, t)$ is the displacement field. The material deformation gradient is defined by $\mathbf{F}(\mathbf{u}) :=$

$\nabla\varphi(\mathbf{X}, t) = \mathbf{1} + \nabla\mathbf{u}(\mathbf{X}, t)$ with Jacobian $J(\mathbf{u}) := \det\mathbf{F} > 0$. This deformation gradient tensor is decomposed into an elastic \mathbf{F}_e and a plastic \mathbf{F}_p parts as

$$\mathbf{F} = \mathbf{F}_e \mathbf{F}_p \quad (7.2)$$

representing finite deformation plasticity. In this work, the isochoric von Mises J_2 -plasticity theory is considered. Thus, the volume change due to plasticity can be neglected

$$J_p = \det\mathbf{F}_p = 1 \quad \text{yields} \quad J = J_e J_p = J_e = \det\mathbf{F}_e, \quad (7.3)$$

in terms of the elastic J_e and the plastic J_p parts of the Jacobian. The elastic part of the left Cauchy-Green tensor \mathbf{b}_e is formulated by the total deformation gradient and the inverse of the plastic part of the right Cauchy-Green tensor \mathbf{C}_p as

$$\mathbf{b}_e = J_e^{\frac{2}{3}} \bar{\mathbf{b}}_e = \mathbf{F}_e \mathbf{F}_e^T = \mathbf{F} \mathbf{C}_p^{-1} \mathbf{F}^T \quad \text{with} \quad \mathbf{C}_p = \mathbf{F}_p^T \mathbf{F}_p \quad \text{and} \quad \det\mathbf{b}_e = J_e^2 \quad (7.4)$$

where $\bar{\mathbf{b}}_e$ is the deviatoric part of the elastic left Cauchy-Green tensor \mathbf{b}_e with $\det\bar{\mathbf{b}}_e = 1$. The solid is loaded by a Dirichlet- and Neumann-type boundary conditions as

$$\varphi(\mathbf{X}, t) = \bar{\varphi}(\mathbf{X}, t) \quad \text{on} \quad \partial\Omega_\varphi \quad \text{and} \quad \mathbf{PN} = \bar{\mathbf{t}}(\mathbf{X}, t) \quad \text{on} \quad \partial\Omega_t \quad (7.5)$$

with a prescribed deformation $\bar{\varphi}$, external traction $\bar{\mathbf{t}}$ and outward normal \mathbf{N} to the surface $\partial\Omega = \partial\Omega_\varphi \cup \partial\Omega_t$ of the undeformed configuration, as depicted in Figure 7.1(a). The first Piola stress tensor \mathbf{P} is the thermodynamic dual to \mathbf{F} . To account for phenomenological hardening/softening response, we define the equivalent plastic strain variable α by the evolution equation

$$\dot{\alpha} = \dot{\gamma} \quad \text{with} \quad \dot{\alpha} \geq 0 \quad (7.6)$$

as a local internal variable, where $\dot{\gamma} \geq 0$ is the plastic Lagrange multiplier. The hardening variable starts to evolve from the initial condition $\alpha(\mathbf{X}, 0) = 0$.

For the thermal problem, we define the absolute temperature field $T(\mathbf{X}, t) > 0$ on the reference configuration Ω of the solid along with the boundary conditions as

$$T = \bar{T} \quad \text{on} \quad \partial\Omega_T \quad \text{and} \quad \mathbf{QN} = \bar{h} \quad \text{on} \quad \partial\Omega_h \quad (7.7)$$

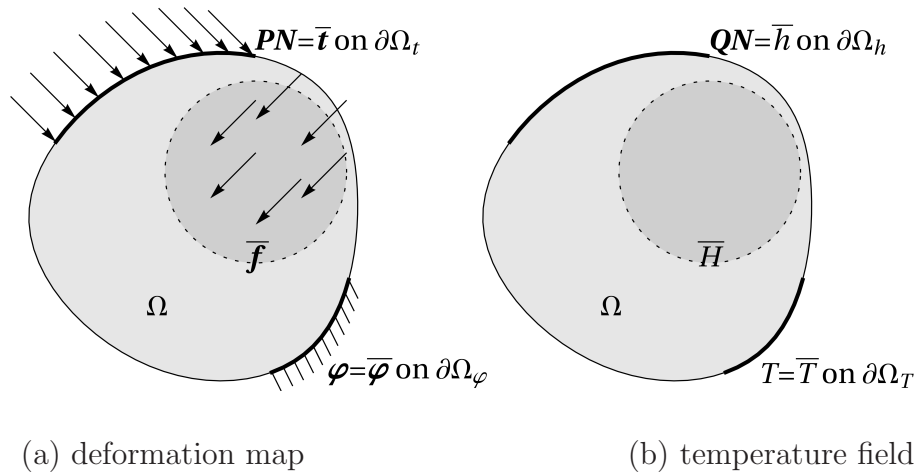


Figure 7.1: Solid with boundary conditions for the coupled problem.

with a *prescribed* temperature field \bar{T} and heat flux \bar{h} , as shown in Figure 7.1(b). The Lagrangian heat flux vector \mathbf{Q} is assumed to be governed by a Fourier-type law

$$\mathbf{Q} = -JK_T \mathbf{F}^{-1} \mathbf{F}^{-T} \nabla T \quad (7.8)$$

where ∇T is the material temperature gradient and K_T is the thermal conductivity which must be positive ($K_T > 0$) in order to achieve thermodynamical consistency. In this contribution, the gradient operator is a referential quantity, i.e. $\nabla \equiv \nabla_{\mathbf{X}}$.

The above introduced variables will characterize a multi-field setting of thermo-mechanical finite strain plasticity based on two *global primary fields*

$$\mathfrak{U} := \{\mathbf{u}, T\}. \quad (7.9)$$

The subsequent constitutive approach to the coupled problem focuses on the set

$$\mathfrak{C} := \{\mathbf{F}, T, \nabla T, \mathbf{h}\} \quad \text{with} \quad \mathbf{h} := \{\mathbf{C}_p^{-1}, \alpha\}, \quad (7.10)$$

in terms of the history field array \mathbf{h} for the plastic strain measures and the hardening variable.

7.2.2. Energetic and dissipative response functions. Following the works [288, 327, 13, 11], the free energy function for the coupled thermo-plasticity problem at finite strains takes the form

$$\widehat{\Psi}(\mathfrak{C}) = \psi_{e,vol}(J_e) + \psi_{e,iso}(\bar{\mathbf{b}}_e) + \psi_{e,th}(J_e, T) + \psi_{th}(T) + \psi_p(\alpha, T) \quad (7.11)$$

in terms of the state variables introduced in (7.10). The volumetric and isochoric elastic parts of the isotropic energetic response function are assumed to have the form

$$\psi_{e,vol}(J_e) = \frac{\kappa}{4}(J_e^2 - 1 - 2 \ln J_e) \quad \text{and} \quad \psi_{e,iso}(\bar{\mathbf{b}}_e) = \frac{\mu}{2}(\text{tr } \bar{\mathbf{b}}_e - 3) \quad (7.12)$$

in terms of the elastic bulk modulus κ , the shear modulus μ and the elastic part of the Jacobian computed as $J_e = \sqrt{\det \bar{\mathbf{b}}_e}$. Following the Coleman-Noll procedure, the Kirchhoff stress tensor $\boldsymbol{\tau}$ and the first Piola-Kirchhoff stress tensor \mathbf{P} are obtained from the volumetric-isochoric elastic parts of the free energy function $\widehat{\Psi}(\mathfrak{C})$ for isotropic material behavior as

$$\boldsymbol{\tau} = 2\bar{\mathbf{b}}_e \frac{\partial \widehat{\Psi}}{\partial \bar{\mathbf{b}}_e} \quad \text{and} \quad \mathbf{P} = \boldsymbol{\tau} \mathbf{F}^{-T} \quad (7.13)$$

The coupled thermoelastic part and the pure thermal contribution of the free energy are defined as

$$\psi_{e,th}(J_e, T) = -3\alpha_T(T - T_0) \partial_{J_e} \psi_{e,vol} \quad \text{and} \quad \psi_{th}(T) = c \left(T - T_0 - T \log \frac{T}{T_0} \right) \quad (7.14)$$

where $\partial_{J_e} \psi_{e,vol} = \frac{\kappa}{2}(J_e - \frac{1}{J_e})$, T_0 is the reference temperature, α_T is the thermal expansion coefficient and c is the heat capacity. The absolute temperature field $T > 0$ is strictly positive. The plastic potential is given by

$$\psi_p(\alpha, T) = Y_0(T) \alpha + \frac{H(T)}{2} \alpha^2 + [Y_\infty(T) - Y_0(T)] [\alpha + \exp(-\delta\alpha)/\delta] \quad (7.15)$$

in terms of the temperature dependent material parameters $Y_0 > 0$, $Y_\infty \geq Y_0$ and $H \geq 0$ defined as

$$\begin{aligned} Y_0(T) &:= Y_0[1 - w_0(T - T_0)] \\ Y_\infty(T) &:= Y_\infty[1 - w_h(T - T_0)] \\ H(T) &:= H[1 - w_h(T - T_0)] \end{aligned} \quad (7.16)$$

as outlined in [288], where w_h is the hardening/softening parameter, w_0 is the flow stress softening parameter and δ is the saturation parameter.

The yield function of von Mises-type finite thermo-plasticity χ restricts the elastic region and has the form

$$\chi = \sqrt{3/2} |\mathbf{s}| - \sigma_y(\alpha, T) \quad \text{with} \quad \mathbf{s} := \text{dev}\boldsymbol{\tau} = \boldsymbol{\tau} - \frac{1}{3}\text{tr}\boldsymbol{\tau}\mathbf{1} \quad \text{and} \quad \sigma_y(\alpha, T) := \partial_\alpha \widehat{\Psi} \quad (7.17)$$

in terms of the deviatoric plastic driving force \mathbf{s} and the resistance force σ_y . With the yield function χ at hand, we can define the dual dissipation function for visco-plasticity according to Perzyna-type model as

$$\Phi^*(\mathbf{s}, \sigma_y) = \frac{1}{2\eta_p} \langle \chi \rangle_+^2 \quad (7.18)$$

with η_p being the viscosity parameter of the rate dependent plastic deformation. The evolution equations for the plastic variables are

$$-\frac{1}{2}\mathcal{L}_v \mathbf{b}_e = \dot{\gamma} \mathbf{n} \mathbf{b}_e \quad \text{with} \quad \mathbf{n} = \frac{\partial \chi}{\partial \mathbf{s}} \quad \text{and} \quad \dot{\alpha} = \dot{\gamma} := \frac{1}{\eta_p} \langle \chi \rangle_+, \quad (7.19)$$

where $\mathcal{L}_v \mathbf{b}_e$ denotes the Lie derivative or Oldroyd rate of \mathbf{b}_e and \mathbf{n} is the flow direction. The evolution equation (7.19)₁ can be recast with (7.4) in an alternative form

$$\dot{\mathbf{C}}_p^{-1} = -2\dot{\gamma} \mathbf{F}^{-1} \mathbf{n} \mathbf{F} \mathbf{C}_p^{-1} \quad (7.20)$$

which will be used later for the algorithmic treatment of plasticity within the numerical solution algorithm, see e.g. [183]. The Kuhn-Tucker conditions for the elasto-plastic model are

$$\chi \leq 0 \quad , \quad \dot{\gamma} \geq 0 \quad \text{and} \quad \chi \dot{\gamma} = 0 \quad (7.21)$$

The discretized form of the evolution equation (7.20) follows from [288, 183], and together with the conditions (7.21) forms the local residual of the problem:

$$\mathbf{F} \mathbf{C}_p^{-1} - \exp[-2(\alpha - \alpha_n) \mathbf{n}] \mathbf{F} \mathbf{C}_{p,n}^{-1} = 0 \quad \text{and} \quad \chi = 0 \quad , \quad (7.22)$$

where $\mathbf{C}_{p,n}^{-1}$ and α_n are the converged history values at the previous step. The system of equations (7.22) has to be solved locally at the element level only when $\chi > 0$. This yields an updated history field array $\mathbf{h} = \{\mathbf{C}_p^{-1}, \alpha\}$. If $\chi < 0$, then the history field will remain same, i.e. $\mathbf{C}_p^{-1} = \mathbf{C}_{p,n}^{-1}$ and $\alpha = \alpha_n$. For further details on the algorithmic treatment of the plastic history field array \mathbf{h} , we refer to the works [288, 169, 323].

With regard to the spatial discretization, the plastic history variables are computed from the consistency term, introduced in Section 7.3. These variables are then used as given and fixed history values in the stabilization procedure.

7.2.3. Global constitutive equations. The global governing equations describing the coupled problem are the balance of linear momentum and the absolute temperature evolution defined as

$$\begin{aligned} \text{Div}[\mathbf{P}] + \bar{\mathbf{f}} &= \mathbf{0} \\ c \dot{T} + \text{Div}[\mathbf{Q}] - \mathcal{D}_{loc}^{red} + \mathcal{H} - \mathcal{R} &= 0 \end{aligned} \quad (7.23)$$

along with the Neumann-type boundary conditions in (7.5),(7.7) and the prescribed body force $\bar{\mathbf{f}}$ and heat source \mathcal{R} . The reduced local dissipation density function takes the form

$$\mathcal{D}_{loc}^{red} := \zeta \sigma_y(\alpha, T) \dot{\alpha} \quad \text{with} \quad \dot{\alpha} := \frac{\alpha - \alpha_n}{\Delta t} \quad (7.24)$$

where $\zeta \in [0, 1]$ is a constant dissipation factor, as outlined in the work of [288]. The heat capacity c and the latent heating \mathcal{H} in (7.23) are defined as

$$c := -T \partial_{TT}^2 \widehat{\Psi}(\mathbf{e}) \quad \text{and} \quad \mathcal{H} := -T \partial_T \left[\mathbf{P} \cdot \dot{\mathbf{F}} - \mathcal{D}_{loc}^{red} \right] \quad (7.25)$$

With the above set of constitutive equations, the coupled thermo-mechanical problem is formulated. As a starting point for the development of a discretization method, the weak form of equilibrium can be used. In this work, the weak form is decomposed into mechanical M and thermal T parts as

$$\begin{aligned} G(\mathbf{u}, T) &= G_M(\mathbf{u}) + G_T(T) \\ G_M(\mathbf{u}) &= \int_{\Omega} [\mathbf{P}(\mathbf{u}, \mathbf{h}) \cdot \mathbf{F}(\delta \mathbf{u}) - \bar{\mathbf{f}} \cdot \delta \mathbf{u}] d\Omega - \int_{\partial\Omega} \bar{\mathbf{t}} \cdot \delta \mathbf{u} d\Gamma \\ G_T(T) &= \int_{\Omega} \delta T \left[\frac{c}{\Delta t} (T - T_n) + \mathcal{H} - \mathcal{D}_{loc}^{red} - \mathcal{R} \right] d\Omega - \int_{\partial\Omega} \nabla \delta T \cdot \mathbf{Q} d\Omega - \int_{\partial\Omega} \bar{h} \delta T d\Gamma \end{aligned} \quad (7.26)$$

here $\delta \mathbf{u}, \delta T$ are the test functions for the displacement and the temperature fields, respectively. However, it is computationally more efficient to start the development of the thermo-elasto-plastic formulations from a pseudo-potential energy function directly instead of using the weak form (7.26). This is especially advantageous when the code is automatically generated using the software tool *AceGen*, see [184]. The pseudo-potential energy depends on the thermo-elastic parts and *keeps* the plastic history field array \mathbf{h} *constant* during the first variation

$$U(\mathbf{u}, T; \mathbf{h}) = \int_{\Omega} [\Psi(\mathbf{e}; \mathbf{h}) - \bar{\mathbf{f}} \cdot \mathbf{u} - \mathcal{R}T] d\Omega - \int_{\partial\Omega} [\bar{\mathbf{t}} \cdot \mathbf{u} + \bar{h}T] d\Gamma \quad (7.27)$$

in terms of the thermo-mechanical energy function

$$\Psi(\mathbf{e}; \mathbf{h}) = \Psi_M + \Psi_T \quad \text{with} \quad \begin{aligned} \Psi_M &= \psi_{e,vol} + \psi_{e,iso} - [3\alpha_T(T - T_0)]_{ct} \partial_{J_e} \psi_{e,vol} \\ \Psi_T &= \frac{c}{2\Delta t} (T - T_n)^2 + T [\mathcal{H} - \mathcal{D}_{loc}^{red}]_{ct} - \nabla T \cdot [\mathbf{Q}]_{ct} \end{aligned} \quad (7.28)$$

the components inside square bracket $[-]_{ct}$ are kept *constant* during the variation of potential in *AceGen*. For more information about the construction of such a pseudo-potential, we refer the interested reader to [184]. It can be shown that the first variation

of (7.27) when keeping part $[-]_{ct}$ constant leads to the same results as the weak form (7.26).

On the computational side, one may employ either a monolithic or a staggered algorithm to compute the unknowns, in which the displacement and the absolute temperature field are computed either simultaneously or alternatively. In this work, a robust and efficient monolithic scheme is employed in the numerical implementation using the software tool *AceGen*, see [184].

7.3. Virtual element discretization

Within the virtual element method (VEM), proposed in [47] for the linear elastic case, a Galerkin projection of the deformation or displacement is made that maps the unknown variables onto a specific polynomial ansatz space. The special advantage is that the domain Ω can be partitioned into non-overlapping polyhedral elements which are allowed to have arbitrary shapes including non-convex forms. For large strain applications VEM was used so far to formulate different models with hyperelastic material equations in two and three-dimensions, see e.g. [85] and [329]. Elasto-plastic problems of two dimensions were investigated in [37] using higher order virtual elements. This chapter extends VEM to finite strain thermo-elasto-plasticity employing a low order virtual element ansatz space. Here the domain Ω is partitioned into arbitrary non-overlapping polyhedral elements with polygonal faces.

In this work the ansatz for the virtual elements will be based on linear functions. Using this low order ansatz the element nodes can be placed entirely at the vertices of the polyhedral elements, see e.g. [47]. The discrete space of test functions on Ω is denoted by V_h , and for a conforming approach we require that $V_h \subset V$. This requirement is met by defining the shape or basis functions in V_h as linear functions in the 3D space. This yields continuous functions within an element Ω_e . Furthermore, the restriction of the element shape functions to the element boundaries are linear functions, see Figure 7.2.

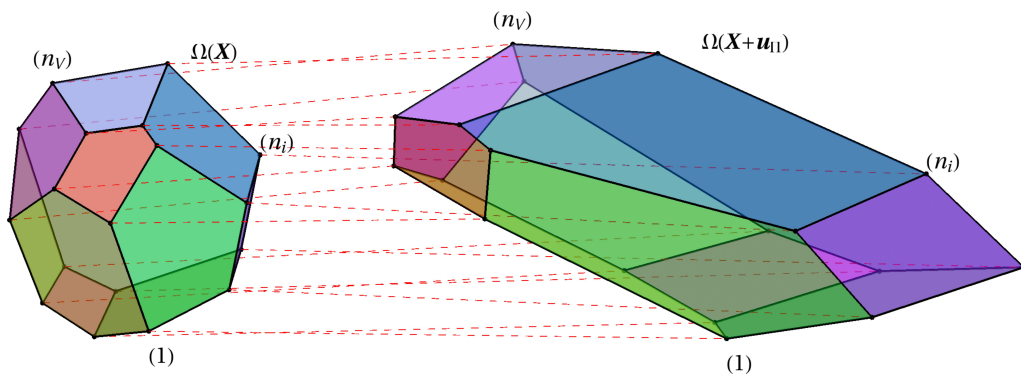


Figure 7.2: The deformation map of polynomial basis function for the virtual element ansatz.

Generally the virtual element method for finite strains has to discretize the deformation map $\varphi = \mathbf{X} + \mathbf{u}$. Since the coordinates \mathbf{X} are exactly known in the initial configuration, we can restrict the discretization to the displacement field $\mathbf{u} = u_i \mathbf{E}_i$ where \mathbf{E}_i are the basis vectors with respect to the initial configuration in the three-dimensional space $i \in \{1, 2, 3\}$.

Based on that, the virtual element method relies on the split of the ansatz space into a part \mathfrak{U}_Π representing the projected primary fields defined in (7.9) and a remainder

$$\mathfrak{U} = \mathfrak{U}_\Pi + (\mathfrak{U} - \mathfrak{U}_\Pi) \quad \text{with} \quad \mathfrak{U}_\Pi := \{\mathbf{u}_\Pi, T_\Pi\} \quad (7.29)$$

The simplest form for the projection \mathfrak{U}_Π is given at element level by the linear ansatz

$$\mathfrak{U}_\Pi = \begin{bmatrix} u_{X\Pi} \\ u_{Y\Pi} \\ u_{Z\Pi} \\ T_\Pi \end{bmatrix} = \mathbf{a} \cdot \mathbf{N}_\Pi = \begin{bmatrix} a_1 & a_5 & a_9 & a_{13} \\ a_2 & a_6 & a_{10} & a_{14} \\ a_3 & a_7 & a_{11} & a_{15} \\ a_4 & a_8 & a_{12} & a_{16} \end{bmatrix} \begin{bmatrix} 1 \\ X \\ Y \\ Z \end{bmatrix} \quad (7.30)$$

with the sixteen unknowns \mathbf{a} which have to be determined. Here the same procedure as in [169, 6, 8] will be applied to define the ansatz function of the virtual element. This is based on two conditions for the low order ansatz space:

(i) The gradient $\nabla \mathfrak{U}_\Pi$ of the projection ansatz (7.30) is constant at the element level and is defined as the mean value of the *true* gradient $\text{Grad } \mathfrak{U}$. The value of $\text{Grad } \mathfrak{U}$ is unknown, however the mean value can be evaluated over the element boundary as follows:

$$\int_{\Omega_e} \nabla \mathfrak{U}_\Pi \, d\Omega \stackrel{!}{=} \int_{\Omega_e} \text{Grad } \mathfrak{U} \, d\Omega \quad \rightarrow \quad \nabla \mathfrak{U}_\Pi^e = \frac{1}{\Omega_e} \int_{\partial\Omega_e} \mathfrak{U} \otimes \mathbf{N} \, d\Omega, \quad (7.31)$$

with an ansatz for \mathfrak{U} at the boundary $\partial\Omega_e$ of the virtual element domain Ω_e . \mathbf{N} is the normal at the boundary of a virtual element e , as shown in Figure 7.3.

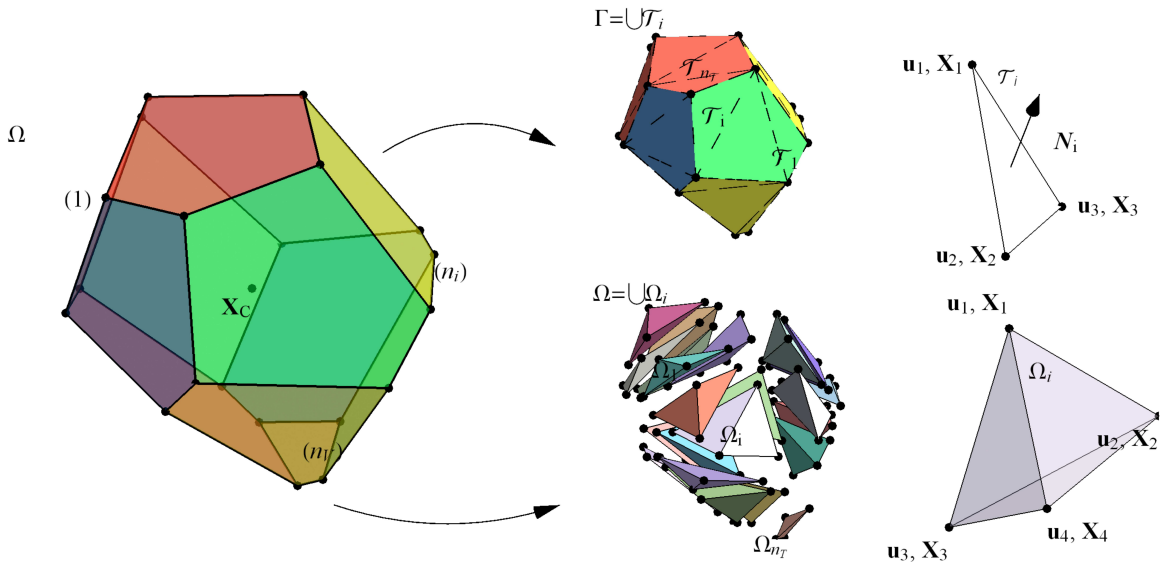


Figure 7.3: Virtual element ansatz. Internal tetrahedral mesh and virtual element faces split into multiple triangles.

(ii) The sum of the nodal values \mathbf{u} and of its projections \mathbf{u}_Π are equal, as follows

$$\frac{1}{n_V} \sum_{I=1}^{n_V} \mathbf{u}_\Pi(\mathbf{X}_I) = \frac{1}{n_V} \sum_{I=1}^{n_V} \mathbf{u}(\mathbf{X}_I), \quad (7.32)$$

where \mathbf{X}_I are the initial coordinates of the nodal point I and the sum includes all n_V element nodes. \mathbf{u}_Π is now computable in terms of the nodal values of \mathbf{u} .

Based on the split in (7.29), the pseudo-potential function defined in (7.27) can be rewritten by summing up all element contributions for the n_e virtual elements as

$$U(\mathbf{u}; \mathbf{h}) = \bigwedge_{e=1}^{n_e} U(\mathbf{u}_e; \mathbf{h}_e) \quad \text{with} \quad U(\mathbf{u}_e; \mathbf{h}_e) := U_c(\mathbf{u}_\Pi, \mathbf{h})|_e + U_{stab}(\mathbf{u} - \mathbf{u}_\Pi, \mathbf{h})|_e, \quad (7.33)$$

with a constant compatibility part U_c and an associated stabilization term U_{stab} . Hereby the history field array \mathbf{h}_e contains local variables evaluated by *local Newton-Raphson iteration procedure* at element centroid \mathbf{X}_c^i as a single Gauss point of the element and used in both parts (compatibility U_c and stabilization U_{stab}) of the pseudo-potential function. A summary of the algorithmic treatment of the history field for the plastic strain measures is outlined in Box 1 of the reference works [169, 8]. By neglecting the body and traction forces of the coupled problem, the compatibility part in (7.33) can be computed for each virtual element by integrating specific pseudo-potential energy Ψ (7.28) over element domain Ω_e as

$$U_c(\mathbf{u}_\Pi, \mathbf{h})|_e = \int_{\Omega_e} \Psi(\mathbf{e}_\Pi) d\Omega = \Psi(\mathbf{e}_\Pi)|_c \Omega_e \quad \text{with} \quad \mathbf{e}_\Pi := \{\nabla \varphi_\Pi, T_\Pi, \nabla T_\Pi, \mathbf{h}\} \quad (7.34)$$

where the primary fields \mathbf{u}_Π are linear functions and their gradient $\nabla \mathbf{u}_\Pi$ are constant over the area of the virtual element Ω_e . As a consequence, the pseudo-energy Ψ is integrated by evaluating the function at the element centroid \mathbf{X}_c and multiplying it with domain size Ω_e (element volume). This procedure is analogous to the standard Gauss integration scheme in FEM. The label $\square|_c$ refers to quantities evaluated at the element centroid \mathbf{X}_c , as depicted in Figure 7.3.

Next, the stabilization potential has to be constructed for the coupled problem. Following the recent works [6, 8, 169, 324], we introduce a non-linear stabilization procedure, that takes the final form

$$U_{stab}(\mathbf{u} - \mathbf{u}_\Pi, \mathbf{h})|_e = \sum_{s \in \{M, T\}} \beta_s \left(\sum_i^{n_T} \Omega_e^i \Psi_s(\mathbf{e})|_c - \Psi_s(\mathbf{e}_\Pi)|_c \Omega_e \right) \quad (7.35)$$

with Ω_e^i being the area of the i^{th} triangle in the element e and n_T is the number of the internal triangles in e . The potential $\Psi_s(\mathbf{e})|_c$ is computed by applying a standard FEM procedure, i.e. by first discretizing the virtual element domain Ω_e into an internal triangle (2D) / tetrahedral (3D) mesh as plotted in Figure 7.3. Then the potential is evaluated at the centroid \mathbf{X}_c^i of triangle i using a linear ansatz for the primary fields \mathbf{u} , see [329, 6, 169]. To obtain the triangularization of the virtual element, we have used the triangulation algorithms provided by *Wolfram Mathematica 11.3* (WWW.WOLFRAM.COM) software tool (Commands `ToElementMesh` or `TriangulateMesh`), which are very robust.

Furthermore, the quality of the created triangulation can be controlled by user. The set of stabilization parameters $\boldsymbol{\beta}$ for the coupled problem composes of

$$\boldsymbol{\beta} := \left\{ \beta_M, \beta_T \right\} \quad (7.36)$$

mechanical (elastic-plastic) part (M) and a thermal part (T). For the thermal problem, we propose a constant value for β_T taken from the interval:

$$0 < \beta_T \leq 1 . \quad (7.37)$$

Note that for β_T approaching zero, the thermal part of the potential $U(\boldsymbol{\mathfrak{u}}, \mathbf{h})$ in (7.33) will depend only on the projection part $U_c(\boldsymbol{\mathfrak{u}}_\Pi, \mathbf{h})$, leading to rank deficiency. However when $\beta_T = 1$ the FEM results related to the internal mesh will be reproduced. The optimal ratio extrapolated from various numerical examples is around $\beta_T \in [0.2, 0.6]$ see e.g. [6, 169], here we chose $\beta_T = 0.4$ in all the simulations. In case of a *pure elastic-plastic state*, the stabilization parameter β_M derives from the same procedure introduced in [169, 324, 8]. It takes the form

$$\beta_M = \min \left\{ 0.4, \frac{\sigma_{VM}}{E \alpha} \right\} , \quad (7.38)$$

where $\sigma_{VM} = \sqrt{3/2} |\mathbf{s}|$ is the von Mises stress, E is the Young's modulus and α is the equivalent plastic strain providing an approximation for the tangent of the hardening curve. A numerical study of the influence of the stabilization parameter on the load-deflection curves of the overall structural response will be investigated in Section 7.4. Therein, the necessity of utilizing the softening part ($\sigma_{VM}/E \alpha$) in the plastic state is illustrated by means of the 3D Necking example, see Figure 7.11.

All further derivations leading to the residual vector \mathbf{R}_e and the tangent matrix \mathbf{K}_e of the virtual element were performed with the software tool *AceGen*. This yields for (7.33) along with the potentials (7.34) and (7.35) the following:

$$\mathbf{R}_e = \left. \frac{\partial U(\boldsymbol{\mathfrak{u}}_e; \mathbf{h}_e)}{\partial \boldsymbol{\mathfrak{u}}_e} \right|_{\mathbf{h}_e = \text{const}} \quad \text{and} \quad \mathbf{K}_e = \frac{\partial \mathbf{R}_e}{\partial \boldsymbol{\mathfrak{u}}_e} \quad (7.39)$$

where the already calculated history variables are treated as fixed fields in (7.39) during the first variation only, i.e. $\partial_{\boldsymbol{\mathfrak{u}}_e} \mathbf{h}_e = \mathbf{0}$. With these expressions at hand, we proceed further to compute the global primary fields $\boldsymbol{\mathfrak{u}}$ in a typical Newton-type iterative solution step, similar to standard FEM.

we adopt a global Newton-Raphson algorithm for the coupled problem, resulting to the following linearized system

$$\mathbf{R} + \mathbf{K} \Delta \boldsymbol{\mathfrak{u}} = \mathbf{0} \quad \text{with} \quad \mathbf{R} = \bigwedge_{e=1}^{n_e} \mathbf{R}_e \quad , \quad \mathbf{K} = \bigwedge_{e=1}^{n_e} \mathbf{K}_e \quad \text{and} \quad \boldsymbol{\mathfrak{u}} = \bigwedge_{e=1}^{n_e} \boldsymbol{\mathfrak{u}}_e \quad (7.40)$$

that determines at given global primary fields $\boldsymbol{\mathfrak{u}}$ their linear increment $\Delta \boldsymbol{\mathfrak{u}}$ in a typical Newton-type iterative solution step. This system of nonlinear equations has to be solved in a nested algorithm, where the deformation map and the temperature field are the global unknown variables.

7.4. Representative numerical examples

In this section, the performance of the proposed two and three dimensional virtual element formulation for modeling finite strain thermo-elasto-plastic problems will be demonstrated by means of representative numerical examples. For comparison purposes, results of standard finite elements (FEM) are also included. The material parameters for metals used in the simulations are obtained from the reference works [10, 287, 155] and are outlined in Table 7.1.

Table 7.1: Material parameters used for the numerical examples.

No.	Parameter	Label	Value	Unit
1	Elastic modulus	E	206.9	kN/mm^2
2	Poisson ratio	ν	0.29	–
3	Initial yield stress	Y_0	0.45	kN/mm^2
4	Infinite yield stress	Y_∞	1.165	kN/mm^2
5	Hardening coefficient	H	0.129	kN/mm^2
6	Saturation exponent	δ	16.93	–
7	Flow stress softening	ω_0	0.002	$1/K$
8	Hardening softening	ω_h	0.002	$1/K$
9	Dissipation factor	ζ	0.9	–
10	Thermal expansion coefficient	α_T	0.000012	$1/K$
11	Thermal conductivity	K_T	0.045	$kN/(sK)$
12	Heat capacity	c	0.003588	$kN/(mm^2K)$

The following mesh types are introduced for the computations using the virtual element method:

- 2D regular mesh with 4 noded quadrilateral elements denoted as Q1,
- 3D regular mesh with 8 noded hexahedral elements denoted as H1,
- 2D regular mesh with 8 noded quadrilateral elements denoted as Q2S,
- 2D/3D Voronoi cell mesh with arbitrary number of element nodes denoted as VO.

Note that all these meshes represent a *first order* virtual element discretization. In order to test the robustness of VEM, the following finite element formulations were selected for comparison:

- FEM-Q1/H1 denotes a standard first order finite element with linear interpolation representing the Q1/H1 element types for 2D/3D, run on meshes introduced above,
- FEM-Q1P0/H1P0 denotes a Hu-Washizu mixed finite element with two additional element degrees of freedom p/θ yielding: $\Psi_{HW} = \Psi_M(\theta, \bar{\mathbf{b}}_e) + p(J_e - \theta)$. This represents a regular mesh with a mixed Q1P0/H1P0 finite element which does not lock in case of plastic incompressibility, see [289, 323, 227],

- FEM-CG4/CG9 denotes a modified enhanced assumed strain, representing a standard first order finite element with linear interpolation of primary field and additionally a modified displacement gradient with internal 4/9 enhanced modes $\mathbf{F} := \mathbf{1} + \nabla \mathbf{u} + \tilde{\mathbf{H}}$, where the enhanced displacement gradient $\tilde{\mathbf{H}}$ is condensed out at the element level. See [178, 325, 185, 326].

7.4.1. Necking of a bar. In the first numerical example, a high temperature distribution and heat dissipation arising due to mechanical loading are considered. To this end, we investigate the necking phenomenon in a bar due to prescribed displacement along axial direction, as outlined in [13, 11, 169]. This will be used to test the robustness of the proposed virtual element formulation.

Two dimensional case:. For the 2D case, the geometrical setup and the boundary conditions of the rectangular bar with height $H = 1 \text{ mm}$ and length $L = 10 \text{ mm}$ are illustrated in Fig. 7.4. Plane strain is considered in this investigation. A geometrical imperfection is introduced in the central zone to trigger necking and localization in the bar center. Both edges of the bar are fixed, additionally a prescribed horizontal displacement with magnitude of $\bar{u} = 0.2L = 2 \text{ mm}$ is applied at the right side.

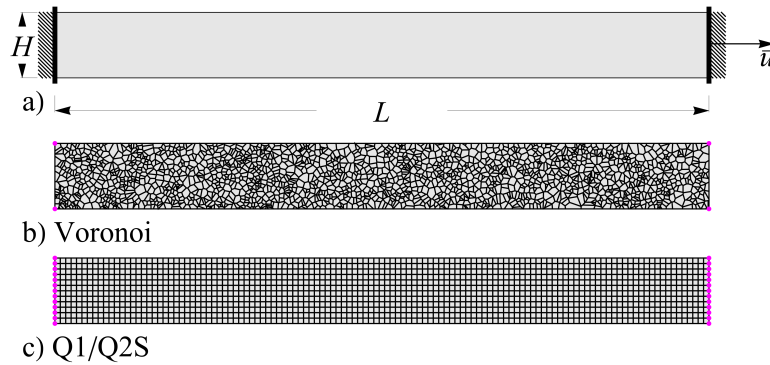


Figure 7.4: 2D Necking of a bar. (a) Geometry and boundary conditions, (b) VEM with Voronoi mesh and (c) regular Q1/Q2S finite element mesh.

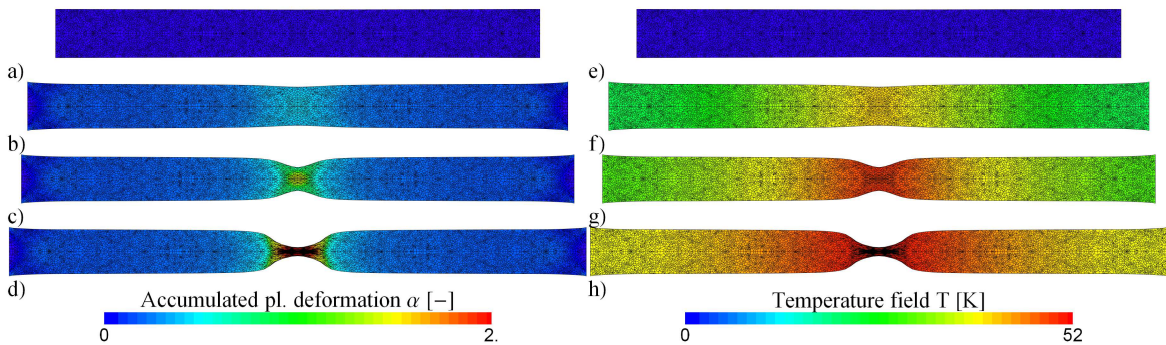


Figure 7.5: 2D Necking of a bar. Contour plots of the equivalent plastic strain in (a)–(d) and the absolute temperature field in (e)–(h) at different deformation states using VEM-VO.

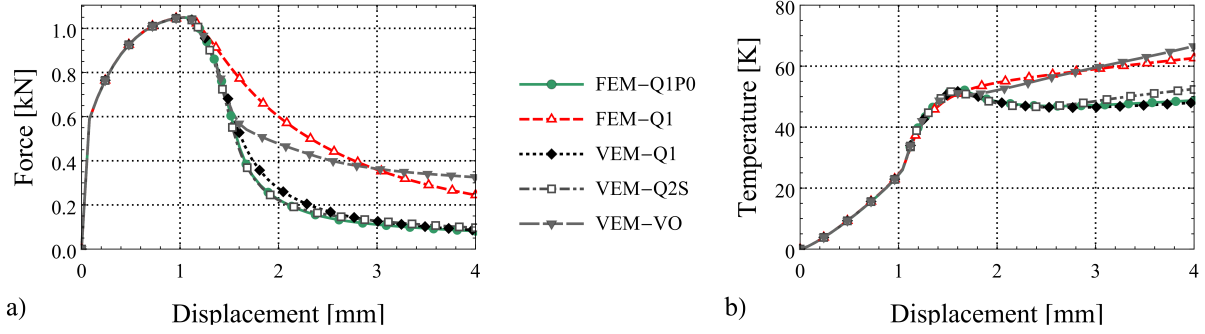


Figure 7.6: 2D Necking of a bar: (a) Force-displacement and (b) temperature-displacement curves for different types of elements.

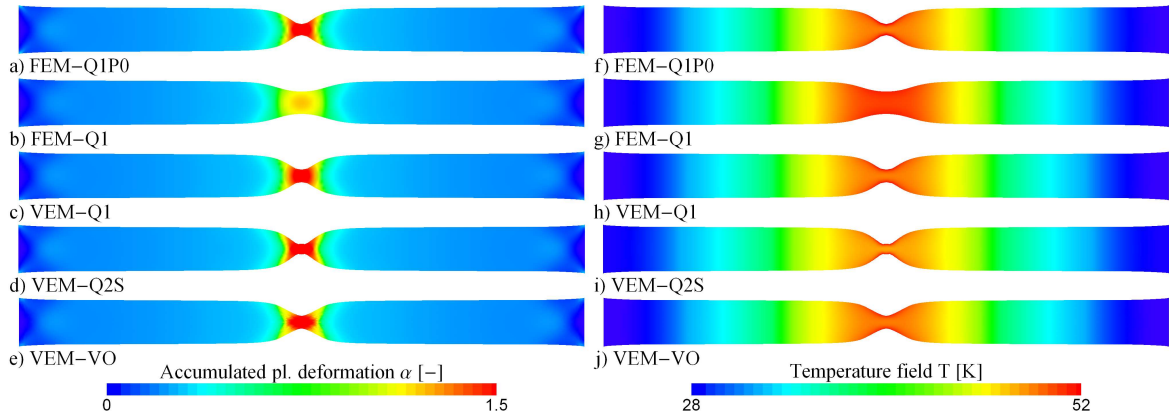


Figure 7.7: 2D Necking of a bar. Distribution of the equivalent plastic strain α and the absolute temperature field T at the final deformation state for all elements.

Figure 7.5 depicts the evolution of the equivalent plastic strain α in (a)–(d) and the absolute temperature field T in (e)–(h) at different stages of deformations using VEM-VO mesh. We observe a huge plastic deformations as a necking zone and heat concentration at the centre of the bar.

The load-displacement curves for different element formulations are demonstrated in Figure 7.6(a). All elements recover the constant strain part before the necking occurs. Thereafter, the virtual elements with regular meshes and the mixed finite element formulation (FEM-Q1P0) yield close result, showing the very good response for very large strains. Due to the thermo-mechanical coupling, a further softening response is noted compared with the isothermal case as in [169]. The corresponding temperature evolution is illustrated in Figure 7.6(b) for all element types at the centre of the bar. The results for VEM-VO are a bit stiffer due to the distorted nature of the mesh. It was shown in [169], that the distorted H1 mesh performs much worse than regular H1 mesh.

Figure 7.7 shows a good agreement between all elements, except standard FEM-Q1, in the necking area and the capability of the virtual element to solve finite thermo-elasto-plastic strain problems. The meshes with FEM-Q1P0 and VEM-Q2S produce more localized shapes than the other meshes. The Voronoi and especially Q1 example exhibit

a stiffer response, which results in a larger necking diameter. This applies especially to the deformation range of post initial softening behaviour.

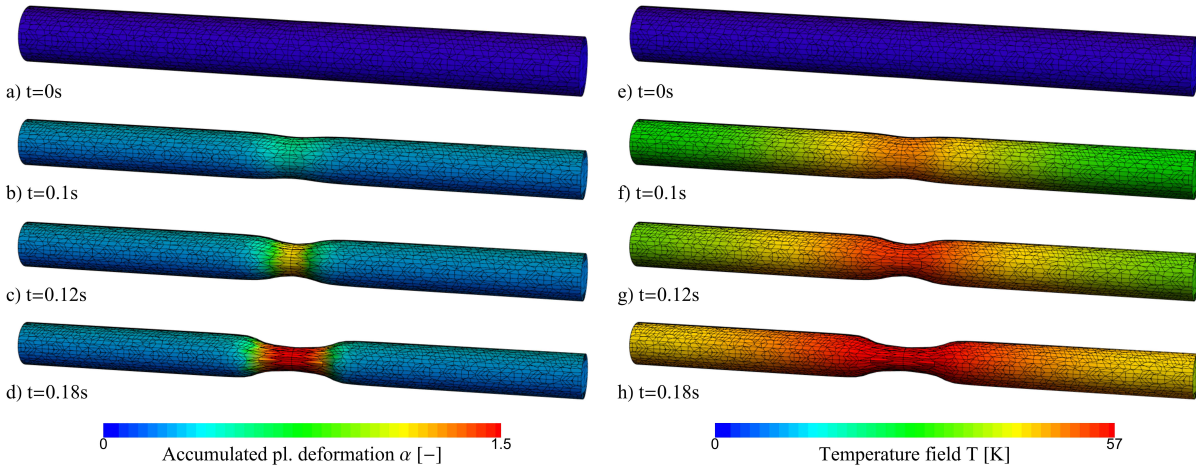


Figure 7.8: 3D Necking of a cylindrical bar. Distribution of the equivalent plastic strain α in (a)–(d) and the absolute temperature field T in (e)–(h) for different deformation states using VEM-Voronoi.

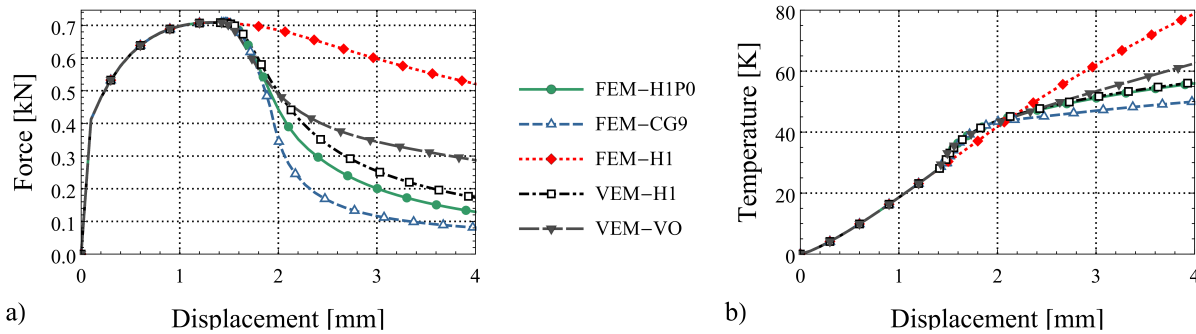


Figure 7.9: Three dimensional necking of a cylindrical bar: (a) Force-displacement and (b) Temperature-displacement curves for different types of elements.

Three dimensional case:. To illustrate the necking zone along with the temperature evolution in a cylindrical bar under tension loading, we extend the two dimensional BVP introduced in Figure 7.4 to three dimensional setting. The cylindrical bar diameter is chosen to be $D = H$ and the length is set to L . Figure 7.8 demonstrates the equivalent plastic strain α and the absolute temperature field T evolutions for different deformation stages using VEM-Voronoi. Furthermore, Figure 7.9 illustrates the load-displacement curves and the corresponding temperature evolution for different element formulations. Similar to the 2D case, the capability of VEM is comparable to using mixed/enhanced finite elements (FEM-H1P0/CG9).

Next, the mesh convergence study was performed based on three different FEM discretizations versus the virtual element formulation VEM-H1. Figure 7.10a demonstrates the peak force versus the *logarithmically scaled* mesh sizes ($N = \{1, 2, 4, 8, 10\}$) of a hexahedral mesh with element division: $N_{\text{Elements}} = 10N \times N \times N$. The peak force converges

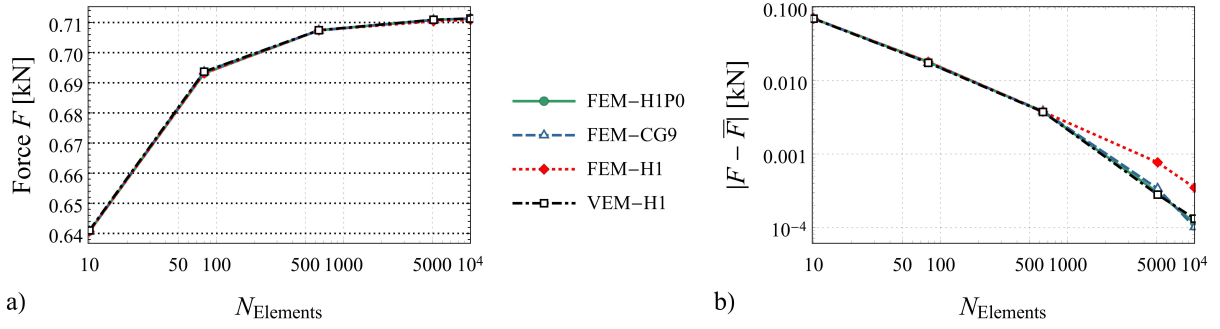


Figure 7.10: Three dimensional necking of a cylindrical bar for various mesh sizes ($N_{\text{Elements}} = 10N \times N \times N$): (a) Convergence of the VEM and FEM resulting peak force and (b) error estimate analysis at the peak force $|F - \bar{F}|$ at logarithmic scale.

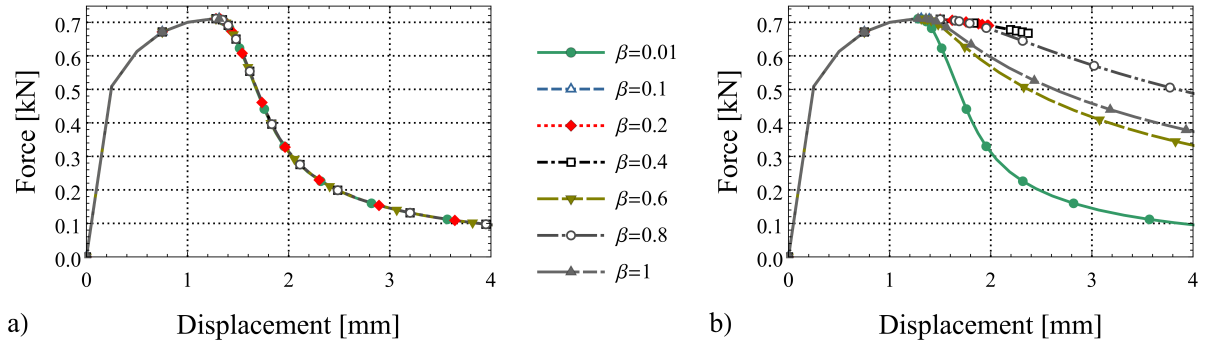


Figure 7.11: Three dimensional necking of a cylindrical bar with mesh size $N_{\text{Elements}} = 80 \times 8 \times 8$: Force-displacement curves for various values of β based on two different criteria: (a) As proposed in eq. (7.38) and (b) for constant choice of β .

with the same ratio towards a constant value of around 0.711 for VEM-H1, FEM-CG9 and FEM-H1P0 elements compared with FEM-H1. The error analysis of the peak force $|F - \bar{F}|$ versus the mesh size is depicted in Figure 7.10b, where \bar{F} is the mean value of the finer mesh. Thus we can conclude that VEM can reproduce the results of the enhanced and mixed FEM on the same mesh. However convergence in the softening regime cannot be achieved by standard FEM and VEM due to the mesh dependent nature of the problem. One possibility to overcome this non-physical behavior are gradient-enhanced plasticity models as regularization methods, which introduce a length scale, see for example [10, 4, 229].

Finally, Figure 7.11 depicts the influence of the stabilization parameter β on the load-deflection curves of the overall structural response. In Figure 7.11a, the proposed criteria for the mechanical stabilization parameter $\beta_M := \min\{\beta, \frac{\sigma_{VM}}{E\alpha}\}$ in eq. (7.38) is used, while in Figure 7.11b a constant β was chosen for the entire simulation $\beta_M := \beta$. Note that the thermal stabilization parameter, due to its small influence on the simulation, was set to $\beta_T = \beta$. Since the major heat generation is related to the mechanical part. The results show that the value of β has barely any influence on the result until the peak force is reached. In fact the error is in a range of 10^{-8} . However β has a pronounced influence in the softening response. In case of the constant stabilization parameter β , the elements

exhibit volumetric locking behavior for bigger β , due to the internal tetrahedral mesh, which prevents the triggering of softening behavior, as outlined in Figure 7.11b. However, by defining β in terms of the plastic stress and strain ratio (7.38), our choice of β has no influence on the softening part since the ratio will be active, i.e. $\beta > \sigma_{VM}/E\alpha$, see Figure 7.11a.

7.4.2. Forming of a steel bolt. The second model problem is concerned with forming process of a steel bolt under both thermal and mechanical loading conditions, as discussed in the reference works [32, 33].

Two dimensional case:. For the 2D case, the geometry and the coupled loading on the specimen are given in Figure 7.12(a). The size of the specimen is chosen to be: $H = 50 \text{ mm}$ and $L = 20 \text{ mm}$ under plane strain conditions. In the lower and upper parts of the specimen the vertical displacement is constrained, as depicted in Figure 7.12(a). The external heat source of $\bar{h} = 5 \text{ kN/mm s}$ is applied for 1.6 s at the top face. After that time the \bar{h} is set to zero and the specimen "rests" without any load for 1.6 s . Then a vertical displacement with magnitude of $\bar{u} = 0.125H$ is applied at the upper part of the specimen in 0.83 s .

The evolutions of the absolute temperature field T and the equivalent plastic strain α for different states of the forming process are shown in Figure 7.13. Herein, we first apply thermal loading as illustrated in Figure 7.14(b), resulting with thermo-elastic deformation and increase of the temperature, as depicted in Figure 7.13(f)–(g). The plasticity starts to initiate when the applied load reaches to a threshold, resulting in a cross shear localization, as plotted in Figure 7.13(d). Thereafter thermo-plastic deformation continue to evolve until the final forming of the bolt, see Figure 7.13(e),(j). The corresponding thermo-mechanical load versus time curves for different element formulations are demonstrated in Figure 7.14. All VEM type elements yield the same result as the FEM-Q1P0 and CG4 elements. Figure 7.15 shows a good agreement between all elements for this forming process of steel bolt.

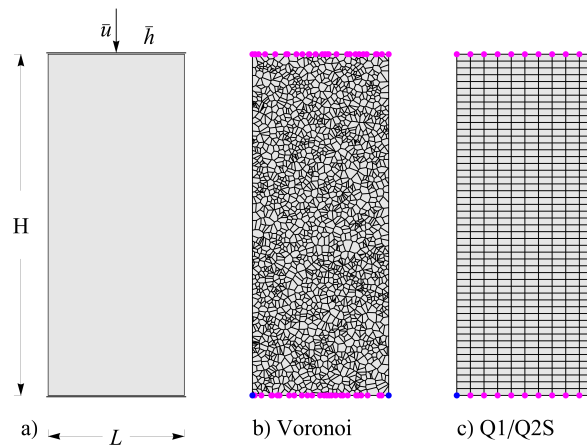


Figure 7.12: Forming of a steel bolt. (a) Geometry and boundary conditions, (b) VEM with Voronoi mesh and (c) regular Q1/Q2S finite element mesh.

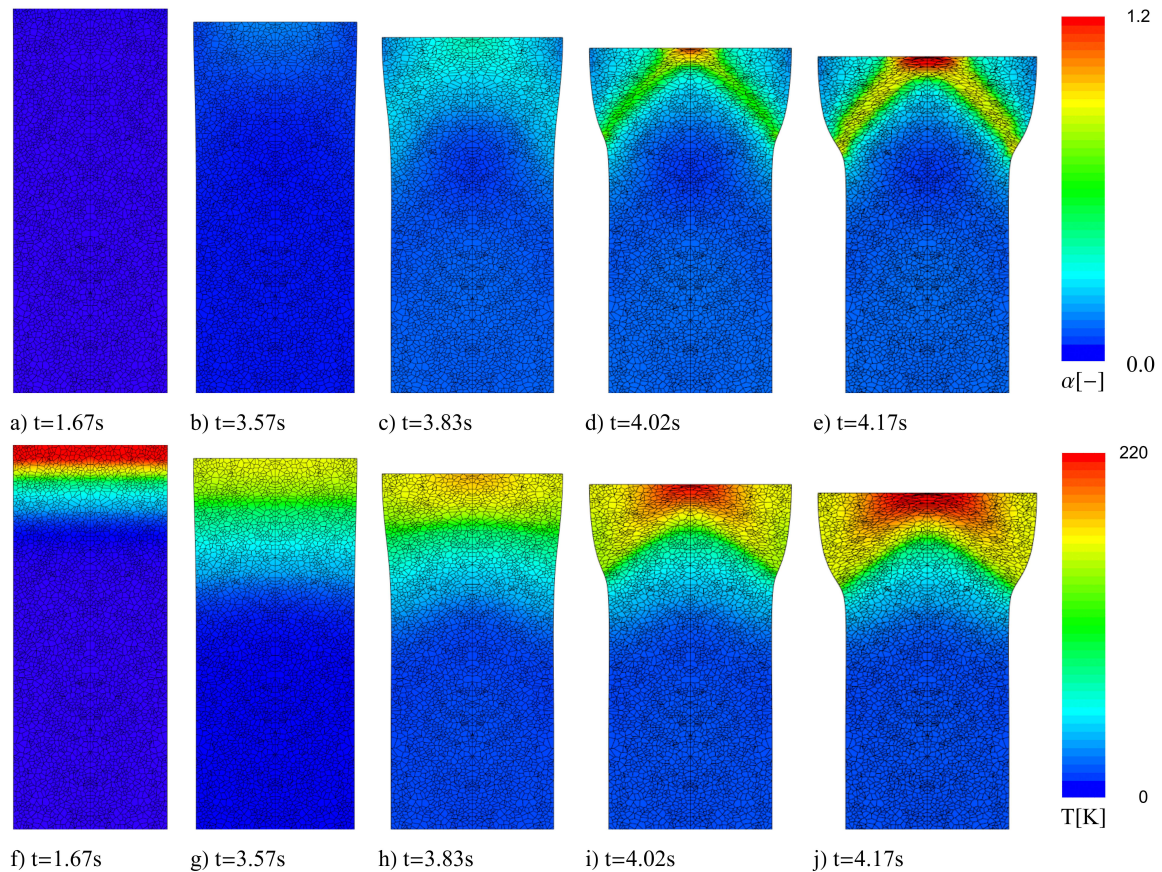


Figure 7.13: Forming of a steel bolt. Contour plots of the equivalent plastic strain in (a)–(e) and the absolute temperature field in (f)–(j) at different deformation states using VEM-Voronoi.

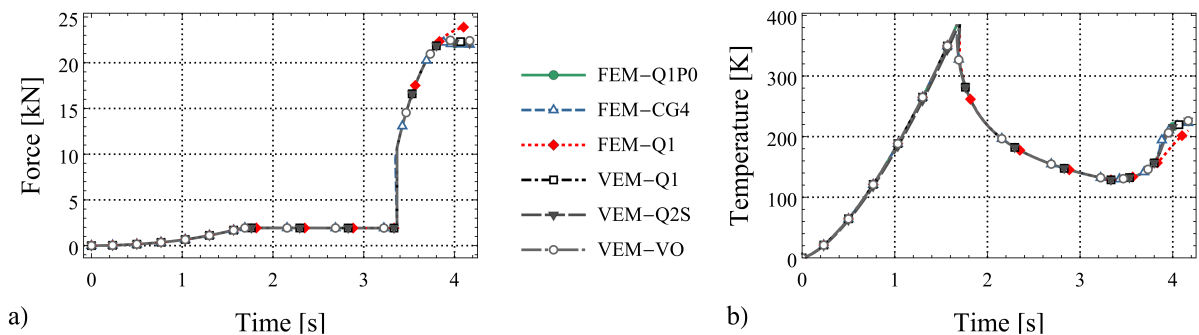


Figure 7.14: Forming of a steel bolt. (a) Force-time and (b) temperature-time curves for different types of elements.

Three dimensional case:. In this case, a 3D extension of the two dimensional steel bolt using VEM-VO is investigated as illustrated in Figure 7.16. The cylindrical bar diameter is chosen to be $D = L$ and the height is set to H . Hereby the shear band is not that pronounced, since in this case an *axisymmetrical* response is obtained compared with the *2D plane strain problem* of Figure 7.13. Therefore the displacement load was increased to $\bar{u} = 0.25H$ until the final forming process. The load-displacement curves and

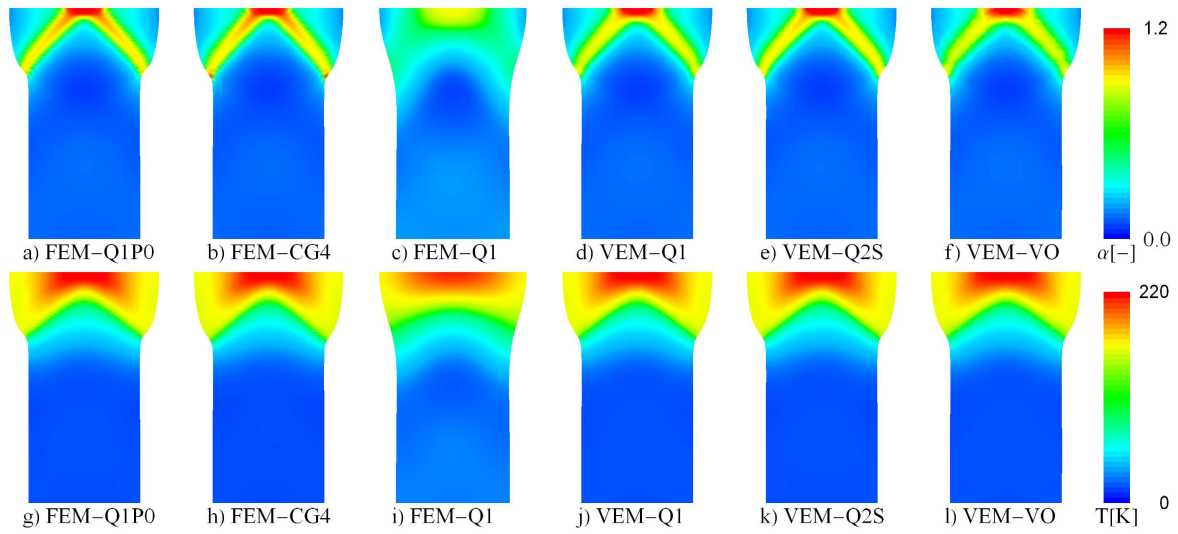


Figure 7.15: Forming of a steel bolt. Distribution of the equivalent plastic strain α and the absolute temperature field T at the final deformation state for all elements.

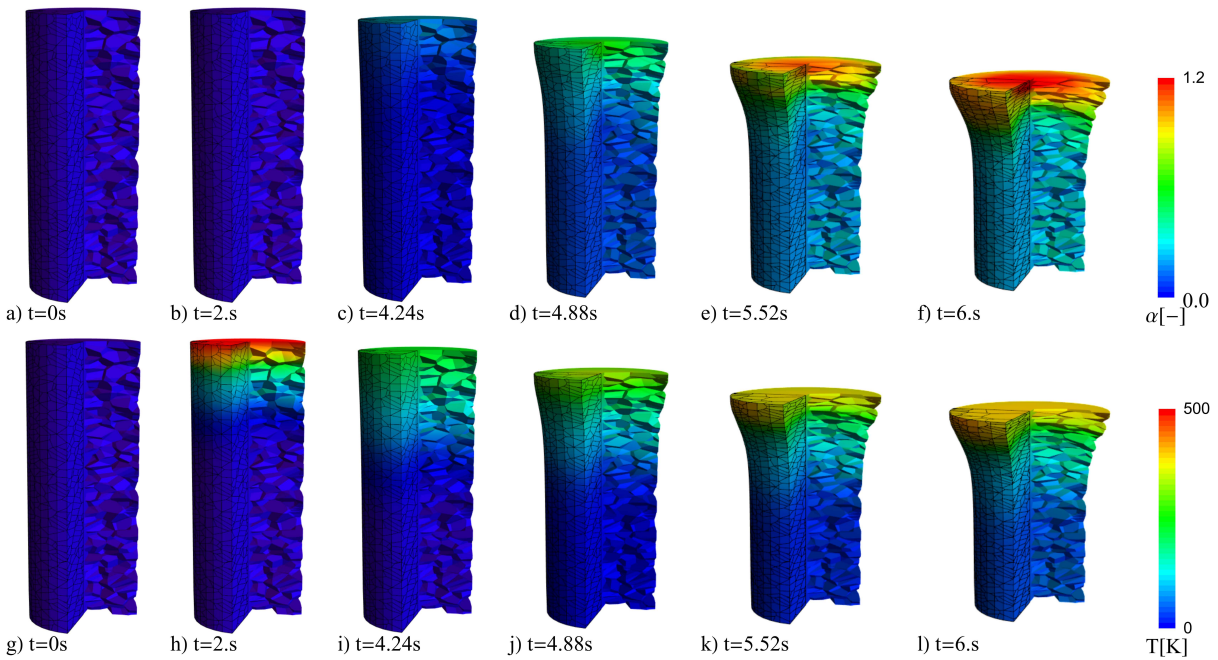


Figure 7.16: 3D Forming of a steel bolt. Distribution of the equivalent plastic strain α in (a)–(f) and the absolute temperature field T in (g)–(l) at different deformation states using VEM-VO.

the corresponding temperature evolution are qualitatively similar to the two dimensional case and thus not shown here.

8. Micromorphic approach for 3D gradient thermo-plastic solids

In the previous investigation of inelastic deformations (Chapter 6 and Chapter 7) the *local* theory of plasticity was considered in the constitutive modeling. However, a significant numerical limitation of that using the virtual/finite element techniques is the pathological mesh dependency which leads to loss of ellipticity of the governing equations. To overcome this non-physical behavior in a coupled thermo-mechanical response, an extended-gradient theory that accounts for micro-structure based size effects is outlined within this chapter. From the computational viewpoint, the finite element design of the coupled problem is not straightforward and requires additional strategies due to the difficulties near the elastic-plastic boundaries (EPBs). To simplify the finite element formulation, we extend it towards the *micromorphic approach* to gradient thermo-plasticity model in the logarithmic strain space. The key point is the introduction of dual local-global field variables via a penalty method, where only the global fields are restricted by boundary conditions. Hence, the problem of restricting the gradient variable to the plastic domain is relaxed, which makes the formulation very attractive for finite element implementation. The contents of this chapter is based on the following publication ALDAKHEEL [11].

8.1. Introduction

The modeling of size effects in elastic-plastic solids must be based on non-standard theories which incorporate length-scales. Hereby, additional internal variables and their nonlocal counterparts can be introduced to reflect the micro-structural response. Various observations underline the need for such extended continuum theories of inelasticity. A first physically-based motivation is the experimentally observed *increase in strength* of metallic structures with diminishing size, resulting from dislocation related hardening effects, see for example FLECK ET AL. [128]. A further key motivation for the use of strain gradient theory arises from the computation of localized plastic deformation in softening materials with *finite element techniques*, yielding for local theories the pathological mesh dependencies for zero length scale. To overcome this non-physical behavior, gradient-enhanced plasticity models are used as *regularization methods*, which provide the existence of a length scale, see for example DE BORST & MÜHLHAUS [100], LIEBE & STEINMANN [204] and ENGELEN ET AL. [116]. The gradient-enhanced models are naturally rooted in the micro-mechanical descriptions of the dislocation flow in crystals, where the *plastic length scale* is related to the lattice spacing. Associated models of gradient crystal plasticity are proposed by many authors, e.g. GURTIN [150], SVENDSEN & BARGMANN [296], WULFINGHOFF & BÖHLKE [335], KLUSEMANN & YALCINKAYA [182] and MIEHE ET AL. [228]. In contrast, pure phenomenologically-based theories of gradient plasticity often use plastic length scales as limiters of localized zones determined by macroscopic experiments, see for example FOREST & SIEVERT [132], GUDMUNDSON [148], ANAND ET AL. [29], REDDY ET AL. [274], FLECK & WILLIS [126, 127], POLIZOTTO [271], FOREST [129, 130], VOYIADJIS ET AL. [308], KURODA & TVERGAARD [192] and MIEHE ET AL. [227, 229].

Despite the fact that temperature distribution during heat accumulation has a strong influence on the mechanical properties, thermal effects were not included in the constitutive formulation of most of the recently developed strain gradient theories. Thermo-mechanical problems can be seen in different engineering applications [87], which exhibit

a two-side coupling phenomenon. First, the effects of the thermal field on the mechanical field resulting in thermal expansion and temperature dependence of the mechanical properties, for instance the bridge joint expansion/contraction and the buckled railway-tracks as a result of changes in the ambient temperature. On the contrary, the action of the mechanical field on the thermal field which lead to high temperature distribution and heat dissipation, such as the frictional heating of disc brakes in automotive industry. To this end, WRIGGERS ET AL. [327] investigate the thermo-mechanical behavior of the necking problem in classical elasto-plasticity. Here the authors observed that, the development of a neck in a uniaxial tension test is influenced by the heat production due to inelastic deformation. ANAND ET AL. [30] proposed a coupled thermo-mechanical elasto-viscoplasticity theory to model strain rate and temperature dependent large-deformation response of amorphous polymeric materials. A variational formulation for the thermo-mechanical coupling in finite strain plasticity theory with non-linear kinematic hardening is outlined in CANADIJA & MOSLER [76] based on the works YANG ET AL. [337] and STAINIER & ORTIZ [293]. However no size effects were involved in the constitutive formulation. This has motivated VOYIADJIS & FAGHIHI [309] and FAGHIHI ET AL. [117] to propose a nonlocal thermodynamic consistent framework with energetic and dissipative gradient length scales that addressing the coupled thermal and mechanical responses of materials in small scales and fast transient process. In this context, FOREST & AIFANTIS [131] introduced some links between recent gradient thermo-elasto-plasticity theories and the thermo-mechanics of generalized continua based on the micromorphic approach. Extensions to an anisotropic model for gradient thermo-plasticity can be seen in the work of BERTRAM & FOREST [56]. Recently WCISLO & PAMIN [311] developed a gradient-enhanced thermomechanical model that is strictly related to the phenomenon of thermal softening. It incorporates higher order gradients of the temperature field. In this work, we extend the above mentioned gradient plasticity model introduced in MIEHE ET AL. [229] to account for thermal effects at finite deformations in the logarithmic strain space. The key goal of this work is the extension towards the *micromorphic regularization* of the coupled problem to simplify the mixed finite element formulation as outlined in the recent works MIEHE ET AL. [238, 233]. This is achieved by considering an extended set of plastic variables which are linked by penalty term in a modified energetic response function as discussed in FOREST [129, 130] and MIEHE ET AL. [238]. The advantage of such a formulation lies on the computational side, in particular on the side of gradient plasticity. It allows a straightforward finite element formulation of gradient plasticity that does not need to account of sharp plastic boundaries. From the numerical implementation aspects, an operator split scheme is considered for the coupled problem, in line with our recent works ALDAKHEEL [10] and ALDAKHEEL & MIEHE [13] at small strains. It leads to a two step solution procedure $ALGO_{TM} = ALGO_{Thermo} \circ ALGO_{Mech}$, where the mechanical and thermal problems are solved separately. The idea here is to decompose the coupled field equations of finite gradient thermo-plasticity into an elasto-plastic problem $ALGO_{Mech}$ with frozen temperature, followed by a heat conduction problem $ALGO_{Thermo}$ at fixed updated mechanical configuration. These two sub-problems are then coupled via the plastic structural heating and the mechanical dissipation. Due to the two steps solution procedure, we end up with a *symmetric structure* for each sub-problem, for further details on the numerical analysis, we refer to our recent work ALDAKHEEL & MIEHE [13] at small strains.

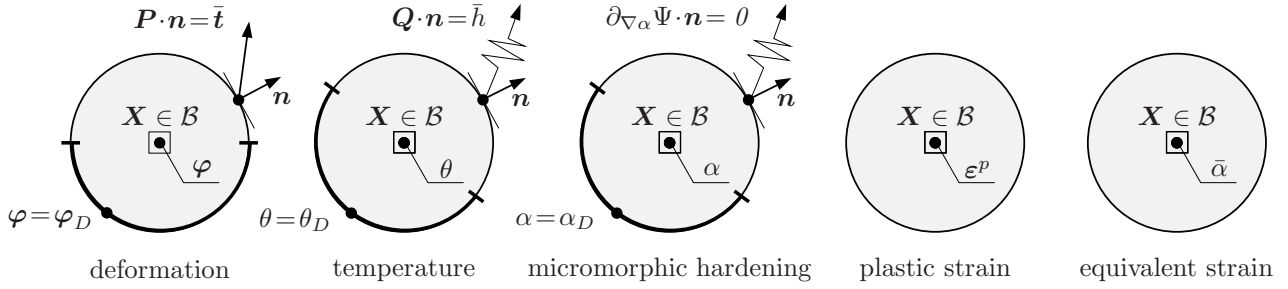


Figure 8.1: Primary fields. a) The macro-motion field φ is constrained by the Dirichlet- and Neumann-type BCs $\varphi = \varphi_D$ on $\partial\mathcal{B}^\varphi$ and $\mathbf{P} \cdot \mathbf{n} = \bar{\mathbf{t}}$ on $\partial\mathcal{B}^t$. b) The absolute temperature field θ is constrained by the Dirichlet- and Neumann-type BCs $\theta = \theta_D$ on $\partial\mathcal{B}^\theta$ and $\mathbf{Q} \cdot \mathbf{n} = \bar{h}$ on $\partial\mathcal{B}^h$. c) The long-range micro-motion field α is restricted by the conditions $\alpha = \alpha_D$ on $\partial\mathcal{B}^\alpha$ and $\partial_{\nabla\alpha}\Psi \cdot \mathbf{n} = 0$ on $\partial\mathcal{B}^f$. d)-e) The short-range micro-motion fields ε^p and $\bar{\alpha}$ are locally defined and not constrained by boundary conditions.

8.2. Introduction of Primary Field Variables

8.2.1. Deformation map and temperature field. Let $\mathcal{B} \in \mathcal{R}^d$ with $d = 2, 3$ be the reference configuration of the body of interest. We study thermo-elasto-plastic deformations at time $t \in \mathcal{R}_+$, described by the *deformation map* $\varphi(\mathbf{X}, t)$ and the *temperature field* $\theta(\mathbf{x}, t) > 0$

$$\varphi : \begin{cases} \mathcal{B} \times \mathcal{T} \rightarrow \mathcal{R}^3 \\ (\mathbf{X}, t) \mapsto \mathbf{x} = \varphi(\mathbf{X}, t) \end{cases} \quad \theta : \begin{cases} \mathcal{B} \times \mathcal{T} \rightarrow \mathcal{R} \\ (\mathbf{X}, t) \mapsto \theta(\mathbf{X}, t) \end{cases} \quad (8.1)$$

as depicted in Figure 8.1. The material deformation gradient is defined by $\mathbf{F} := \nabla\varphi_t(\mathbf{X})$ with $J := \det[\mathbf{F}] > 0$. The solid is loaded by prescribed deformations and external traction on the boundary, defined by time-dependent ("active") Dirichlet- and Neumann conditions

$$\varphi = \bar{\varphi}(\mathbf{X}, t) \text{ on } \partial\mathcal{B}^\varphi \quad \text{and} \quad \mathbf{P}\mathbf{n} = \bar{\mathbf{t}}(\mathbf{X}, t) \text{ on } \partial\mathcal{B}^t \quad (8.2)$$

on the surface $\partial\mathcal{B} = \partial\mathcal{B}^\varphi \cup \partial\mathcal{B}^t$ of the undeformed configuration. The first Piola stress tensor \mathbf{P} is the thermodynamic dual to \mathbf{F} . For the thermal problem, the time-dependent ("active") Dirichlet- and Neumann conditions of the absolute temperature field θ are defined as

$$\theta = \theta_D \text{ on } \partial\mathcal{B}^\theta \quad \text{and} \quad \mathbf{Q} \cdot \mathbf{n} = \bar{h} \text{ on } \partial\mathcal{B}^h \quad (8.3)$$

with a *prescribed* temperature field θ_D and heat flux \bar{h} . Note that the nominal heat flux vector $\mathbf{Q} = J\mathbf{F}^{-1}\mathbf{q}$ is given by Fourier's law which states that heat exchanges always from hotter to colder regions, i.e.

$$\mathbf{q} := -K\nabla\theta \quad (8.4)$$

where $\nabla\theta$ is the gradient of the temperature field and K is the thermal conductivity which must be positive ($K > 0$) in order to achieve thermodynamical consistency. Following MIEHE ET AL. [223], we focus on a phenomenological setting of finite thermo-plasticity based on an additive decomposition of a *Lagrangian Hencky strain* ε . This allows to defines a stress producing elastic strain measure

$$\varepsilon^e := \varepsilon - \varepsilon^p - \varepsilon^\theta \quad \text{with} \quad \varepsilon := \frac{1}{2} \ln \mathbf{C} \quad \text{and} \quad \mathbf{C} := \mathbf{F}^T \mathbf{g} \mathbf{F}, \quad (8.5)$$

where \mathbf{C} is the right Cauchy-Green tensor, i.e. the representation of the Eulerian standard metric \mathbf{g} in the reference configuration. The *Lagrangian plastic strain measure* $\boldsymbol{\varepsilon}^p$ is chosen as a local internal variable. It starts to evolve from the initial condition $\boldsymbol{\varepsilon}^p(\mathbf{X}, t_0) = \mathbf{0}$. The thermal contribution to the total deformation is defined as

$$\boldsymbol{\varepsilon}^\theta = \alpha_T(\theta - \theta_0)\mathbf{1} \quad (8.6)$$

representing an expansion of the body under thermal loading. Here, α_T is the linear thermal expansion modulus and θ_0 a reference temperature.

8.2.2. Isotropic strain-gradient plasticity. We consider a framework of isotropic gradient plasticity in the micromorphic regularization setting. To this end, a scalar *isotropic hardening variable* $\alpha(\mathbf{X}, t)$ is introduced, that defines the micromorphic hardening variable by the modified Helmholtz equation

$$\alpha - l_{mp}^2 \Delta \alpha = \bar{\alpha} \quad (8.7)$$

determining the link of the local equivalent plastic strain variable $\bar{\alpha}$ to the micromorphic variable α , in line with the pioneering works of ENGELEN ET AL. [116], GEERS ET AL. [139], PEERLINGS ET AL. [265, 266] and FOREST [129]. l_{mp} is the *plastic length scale* in the micromorphic setting, that accounts for size effects to overcome the non-physical mesh sensitivity of the localized plastic deformation in softening materials. The generalized internal variable field α is considered as passive in the sense that an external driving is not allowed. This is consistent with the time-independent (*passive*) Dirichlet- and Neumann conditions

$$\alpha = 0 \text{ on } \partial\mathcal{B}^\alpha \quad \text{and} \quad \nabla\alpha \cdot \mathbf{n} = \mathbf{0} \text{ on } \partial\mathcal{B}^{\nabla\alpha} \quad (8.8)$$

on the surface $\partial\mathcal{B}$ as illustrated in Figure 8.1, defining "micro-clamped" and "free" constraints for the evolution of the plastic deformation. Note carefully, that the variable α is now defined in the full domain, and not restricted to the plastic zone. Whereas the linear hardening variable $\bar{\alpha}$ is *locally* defined by the ordinary differential evolution equation

$$\dot{\bar{\alpha}} = \sqrt{\frac{2}{3}} \|\dot{\boldsymbol{\varepsilon}}^p\| \quad \text{with} \quad \dot{\bar{\alpha}} \geq 0. \quad (8.9)$$

8.2.3. Global primary fields and constitutive state variables. The above introduced variables will characterize a multi-field setting of thermo-mechanical strain gradient plasticity based on three *global primary fields*

$$\boldsymbol{\mathfrak{U}} := \{\boldsymbol{\varphi}, \theta, \alpha\}, \quad (8.10)$$

the deformation map $\boldsymbol{\varphi}$, the absolute temperature field θ and the micromorphic hardening variable α . In addition, the plastic strain field $\boldsymbol{\varepsilon}^p$ and the local equivalent plastic strain $\bar{\alpha}$ serve as additional *local primary fields*, as demonstrated in Figure 8.1. The subsequent constitutive approach to the coupled gradient thermo-plasticity focuses on the set

$$\boldsymbol{\mathfrak{C}} := \{\boldsymbol{\varepsilon}, \boldsymbol{\varepsilon}^p, \bar{\alpha}, \theta, \alpha, \nabla\theta, \nabla\alpha\}. \quad (8.11)$$

The gradient of the plastic strains do not enter the constitutive state. Thus, $\boldsymbol{\varepsilon}^p$ and $\bar{\alpha}$ are *short-range* variables, whose evolution are described by an ODE, while the micromorphic hardening variable α is a *long-range* field with a PDE-type evolution.

8.3. Constitutive Functions of the Coupled Problem

8.3.1. Energetic response function. With the constitutive state variables introduced in (8.11), the free energy function for the coupled thermo-mechanical strain gradient plasticity at finite strains takes the form

$$\widehat{\Psi}(\mathbf{C}) = U(J) + \bar{\Psi}_{\log}^e(\bar{\boldsymbol{\varepsilon}}^e) + \bar{\Psi}^p(\bar{\alpha}, \alpha, \nabla\alpha; \theta) + M(J, \theta) + T(\theta). \quad (8.12)$$

Elastic contribution. The isotropic elastic contribution is assumed to be a quadratic function and is decomposed into volumetric and isochoric parts as

$$U(J) = \frac{\kappa}{2}(J-1)^2 \quad \text{and} \quad \bar{\Psi}_{\log}^e(\bar{\boldsymbol{\varepsilon}}^e) = \mu \|\bar{\boldsymbol{\varepsilon}}^e\|^2, \quad (8.13)$$

in terms of the elastic bulk modulus κ and the shear modulus μ . In this model, both κ and μ are considered as constants material parameters. The isochoric elastic strain tensor is defined in the logarithmic strain space as

$$\bar{\boldsymbol{\varepsilon}}^e := \bar{\boldsymbol{\varepsilon}} - \boldsymbol{\varepsilon}^p \quad \text{with} \quad \bar{\boldsymbol{\varepsilon}} := \frac{1}{2} \ln \bar{\mathbf{C}} \quad \text{and} \quad \bar{\mathbf{C}} := J^{-2/3} \mathbf{C} \quad (8.14)$$

Plastic contribution. The plastic part of the energy function (8.12) is decomposed into local and gradient parts, in terms of variables which describe the strain gradient hardening effect. For the modeling of length scale effects in isotropic gradient plasticity, we focus on the micromorphic hardening variable α and its gradient $\nabla\alpha$ in addition to the local equivalent plastic strain $\bar{\alpha}$. It is assumed to have the form

$$\bar{\Psi}^p = \frac{h(\theta)}{2} \bar{\alpha}^2 + [y_\infty(\theta) - y_0(\theta)](\bar{\alpha} + \exp[-\delta\bar{\alpha}]/\delta) + \frac{\mu l_p^2}{2} \|\nabla\alpha\|^2 + \frac{\epsilon_p}{2} (\bar{\alpha} - \alpha)^2. \quad (8.15)$$

The first and second contributions characterize a local plastic hardening and thermal softening mechanism. $l_p \geq 0$ is a plastic length scale related to a strain-gradient hardening effect. The local variable $\bar{\alpha}$ is then linked to the global micromorphic field variable α by the quadratic penalty term, where ϵ_p is an additional material parameter. Note that for $\epsilon_p \rightarrow \infty$ the above micromorphic extensions recover the original setting of the gradient-extended theory introduced in MIEHE ET AL. [229]. The three temperature dependent material parameters $y_0 > 0$, $y_\infty \geq y_0$ and $h \geq 0$ in (8.15) defined as

$$\begin{aligned} h(\theta) &:= h[1 - w_h(\theta - \theta_0)] \\ y_0(\theta) &:= y_0[1 - w_0(\theta - \theta_0)] \\ y_\infty(\theta) &:= y_\infty[1 - w_h(\theta - \theta_0)] \end{aligned} \quad (8.16)$$

as outlined in SIMO & MIEHE [288], where w_h is the hardening/softening parameter, w_0 is the flow stress softening parameter and δ is the saturation parameter. The initial yield stress y_0 determines the threshold of the elastic response. Note that the parameters: δ , μ , l_p and ϵ_p are considered as constants in equation (8.15).³

³The shear modulus μ could be also dependent on the temperature as suggested in BOYCE ET AL. [70] through the empirical relation

$$\widehat{\mu}(\theta) = \exp[\log(\mu_0) - C_s(\theta - \theta_0)] \quad (8.17)$$

in terms of the modulus μ_0 at the reference temperature θ_0 and a sensitivity parameter C_s .

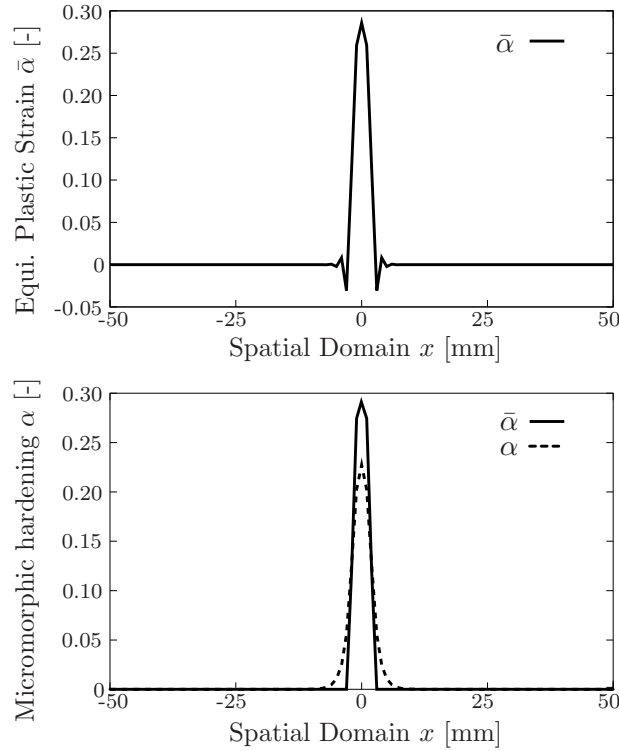


Figure 8.2: Canonical versus micromorphic formulation of gradient plasticity. Standard one-dimensional finite element solutions of gradient plasticity for a) canonical setting results in nonphysical oscillations at the elastic-plastic boundary, which are relaxed in b) by the micromorphic approach according to equation (8.24).

Thermoelastic contribution. The coupled thermoelastic part of the free energy is linear and has the simple form

$$M(J, \theta) = -\kappa \alpha_T (J - 1)(\theta - \theta_0) , \quad (8.18)$$

where α_t is the thermal expansion coefficient and θ_0 is the reference temperature.

Thermal contribution. The purely thermal part is defined as

$$T(\theta) = c \left[(\theta - \theta_0) - \theta \ln \frac{\theta}{\theta_0} \right] , \quad (8.19)$$

where c is the heat capacity coefficient.

8.3.2. Dissipative response function. For the subsequent modeling of thermo-plasticity, we introduce dissipative force fields on the solid domain \mathcal{B} dual to the constitutive state \mathfrak{C} introduced in (8.11) as

$$\bar{\mathfrak{s}} := -\partial_{\varepsilon^p} \widehat{\Psi} , \quad f^\alpha := \partial_{\bar{\alpha}} \widehat{\Psi} , \quad \delta_{\bar{\alpha}} \widehat{\Psi} = 0 . \quad (8.20)$$

where $\bar{\mathfrak{s}}$ is dual to ε^p and f^α dual to $\bar{\alpha}$. For a simple model of von Mises-type gradient thermo-plasticity, the yield criterion function based on the driving forces and the temperature field θ is defined as

$$\chi(f^\alpha, \bar{\mathfrak{s}}, \theta) := \|\bar{\mathfrak{s}}\| - \sqrt{\frac{2}{3}} [y_0(\theta) + f^\alpha] \quad (8.21)$$

where $y_0(\theta)$ is the temperature dependent yield strength defined in (8.16). With the yield function at hand, one can define the dual dissipation function for gradient-type thermal viscoplasticity according to Perzyna-type viscoplasticity model as

$$\Phi^*(f^\alpha, \bar{\mathbf{s}}, \theta) := \frac{1}{2\eta_p} \left\langle \|\bar{\mathbf{s}}\| - \sqrt{\frac{2}{3}} [y_0(\theta) + f^\alpha] \right\rangle^2 \quad (8.22)$$

with η_p being the viscosity parameter that accounts for rate dependency. Here, $\langle x \rangle := (x + |x|)/2$ is the Macaulay bracket. In equation (8.20), $\delta_\alpha \widehat{\Psi}$ denotes the variational derivative of $\widehat{\Psi}$ with respect to the global micromorphic variable α , defining the additional micromorphic balance equation that links the local variable $\bar{\alpha}$ to the global field α

$$\delta_\alpha \widehat{\Psi} = \partial_\alpha \widehat{\Psi} - \text{Div} [\partial_{\nabla\alpha} \widehat{\Psi}] = 0, \quad (8.23)$$

along with the Neumann-type boundary conditions defined in equation (8.8). Taking the necessary derivatives, we end up with the modified Helmholtz equation determining the link of the local variable $\bar{\alpha}$ to the micromorphic variable α

$$\alpha - l_{mp}^2 \Delta \alpha = \bar{\alpha} \quad \text{with} \quad l_{mp} := l_p \sqrt{\mu/\epsilon_p} \quad (8.24)$$

where l_{mp} is the plastic length scale of the micromorphic theory⁴. Note carefully, that the variable α is now defined in the full domain, and not restricted to the plastic zone. Whereas the linear hardening variable $\bar{\alpha}$ is *locally* defined by the ordinary differential evolution equation introduced in (8.9). This provides a substantial simplification with regard to the finite element implementation without tracking of elastic-plastic boundaries. To this end, we depict in Figure 8.2a a one-dimensional finite element solutions of gradient plasticity for canonical setting in which the global equivalent plastic strains evolution is $\dot{\bar{\alpha}} = \partial_{f^\alpha} \Phi^*$, see MIEHE ET AL. [229], which is restricted to the plastic domain resulting in nonphysical oscillations at the elastic-plastic boundary, these are relaxed in Figure 8.2b by the micromorphic approach according to equations (8.23) and (8.24).

8.3.3. Local-global constitutive equations. The balance and evolution equations describing the coupled problem are split up into **Local** and **Global** constitutive equations in the micromorphic regularization setting as

$$\left. \begin{array}{ll} 1. \text{ Stress equilibrium} & \text{Div} [\partial_{\mathbf{F}} \widehat{\Psi}] = \mathbf{0} \\ 2. \text{ Micromorphic hardening} & \partial_\alpha \widehat{\Psi} - \text{Div} [\partial_{\nabla\alpha} \widehat{\Psi}] = 0 \\ 3. \text{ Temperature field} & c \dot{\theta} + \text{Div} [\mathbf{Q}] - \mathcal{D}_{loc}^{red} = 0 \\ 4. \text{ Hardening force} & \partial_{\bar{\alpha}} \widehat{\Psi} - f^\alpha = 0 \\ 5. \text{ Plastic force} & \partial_{\epsilon^p} \widehat{\Psi} + \bar{\mathbf{s}} = \mathbf{0} \\ 6. \text{ Equivalent strain} & -\dot{\bar{\alpha}} + \partial_{f^\alpha} \Phi^* = 0 \\ 7. \text{ Plastic strains} & \dot{\epsilon}^p - \partial_{\bar{\mathbf{s}}} \Phi^* = \mathbf{0} \end{array} \right\} \begin{array}{l} \text{(G)} \\ \text{(L)} \end{array} \quad (8.26)$$

⁴If the shear modulus $\mu = \widehat{\mu}(\theta)$ is assumed to be temperature dependent, additional term must be defined in equation (8.24) to account for thermal effects

$$\alpha - \frac{l_p^2}{\epsilon_p} \widehat{\mu}(\theta) \Delta \alpha - \frac{l_p^2}{\epsilon_p} \partial_\theta \widehat{\mu}(\theta) \nabla \theta \cdot \nabla \alpha = \bar{\alpha} \quad \text{with} \quad \partial_\theta \widehat{\mu}(\theta) = -C_s \widehat{\mu}(\theta) \quad (8.25)$$

as outlined in the work of FOREST [129].

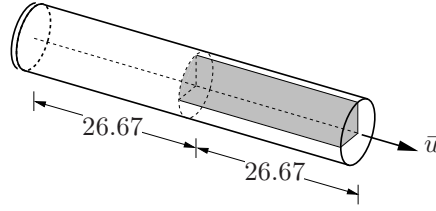


Figure 8.3: Necking of cylindrical bar. Geometry and boundary conditions. Due to the symmetry of the boundary value problem only the shaded area is discretized.

in terms of the reduced local dissipation density function defined as

$$\mathcal{D}_{loc}^{red} = \partial_{\hat{\boldsymbol{\varepsilon}}} \hat{\Psi} : \dot{\boldsymbol{\varepsilon}}^p - \partial_{\hat{\alpha}} \hat{\Psi} \dot{\alpha} - \partial_{\alpha} \hat{\Psi} \dot{\alpha} - \partial_{\nabla \alpha} \hat{\Psi} \cdot \nabla \dot{\alpha} \quad (8.27)$$

along with the Neumann-type boundary conditions

$$\partial_{\mathbf{F}} \hat{\Psi} \cdot \mathbf{n} = \bar{\mathbf{t}} \text{ on } \partial \mathcal{B}^t, \quad \partial_{\nabla \alpha} \hat{\Psi} \cdot \mathbf{n} = \mathbf{0} \text{ on } \partial \mathcal{B}^f \quad \text{and} \quad \mathbf{Q} \cdot \mathbf{n} = 0 \text{ on } \partial \mathcal{B}^h \quad (8.28)$$

associated with the macro-motion field $\boldsymbol{\varphi}$, the micromorphic hardening variable α and the absolute temperature field θ . Here, \mathbf{P} is denoted as the energetic first Piola nominal stress defined as

$$\mathbf{P} := \partial_{\mathbf{F}} \hat{\Psi} = \partial_{\boldsymbol{\varepsilon}} \hat{\Psi} : \mathbb{P}_{log} \quad \text{with} \quad \mathbb{P}_{log} := \partial_{\mathbf{F}} \boldsymbol{\varepsilon} \quad (8.29)$$

in terms of the fourth-order nominal transformation tensor \mathbb{P}_{log} outlined in the work of MIEHE & LAMBRECHT [222]. To solve for the above system of equations (8.26), we applied staggered solution scheme in line with our recent work ALDAKHEEL & MIEHE [13].

8.4. Representative Numerical Example

The capability of the model is pointed out by investigating the necking of cylindrical bar subjected to tensile loading. The geometric setup and the boundary conditions of the

Table 8.1: Material parameters used for the numerical examples.

No.	Parameter	Name	Value	Unit
1.	κ	bulk modulus	164.2	GPa
2.	μ	shear modulus	80.2	GPa
3.	h	hardening parameter	± 0.13	GPa
4.	ϵ_p	penalty parameter	4.0	GPa
5.	y_0	yield stress	0.45	GPa
6.	η_p	viscosity	10^{-7}	GPa.s
7.	α_t	expansion coefficient	10^{-5}	K ⁻¹
8.	K	thermal conductivity	0.045	KN/sK
9.	c	heat capacity	$3.588 \cdot 10^{-3}$	GPa/K
10.	w_h	thermal softening	0.002	K ⁻¹
11.	w_0	flow stress softening	0.002	K ⁻¹
12.	y_∞	infinite yield stress	1.165	GPa
13.	δ	saturation parameter	16.96	–

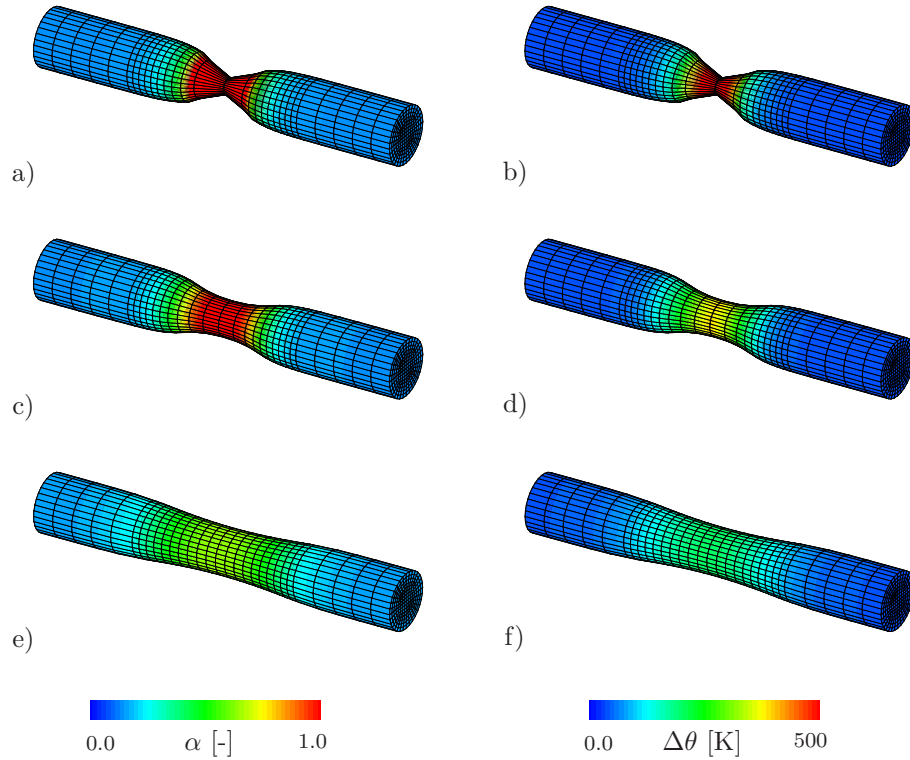


Figure 8.4: Necking of cylindrical bar. Distribution of the micromorphic hardening variable α and the incremental temperature field θ at the final deformation $\bar{u} = 10.0$ mm in combination with several plastic length scales parameter. a)–b) Local analysis ($l_p = 0.0$ mm), c)–d) $l_p = 0.2$ mm, and e)–f) $l_p = 0.5$ mm.

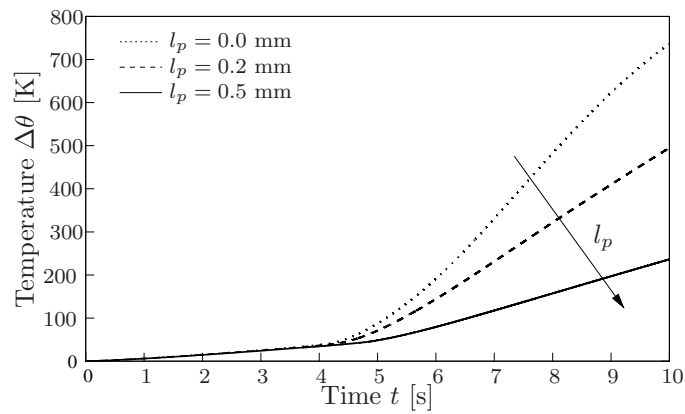


Figure 8.5: Necking of cylindrical bar. Temperature-time curves at the center of the specimen for three different plastic length scales l_p .

cylindrical bar with radius 6.4135 mm are illustrated in Figure 8.3. To trigger localization in the center of the specimen, the yield limit y_0 in the center is reduced by 10%. The material parameters used in this example are given in Table 8.1 for metals. Regarding to the selection of the material parameters we refer to the works of HALLQUIST [155], SIMO [287] and SIMO & MIEHE [288]. Figure 8.4 depicts the distribution of the micromorphic hardening variable α and the incremental temperature field θ at the final deformation $\bar{u} = 10.0$ mm for several plastic length scales parameter l_p . For local plasticity, a sharp necked zone with concentrated micromorphic hardening variable α and temperature field

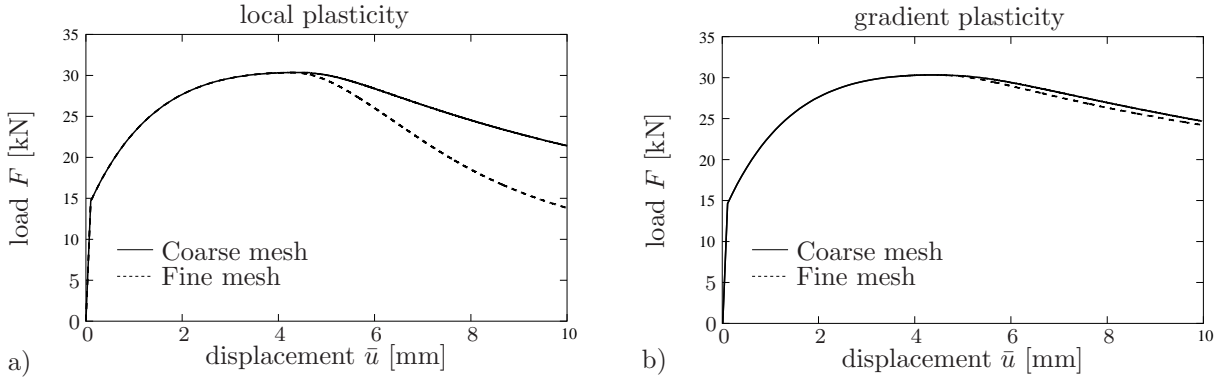


Figure 8.6: Necking of cylindrical bar. Load-displacement curves for two different mesh sizes: a) For local plasticity $l_p = 0$ mm and b) gradient plasticity with $l_p = 0.2$ mm.

θ is illustrated in Figure 8.4a for α and Figure 8.4b for θ . By increasing l_p the necking zone smears out and the hardening variable α as well as the temperature field θ will spread over several elements. Figure 8.5 demonstrates the influence of the plastic length scale on the temperature evolution over time at the center of the specimen. As documented in Figure 8.4, for local plasticity the temperature field θ has the highest value and by increasing the plastic length scale l_p the maximum value will be decreased. As the length scale parameter $l_p \propto 1/L$ with L being the macroscopic characteristic size, increasing the plastic length scale is equivalent to a decrease in specimen size and, thus, temperature dissipates faster from a small size medium as illustrated in the work of FAGHIHI ET AL. [117], VOYIADJIS & FAGHIHI [309]. The load-displacement curves of the overall structural response are illustrated in Figure 8.6. For local theory of plasticity, mesh sensitive results are observed in Figure 8.6a. In contrast, Figure 8.6b shows results for gradient plasticity with $l_p = 0.2$ mm and two different mesh sizes, where mesh objectivity is obtained. Thus, the incorporation of the length scale parameter l_p enables us not only to *predict a size-independent structural response*, but also to *control the shape of the necking zone*.

9. Conclusion and outlook

9.1. Global-Local approach for multi-physics problems at fracture

In **Part I** of this work, a robust and efficient Global-Local (GL) approach for treating phase-field fracture problems was developed. Such a multi-scale schemes are advantageous when large-scale problems are considered in which the fracture state only develops in smaller, localized, regions. The first aim was to extend the phase-field model to multi-physics problems at fracture. Next, an adaptive scheme was utilized in which the local domains were advanced dynamically during a computation. This approach was realized in terms of a predictor-corrector scheme. Hereby the new local domains are predicted and then the solution is again computed considering the new local regions. In this regard, the interface conditions represent an important challenge for the coupling of the two-nested models denoted by the local and global domains in a variational consistent way. For that purpose Robin-type boundary conditions were formulated to efficiently relax the stiff Local response at the Global scale and enhance the stabilization of the iterative Global-Local approach. Moreover, non-matching grids were allowed such that the local and global domains can be updated independently of any additional conditions on the mesh.

In the numerical tests, it was shown that the GL approach besides its feasibility for having two different element formulations for the global and local domain, enabled computations with legacy codes. Additionally, it required significantly less degrees of freedom than the single-scale model, leads to a remarkable reduction of the computational time. In particular, the GL approach was up to few hundred times faster than the standard phase-field formulation (single-scale solution) in the numerical examples. Yet, an excellent performance of the proposed framework in all examples was observed.

In summary, key aspects of Part I were:

- A modular framework for a phase-field formulation of fracture;
- GL approach in order to capture the full Local resolution at the Global level;
- Robin-type boundary conditions between the Local and the Global domains;
- A non-matching element discretization for achieving sufficient regularity along the coupling interface;
- A predictor-corrector adaptive scheme in which the Local domains are dynamically updated during the computation;
- A coarse representation of the crack phase-field at the Global level;
- A microscale model for Local failure in multi-physics environments.

In the last section of this Part, the focus was put on the Local (lower) scale by developing a micromechanical model for failure in multi-physics problems. Here, the average size of this heterogeneous Local domain is much smaller than its Global specimen size. This was achieved using the recently developed virtual element method (VEM).

As a future direction, the 2D multi-scale approach will be further extended to a three-dimensional setting at finite strains.

9.2. Virtual Elements for engineering applications

Part II of this work explored the recently developed virtual element method (VEM) as a new discretization scheme for solving failure-mechanics problems numerically. In comparison with different element technologies VEM had proven to be a competitive discretization scheme for meshes with highly irregular shaped elements that can even become non-convex. It represents a generalization of the finite element method FEM, which has inspired from modern mimetic finite difference schemes. In this regard, a stabilization procedure was required in the virtual element method.

The performance of the virtual element method was comparable to using finite elements of higher order. Moreover, locking-free behavior was observed here, even at finite plastic strain states. In case of a severe distortion of the element, VEM showed more robust behavior than FEM. However, this comes with extra computational costs due to the additional amount of data required in the stabilization term to store the triangulation. Furthermore the preprocessing of meshes was more demanding in VEM (e.g. voronoi 3D cells). Numerically, a robust and efficient monolithic scheme was employed using the software tool AceFEM program in the implementation to compute the unknowns;

In summary, the key points of this Part were:

- VEM for the variational phase field modeling of isotropic brittle and ductile fracture;
- Extension towards three-dimensional multi-physics problems;
- Coupled thermomechanical response of gradient plasticity.

In the last section of this Part, the focus was put on gradient-extended framework of inelasticity to overcome the non-physical mesh dependency response of local theory.

This element technology is amenable to extensions of various kinds: for example to solid-fluid interaction, 3D contact mechanics and 3D fracture and damage mechanics problems. These topics await investigation. Finally, in Part I of this Habilitation, we demonstrated the flexibility of the Global-Local approaches in handling different spatial discretizations, i.e. VEM (Local-domain) / FEM (Global-domain) as sketched in Figure 1.3. Hence, a link between Part II and part I of this contribution is an open challenging task to be considered in future works.

References

- [1] <https://www.sfb1153.uni-hannover.de/>.
- [2] <https://www.spp2020.uni-hannover.de/>.
- [3] <https://www.uni-due.de/spp1748/>.
- [4] ALDAKHEEL, F.; MAUTHE, S.; MIEHE, C. [2014]: *Towards phase field modeling of ductile fracture in gradient-extended elastic-plastic solids*. Proceedings in Applied Mathematics and Mechanics, 14: 411–412.
- [5] ALDAKHEEL, F.; KIENLE, D.; KEIP, M.-A.; MIEHE, C. [2017]: *Phase field modeling of ductile fracture in soil mechanics*. Proceedings in Applied Mathematics and Mechanics, 17(1): 383–384.
- [6] ALDAKHEEL, F.; HUDOBIVNIK, B.; HUSSEIN, A.; WRIGGERS, P. [2018]: *Phase-field modeling of brittle fracture using an efficient virtual element scheme*. Computer Methods in Applied Mechanics and Engineering, 341: 443–466.
- [7] ALDAKHEEL, F.; HUDOBIVNIK, B.; WRIGGERS, P. [2019]: *Virtual elements for finite thermo-plasticity problems*. Computational Mechanics, 64(5): 1347–1360.
- [8] ALDAKHEEL, F.; HUDOBIVNIK, B.; WRIGGERS, P. [2019]: *Virtual element formulation for phase-field modeling of ductile fracture*. International Journal for Multiscale Computational Engineering, 17(2): 181–200.
- [9] ALDAKHEEL, F.; HUDOBIVNIK, B.; ARTIOLI, E.; DA VEIGA, L. B. AO ; WRIGGERS, P. [2020]: *Curvilinear virtual elements for contact mechanics*. Computer methods in applied mechanics and engineering, 372: 113394.
- [10] ALDAKHEEL, F. [2016]: *Mechanics of Nonlocal Dissipative Solids: Gradient Plasticity and Phase Field Modeling of Ductile Fracture*. Ph.D. Thesis, Institute of Applied Mechanics (CE), Chair I, University of Stuttgart. <http://dx.doi.org/10.18419/opus-8803>.
- [11] ALDAKHEEL, F. [2017]: *Micromorphic approach for gradient-extended thermo-elastic-plastic solids in the logarithmic strain space*. Continuum Mechanics and Thermodynamics, 29(6): 1207–1217.
- [12] ALDAKHEEL, F. [2020]: *A microscale model for concrete failure in poro-elasto-plastic media*. Theoretical and Applied Fracture Mechanics, 107: 102517.
- [13] ALDAKHEEL, F.; MIEHE, C. [2017]: *Coupled thermomechanical response of gradient plasticity*. International Journal of Plasticity, 91: 1–24.
- [14] ALDAKHEEL, F.; WRIGGERS, P.; MIEHE, C. [2018]: *A modified gurson-type plasticity model at finite strains: Formulation, numerical analysis and phase-field coupling*. Computational Mechanics, 62: 815–833.
- [15] ALDAKHEEL, F.; TOMANN, C.; LOHAUS, L.; WRIGGERS, P. [2019]: *Water-induced failure mechanics for concrete*. Proceedings in Applied Mathematics and Mechanics, 19(1). <https://doi.org/10.1002/pamm.201900140>.
- [16] ALDAKHEEL, F.; NOII, N.; WICK, T.; OLIVIER, A.; WRIGGERS, P. [2021]: *A global-local approach for phase-field modeling of ductile fracture*. Computer methods in applied mechanics and engineering, 387: 114175.
- [17] ALDAKHEEL, F.; NOII, N.; WICK, T.; WRIGGERS, P. [2021]: *A global-local approach for hydraulic phase-field fracture in poroelastic media*. Computers & Mathematics with Applications, 91: 99–121.
- [18] ALESSI, R.; AMBATI, M.; GERASIMOV, T.; VIDOLI, S.; DE LORENZIS, L. [2018]: *Comparison of Phase-Field Models of Fracture Coupled with Plasticity*, pp. 1–21.

- Advances in Computational Plasticity 46, Springer International Publishing.
- [19] ALESSI, R.; MARIGO, J.-J.; MAURINI, C.; VIDOLI, S. [2018]: *Coupling damage and plasticity for a phase-field regularisation of brittle, cohesive and ductile fracture: One-dimensional examples*. International Journal of Mechanical Sciences, 149: 559–576.
- [20] ALESSI, R.; VIDOLI, S.; DE LORENZIS, L. [2018]: *A phenomenological approach to fatigue with a variational phase-field model: The one-dimensional case*. Engineering Fracture Mechanics, 190: 53–73.
- [21] ALIABADI, M. H. [2002]: *The boundary element method, volume 2: applications in solids and structures*, Vol. 2. John Wiley & Sons.
- [22] AMBATI, M.; GERASIMOV, T.; DE LORENZIS, L. [2015]: *Phase-field modeling of ductile fracture*. Computational Mechanics, 55: 1017–1040.
- [23] AMBATI, M.; KRUSE, R.; DE LORENZIS, L. [2016]: *A phase-field model for ductile fracture at finite strains and its experimental verification*. Computational Mechanics, 57: 149–167.
- [24] AMBATI, M.; GERASIMOV, T.; DE LORENZIS, L. [2015]: *A review on phase-field models of brittle fracture and a new fast hybrid formulation*. Computational Mechanics, 55(2): 383–405.
- [25] AMBROSIO, L.; TORTORELLI, V. M. [1990]: *Approximation of functionals depending on jumps by elliptic functionals via Γ -convergence*. Communications on Pure and Applied Mathematics, 43: 999–1036.
- [26] AMBROSIO, L.; TORTORELLI, V. [1990]: *Approximation of functionals depending on jumps by elliptic functionals via γ -convergence*. Communications on Pure and Applied Mathematics, 43: 999–1036.
- [27] AMBROSIO, L.; TORTORELLI, V. [1992]: *On the approximation of free discontinuity problems*. Bollettino dell’Unione Matematica Italiana, 6: 105–123.
- [28] AMOR, H.; MARIGO, J.; MAURINI, C. [2009]: *Regularized formulation of the variational brittle fracture with unilateral contact: Numerical experiments*. Journal of the Mechanics and Physics of Solids, 57: 1209–1229.
- [29] ANAND, L.; ASLAN, O.; CHESTER, S. A. [2012]: *A large-deformation gradient theory for elastic-plastic materials: Strain softening and regularization of shear bands*. International Journal of Plasticity, 30-31: 116–143.
- [30] ANAND, L.; AMES, N. M.; SRIVASTAVA, V.; CHESTER, S. A. [2009]: *A thermomechanically coupled theory for large deformations of amorphous polymers. part i: Formulation*. International Journal of Plasticity, 25: 1474–1494.
- [31] ANDERSON, T. L. [1995]: *Fracture Mechanics: Fundamentals and Applications*. CRC Press, 2nd Edition.
- [32] ARGYRIS, J.; DOLTSINIS, J. [1981]: *On the natural formulation and analysis of large deformation coupled thermomechanical problems*. Computer Methods in Applied Mechanics and Engineering, 25: 195–253.
- [33] ARGYRIS, J.; DOLTSINIS, J. [1982]: *Thermomechanical response of solids at high strains - natural approach*. Computer Methods in Applied Mechanics and Engineering, 32: 3–57.
- [34] ARMERO, F. [1999]: *Formulation and finite element implementation of a multiplicative model of coupled poro-plasticity at finite strains under fully saturated conditions*. Computer methods in applied mechanics and engineering, 171(3-4): 205–241.
- [35] ARTINA, M.; FORNASIER, M.; MICHELETTI, S.; PEROTTO, S. [2015]:

- Anisotropic mesh adaptation for crack detection in brittle materials.* SIAM J. Sci. Comput., 37(4): B633–B659.
- [36] ARTIOLI, E.; VEIGA, L. BEIRÃO DA ; LOVADINA, C.; SACCO, E. [2017]: *Arbitrary order 2D virtual elements for polygonal meshes: part I, elastic problem.* Computational Mechanics, 60(3): 355–377.
- [37] ARTIOLI, E.; VEIGA, L. B. D.; LOVADINA, C.; SACCO, E. [2017]: *Arbitrary order 2d virtual elements for polygonal meshes: Part ii, inelastic problem.* Computational Mechanics, 60: 643–657.
- [38] BABUŠKA, I.; BANERJEE, U.; OSBORN, J. E. [2003]: *Survey of meshless and generalized finite element methods: a unified approach.* Acta Numerica, 12: 1–125.
- [39] BALZANI, D.; NEFF, P.; SCHRÖDER, J.; HOLZAPFEL, G. [2006]: *A polyconvex framework for soft biological tissues. adjustment to experimental data.* International Journal of Solids and Structures, 43: 6052–6070.
- [40] BANERJEE, P. K.; BUTTERFIELD, R. [1981]: *Boundary element methods in engineering science*, Vol. 17. McGraw-Hill London.
- [41] BANGERTH, W.; HARTMANN, R.; KANSCHAT, G. [2007]: *deal.II – a general purpose object oriented finite element library.* ACM Transactions on Mathematical Software, 33(4): 24/1–24/27.
- [42] BARTELS, A.; BARTEL, T.; CANADIJA, M.; MOSLER, J. [2015]: *On the thermo-mechanical coupling in dissipative materials: A variational approach for generalized standard materials.* Journal of the Mechanics and Physics of Solids, 82: 218–234.
- [43] BATHE, K. J. [1996]: *Finite Element Procedures.* Prentice-Hall, Englewood Cliffs, New Jersey.
- [44] BEESE, S.; LOEHNERT, S.; WRIGGERS, P. [2017]: *3D ductile crack propagation within a polycrystalline microstructure using XFEM.* Computational Mechanics. <https://doi.org/10.1007/s00466-017-1427-y>.
- [45] BEHRENS, B.-A.; MAIER, H. J.; POLL, G.; WRIGGERS, P.; ALDAKHEEL, F.; KLOSE, C.; NÜRNBERGER, F.; PAPE, F.; BÖHM, C.; CHUGREEVA, A.; COORS, T.; DURAN, D.; THÜRER, S. E.; HERBST, S.; HWANG, J.; MATTHIAS, T.; HEIMES, N.; UHE, J. [2020]: *Numerical investigations regarding a novel process chain for the production of a hybrid bearing bushing.* Production Engineering, 14: 569–581.
- [46] BEIRÃO DA VEIGA, L.; BREZZI, F.; CANGIANI, A.; MANZINI, G.; MARINI, L. D.; RUSSO, A. [2013]: *Basic principles of virtual element methods.* Mathematical Models and Methods in Applied Sciences, 23(01): 199–214.
- [47] BEIRÃO DA VEIGA, L.; BREZZI, F.; MARINI, L. D. [2013]: *Virtual Elements for linear elasticity problems.* SIAM Journal on Numerical Analysis, 51(2): 794–812.
- [48] BEIRÃO DA VEIGA, L.; BREZZI, F.; DASSI, F.; MARINI, L. D.; RUSSO, A. [2017]: *Virtual element approximation of 2d magnetostatic problems.* Computer Methods in Applied Mechanics and Engineering, 327: 173–195.
- [49] BEIRÃO DA VEIGA, L.; BREZZI, F.; DASSI, F.; MARINI, L. D.; RUSSO, A. [2018]: *Serendipity virtual elements for general elliptic equations in three dimensions.* Chinese Annals of Mathematics, Series B, 39(2): 315–334.
- [50] BELYTSCHKO, T.; BINDEMAN, L. P. [1991]: *Assumed strain stabilization of the 4-node quadrilateral with 1-point quadrature for nonlinear problems.* Computer Methods in Applied Mechanics and Engineering, 88(3): 311–340.
- [51] BELYTSCHKO, T.; BLACK, T. [1999]: *Elastic crack growth in finite elements with*

- minimal remeshing*. International Journal for Numerical Methods in Engineering, 45: 601–620.
- [52] BELYTSCHKO, T.; LIU, W. K.; MORAN, B.; ELKHODARY, K. [2014]: *Nonlinear Finite Elements for Continua and Structures*. John Wiley and Sons, Ltd., United Kingdom.
- [53] BELYTSCHKO, T.; KRONGAUZ, Y.; ORGAN, D.; FLEMING, M.; KRYSL, P. [1996]: *Meshless methods: an overview and recent developments*. Computer methods in applied mechanics and engineering, 139(1): 3–47.
- [54] BENEDETTO, M. F.; BERRONE, S.; SCIALÓ, S. [2016]: *A globally conforming method for solving flow in discrete fracture networks using the virtual element method*. Finite Elements in Analysis and Design, 109: 23–36.
- [55] BENEDETTO, M. F.; BORIO, A.; SCIALÓ, S. [2017]: *Mixed virtual elements for discrete fracture network simulations*. Finite Elements in Analysis and Design, 134: 55–67.
- [56] BERTRAM, A.; FOREST, S. [2014]: *The thermodynamics of gradient elastoplasticity*. Continuum Mechanics and Thermodynamics, 26: 269–286.
- [57] BESSON, J. [2010]: *Continuum models of ductile fracture: A review*. International Journal of Damage Mechanics, 19: 3–52.
- [58] BIOT, M. [1972]: *Theory of finite deformations of porous solids*. Indiana University Mathematics Journal, 21: 597–620.
- [59] BLEYER, J.; ALESSI, R. [2018]: *Phase-field modeling of anisotropic brittle fracture including several damage mechanisms*. Computer Methods in Applied Mechanics and Engineering, 336: 213–236.
- [60] BOERNER, E.; LOEHNERT, S.; WRIGGERS, P. [2007]: *A new finite element based on the theory of a cosserat point - extension to initially distorted elements for 2d plane strain*. International Journal for Numerical Methods in Engineering, 71: 454–472.
- [61] BÖGER, L.; KEIP, M.-A.; MIEHE, C. [2017]: *Minimization and saddle-point principles for the phase-field modeling of fracture in hydrogels*. Computational Materials Science, 138: 474–485.
- [62] BORDEN, M. J.; VERHOESEL, C. V.; SCOTT, M. A.; HUGHES, T. J. R.; LANDIS, C. M. [2012]: *A phase-field description of dynamic brittle fracture*. Computer Methods in Applied Mechanics and Engineering, 217-220: 77–95.
- [63] BORDEN, M. J.; HUGHES, T. J. R.; LANDIS, C. M.; VERHOESEL, C. V. [2014]: *A higher-order phase-field model for brittle fracture: Formulation and analysis within the isogeometric analysis framework*. Computer Methods in Applied Mechanics and Engineering, 273: 100–118.
- [64] BORDEN, M. J.; HUGHES, T. J.; LANDIS, C. M.; ANVARI, A.; LEE, I. J. [2016]: *A phase-field formulation for fracture in ductile materials: Finite deformation balance law derivation, plastic degradation, and stress triaxiality effects*. Computer Methods in Applied Mechanics and Engineering, 312: 130–166.
- [65] BOURDIN, B. [1999]: *Image segmentation with a finite element method*. Mathematical Modelling and Numerical Analysis, 33(2): 229–244.
- [66] BOURDIN, B. [2007]: *Numerical implementation of the variational formulation for quasi-static brittle fracture*. Interfaces and free boundaries, 9: 411–430.
- [67] BOURDIN, B.; FRANCFORT, G.; MARIGO, J.-J. [2000]: *Numerical experiments in revisited brittle fracture*. Journal of the Mechanics and Physics of Solids, 48(4):

- 797–826.
- [68] BOURDIN, B.; FRANCFORT, G.; MARIGO, J.-J. [2008]: *The variational approach to fracture*. Journal of Elasticity, 91: 5–148.
- [69] BOURDIN, B.; CHUKWUDOZIE, C.; YOSHIOKA, K. [2012]: *A variational approach to the numerical simulation of hydraulic fracturing*. SPE Journal, Conference Paper 159154-MS.
- [70] BOYCE, M. C.; MONTAGUT, E. L.; ARGON, A. S. [1992]: *The effects of thermomechanical coupling on the cold drawing process of glassy polymers*. Polymer Engineering and Science, 32(16): 1073–1085.
- [71] BREZZI, F.; BUFFA, A.; LIPNIKOV, K. [2009]: *Mimetic finite differences for elliptic problems*. ESAIM: Mathematical Modelling and Numerical Analysis, 43(2): 277–295.
- [72] BRUN, M. K.; WICK, T.; BERRE, I.; NORDBOTTEN, J. M.; RADU, F. A. [2020]: *An iterative staggered scheme for phase field brittle fracture propagation with stabilizing parameters*. Computer Methods in Applied Mechanics and Engineering, 361: 112752.
- [73] BURKE, S.; ORTNER, C.; SÜLI, E. [2010]: *An adaptive finite element approximation of a variational model of brittle fracture*. SIAM J. Numer. Anal., 48(3): 980–1012.
- [74] BURKE, S.; ORTNER, C.; SÜLI, E. [2013]: *An adaptive finite element approximation of a generalized Ambrosio-Tortorelli functional*. M3AS, 23(9): 1663–1697.
- [75] CAJUHI, T.; SANAVIA, L.; DE LORENZIS, L. [2017]: *Phase-field modeling of fracture in variably saturated porous media*. Computational Mechanics.
- [76] CANADIJA, M.; MOSLER, J. [2011]: *On the thermomechanical coupling in finite strain plasticity theory with non-linear kinematic hardening by means of incremental energy minimization*. International Journal of Solids and Structures, 48: 1120–1129.
- [77] CANGIANI, A.; MANZINI, G.; RUSSO, A.; SUKUMAR, N. [2015]: *Hourglass stabilization and the virtual element method*. International Journal for Numerical Methods in Engineering, 102(3-4): 404–436.
- [78] CAROL, I.; JIRÁSEK, M.; BAŽANT, Z. [2001]: *A thermodynamically consistent approach to microplane theory. part i. free energy and consistent microplane stresses*. International journal of solids and structures, 38(17): 2921–2931.
- [79] CAROLLO, V.; PAGGI, M.; REINOSO, J. [2019]: *The steady-state archard adhesive wear problem revisited based on the phase field approach to fracture*. International Journal of Fracture, 215(1-2): 39–48.
- [80] CARRARA, P.; AMBATI, M.; ALESSI, R.; DE LORENZIS, L. [2020]: *A framework to model the fatigue behavior of brittle materials based on a variational phase-field approach*. Computer Methods in Applied Mechanics and Engineering, 361: 112731.
- [81] CERECEDA, D.; DIEHL, M.; ROTERS, F.; RAABE, D.; PERLADO, J. M.; MARIAN, J. [2016]: *Unraveling the temperature dependence of the yield strength in single-crystal tungsten using atomistically-informed crystal plasticity calculations*. International Journal of Plasticity, 78: 242 – 265.
- [82] CHAPMAN, S. J. [2003]: *Fortran 90/95 for Scientists and Engineers*. McGraw-Hill, Inc., New York, NY, USA, 2 Edition.
- [83] CHAPUIS, A.; DRIVER, J. H. [2011]: *Temperature dependency of slip and twinning in plane strain compressed magnesium single crystals*. Acta Materialia, 59(5): 1986 – 1994.

- [84] CHEVREUIL, M.; NOUY, A.; SAFATLY, E. [2013]: *A multiscale method with patch for the solution of stochastic partial differential equations with localized uncertainties*. Computer Methods in Applied Mechanics and Engineering, 255: 255–274.
- [85] CHI, H.; BEIRÃO DA VEIGA, L.; PAULINO, G. [2017]: *Some basic formulations of the virtual element method (vem) for finite deformations*. Computer Methods in Applied Mechanics and Engineering, 318: 148–192.
- [86] CHOO, J.; SUN, W. [2018]: *Coupled phase-field and plasticity modeling of geological materials: From brittle fracture to ductile flow*. Computer Methods in Applied Mechanics and Engineering, 330: 1–32.
- [87] CHUGREEVA, A.; INCE, C.; BÖHM, C.; ALDAKHEEL, F.; WRIGGERS, P.; BEHRENS, B.-A.; RAATZ, A. [2021]: *Design of active cooling of titanium-aluminium workpieces during the inductive heating*. Production Engineering, 15: 177–186.
- [88] CHUKWUDOZIE, C.; BOURDIN, B.; YOSHIOKA, K. [2019]: *A variational phase-field model for hydraulic fracturing in porous media*. Computer Methods in Applied Mechanics and Engineering, 347: 957 – 982.
- [89] CIARLET, P. G. [1987]: *The finite element method for elliptic problems*. North-Holland, Amsterdam [u.a.], 2. pr. Edition.
- [90] CIHAN, M.; ALDAKHEEL, F.; HUDOBIVNIK, B.; WRIGGERS, P. [2020]: *Virtual element formulation for finite strain elastodynamics*. arXiv preprint arXiv:2002.02680.
- [91] COORS, T.; BÖHM, C.; HUDOBIVNIK, B.; PAPE, F.; ALDAKHEEL, F.; POLL, G.; WRIGGERS, P. [2020]: *Phenomenological lifetime prediction of hybrid structures - a multiscale supported approach*. To be submitted to Metals.
- [92] COTTRELL, J.; HUGHES, T.; BAZILEVS, Y. [2009]: *Isogeometric analysis: toward integration of CAD and FEA*. John Wiley & Sons.
- [93] COUSSY, O. [1995]: *Mechanics of porous continua*. Wiley.
- [94] DANA, S.; WHEELER, M. F. [2018]: *Convergence analysis of two-grid fixed stress split iterative scheme for coupled flow and deformation in heterogeneous poroelastic media*. Computer Methods in Applied Mechanics and Engineering, 341: 788–806.
- [95] DANA, S.; GANIS, B.; WHEELER, M. F. [2018]: *A multiscale fixed stress split iterative scheme for coupled flow and poromechanics in deep subsurface reservoirs*. Journal of Computational Physics, 352: 1–22.
- [96] DE BELLIS, M. L.; WRIGGERS, P.; HUDOBIVNIK, B.; ZAVARISE, G. [2018]: *Virtual element formulation for isotropic damage*. Finite Elements in Analysis and Design, 144: 38–48.
- [97] DE BELLIS, M. L.; WRIGGERS, P.; HUDOBIVNIK, B. [2019]: *Serendipity virtual element formulation for nonlinear elasticity*. Computers & Structures, 223: 106094.
- [98] DE BOER, R.; EHLERS, W. [1990]: *The development of the concept of effective stresses*. Acta Mechanica, 83(1-2): 77–92.
- [99] DE BOER, R. [2000]: *Theory of porous media: highlights in historical development and current state*. Springer Science & Business Media.
- [100] DE BORST, R.; MÜHLHAUS, H. B. [1992]: *Gradient-dependent plasticity: formulation and algorithmic aspects*. International Journal for Numerical Methods in Engineering, 35: 521–539.
- [101] DE LORENZIS, L.; MCBRIDE, A.; REDDY, B. [2016]: *Phase-field modelling of fracture in single crystal plasticity*. GAMM-Mitteilungen, 39(1): 7–34.

- [102] DE LORENZIS, L.; GERASIMOV, T. [2020]: *Numerical implementation of phase-field models of brittle fracture*. In *Modeling in Engineering Using Innovative Numerical Methods for Solids and Fluids*, pp. 75–101. Springer.
- [103] DEAN, A.; SAHRAEE, S.; ÖZENC, K.; REINOSO, J.; ROLFES, R.; KALISKE, M. [2017]: *A thermodynamically consistent framework to couple damage and plasticity microplane-based formulations for fracture modeling: development and algorithmic treatment*. *International Journal of Fracture*, 203(1-2): 115–134.
- [104] DEAN, A.; REINOSO, J.; JHA, N.; MAHDI, E.; ROLFES, R. [2020]: *A phase field approach for ductile fracture of short fibre reinforced composites*. *Theoretical and Applied Fracture Mechanics*, page 102495. <https://doi.org/10.1016/j.tafmec.2020.102495>.
- [105] DEPARIS, S.; DISCACCIATI, M.; FOURESTAY, G.; QUARTERONI, A. [2007]: *Heterogeneous domain decomposition methods for fluid-structure interaction problems*. *Domain Decomposition Methods in Science and Engineering XVI. Lecture Notes in Computational Science and Engineering*, 55: 41–52.
- [106] DIAMOND, S. [2004]: *The microstructure of cement paste and concrete—a visual primer*. *Cement and Concrete Composites*, 26(8): 919–933.
- [107] DITTMANN, M.; HESCH, C.; SCHULTE, J.; ALDAKHEEL, F.; FRANKE, M. [2017]: *Multi-field modelling and simulation of large deformation ductile fracture*. *Proceedings of the XIV International Conference on Computational Plasticity. Fundamentals and Applications*, pp. 556–567.
- [108] DITTMANN, M.; ALDAKHEEL, F.; SCHULTE, J.; WRIGGERS, P.; HESCH, C. [2018]: *Variational phase-field formulation of non-linear ductile fracture*. *Computer Methods in Applied Mechanics and Engineering*, 342: 71–94.
- [109] DITTMANN, M.; KRÜGER, M.; SCHMIDT, F.; SCHUSS, S.; HESCH, C. [2018]: *Variational modeling of thermomechanical fracture and anisotropic frictional mortar contact problems with adhesion*. *Computational Mechanics*. <https://doi.org/10.1007/s00466-018-1610-9>.
- [110] DITTMANN, M.; ALDAKHEEL, F.; SCHULTE, J.; SCHMIDT, F.; KRÜGER, M.; WRIGGERS, P.; HESCH, C. [2019]: *Phase-field modeling of porous-ductile fracture in non-linear thermo-elasto-plastic solids*. *Computer Methods in Applied Mechanics and Engineering*, page 112730. <https://doi.org/10.1016/j.cma.2019.112730>.
- [111] DONATH, F. A. [1961]: *Experimental study of shear failure in anisotropic rocks*. *GSA Bulletin*, 72(6): 985–989.
- [112] DRUCKER, D. C.; PRAGER, W. [1952]: *Soil mechanics and plastic analysis or limit design*. *Quarterly of applied mathematics*, 10(2): 157–165.
- [113] DUDA, F. P.; CIARBONETTI, A.; SÁNCHEZ, P. J.; HUESPE, A. E. [2014]: *A phase-field/gradient damage model for brittle fracture in elastic-plastic solids*. *International Journal of Plasticity*, 65: 269–296.
- [114] EHLERS, W. [2002]: *Foundations of multiphasic and porous materials*, pp. 3–86. Springer Berlin Heidelberg, Berlin, Heidelberg.
- [115] EHLERS, W.; LUO, C. [2017]: *A phase-field approach embedded in the theory of porous media for the description of dynamic hydraulic fracturing*. *Computer Methods in Applied Mechanics and Engineering*, 315: 348–368.
- [116] ENGELEN, R. A. B.; GEERS, M. G. D.; BAAIJENS, F. P. T. [2003]: *Nonlocal implicit gradient-enhanced elasto-plasticity for the modelling of softening behavior*. *International Journal of Plasticity*, 19: 403–433.

- [117] FAGHIHI, D.; VOYIADJIS, Z.; PARK, T. [2013]: *Coupled thermomechanical modeling of small volume fcc metals*. Journal of Engineering Materials and Technology, 135: 1–17.
- [118] FANG, J.; WU, C.; LI, J.; LIU, Q.; WU, C.; SUN, G.; LI, Q. [2019]: *Phase field fracture in elasto-plastic solids: Variational formulation for multi-surface plasticity and effects of plastic yield surfaces and hardening*. International Journal of Mechanical Sciences, 156: 382–396.
- [119] FANTONI, F.; BACIGALUPO, A.; PAGGI, M.; REINOSO, J. [2019]: *A phase field approach for damage propagation in periodic microstructured materials*. International Journal of Fracture, pp. 1–24.
- [120] FARHAT, C.; ROUX, F. [1991]: *A method of finite element tearing and interconnecting and its parallel solution algorithm*. International Journal for Numerical Methods in Engineering, 32: 1205–1227.
- [121] FARHAT, C.; MACEDO, A.; LESOINNE, M.; ROUX, F.-X.; MAGOULÉS, F.; BOURDONNAIE, A. D. L. [2000]: *Two-level domain decomposition methods with lagrange multipliers for the fast iterative solution of acoustic scattering problems*. Computer Methods in Applied Mechanics and Engineering, 184: 213–239.
- [122] FARRELL, P. E.; MAURINI, C. [2017]: *Linear and nonlinear solvers for variational phase-field models of brittle fracture*. International Journal for Numerical Methods in Engineering, 109: 648–667.
- [123] FISH, J.; WAGIMAN, A. [1993]: *Multiscale finite element method for a locally nonperiodic heterogeneous medium*. Computational Mechanics, 12(3): 164–180.
- [124] FISH, J. [2014]: *Practical Multiscale*. John Wiley and Sons, Ltd., United Kingdom.
- [125] FLANAGAN, D.; BELYTSCHKO, T. [1981]: *A uniform strain hexahedron and quadrilateral with orthogonal hour-glass control*. International Journal for Numerical Methods in Engineering, 17: 679–706.
- [126] FLECK, N. A.; WILLIS, J. R. [2009]: *A mathematical basis for strain-gradient plasticity theory. part i: scalar plastic multiplier*. Journal of the Mechanics and Physics of Solids, 57: 161–177.
- [127] FLECK, N. A.; WILLIS, J. R. [2009]: *A mathematical basis for strain-gradient plasticity theory. part ii: tensorial plastic multiplier*. Journal of the Mechanics and Physics of Solids, 57: 1045–1057.
- [128] FLECK, N. A.; MULLER, G. M.; ASHBY, M. F.; HUTCHINSON, J. W. [1994]: *Strain gradient plasticity: theory and experiment*. Acta Materialia, 42: 475–487.
- [129] FOREST, S. [2009]: *Micromorphic approach for gradient elasticity, viscoplasticity, and damage*. Journal of Engineering Mechanics, 135: 117–131.
- [130] FOREST, S. [2016]: *Nonlinear regularization operators as derived from the micromorphic approach to gradient elasticity, viscoplasticity and damage*. Proceedings of the Royal Society of London A: Mathematical, Physical and Engineering Sciences, 472(2188).
- [131] FOREST, S.; AIFANTIS, E. [2010]: *Some links between recent gradient thermo-elasto-plasticity theories and the thermomechanics of generalized continua*. International Journal of Solids and Structures, 47: 3367–3376.
- [132] FOREST, S.; SIEVERT, R. [2003]: *Elastoviscoplastic constitutive frameworks for generalized continua*. Acta Mechanica, 160: 71–111.
- [133] FORSYTHE, G. E.; WASOW, W. R. [1960]: *Finite difference methods*. Partial

- Differential.
- [134] FRANCFORT, G.; MARIGO, J.-J. [1998]: *Revisiting brittle fracture as an energy minimization problem*. Journal of the Mechanics and Physics of Solids, 46(8): 1319–1342.
 - [135] GAIN, A. L.; TALISCHI, C.; PAULINO, G. H. [2014]: *On the virtual element method for three-dimensional linear elasticity problems on arbitrary polyhedral meshes*. Computer Methods in Applied Mechanics and Engineering, 282: 132 – 160.
 - [136] GANDER, M.; HALPERN, L.; MAGOULES, F. [2007]: *An optimized schwarz method with two-sided robin transmission conditions for the helmholtz equation*. International Journal for Numerical Methods in Fluids, 55: 163–175.
 - [137] GEBUHR, G.; PISE, M.; SARHIL, M.; ANDERS, S.; BRANDS, D.; SCHRÖDER, J. [2019]: *Analysis and evaluation of the pull-out behavior of hooked steel fibers embedded in high and ultra-high performance concrete for calibration of numerical models*. Structural Concrete, 20: 1254–1264.
 - [138] GEELLEN, R.; PLEWS, J.; TUPEK, M.; DOLBOW, J. [2020]: *An extended/generalized phase-field finite element method for crack growth with global-local enrichment*. International Journal for Numerical Methods in Engineering, 121(11): 2534–2557.
 - [139] GEERS, M. G. D.; PEERLINGS, R. H. J.; BREKELMANS, W. A. M.; DE BORST, R. [2000]: *Phenomenological nonlocal approaches based on implicit gradient-enhanced damage*. Acta Mechanica, 144: 1–15.
 - [140] GENDRE, L.; ALLIX, O.; GOSSELET, P.; COMTE, F. [2009]: *Non-intrusive and exact global/local techniques for structural problems with local plasticity*. Computational Mechanics, 44: 233–245.
 - [141] GENDRE, L.; ALLIX, O.; GOSSELET, P. [2011]: *A two-scale approximation of the schur complement and its use for non-intrusive coupling*. International Journal for Numerical Methods in Engineering, 87: 889–905.
 - [142] GERASIMOV, T.; LORENZIS, L. D. [2016]: *A line search assisted monolithic approach for phase-field computing of brittle fracture*. Computer Methods in Applied Mechanics and Engineering, 312: 276–303.
 - [143] GERASIMOV, T.; NOII, N.; ALLIX, O.; DE LORENZIS, L. [2018]: *A non-intrusive global/local approach applied to phase-field modeling of brittle fracture*. Advanced Modeling and Simulation in Engineering Sciences, 5(1): 14.
 - [144] GIRAULT, V.; PENCHEVA, G.; WHEELER, M. F.; WILDEY, T. [2011]: *Domain decomposition for poroelasticity and elasticity with dg jumps and mortars*. Mathematical Models and Methods in Applied Sciences, 21(01): 169–213.
 - [145] GIRAULT, V.; PENCHEVA, G. V.; WHEELER, M. F.; WILDEY, T. M. [2009]: *Domain decomposition for linear elasticity with dg jumps and mortars*. Computer methods in applied mechanics and engineering, 198(21-26): 1751–1765.
 - [146] GOSSELET, P.; REY, C. [2006]: *Non-overlapping domain decomposition methods in structural mechanics*. Archives of Computational Methods in Engineering, 13: 515–572.
 - [147] GREER, N.; LOISEL, S. [2015]: *The optimised schwarz method and the two-lagrange multiplier method for heterogeneous problems in general domains with two general subdomains*. Numerical Algorithms, 69: 737–762.
 - [148] GUDMUNDSON, P. [2004]: *A unified treatment of strain gradient plasticity*. Journal of the Mechanics and Physics of Solids, 52: 1379–1406.

- [149] GÜLTEKIN, O.; DAL, H.; HOLZAPFEL, G. A. [2016]: *A phase-field approach to model fracture of arterial walls: Theory and finite element analysis*. Computer Methods in Applied Mechanics and Engineering, 312: 542–566.
- [150] GURTIN, E. [2008]: *A finite-deformation, gradient theory of single-crystal plasticity with free energy dependent on densities of geometrically necessary dislocations*. International Journal of Plasticity, 24: 702–725.
- [151] HACKL, K. [1997]: *Generalized standard media and variational principles in classical and finite strain elastoplasticity*. Journal of the Mechanics and Physics of Solids, 45(5): 667–688.
- [152] HAIN, M.; WRIGGERS, P. [2008]: *Computational homogenization of microstructural damage due to frost in hardened cement paste*. Finite Elements in Analysis and Design, 44(5): 233 – 244. The Nineteenth Annual Robert J. Melosh Competition.
- [153] HAIN, M.; WRIGGERS, P. [2008]: *Numerical homogenization of hardened cement paste*. Computational Mechanics, 42(2): 197–212.
- [154] HAKIM, V.; KARMA, A. [2009]: *Laws of crack motion and phase-field models of fracture*. Journal of the Mechanics and Physics of Solids, 57(2): 342 – 368.
- [155] HALLQUIST, J. O. [1984]: *Nike 2D: An implicit, finite deformation, finite element code for analyzing the static and dynamic response of two-dimensional solids*. Rept. UCRL-52678, Lawrence Livermore National Laboratory, University of California, Livermore, CA.
- [156] HAN, T.-S.; ZHANG, X.; KIM, J.-S.; CHUNG, S.-Y.; LIM, J.-H.; LINDER, C. [2018]: *Area of lineal-path function for describing the pore microstructures of cement paste and their relations to the mechanical properties simulated from μ -ct microstructures*. Cement and Concrete Composites, 89: 1 – 17.
- [157] HAUTEFEUILLE, M.; COLLIAT, J.-B.; IBRAHIMBEGOVIC, A.; MATTHIES, H.; VILLON, P. [2012]: *A multi-scale approach to model localized failure with softening*. Computers & Structures, 94-95: 83–95.
- [158] HECHT, F.; LOZINSKI, A.; PIRONNEAU, O. [2009]: *Numerical zoom and the schwarz algorithm*. Domain Decomposition Methods in Science and Engineering XVIII, 70: 63–73.
- [159] HEIDER, Y.; MARKERT, B. [2017]: *A phase-field modeling approach of hydraulic fracture in saturated porous media*. Mechanics Research Communications, 80: 38–46.
- [160] HEIDER, Y.; SUN, W. [2020]: *A phase field framework for capillary-induced fracture in unsaturated porous media: Drying-induced vs. hydraulic cracking*. Computer Methods in Applied Mechanics and Engineering, 359: 112647.
- [161] HEIDER, Y.; REICHE, S.; SIEBERT, P.; MARKERT, B. [2018]: *Modeling of hydraulic fracturing using a porous-media phase-field approach with reference to experimental data*. Engineering Fracture Mechanics, 202: 116–134.
- [162] HEISTER, T.; WHEELER, M. F.; WICK, T. [2015]: *A primal-dual active set method and predictor-corrector mesh adaptivity for computing fracture propagation using a phase-field approach*. Computer Methods in Applied Mechanics and Engineering, 290: 466 – 495.
- [163] HEISTER, T.; WICK, T. [2018]: *Parallel solution, adaptivity, computational convergence, and open-source code of 2d and 3d pressurized phase-field fracture problems*. PAMM, 18(1): e201800353.

- [164] HESCH, C.; WEINBERG, K. [2014]: *Thermodynamically consistent algorithms for a finite-deformation phase-field approach to fracture*. International Journal for Numerical Methods in Engineering, 99: 906–924.
- [165] HESCH, C.; FRANKE, M.; DITTMANN, M.; TEMIZER, I. [2016]: *Hierarchical nurbs and a higher-order phase-field approach to fracture for finite-deformation contact problems*. Computer Methods in Applied Mechanics and Engineering, 301: 242 – 258.
- [166] HILL, R. [1965]: *A self-consistent mechanics of composite materials*. Journal of the Mechanics and Physics of Solids, 13(4): 213–222.
- [167] HINOJOSA, J.; ALLIX, O.; GUIDAULT, P.-A.; CRESTA, P. [2014]: *Domain decomposition methods with nonlinear localization for the buckling and post-buckling analyses of large structures*. Advances in Engineering Software, 70: 13–24.
- [168] HOLZAPFEL, G. A.; GASSER, T., C.; OGDEN, R., W. [2000]: *A new constitutive framework for arterial wall mechanics and a comparative study of material models*. Journal of Elasticity, 61: 1–48.
- [169] HUDOBIVNIK, B.; ALDAKHEEL, F.; WRIGGERS, P. [2018]: *A low order 3d virtual element formulation for finite elasto-plastic deformations*. Computational Mechanics, 63(2): 253–269.
- [170] HUDOBIVNIK, B.; ALDAKHEEL, F.; WRIGGERS, P. [2019]: *A low order 3d virtual element formulation for finite elasto-plastic deformations*. Computational Mechanics, 63(2): 253–269.
- [171] HUERTA, A.; FERNÁNDEZ-MÉNDEZ, S. [2000]: *Enrichment and coupling of the finite element and meshless methods*. International Journal for Numerical Methods in Engineering, 48(11): 1615–1636.
- [172] HUET, C. [1995]: *A continuum thermodynamics approach studying microstructural effects on the non-linear fracture behaviour of concrete seen as multicroaked granular composite material*. Fracture Mechanics of Concrete Structures, pp. 1089–1108.
- [173] HUGHES, T. J.; FEIJÓO, G. R.; MAZZEI, L.; QUINCY, J.-B. [1998]: *The variational multiscale method—a paradigm for computational mechanics*. Computer Methods in Applied Mechanics and Engineering, 166(1): 3–24. Advances in Stabilized Methods in Computational Mechanics.
- [174] HUGHES, T.; COTTRELL, J.; BAZILEVS, Y. [2005]: *Isogeometric analysis: Cad, finite elements, nurbs, exact geometry and mesh refinement*. Computer Methods in Applied Mechanics and Engineering, 194(39): 4135 – 4195.
- [175] HUSSEIN, A.; ALDAKHEEL, F.; HUDOBIVNIK, B.; WRIGGERS, P.; GUIDAULT, P.-A.; ALLIX, O. [2019]: *A computational framework for brittle crack-propagation based on efficient virtual element method*. Finite Elements in Analysis and Design, 159: 15–32.
- [176] KAKOURIS, E. G.; TRIANTAFYLLOU, S. P. [2017]: *Phase-field material point method for brittle fracture*. International Journal for Numerical Methods in Engineering, 112(12): 1750–1776.
- [177] KHOROMSKIJ, B.; WITTUM, G. [1998]: *Robust Interface Reduction for Highly Anisotropic Elliptic Equations*. Springer-Verlag Berlin Heidelberg.
- [178] KIENLE, D.; ALDAKHEEL, F.; KEIP, M.-A. [2019]: *A finite-strain phase-field approach to ductile failure of frictional materials*. International Journal of Solids and Structures, 172: 147–162.
- [179] KIKUCHI, N.; ODEN, J. [1988]: *Contact problems in elasticity*. Studies in Applied

- Mathematics. Society for Industrial and Applied Mathematics (SIAM), Philadelphia, PA.
- [180] KIM, S.-M.; AL-RUB, R. K. A. [2011]: *Meso-scale computational modeling of the plastic-damage response of cementitious composites*. Cement and Concrete Research, 41(3): 339–358.
- [181] KINDERLEHRER, D.; STAMPACCHIA, G. [2000]: *An Introduction to Variational Inequalities and Their Applications*. Classics in Applied Mathematics. Society for Industrial and Applied Mathematics.
- [182] KLUSEMANN, B.; YALCINKAYA, T. [2013]: *Plastic deformation induced microstructure evolution through gradient enhanced crystal plasticity based on a non-convex helmholtz energy*. International Journal of Plasticity, 48: 168–188.
- [183] KORELC, J.; STUPKIEWICZ, S. [2014]: *Closed-form matrix exponential and its application in finite-strain plasticity*. International Journal for Numerical Methods in Engineering, 98: 960–987.
- [184] KORELC, J.; WRIGGERS, P. [2016]: *Automation of Finite Element Methods*. Springer. <https://doi.org/10.1007/978-3-319-39005-5>.
- [185] KORELC, J.; SOLINC, U.; WRIGGERS, P. [2010]: *An improved EAS brick element for finite deformation*. Computational Mechanics, 46: 641–659.
- [186] KRÜGER, M.; DITTMANN, M.; ALDAKHEEL, F.; HÄRTEL, A.; WRIGGERS, P.; HESCH, C. [2019]: *Porous-ductile fracture in thermo-elasto-plastic solids with contact applications*. Computational Mechanics, pp. 1–26. <https://doi.org/10.1007/s00466-019-01802-3>.
- [187] KRYSL, P. [2015]: *Mean-strain eight-node hexahedron with optimized energy-sampling stabilization for large-strain deformation*. International Journal for Numerical Methods in Engineering, 103: 650–670.
- [188] KUHN, C.; MÜLLER, R. [2010]: *A continuum phase field model for fracture*. Engineering Fracture Mechanics, 77(18): 3625 – 3634.
- [189] KUHN, C.; SCHLÜTER, A.; MÜLLER, R. [2015]: *On degradation functions in phase field fracture models*. Computational Materials Science, 108: 374 – 384.
- [190] KUHN, C.; NOLL, T.; MÜLLER, R. [2016]: *On phase field modeling of ductile fracture*. GAMM-Mitteilungen, 39(1): 35–54.
- [191] KUNA, M. [2008]: *Numerische Beanspruchungsanalyse von Rissen*, Vol. 2. Springer.
- [192] KURODA, M.; TVERGAARD, V. [2010]: *An alternative treatment of phenomenological higher-order strain-gradient plasticity theory*. International Journal of Plasticity, 26: 507–515.
- [193] LAMBRECHT, M.; MIEHE, C. [2001]: *A note on formulas for localized failure of frictional materials in compression and biaxial loading modes*. International journal for numerical and analytical methods in geomechanics, 25(10): 955–971.
- [194] LAPIDUS, L.; PINDER, G. F. [2011]: *Numerical solution of partial differential equations in science and engineering*. John Wiley & Sons.
- [195] LEBLOND, J.; PERRIN, G.; DEVAUS, J. [1995]: *An improved gurson-type model for hardenable ductile metals*. European Journal of Mechanics - A/Solids, 14: 499–527.
- [196] LEE, S.; WHEELER, M. F.; WICK, T. [2016]: *Pressure and fluid-driven fracture propagation in porous media using an adaptive finite element phase field model*. Computer Methods in Applied Mechanics and Engineering, 305: 111 – 132.
- [197] LEE, S.; MIKELIC, A.; WHEELER, M.; WICK, T. [2018]: *Phase-field modeling of two phase fluid filled fractures in a poroelastic medium*. Multiscale Modeling &

- Simulation, 16(4): 1542–1580.
- [198] LEE, S.; MIKELIĆ, A.; WHEELER, M. F.; WICK, T. [2016]: *Phase-field modeling of proppant-filled fractures in a poroelastic medium*. Computer Methods in Applied Mechanics and Engineering, 312: 509 – 541.
- [199] LEE, S.; WHEELER, M. F.; WICK, T.; SRINIVASAN, S. [2017]: *Initialization of phase-field fracture propagation in porous media using probability maps of fracture networks*. Mechanics Research Communications, 80: 16 – 23. Multi-Physics of Solids at Fracture.
- [200] LEE, S.; MIN, B.; WHEELER, M. F. [2018]: *Optimal design of hydraulic fracturing in porous media using the phase field fracture model coupled with genetic algorithm*. Computational Geosciences, 22(3): 833–849.
- [201] LEMAITRE, J. [1992]: *A course on damage mechanics*. Springer.
- [202] LEMAITRE, J.; CHABOCHE, J. [1990]: *Mechanics of Solid Materials*. Cambridge University Press.
- [203] LI, B.; MAURINI, C. [2019]: *Crack kinking in a variational phase-field model of brittle fracture with strongly anisotropic surface energy*. Journal of the Mechanics and Physics of Solids, 125: 502 – 522.
- [204] LIEBE, T.; STEINMANN, P. [2001]: *Theory and numerics of a thermodynamically consistent framework for geometrically linear gradient plasticity*. International Journal for Numerical Methods in Engineering, 51: 1437–1467.
- [205] LION, A. [2000]: *Constitutive modelling in finite thermoviscoplasticity: a physical approach based on nonlinear rheological models*. International Journal of Plasticity, 16(5): 469 – 494.
- [206] LLOBERAS-VALLS, O.; RIXEN, D. J.; SIMONE, A.; SLUYS, L. J. [2012]: *Multi-scale domain decomposition analysis of quasi-brittle heterogeneous materials*. International Journal for Numerical Methods in Engineering, 83: 1337–1366.
- [207] LOEHNERT, S.; BELYTSCHKO, T. [2007]: *A multiscale projection method for macro/microcrack simulations*. International Journal for Numerical Methods in Engineering, 71(12): 1466–1482.
- [208] LOHAUS, L.; ONESCHKOW, N.; WEFER, M. [2012]: *Design model for the fatigue behaviour of normal-strength, high-strength and ultra-high-strength concrete*. Structural Concrete, 13(3): 182–192.
- [209] LUKOVIC, M.; SCHLANGEN, E.; YE, G. [2015]: *Combined experimental and numerical study of fracture behaviour of cement paste at the microlevel*. Cement and Concrete Research, 73: 123 – 135.
- [210] MADAY, Y.; MAGOULÉS, F. [2006]: *Absorbing interface conditions for domain decomposition methods: A general presentation*. International Journal for Numerical Methods in Fluids, 195: 3880–3900.
- [211] MAGOULES, F.; ROUX, F. X.; SERIES, L. [2006]: *Algebraic approximation of dirichlet-to-neumann maps for the equations of linear elasticity*. Computer Methods in Applied Mechanics and Engineering, 195: 3742–3759.
- [212] MANDEL, J. [1993]: *Balancing domain decomposition*. Communications in Applied Numerical Methods, 9(4): 233–241.
- [213] MANG, K.; WICK, T. [2019]: *Numerical methods for variational phase-field fracture problems*. Lecture notes at Leibniz University Hannover.
- [214] MARKERT, B. [2007]: *A constitutive approach to 3-d nonlinear fluid flow through finite deformable porous continua*. Transport in Porous Media, 70(3): 427.

- [215] MARKOVIC, D.; IBRAHIMBEGOVIC, A. [2004]: *On micro-macro interface conditions for micro scale based fem for inelastic behavior of heterogeneous materials*. Computer Methods in Applied Mechanics and Engineering, 193(48): 5503–5523. Advances in Computational Plasticity.
- [216] MATLAB [2018]: *version 9.5.0.944444 (R2018b)*. The MathWorks Inc., Natick, Massachusetts.
- [217] MAZARS, J.; PIJAUDIER-CABOT, G. [1989]: *Continuum damage theory-application to concrete*. Journal of Engineering Mechanics, 115(2): 345–365.
- [218] MESGARNEJAD, A.; BOURDIN, B.; KHONSARI, M. [2015]: *Validation simulations for the variational approach to fracture*. Computer Methods in Applied Mechanics and Engineering, 290: 420–437.
- [219] MICHEL, J.; MOULINEC, H.; SUQUET, P. [1999]: *Effective properties of composite materials with periodic microstructure: a computational approach*. Computer Methods in Applied Mechanics and Engineering, 172(1): 109–143.
- [220] MIEHE, C. [2011]: *A multi-field incremental variational framework for gradient-extended standard dissipative solids*. Journal of the Mechanics and Physics of Solids, 59: 898–923.
- [221] MIEHE, C.; BAYREUTHER, C. [2007]: *On multiscale fe analyses of heterogeneous structures: from homogenization to multigrid solvers*. International Journal for Numerical Methods in Engineering, 71: 1135–1180.
- [222] MIEHE, C.; LAMBRECHT, M. [2001]: *Algorithms for computation of stresses and elasticity moduli in terms of Seth-Hill’s family of generalized strain tensors*. Communications in Numerical Methods in Engineering, 17: 337–353.
- [223] MIEHE, C.; APEL, N.; LAMBRECHT, M. [2002]: *Anisotropic additive plasticity in the logarithmic strain space. modular kinematic formulation and implementation based on incremental minimization principles for standard materials*. Computer Methods in Applied Mechanics and Engineering, 191: 5383–5425.
- [224] MIEHE, C.; HOFACKER, M.; WELSCHINGER, F. [2010]: *A phase field model for rate-independent crack propagation: Robust algorithmic implementation based on operator splits*. Comput. Meth. Appl. Mech. Engrg., 199: 2765–2778.
- [225] MIEHE, C.; WELSCHINGER, F.; HOFACKER, M. [2010]: *Thermodynamically consistent phase-field models of fracture: Variational principles and multi-field FE implementations*. International Journal for Numerical Methods in Engineering, 83: 1273–1311.
- [226] MIEHE, C.; MÉNDEZ DIEZ, J.; GÖKTEPE, S.; SCHÄNZEL, L. [2011]: *Coupled thermoviscoplasticity of glassy polymers in the logarithmic strain space based on the free volume theory*. International Journal of Solids and Structures, 48: 1799–1817.
- [227] MIEHE, C.; ALDAKHEEL, F.; MAUTHE, S. [2013]: *Mixed variational principles and robust finite element implementations of gradient plasticity at small strains*. International Journal for Numerical Methods in Engineering, 94: 1037–1074.
- [228] MIEHE, C.; MAUTHE, S.; HILDEBRAND, F. E. [2014]: *Variational gradient plasticity at finite strains. Part III: Local-global updates and regularization techniques in multiplicative plasticity for single crystals*. Computer Methods in Applied Mechanics and Engineering, 268: 735–762.
- [229] MIEHE, C.; WELSCHINGER, F.; ALDAKHEEL, F. [2014]: *Variational gradient plasticity at finite strains. Part II: Local-global updates and mixed finite elements for additive plasticity in the logarithmic strain space*. Computer Methods in Applied

- Mechanics and Engineering, 268: 704–734.
- [230] MIEHE, C.; HOFACKER, M.; SCHÄNZEL, L.-M.; ALDAKHEEL, F. [2015]: *Phase field modeling of fracture in multi-physics problems. Part II. brittle-to-ductile failure mode transition and crack propagation in thermo-elastic-plastic solids*. Computer Methods in Applied Mechanics and Engineering, 294: 486–522.
- [231] MIEHE, C.; SCHÄNZEL, L.; ULMER, H. [2015]: *Phase field modeling of fracture in multi-physics problems. Part I. balance of crack surface and failure criteria for brittle crack propagation in thermo-elastic solids*. Computer Methods in Applied Mechanics and Engineering, 294: 449–485.
- [232] MIEHE, C.; ALDAKHEEL, F.; RAINA, A. [2016]: *Phase field modeling of ductile fracture at finite strains. a variational gradient-extended plasticity-damage theory*. International Journal of Plasticity, 84: 1–32.
- [233] MIEHE, C.; TEICHTMEISTER, S.; ALDAKHEEL, F. [2016]: *Phase-field modeling of ductile fracture: A variational gradient-extended plasticity-damage theory and its micromorphic regularization*. Philosophical Transactions of the Royal Society A: Mathematical, Physical and Engineering Sciences, 374(2066).
- [234] MIEHE, C.; MAUTHE, S. [2016]: *Phase field modeling of fracture in multi-physics problems. part iii. crack driving forces in hydro-poro-elasticity and hydraulic fracturing of fluid-saturated porous media*. Computer Methods in Applied Mechanics and Engineering, 304: 619–655.
- [235] MIEHE, C.; MAUTHE, S.; TEICHTMEISTER, S. [2015]: *Minimization principles for the coupled problem of darcy-biot-type fluid transport in porous media linked to phase field modeling of fracture*. Journal of the Mechanics and Physics of Solids, 82: 186 – 217.
- [236] MIEHE, C.; MAUTHE, S.; TEICHTMEISTER, S. [2015]: *Minimization principles for the coupled problem of darcy-biot-type fluid transport in porous media linked to phase field modeling of fracture*. Journal of the Mechanics and Physics of Solids, 82: 186–217.
- [237] MIEHE, C.; KIENLE, D.; ALDAKHEEL, F.; TEICHTMEISTER, S. [2016]: *Phase field modeling of fracture in porous plasticity: A variational gradient-extended eulerian framework for the macroscopic analysis of ductile failure*. Computer Methods in Applied Mechanics and Engineering, 312: 3–50.
- [238] MIEHE, C.; ALDAKHEEL, F.; TEICHTMEISTER, S. [2017]: *Phase-field modeling of ductile fracture at finite strains: A robust variational-based numerical implementation of a gradient-extended theory by micromorphic regularization*. International Journal for Numerical Methods in Engineering, 111(9): 816–863.
- [239] MIKELIĆ, A.; WHEELER, M. F.; WICK, T. [2015]: *A phase-field method for propagating fluid-filled fractures coupled to a surrounding porous medium*. SIAM Multiscale Model. Simul., 13(1): 367–398.
- [240] MIKELIĆ, A.; WHEELER, M. F.; WICK, T. [2015]: *A quasi-static phase-field approach to pressurized fractures*. Nonlinearity, 28(5): 1371–1399.
- [241] MIKELIĆ, A.; WHEELER, M. F.; WICK, T. [2019]: *Phase-field modeling through iterative splitting of hydraulic fractures in a poroelastic medium*. GEM - International Journal on Geomathematics, 10(1). <https://doi.org/10.1007/s13137-019-0113-y>.
- [242] MIKELIĆ, A.; WHEELER, M. F.; WICK, T. [2019]: *Phase-field modeling through iterative splitting of hydraulic fractures in a poroelastic medium*. GEM - Inter-

- national Journal on Geomathematics, 10(1). <https://doi.org/10.1007/s13137-019-0113-y>.
- [243] MOËS, N.; DOLBOW, J.; BELYTSCHKO, T. [1999]: *A finite element method for crack growth without remeshing*. International Journal for Numerical Methods in Engineering, 46: 131–150.
- [244] MOTA, A.; TEZAUR, I.; ALLEMAN, C. [2017]: *The schwarz alternating method in solid mechanics*. Computer Methods in Applied Mechanics and Engineering, 319: 19–51.
- [245] MSEKH, M. A.; CUONG, N.; ZI, G.; AREIAS, P.; ZHUANG, X.; RABCZUK, T. [2018]: *Fracture properties prediction of clay/epoxy nanocomposites with interphase zones using a phase field model*. Engineering Fracture Mechanics, 188: 287–299.
- [246] MUELLER-HOEPPE, D. S.; LOEHNERT, S.; WRIGGERS, P. [2009]: *A finite deformation brick element with inhomogeneous mode enhancement*. International Journal for Numerical Methods in Engineering, 78: 1164–1187.
- [247] MUMFORD, D.; SHAH, J. [1989]: *Optimal approximations by piecewise smooth functions and associated variational problems*. Communications on Pure and Applied Mathematics, 42: 577–685.
- [248] NA, S.; SUN, W. [2018]: *Computational thermomechanics of crystalline rock, part I: A combined multi-phase-field/crystal plasticity approach for single crystal simulations*. Computer Methods in Applied Mechanics and Engineering. <https://doi.org/10.1016/j.cma.2017.12.022>.
- [249] NADLER, B.; RUBIN, M. [2003]: *A new 3-d finite element for nonlinear elasticity using the theory of a cosserat point*. Int. J. of Solids and Structures, 40: 4585–4614.
- [250] NAGARAJA, S.; ELHADDAD, M.; AMBATI, M.; KOLLMANNNSBERGER, S.; DE LORENZIS, L.; RANK, E. [2019]: *Phase-field modeling of brittle fracture with multi-level hp-fem and the finite cell method*. Computational Mechanics, 63(6): 1283–1300.
- [251] NASSERI, M.; MOHANTY, B. [2008]: *Fracture toughness anisotropy in granitic rocks*. International Journal of Rock Mechanics and Mining Sciences, 45(2): 167 – 193.
- [252] NEEDLEMAN, A.; TVERGAARD, V. [1984]: *An analysis of ductile rupture in notched bars*. Journal of the Mechanics and Physics of Solids, 32: 461–490.
- [253] NGUYEN, L. H.; SCHILLINGER, D. [2019]: *The multiscale finite element method for nonlinear continuum localization problems at full fine-scale fidelity, illustrated through phase-field fracture and plasticity*. Journal of Computational Physics, 396: 129–160.
- [254] NGUYEN, T. T.; RÉTHORÉ, J.; BAIETTO, M.-C. [2017]: *Phase field modelling of anisotropic crack propagation*. European Journal of Mechanics - A/Solids, 65: 279 – 288.
- [255] NGUYEN, V. P.; RABCZUK, T.; BORDAS, S.; DUFLOT, M. [2008]: *Meshless methods: a review and computer implementation aspects*. Mathematics and computers in simulation, 79(3): 763–813.
- [256] NGUYEN-THANH, V.; ZHUANG, X.; NGUYEN-XUAN, H.; RABCZUK, T.; WRIGGERS, P. [2018]: *A virtual element method for 2d linear elastic fracture analysis*. Computer Methods in Applied Mechanics and Engineering, 340: 366 – 395.
- [257] NOII, N.; WICK, T. [2019]: *A phase-field description for pressurized and non-isothermal propagating fractures*. Computer Methods in Applied Mechanics and

- Engineering, 351: 860 – 890.
- [258] NOII, N.; ALDAKHEEL, F.; WICK, T.; WRIGGERS, P. [2020]: *An adaptive global–local approach for phase-field modeling of anisotropic brittle fracture*. Computer Methods in Applied Mechanics and Engineering, 361: 112744. <https://doi.org/10.1016/j.cma.2019.112744>.
- [259] PAGGI, M.; REINOSO, J. [2017]: *Revisiting the problem of a crack impinging on an interface: a modeling framework for the interaction between the phase field approach for brittle fracture and the interface cohesive zone model*. Computer Methods in Applied Mechanics and Engineering, 321: 145 – 172.
- [260] PARK, K.; FELIPPA, C. [2000]: *A variational principle for the formulation of partitioned structural systems*. International Journal for Numerical Methods in Engineering, 47: 395–418.
- [261] PARK, K.; FELIPPA, C. [2002]: *A simple algorithm for localized construction of non-matching structural interfaces*. International Journal for Numerical Methods in Engineering, 53(9): 2117–2142.
- [262] PARTRIDGE, P. W.; BREBBIA, C. A., ET AL. [2012]: *Dual reciprocity boundary element method*. Springer Science & Business Media.
- [263] PATEL, R. A.; PERKO, J.; JACQUES, D.; SCHUTTER, G. D.; YE, G.; BRUEGEL, K. V. [2018]: *Effective diffusivity of cement pastes from virtual microstructures: Role of gel porosity and capillary pore percolation*. Construction and Building Materials, 165.
- [264] PEDERSEN, R.; SIMONE, A.; SLUYS, L. [2008]: *An analysis of dynamic fracture in concrete with a continuum visco-elastic visco-plastic damage model*. Engineering fracture mechanics, 75(13): 3782–3805.
- [265] PEERLINGS, R. H. J.; GEERS, M. G. D.; DE BORST, R.; BREKELMANS, W. A. M. [2001]: *A critical comparison of nonlocal and gradient-enhanced softening continua*. International Journal of Solids and Structures, 38: 7723–7746.
- [266] PEERLINGS, R. H. J.; MASSART, T. J.; GEERS, M. G. D. [2004]: *A thermodynamically motivated implicit gradient damage framework and its application to brick masonry cracking*. Computer Methods in Applied Mechanics and Engineering, 193: 3403–3417.
- [267] PHAM, K.; AMOR, H.; MARIGO, J.; MAURINI, C. [2011]: *Gradient damage models and their use to approximate brittle fracture*. International Journal of Damage Mechanics, 20(4): 618–652.
- [268] PHAM, K.; AMOR, H.; MARIGO, J.-J.; MAURINI, C. [2011]: *Gradient damage models and their use to approximate brittle fracture*. International Journal of Damage Mechanics, 20(4): 618–652.
- [269] PICHLER, B.; HELLMICH, C.; EBERHARDSTEINER, J.; WASSERBAUER, J.; TERMKHAJORKIT, P.; BARBARULO, R.; CHANVILLARD, G. [2013]: *Effect of gel-space ratio and microstructure on strength of hydrating cementitious materials: An engineering micromechanics approach*. Cement and Concrete Research, 45: 55–68.
- [270] PILLAI, U.; HEIDER, Y.; MARKERT, B. [2018]: *A diffusive dynamic brittle fracture model for heterogeneous solids and porous materials with implementation using a user-element subroutine*. Computational Materials Science, 153: 36–47.
- [271] POLIZZOTTO, C. [2009]: *A nonlocal strain gradient plasticity theory for finite deformations*. International Journal of Plasticity, 25: 1280–1300.

- [272] PORTELA, A.; ALIABADI, M.; ROOKE, D. [1992]: *The dual boundary element method: effective implementation for crack problems*. International journal for numerical methods in engineering, 33(6): 1269–1287.
- [273] REDDY, B. D.; HUYSSTEEN, D. VAN [2019]: *A virtual element method for transversely isotropic elasticity*. Computational Mechanics. <https://doi.org/10.1007/s00466-019-01690-7>.
- [274] REDDY, B.; EBOBISSE, F.; MCBRIDE, A. [2008]: *Well-posedness of a model of strain gradient plasticity for plastically irrotational materials*. International Journal of Plasticity, 24: 55–73.
- [275] REESE, S.; WRIGGERS, P. [2000]: *A new stabilization concept for finite elements in large deformation problems*. International Journal for Numerical Methods in Engineering, 48: 79–110.
- [276] REESE, S.; KUESSNER, M.; REDDY, B. D. [1999]: *A new stabilization technique to avoid hourglassing in finite elasticity*. International Journal for Numerical Methods in Engineering, 44: 1617–1652.
- [277] REINOSO, J.; PAGGI, M.; LINDER, C. [2017]: *Phase field modeling of brittle fracture for enhanced assumed strain shells at large deformations: formulation and finite element implementation*. Computational Mechanics, 59(6): 981–1001.
- [278] REIS, F.; PIRES, F. A. [2014]: *A mortar based approach for the enforcement of periodic boundary conditions on arbitrarily generated meshes*. Computer Methods in Applied Mechanics and Engineering, 274: 168–191.
- [279] RICE, J. [1968]: *Mathematical analysis in the mechanics of fracture*. Academic Press, New York, chapter 3 of fracture: An advanced treatise edition, 3: 191–311.
- [280] SARGADO, J.; KEILEGAVLEN, E.; BERRE, I.; NORDBOTTEN, J. [2017]: *High-accuracy phase-field models for brittle fracture based on a new family of degradation functions*. Journal of the Mechanics and Physics of Solids.
- [281] SCHÄFER, N.; GUDŽULIĆ, V.; TIMOTHY, J. J.; BREITENBÜCHER, R.; MESCHKE, G. [2019]: *Fatigue behavior of hpc and frc under cyclic tensile loading: Experiments and modeling*. Structural Concrete, 20(4): 1265–1278.
- [282] SCHLANGEN, E.; VAN MIER, J. [1992]: *Micromechanical analysis of fracture of concrete*. International Journal of Damage Mechanics, 1(4): 435–454.
- [283] SCHREFLER, B. A.; SECCHI, S.; SIMONI, L. [2006]: *On adaptive refinement techniques in multi-field problems including cohesive fracture*. Computer Methods in Applied Mechanics and Engineering, 195(4): 444 – 461. Adaptive Modeling and Simulation.
- [284] SEITZ, A.; FARAH, P.; KREMHELLER, J.; WOHLMUTH, B. I.; WALL, W. A.; POPP, A. [2016]: *Isogeometric dual mortar methods for computational contact mechanics*. Computer Methods in Applied Mechanics and Engineering, 301: 259–280.
- [285] SELEŠ, K.; JURČEVIĆ, A.; TONKOVIĆ, Z.; SORIĆ, J. [2019]: *Crack propagation prediction in heterogeneous microstructure using an efficient phase-field algorithm*. Theoretical and Applied Fracture Mechanics, 100: 289–297.
- [286] SICSIC, P.; MARIGO, J.-J. [2013]: *From gradient damage laws to griffith’s theory of crack propagation*. Journal of Elasticity, 113: 55–74.
- [287] SIMO, J. C. [1988]: *A framework for finite strain elastoplasticity based on maximum plastic dissipation and the multiplicative decomposition. part II: Computational aspects*. Computer Methods in Applied Mechanics and Engineering, 68: 1–31.
- [288] SIMO, J. C.; MIEHE, C. [1992]: *Associative coupled thermoplasticity at finite*

- strains: formulation, numerical analysis and implementation*. Computer Methods in Applied Mechanics and Engineering, 98: 41–104.
- [289] SIMÓ, J. C.; TAYLOR, R. L.; PISTER, K. S. [1985]: *Variational and projection methods for the volume constraint in finite deformation elasto-plasticity*. 51: 177–208.
- [290] SINGH, N.; VERHOOSSEL, C.; BRUMMELEN, E. VAN [2018]: *Finite element simulation of pressure-loaded phase-field fractures*. Meccanica, 53(6): 1513–1545.
- [291] SOBOLEV, K.; SHAH, S. [2008]: *Nanotechnology of concrete: recent developments and future perspectives*. ACI.
- [292] SONG, Y.; YOUN, S.; PARK, K. [2015]: *A gap element for treating non-matching discrete interfaces*. International Journal for Numerical Methods in Engineering, 56(3): 551–563.
- [293] STAINIER, L.; ORTIZ, M. [2010]: *Study and validation of thermomechanical coupling in finite strain visco-plasticity*. International Journal of Solids and Structures, 47: 704–715.
- [294] STAINIER, L.; CUITINO, A.; ORTIZ, M. [2002]: *A micromechanical model of hardening, rate sensitivity and thermal softening in bcc single crystals*. Journal of the Mechanics and Physics of Solids, 50(7): 1511 – 1545.
- [295] STEINKE, C.; KALISKE, M. [2019]: *A phase-field crack model based on directional stress decomposition*. Computational Mechanics, 63(5): 1019–1046.
- [296] SVENDSEN, B.; BARGMANN, S. [2010]: *On the continuum thermodynamic rate variational formulation of models for extended crystal plasticity at large deformation*. Journal of the Mechanics and Physics of Solids, 58: 1253–1271.
- [297] TAKEI, A.; ROMAN, B.; BICO, J.; HAMM, E.; MELO, F. [2013]: *Forbidden directions for the fracture of thin anisotropic sheets: An analogy with the wulff plot*. Physical Review Letters, 110: 144301.
- [298] TAYLOR, R. L.; ARTIOLI, E. [2018]: *VEM for Inelastic Solids*, Vol. 46, pp. 381–394. Springer International Publishing.
- [299] TEICHTMEISTER, S.; KIENLE, D.; ALDAKHEEL, F.; KEIP, M.-A. [2017]: *Phase field modeling of fracture in anisotropic brittle solids*. International Journal of Non-Linear Mechanics, 97: 1–21.
- [300] TERZAGHI, K. [1943]: *Theoretical soil mechanics*. johnwiley & sons. New York, pp. 11–15.
- [301] THOMAS, J. W. [2013]: *Numerical partial differential equations: finite difference methods*, Vol. 22. Springer Science & Business Media.
- [302] TOMANN, C.; ONESCHKOW, N. [2019]: *Influence of moisture content in the microstructure on the fatigue deterioration of high-strength concrete*. Structural Concrete, 20(4): 1204–1211.
- [303] TOMANN, C.; LOHAUS, L.; ALDAKHEEL, F.; WRIGGERS, P. [2019]: *Influence of water-induced damage mechanisms on the fatigue deterioration of high-strength concrete*. Proceedings of 6th International fib Congress: Concrete - innovations in materials, design and structures.
- [304] ULLOA, J.; WAMBACQ, J.; ALESSI, R.; DEGRANDE, G.; FRANÇOIS, S. [2019]: *Phase-field modeling of fatigue coupled to cyclic plasticity in an energetic formulation*. arXiv preprint arXiv:1910.10007.
- [305] UNGER, J. F.; ECKARDT, S.; KÖNKE, C. [2007]: *Modelling of cohesive crack growth in concrete structures with the extended finite element method*. Computer

- Methods in Applied Mechanics and Engineering, 196(41): 4087–4100.
- [306] UNGER, J. F.; ECKARDT, S.; KOENKE, C. [2011]: *A mesoscale model for concrete to simulate mechanical failure*. Computers & Concrete, 8(4): 401–423.
- [307] VERHOOSSEL, C. V.; BORST, R. DE [2013]: *A phase-field model for cohesive fracture*. International Journal for Numerical Methods in Engineering, 96: 43–62.
- [308] VOYIADJIS, G. Z.; PEKMEZI, G.; DELIKTAS, B. [2010]: *Nonlocal gradient-dependent modeling of plasticity with anisotropic hardening*. International Journal of Plasticity, 26: 1335–1356.
- [309] VOYIADJIS, Z.; FAGHIHI, D. [2012]: *Thermo-mechanical strain gradient plasticity with energetic and dissipative length scales*. International Journal of Plasticity, 30–31: 218–247.
- [310] WANG, K.; SUN, W. [2017]: *A unified variational eigen-erosion framework for interacting brittle fractures and compaction bands in fluid-infiltrating porous media*. Computer Methods in Applied Mechanics and Engineering, 318: 1–32.
- [311] WCISLO, B.; PAMIN, J. [2016]: *Local and non-local thermomechanical modeling of elastic-plastic materials undergoing large strains*. International Journal for Numerical Methods in Engineering, 109: 102–124.
- [312] WHEELER, J.; WHEELER, M. [2019]: *IPARS, A New Generation Framework for Petroleum Reservoir Simulation, Technical Reference*. <http://csm.ices.utexas.edu/ipars/>.
- [313] WHEELER, M.; WICK, T.; WOLLNER, W. [2014]: *An augmented-lagrangian method for the phase-field approach for pressurized fractures*. Computer Methods in Applied Mechanics and Engineering, 271: 69–85.
- [314] WICK, T. [2016]: *Goal functional evaluations for phase-field fracture using PU-based DWR mesh adaptivity*. Computational Mechanics, 57(6): 1017–1035.
- [315] WICK, T. [2017]: *Modified Newton methods for solving fully monolithic phase-field quasi-static brittle fracture propagation*. Computer Methods in Applied Mechanics and Engineering, 325: 577 – 611.
- [316] WICK, T. [2017]: *An error-oriented Newton/inexact augmented Lagrangian approach for fully monolithic phase-field fracture propagation*. SIAM Journal on Scientific Computing, 39(4): B589–B617.
- [317] WICK, T.; SINGH, G.; WHEELER, M. [2016]: *Fluid-filled fracture propagation using a phase-field approach and coupling to a reservoir simulator*. SPE Journal, 21(03): 981–999.
- [318] WILSON, Z. A.; LANDIS, C. M. [2016]: *Phase-field modeling of hydraulic fracture*. Journal of the Mechanics and Physics of Solids, 96: 264 – 290.
- [319] WITTMANN, F. [1983]: *Structure of concrete with respect to crack formation*. Fracture mechanics of concrete, 43(5): 6.
- [320] WOHLMUTH, B. [2011]: *Variationally consistent discretization schemes and numerical algorithms for contact problems*. Acta Numerica, 20: 569–734.
- [321] WOHLMUTH, B. [2000]: *A mortar finite element method using dual spaces for the lagrange multiplier*. SIAM Journal on Numerical Analysis, 38(3): 989–1012.
- [322] WOHLMUTH, B. [2002]: *A comparison of dual lagrange multiplier spaces for mortar finite element discretizations*. ESAIM: Mathematical Modelling and Numerical Analysis - Modélisation Mathématique et Analyse Numérique, 36(6): 995–1012.
- [323] WRIGGERS, P. [2008]: *Nonlinear Finite Elements*. Springer, Berlin, Heidelberg, New York.

- [324] WRIGGERS, P.; HUDOBIVNIK, B. [2017]: *A low order virtual element formulation for finite elasto-plastic deformations*. Computer Methods in Applied Mechanics and Engineering, 327: 459–477.
- [325] WRIGGERS, P.; J.KORELC [1996]: *On enhanced strain methods for small and finite deformations of solids*. Computational Mechanics, 18: 413–428.
- [326] WRIGGERS, P.; REESE, S. [1996]: *A note on enhanced strain methods for large deformations*. Computer Methods in Applied Mechanics and Engineering, 135: 201–209.
- [327] WRIGGERS, P.; MIEHE, C.; KLEIBER, M.; SIMÓ, J. [1992]: *A thermomechanical approach to the necking problem*. International Journal for Numerical Methods in Engineering, 33: 869–883.
- [328] WRIGGERS, P.; RUST, W. T.; REDDY, B. D. [2016]: *A virtual element method for contact*. Computational Mechanics, 58(6): 1039–1050.
- [329] WRIGGERS, P.; REDDY, B.; RUST, W.; HUDOBIVNIK, B. [2017]: *Efficient virtual element formulations for compressible and incompressible finite deformations*. Computational Mechanics, 60: 253–268.
- [330] WRIGGERS, P.; HUDOBIVNIK, B.; KORELC, J. [2018]: *Efficient Low Order Virtual Elements for Anisotropic Materials at Finite Strains*, pp. 417–434. Springer International Publishing, Cham.
- [331] WRIGGERS, P.; HUDOBIVNIK, B.; SCHRÖDER, J. [2018]: *Finite and Virtual Element Formulations for Large Strain Anisotropic Material with Inextensive Fibers*, pp. 205–231. Springer International Publishing, Cham.
- [332] WRIGGERS, P.; ALDAKHEEL, F.; HUDOBIVNIK, B. [2019]: *Application of the virtual element method in mechanics*. GAMM-Rundbriefe, pp. 4–10. ISSN: 2196-3789.
- [333] WRIGGERS, P.; HUDOBIVNIK, B.; ALDAKHEEL, F. [2020]: *A virtual element formulation for general element shapes*. Submitted to Computational Mechanics.
- [334] WRIGGERS, P.; MOFTAH, S. [2006]: *Mesoscale models for concrete: Homogenisation and damage behaviour*. Finite elements in analysis and design, 42(7): 623–636.
- [335] WULFINGHOFF, S.; BÖHLKE, T. [2012]: *Equivalent plastic strain gradient enhancement of single crystal plasticity: theory and numerics*. Proceedings of the Royal Society of London A: Mathematical, Physical and Engineering Sciences.
- [336] XIA, L.; YVONNET, J.; GHABEZLOO, S. [2017]: *Phase field modeling of hydraulic fracturing with interfacial damage in highly heterogeneous fluid-saturated porous media*. Engineering Fracture Mechanics, 186: 158–180.
- [337] YANG, Q.; STAINIER, L.; ORTIZ, M. [2006]: *A variational formulation of the coupled thermo-mechanical boundary-value problem for general dissipative solids*. Journal of the Mechanics and Physics of Solids, 54: 401–424.
- [338] YIN, B.; KALISKE, M. [2020]: *A ductile phase-field model based on degrading the fracture toughness: Theory and implementation at small strain*. Computer Methods in Applied Mechanics and Engineering, 366: 113068.
- [339] ZEMENTWERKE EV, V. D. [2002]: *Zement-Taschenbuch 2002. 50. Ausgabe*. Verlag Bau und Technik, Düsseldorf.
- [340] ZHANG, S.; OSKAY, C. [2015]: *Variational multiscale enrichment method with mixed boundary conditions for elasto-viscoplastic problems*. Computational Mechanics, 55(4): 771–787.
- [341] ZHANG, X.; VIGNES, C.; SLOAN, S. W.; SHENG, D. [2017]: *Numerical evalua-*

- tion of the phase-field model for brittle fracture with emphasis on the length scale.* Computational Mechanics, 59(5): 737–752.
- [342] ZHOU, S.; ZHUANG, X.; ZHU, H.; RABCUK, T. [2018]: *Phase field modelling of crack propagation, branching and coalescence in rocks.* Theoretical and Applied Fracture Mechanics, 96: 174–192.
- [343] ZHOU, S.; ZHUANG, X.; RABCUK, T. [2019]: *Phase-field modeling of fluid-driven dynamic cracking in porous media.* Computer Methods in Applied Mechanics and Engineering, 350: 169–198.
- [344] ZIENKIEWICZ, O. C.; TAYLOR, R. L. [2000]: *The Finite Element Method*, Vol. 1. Butterworth-Heinemann, Oxford, UK, 5th Edition.
- [345] ZIENKIEWICZ, O. C.; TAYLOR, R.; ZHU, J. Z. [2005]: *The finite element method: Its basis and fundamentals.* Elsevier.
- [346] ZREID, I.; KALISKE, M. [2018]: *A gradient enhanced plasticity–damage microplane model for concrete.* Computational Mechanics, 62(5): 1239–1257.

Curriculum Vitae

Personal Data

Name: Fadi Aldakheel
Date of Birth: January 01, 1984
Place of Birth: Deirazzor, Syria
Marital Status: Married with two children

University Education

2001 – 2006 Bachelor studies of Mechanical Engineering (*2nd Best Student*), Aleppo University, Syria
2009 – 2011 Master studies in Computational Mechanics of Materials and Structures COMMAS (*Honor Roll Student*), University of Stuttgart
2011 – 2016 PhD studies in Computational Mechanics (*summa cum laude*), University of Stuttgart

Professional Occupation

2006 – 2009 Teaching assistant, Faculty of Petrochemical Engineering, Alfurat University, Syria
2011 – 2017 Research associate and teaching assistant, Institute of Applied Mechanics (Civil Engineering), University of Stuttgart
2012 – 2014 Examination officer master of science study-program COMMAS, University of Stuttgart
2014 – 2017 COMMAS course director, Institute of Applied Mechanics, University of Stuttgart
Since 2017 Group Leader *Material Modeling and Damage Mechanics* at the Institute of Continuum Mechanics, Leibniz Universität Hannover LUH
2020 – 2021 Chief Engineer at the Institute of continuum mechanics, LUH

